

Non-located methods to infer deformation in steel structures

The magnetomechanical effect in cylindrical structures subjected to impact loads

Meijers, P.C.

DOI

[10.4233/uuid:8d278e8f-0972-4d96-8acf-1dcd1cd0e358](https://doi.org/10.4233/uuid:8d278e8f-0972-4d96-8acf-1dcd1cd0e358)

Publication date

2021

Document Version

Final published version

Citation (APA)

Meijers, P. C. (2021). *Non-located methods to infer deformation in steel structures: The magnetomechanical effect in cylindrical structures subjected to impact loads*. [Dissertation (TU Delft), Delft University of Technology]. <https://doi.org/10.4233/uuid:8d278e8f-0972-4d96-8acf-1dcd1cd0e358>

Important note

To cite this publication, please use the final published version (if applicable). Please check the document version above.

Copyright

Other than for strictly personal use, it is not permitted to download, forward or distribute the text or part of it, without the consent of the author(s) and/or copyright holder(s), unless the work is under an open content license such as Creative Commons.

Takedown policy

Please contact us and provide details if you believe this document breaches copyrights. We will remove access to the work immediately and investigate your claim.

Non-collocated methods to infer deformation in steel structures

THE MAGNETOMECHANICAL EFFECT IN CYLINDRICAL
STRUCTURES SUBJECTED TO IMPACT LOADS

Non-collocated methods to infer deformation in steel structures

THE MAGNETOMECHANICAL EFFECT IN CYLINDRICAL
STRUCTURES SUBJECTED TO IMPACT LOADS

Proefschrift

ter verkrijging van de graad van doctor
aan de Technische Universiteit Delft,
op gezag van de Rector Magnificus Prof.dr.ir. T.H.J.J. van der Hagen,
voorzitter van het College voor Promoties,
in het openbaar te verdedigen op dinsdag 25 mei 2021 om 12:30 uur

door

Peter Christiaan MEIJERS

civiel ingenieur, Technische Universiteit Delft, Nederland
geboren te Woudrichem, Nederland.

Dit proefschrift is goedgekeurd door de
promotor: Prof.dr. A.V. Metrikine
copromotor: Dr.ir. A. Tsouvalas

Samenstelling promotiecommissie:

Rector Magnificus,	voorzitter
Prof.dr. A.V. Metrikine,	Technische Universiteit Delft, promotor
Dr.ir. A. Tsouvalas,	Technische Universiteit Delft, copromotor

Onafhankelijke leden:

Prof.dr.ir. E.C. Slob	Technische Universiteit Delft
Prof.dr. P.G. Steeneken	Technische Universiteit Delft
Prof.dr. W. Lacarbonara	Sapienza Università di Roma, Italië
Prof.dr. R. Kouhia	Tampere University of Technology, Finland
Prof.dr. L. Cheng	The Hong Kong Polytechnic University, China

This work is part of the research programme EUROS with project number I4186, which is (partly) financed by the Dutch Research Council (NWO).



Keywords: non-contact measurement, magnetomechanical effect, impact pile driving, large-diameter monopile, plastic deformation, structural health monitoring

Printed by: Gildeprint – Enschede

Front & Back: Enjoying the night sky

Fonts: Alegreya, Alegreya Sans, Asana Math, Ysabeau, Zilla Slab

Copyright © 2021 by P. C. Meijers

ISBN 978-94-6384-217-4

An electronic version of this dissertation is available at
<https://repository.tudelft.nl/>.

*How I could suffer for you
You fascinate and magnetise me*

Bloc Party – *Halo*

Contents

Summary	xi
Samenvatting	xv
Preface	xix
1 Introduction	1
1.1 Problem statement and motivation	2
1.2 Thesis objective	5
1.3 Scope of the research	6
1.4 Thesis outline	7
2 Pile driving dynamics	9
2.1 State of the art of pile driving modelling	10
2.2 Governing equations for elastic deformation of a cylindrical shell	12
2.2.1 Donnell–Mushtari shell theory	12
2.2.2 Governing equations for axi-symmetric deformation.	15
2.2.3 Dispersion characteristics of axially symmetric shells	15
2.2.4 Comparison of the shell theories for a large-diameter monopile	17
2.3 Inclusion of physical non-linearity	19
2.3.1 Plastic deformation in metals	19
2.3.2 Components of the stress and strain tensors.	21
2.3.3 One-dimensional physically non-linear theory.	23
2.4 Soil-structure interaction	24
2.4.1 One-dimensional dispersive driveability model	25
2.4.2 Case set-up	27
2.4.3 Influence of dispersion on the driveability.	28
2.5 Conclusions.	29
3 Quantifying physical damage with non-collocated contact measurements	31
3.1 Method to quantify plastic deformation.	32
3.2 Validation against a lab-scale experiment	36
3.3 Generalisation and limitations	39
3.4 Conclusions.	40

4	Magnetomechanics of steel cylinders	43
4.1	Physics of ferromagnetic materials	44
4.1.1	Magnetic domains.	44
4.1.2	Macroscopic description of ferromagnetism.	46
4.1.3	The magnetisation curve.	47
4.1.4	An hysteretic magnetisation	48
4.2	Magnetomechanical effects	50
4.2.1	External magnetic field	52
4.2.2	Elastic and plastic deformation.	52
4.2.3	Loading history	53
4.2.4	Demagnetising field.	53
4.2.5	Strain rate	55
4.2.6	Discussion	55
4.3	Applications of the magnetomechanical effect	56
4.3.1	Active methods	56
4.3.2	Passive methods	56
4.3.3	Discussion	58
4.4	Magnetomechanical models	59
4.4.1	Particle models	59
4.4.2	Multi-scale models	60
4.4.3	Jiles–Atherton models	61
4.4.4	Discussion	63
4.5	Modelling of the stray field.	64
4.5.1	Magnetostatic equations.	65
4.5.2	The magnetic scalar potential	66
4.5.3	Discretisation of the thin-walled structure.	67
4.5.4	Magnetisation of a cylinder induced by an external field	70
4.5.5	Magnetisation and magnetic stray field due to particular external fields.	71
4.5.6	Discussion	76
4.6	Conclusions	76
5	The remanent magnetic stray field and its sensitivity to physical damage	79
5.1	Irreversible changes of the magnetic stray field	80
5.2	Laboratory-scale experiment	81
5.2.1	Experimental set-up	81
5.2.2	Sensor description.	83
5.2.3	Sources of error	83
5.2.4	Measurement phases	85

5.3	Evolution of the remanent stray field in the elastic regime	85
5.3.1	Measurement procedure.	85
5.3.2	Results	86
5.3.3	Discussion	89
5.4	Detecting and localising regions of plastic deformation	89
5.4.1	Measurement procedure.	89
5.4.2	Results	90
5.4.3	Discussion	96
5.5	Limitations of the method to detect plastic zones	98
5.5.1	The initial magnetic state	98
5.5.2	Application of the load.	99
5.5.3	Sensor position	100
5.6	Generalisation of the proposed method.	100
5.6.1	Quantifying the plastic strain.	100
5.6.2	Pure tensile loads	100
5.6.3	Other load types.	101
5.6.4	Fatigue damage.	101
5.7	Conclusions.	102
6	Strain-induced transient components of the magnetic stray field	103
6.1	Transient strain field generated by an axial impact.	104
6.1.1	Measured impact-induced axial strain	104
6.1.2	Governing equations for an axially symmetric cylinder	105
6.1.3	Simulated impact-induced strain field	108
6.2	Analysis of the transient magnetic stray field	111
6.2.1	Sensor selection and positioning	112
6.2.2	Processing the measured quantities	113
6.2.3	Evolution of the stray field towards a magnetic equilibrium.	116
6.2.4	Consistency of the measured signals	118
6.2.5	Influence of impact height and sensor position	119
6.2.6	Discussion	123
6.3	Modelling the strain-induced transient magnetisation	125
6.3.1	Vectorial effective field for an isotropic magnetoelastic solid subjected to uniaxial stress	126
6.3.2	Computation of the impact-induced transient stray field.	129
6.3.3	Simulated transient stray field	132
6.4	Analysis of the modelling discrepancies.	133
6.4.1	Contributions of circumferential magnetic modes	133
6.4.2	Magnetic anisotropy.	135
6.4.3	Irreversible magnetisation	139

6.5	Generalisation and limitations	140
6.6	Conclusions	141
7	In-situ magnetomechanical response of a steel monopile during pile driving	143
7.1	Set-up of the measurement campaign	144
7.1.1	Sensor description and positioning	146
7.1.2	Measurement systems	147
7.1.3	Data processing	148
7.2	Analysis of data collected by the reduced measurement system	150
7.2.1	Response of the sleeve-based sensors	151
7.2.2	Response of the ground-based sensor	153
7.3	Analysis of data collected by the full measurement system	155
7.3.1	Hammer-induced axial strain	156
7.3.2	Correlation between strain and magnetic stray field measurements	160
7.3.3	Analysis of the impact characteristics	161
7.4	Sources of interference	164
7.4.1	Evolution towards a magnetic equilibrium	164
7.4.2	Magnetic stray fields of other ferromagnetic objects	166
7.4.3	Cap pressure	166
7.4.4	Rotation of the hammer-sleeve assembly	166
7.5	Non-contact strain measurement	167
7.6	Pile penetration monitoring	170
7.6.1	Modelling the pile's stray field	171
7.6.2	Model for the magnetic susceptibility	172
7.6.3	Simulated magnetic signature	173
7.6.4	Discussion	173
7.7	Conclusions	174
8	Conclusions	177
	Bibliography	183
A	Isotropic anhysteretic magnetisation	205
B	Full relations to compute the magnetic field of a thin-walled cylinder	207
B.1	Cartesian coordinates	208
B.2	Cylindrical coordinates	210
B.3	Restrictions on the element size	210
C	Effective stress for coaxial fields	213
	Curriculum Vitæ	215
	List of Publications	217

Summary

Increasing demand for energy from renewable sources has resulted in ambitious plans to construct a large number of offshore wind farms in the coming years. In relatively shallow water depths, the preferred support structure for wind turbines is the steel monopile, which is a thin-walled cylindrical structure. To decrease the cost of the generated electricity, larger wind power generators are commissioned, which has led to a significant increase of the size of the foundation piles. Currently, monopiles are most frequently driven into the seabed by means of hydraulic impact hammering. Aided by the compressive stress wave generated by each hammer blow, the pile gradually progresses to the desired penetration depth.

The stress generated by each hammer blow can inflict plastic deformations at the pile head, which can jeopardise the delicate alignment required for the bolted connection between the superstructure and the monopile. Furthermore, the repeated elastic deformation of the pile leads to material fatigue, which reduces the service life of the structure. Hence, monitoring the deformation and stress resulting from the hammer blows is vital to assess the structural health. Offshore, however, dedicated sensors are seldom employed, due to time constraints and the harsh marine environment. In addition, contact sensors can easily be damaged by hammer-induced high-amplitude strains. To this end, this thesis develops several alternative methods to monitor the deformation in a monopile during installation. These methods are non-collocated (i.e. a quantity is measured at certain location to infer the structural quantity of interest at another position), and, preferably, non-contact.

By considering the propagation of elasto-plastic waves, a non-collocated method to quantify the amount of plastic deformation inflicted by a hammer blow is first proposed. As a part of the energy contained in the stress wave excited by the hammer blow is used to permanently deform the structure, the stress wave becomes distorted. At a certain distance below the pile head, the energy flux is determined that is carried out by the stress wave through a cross-section of the pile. The difference between the measured value and the expected energy flux from a linear-elastic simulation with the same hammer forcing provides an upper bound for the amount plastic deformation inflicted by a hammer blow. The main benefit of this proposed method is that the sensors are employed outside the region where the highest strains occurs, reducing the risk of damaging the sensors. However, data is collected with sensors which are attached to the pile, leaving the aforementioned restrictions to the sensor deployment in place. To enable the widespread monitoring of steel structures subjected to dynamics loads, non-contact methods are needed.

For the development of a non-contact method to infer the hammer-induced deformations, the magnetic stray field of the steel structure is analysed, which permeates the space

around it. As the structure's magnetisation depends on elastic and plastic strains through the magnetomechanical effect, it is expected that the magnetic stray field, which is generated by the magnetisation, conveys the information about the present strain state of the structure to the sensor. Contrary to experiments on the magnetomechanical response of structural steel reported in literature so far, a steel cylinder has a significant demagnetising field due to its geometry, creating a non-uniform spatial distribution of the magnetisation. Additionally, magnetomechanical data under dynamic loads are scarce. Hence, a unique laboratory-scale experiment was designed, in which a steel cylinder was repeatedly impacted by a free-falling concrete mass, providing the first insights into the magnetomechanical effect in dynamically-loaded structures with a substantial demagnetising field.

In between impacts, the magnetic stray field was mapped to analyse the evolution of the remanent stray field, i.e. the stray field when the structure is unloaded. Due to repeated impacts which only generate elastic strains in the structure, the remanent stray field evolves towards a metastable magnetic equilibrium. When a new peak strain is introduced, the stray field converges towards a new equilibrium, displaying a tendency towards a global magnetic equilibrium. However, as soon as plastic deformation forms, the evolution of the remanent field deviates from this trend as a result of the increased dislocation density, which, in turn, reduces the material's ability to remain magnetised. This behaviour serves as a basis for a non-contact method to detect and localise regions of plastic deformation in a steel structure subjected to repeated impact loads. This novel method is the first non-contact technique to infer structural deformation proposed in this dissertation.

In the lab-scale experiment, strain gauges and a magnetometer registered the transient magnetomechanical response during each impact. When the magnetisation is at a magnetic equilibrium, a strong correlation is found between the axial strain and the magnetic field variation around the remanent state. The amplitude and direction of the transient magnetic stray field varies with the circumferential position of the magnetometer, indicating that the response is partly determined by the magnetisation in the vicinity of the sensor. To simulate the measured response, an isotropic magnetomechanical model was developed in this thesis that, for the first time, accounts for the demagnetising field of the structure. The capability of this model to reproduce the measurement results are limited though. It is envisaged that the model may be improved by accounting for anisotropy and by including the remanent magnetisation.

To date, limited data have been published on the in-situ magnetomechanical response of large-scale steel structures in a weak ambient magnetic field. Consequently, an in-situ measurement campaign was performed to measure the magnetomechanical response of a monopile installed onshore with a hydraulic impact hammer. During the campaign, several magnetometers were employed using different sensor configurations. Similar to the lab-scale experiment, the position of the magnetometer relative to the pile determines the amplitude and direction of the transient magnetic field. Next to a good correspondence between the strain and magnetic signals, a polynomial relation was found between the

peak strain and the maximum deviation from the remanent field expressed along the major principle axis. Using the inverse of this relation and a magnetometer which retains its position with respect to the pile, a novel method to infer the elastic strain from the transient stray field is proposed, which shows a promising correspondence between the inferred and measured strain signals. Additionally, the working principles for a new alternative technique to monitor the pile penetration using non-contact sensors are proposed.

For each of the four non-collocated methods introduced in this work, directions for improvements and steps to generalise the techniques are discussed. The main benefit of the non-contacts methods in particular is that they eliminate the onerous process of attaching the sensors, enabling swift deployment and providing the opportunity to reuse the sensors. Although the new methods in this dissertation have mainly been applied to the installation of monopiles, the potential application of these non-collocated methods is much wider. Ultimately, they could be used to monitor any large-scale steel structure subjected to dynamic loads.

Samenvatting

NNaar aanleiding van de toenemende vraag naar duurzaam opgewekte energie zijn er voor de komende jaren ambitieuze plannen ontwikkeld voor de bouw van een groot aantal windparken op zee. In geringe waterdieptes is de meestgebruikte funderingsconstructie voor windturbines de stalen monopaal. Dat is een dunwandige, cilindrische constructie. Om de kosten voor de opgewekte elektriciteit te verlagen, worden steeds grotere windturbines ontworpen. Dit heeft geleid tot een significante toename in grootte van de funderingspalen. Op dit moment worden monopalen meestal in de zeebodem geplaatst met behulp van een hydraulische heimachine. Door middel van de drukgolf die elke slag van de heimachine opwekt, wordt de paal geleidelijk naar de gewenste diepte gebracht.

De door de slaghamer gegenereerde materiaalspanningen kunnen lokaal plastische vervormingen veroorzaken in de paalkop. Deze vervorming kan de precieze uitlijning verstoren die nodig is voor de gebouwte verbinding tussen de paal en de bovenbouw. Verder kan de herhaalde elastische vervorming van de paal leiden tot metaalmoeheid, wat de levensduur van de constructie verkort. Daarom is het monitoren van de vervormingen en spanningen ten gevolge van de hamerslagen essentieel voor de beoordeling van de bouwkundige staat van de constructie. Toch worden voor dit doeleinde ontwikkelde sensoren zelden op zee toegepast vanwege tijdsdruk en het barre milieu. Sensoren die in contact staan met de constructie kunnen bovendien snel beschadigen door de krachten die een hamerslag opwekt. Daarom worden in dit proefschrift alternatieve methodes ontwikkeld om tijdens het heiproces de vervormingen in een monopaal te monitoren. Deze methodes zijn *non-located* en, bij voorkeur, contactloos. In een *non-located* meetmethode wordt een grootte die gemeten is op een bepaalde plaats gebruikt om de grootte van belang op een andere locatie te herleiden.

De eerste *non-located* methode om plastische vervormingen ten gevolge van een hamerslag te kwantificeren is gebaseerd op de voortplanting van elasto-plastische spanningsgolven. Omdat een deel van de energie van de spanningsgolf verbruikt wordt om de constructie permanent te vervormen verandert de spanningsgolf van vorm. Op een bepaalde afstand onder de kop van de paal kan de energieflex door de paaldoorsnede gemeten worden die de spanningsgolf met zich meebrengt. Het verschil tussen de gemeten waarde en de waarde van energieflex die verwacht wordt op basis van een lineair-elastische simulatie met dezelfde hamerkracht bepaalt de bovengrens voor de hoeveelheid plastische vervorming. Het voordeel van deze voorgestelde methode is dat de sensoren toegepast worden buiten het gebied waar de grootste vervormingen plaatsvinden. Dit verlaagt het risico dat de sensoren beschadigen. Echter wordt de data in dit geval nog steeds verzameld met een sensor die in

contact staat met de constructie waardoor de bovengenoemde restricties voor de sensorbevestiging blijven gelden. Daarom zijn om het monitoren van stalen constructies onder dynamische belastingen wijdverspreid mogelijk te maken contactloze methodes nodig.

Voor het ontwikkelen van een contactloze methode om de vervormingen ten gevolge van een hamerslag te herleiden wordt het magnetische strooiveld van de stalen constructie bestudeerd. Dit magnetische veld doordringt de ruimte rond de constructie en wordt opgewekt door diens magnetisatie. Vanwege het magnetomechanische effect hangt de magnetisatie af van de lokale elastische en plastische rek. Daar is het de verwachting dat het magnetische strooiveld de informatie over de huidige rektoestand van de constructie contactloos naar de sensor overbrengt. In tegenstelling tot de tot-op-heden-gepubliceerde experimenten met betrekking tot de magnetomechanische reactie van constructiestaal heeft een stalen cilinder een significant demagnetiserend veld vanwege zijn geometrie. Dit veld leidt tot een niet-uniforme ruimtelijke verdeling van de magnetisatie. Verder is magnetomechanische data onder dynamische belastingen schaars. Daarom is er een uniek experiment ontworpen waarin betonnen massa herhaaldelijk op een stalen cilinder valt. Dit experiment biedt de eerste inzichten in het magnetomechanische effect in constructies met een wezenlijk demagnetiserend veld onder dynamische belastingen.

Na elke klap is het magnetisch veld in kaart gebracht om de verloop van het resterende strooiveld, dat wil zeggen het strooiveld van de onbelaste de constructie, te analyseren. Als gevolg van klappen die enkel elastische rekken opwekken in de cilinder evolueert het resterende strooiveld zich naar een metastabiel magnetisch evenwicht. Zodra een nieuwe piekrek geïntroduceerd wordt, convergeert het strooiveld naar een nieuw evenwicht. In het algemeen heeft het strooiveld de neiging zich naar een globaal magnetisch evenwicht te begeven. Echter, zodra plastische vervormingen ontstaan, wijkt de evolutie van het strooiveld van deze trend af. Dit is een gevolg van de toename van de dislocatiedichtheid wat op zijn beurt het vermogen vermindert van het materiaal om gemagnetiseerd te blijven. Dit gedrag fungeert als de basis voor een contactloze methode om gebieden met plastische vervormingen te detecteren en te lokaliseren in stalen constructies die blootgesteld zijn aan herhaalde stootbelastingen. Deze nieuwe methode is de eerste contactloze techniek waarmee vervormingen herleidt kunnen worden die aangedragen is in dit proefschrift.

In het laboratoriumexperiment leggen rekstroken en een magnetometer de magnetomechanische reactie tijdens elke klap vast. Op het moment dat de magnetisatie zich op een magnetisch evenwicht bevindt, is er tijdens een klap een sterke overeenkomst tussen de axiale rek en de variatie van het magnetische veld. De grootte en richting van deze variatie zijn afhankelijk van de positie van de magneetsensor. Dit is een indicatie dat de magnetomechanische reactie gedeeltelijk wordt bepaald door de magnetisatie in de buurt van de sensor. In dit proefschrift is een isotroop magnetomechanisch model ontwikkeld om de gemeten reactie van de constructie te simuleren. Dit model neemt het eerst het effect van het demagnetiserende veld in ogenschouw. Het vermogen van het model om de meetresultaten

te reproduceren is echter beperkt. Het model kan verbeterd worden door anisotropie en de resterende magnetisatie toe te voegen.

Tot op heden is over de in-situ magnetomechanische reactie van stalen constructies in een zwak magnetisch veld slechts beperkte data gepubliceerd. Daarom is meetcampagne uitgevoerd waarin de magnetomechanische reactie van een monopaal gemeten is tijdens een installatie met een hydraulische heimachine. Tijdens deze meetcampagne zijn meerdere magnetometers gebruikt in verschillende configuraties. Net als in het laboratoriumexperiment bepaalt de positie van de magnetometer ten opzichte van de paal de grootte en richting van de variatie van het magnetische veld. Behalve een goede overeenkomst tussen de rek- en magnetische veldsignalen is vastgesteld dat het verband tussen de piekwaarde van de rek en de grootste afwijking van de eerste hoofdcomponent van het restveld een polynoom is. Met behulp van deze relatie is een nieuwe contactloze methode voorgesteld om de rek in de constructie te herleiden uit het magnetisch veld. De overeenkomst tussen de herleide en gemeten reksignalen is veelbelovend. Verder is het werkingsprincipe gepresenteerd voor een nieuwe alternatieve techniek om met behulp van contactloze metingen de zakking van een stalen paal te bepalen.

Voor elke methode die geïntroduceerd is in dit proefschrift zijn verbeteringsrichtingen en de mogelijkheden om de technieken te generaliseren beschreven. Het grootste voordeel van in het bijzonder de contactloze methodes is dat zij het lastige bevestigingsproces overbodig maken. Hierdoor kunnen de sensoren snel ingezet en hergebruikt worden. Hoewel de nieuwe methodes hier voornamelijk zijn toegepast op de installatie van monopalen is het potentiële toepassingsgebied van deze non-located methodes veel breder. Uiteindelijk zouden zij gebruikt kunnen worden voor het monitoren van grootschalige stalen constructies onder dynamische belastingen.

Preface

*I'm gonna go home and shut up for a year
And when the year is over I'll reappear and have a solution*

dEUS – *The Architect*

It is often said that, as a scientist, you stand on the shoulders of giants, e.g. Newton (1675, February 5), since you build on top the knowledge gathered by your predecessors. For magnetomechanics, in the end the core of this dissertation, these predecessors are some of the greatest minds in the history of science. For example, the first modern scientific account of magnets, *De Magnete*, was written by the London-based physician William Gilbert (1600/1893). Even though he lived more than four centuries ago, he—just as I do in this work—determined the magnetic field generated by a magnetised object. Naturally, his measurements were qualitative, whereas mine are much more precise. Of course, this difference is due to the enormous progress that has been made over the past 200 years in terms of theory and measurement devices. This progress started with Michael Faraday, who conceived the notion of the magnetic field, and James Clerk Maxwell, who described this field and its interactions mathematically and combined it with the electric field to form the electromagnetic field. Of course, from that point onwards many other giants contributed to the knowledge I used as a basis for my research, and they will be named at a more appropriate point in this dissertation. Personally, I feel honoured to humbly follow in their footsteps.

My personal journey started during primary school, where I was interested in a broad range of topics. Moreover, I spent a lot of time constructing the most incredible structures from K'Nex and Lego. So it was pretty obvious that I was destined to become an engineer. However, the question which type of engineer remained. As I was obsessed with bridges at the end of high school, the choice had become easy: Civil Engineering. However, during my bachelor, I felt that the treated theory was too limited in scope. To broaden my horizon, I took a minor in Applied Physics, which was an eye-opener for me. I came to the conclusion that if Civil Engineering was my true love, then Applied Physics was my mistress. (But perhaps it is the other way around...) To have the best of both worlds, I decided to ensure that during my master multiple branches of physics were touched upon. So, the core of my master was centred around fluid-structure interaction. To continue the multi-physics trend in my PhD research, I was able to combine magnetism with structural dynamics, although

that only became apparent at the end of the first year of my PhD. Based on this journey, I am convinced that the most fascinating things happen where several domains of physics meet.

As you continue reading this thesis, you will encounter quotes taken from the lyrics of some of my favourite bands. These quotes are meant to summarise the essence of each chapter in a sentence or two without rendering the message too abstract. For example, the quote above is an accurate description of the workflow of a PhD, especially during a pandemic. Combined, these referenced songs make up the soundtrack of my PhD.

To be successful in academia, simply standing on the shoulders of giants is not enough. Imagine standing alone on top of this enormous mountain of knowledge, trying to withstand the metaphorical head winds, which one may expect at these heights. Keeping you balance up there just by yourself would be an unbearable task for anyone. Fortunately, many people supported me during this project—each in their own way.

First, I want to thank my colleagues for the countless coffee breaks, crazy Christmas dinners and piles of PSOR visits. Thanks to you I cherish many good memories from my time as a PhD. I will not name all of you, as I am doomed to forget some, but realise that I could not have done this without you. Nonetheless, some of you deserve additional thanks. Frank, you showed me the ins and outs of being a PhD, which includes quitting work at 1 pm on a Tuesday to philosophise in the Doerak. Dominik, when we started our PhDs we were the youngsters of the group, but that did not stop up from organising one of the best Christmas parties the group had seen in years. Pim, Timo, you were always up for a good discussion, which were not restricted to work-related topics.

For the lab experiment, I would first like to thank Chris Jolink, "who fought alongside me in the trenches," as you aptly phrased it in the preface of your MSc thesis. Together we managed to find our way out of the maze of seemingly contradictory data, tedious measurement procedures, swinging tree trunks, painstaking floor computations, inaccurate sensors, migrating measurement tables and lengthy periods of downtime. Additionally, the lab experiment was impossible without help of the technicians and support staff of the Stevin lab: Fred Schilperoort, Ruben Kunz, Peter de Vries, John Hermsen, Giorgos Stamoulis, Marten van der Meer, Paul Vermeulen and Ronald van Leeuwen. Moreover, thanks to Léon Roessen and Bert Bakker, who fabricated some of the custom parts in the set-up, and to Ton Blom and Maiko van Leeuwen, who assured the lab experiment (quite literally) became concrete reality. Finally, I owe a great deal to the amazing work of Kees van Beek, who assisted me with the electronics and sensors throughout the lab experiment and the in-situ measurement campaign, for which he designed a dedicated measurement system.

Outside of the university, I would like to thank some people from IHC-IQIP. The discussions with Cornelis van 't Hof and Michael Schaap in the initial stages of the project helped to steer the research into the right direction. In one of these meetings, you turned my attention to the connection between plastic deformation and magnetisation, which turned out to be the golden ticket. In 2019, I got the unique opportunity to measure the magnetomechanical

response of a pile during installation at the IHC-IQIP yard in Sliedrecht. I thank Arjan Roest for the on-site assistance throughout this campaign.

The final colleagues I would like thank are my PhD supervisors, with whom I had countless meetings—AA meetings, as I would call them. Apostolos, thanks for all the extensive discussions we had over the years and for the many times you put me back on track when I was stuck in my own thoughts. Andrei, you are an endless stream of ideas, which is amazing for any starting PhD. In my opinion, your approach to a project can be summarised with a quote by James Clerk Maxwell: "I never try to dissuade a man from trying an experiment; if he does not find what he wants, he may find out something else" (Mahon, 2004, p. 26). For my project this turned out to be more than true. Thank you for your ceaseless support during this whole adventure.

Voor het laatste deel van dit voorwoord schakel ik over naar mijn moerstaal. Juist door het veelvuldig gebruik van het Engels, de *lingua franca* van de academische wereld, heb ik het Nederlands meer leren waarderen. (Al is het schrijven van een goedlopende Nederlandse samenvatting geen gemakkelijke opgave wanneer je vastgeroest zit in de Engelse vaktermen.) En, waarom zou je een vreemde taal gebruiken als de personen tot wie je wilt richten het Nederlands machtig zijn?

Naast mijn collega's had ik dit project nooit tot een goed einde kunnen brengen zonder het luisterende oor van én de broodnodige afleiding door mijn vrienden. Ook hier de kanttekening dat de volgende lijst verre van compleet is. Marijn, bedankt voor het voeden van mijn honger naar natuurkunde via onze onofficiële nerdboekenclub. Arno, een betere ontspanningsmethode dan een muziekconcert/festival kan ik me niet bedenken. Ik vind het geweldig dat we dat al sinds ons zestiende volhouden. Laten we dat in de toekomst ook blijven doen. Unze en Merlin, ik koester onze onbezorgde avonden filosoferen die gepaard gaan met een overmatige bierconsumptie. Dat laatste geldt ook voor avonden met mijn (oud)teamgenoten bij Punch en, na onze overstap, bij Delta.

Zonder mijn familie zou ik nergens zijn. Daarom ben ik mijn moeder, mijn vader en mijn zussen dankbaar voor hun onvoorwaardelijke steun. Bij jullie ben ik altijd op mijn gemak en kan ik alles kwijt, al heb ik jullie de exacte details van mijn bezigheden soms bespaard. Daniëlle, jij bent dat allemaal niet bespaard gebleven. Gelukkig kun je erg goed omgaan met mijn belachelijke perfectionisme en stressvolle momenten. Ondanks dat we al meer dan een jaar thuiswerkcollega's zijn, zijn we nog lang niet klaar met elkaar. Sterker nog, er ligt nog veel moois voor ons in het verschiet. Zonder de gekkigheid van een promovendus. Ik kijk er naar uit om nieuwe uitdagingen op te pakken, samen.

Peter Christiaan Meijers
Delft, April 2021

1

Introduction

*Touching from a distance
Further all the time*

Joy Division – Transmission

DDriven by the ambitious climate goals set out by governments to reduce the emission of greenhouse gasses, the demand for energy generated from renewable sources has soared during the past decade (Perveen et al., 2014). Based on the renewed goals for 2030 and beyond, it is expected that this trend will continue in this new decade (WindEurope, 2020). For countries bordering the North Sea, the most suitable choice from the surfeit of renewable energy sources is wind energy and, in particular, offshore wind energy due to the abundance of wind and space in the marine environment. Typically, wind turbines (Figure 1.1a) are arranged into an offshore wind farm containing a few dozen of these generators.

Despite the plethora of available foundation types for a wind turbine, steel monopiles are the preferred choice in the relatively shallow North Sea (Doherty and Gavin, 2012). Monopiles are thin-walled cylindrical structures with a diameter of several meters and a length of tens of meters. Figure 1.2 shows the size evolution of monopiles used as support structures of offshore wind power generators over the past two decades. The apparent increase in size is a direct consequence of the effort to reduce the cost of the produced electricity by upscaling the wind turbines and constructing wind farms in deeper waters.



Figure 1.1: (a) Wind turbine in the Kentish Flats Offshore Wind Farm. Copyright 2008 by Phil Hollman. (b) Hydraulic impact hammer (IHC-IQIP S350) employed in an onshore monopile installation.

1.1. Problem statement and motivation

In order to drive these large-scale structures into the seabed, several installation techniques exist (Massarsch et al., 2017) or are currently being developed (GROW, 2020). The development of new pile installation techniques is mainly driven by considerations regarding the underwater noise pollution (Tsouvalas and Metrikine, 2016) and the fatigue life of the monopile (Lotsberg et al., 2010a). Despite these developments, however, hydraulic impact hammers (Figure 1.1b) are the preferred choice for monopile installations, which, in 2019, comprise 70% of the newly-installed foundations in European waters (WindEurope, 2020). Each vertical hammer blow generates a compressive stress wave, which propagates downwards along the pile and enables the pile's progression into the seabed. To overcome the increasing soil resistance at greater penetration depths, the input energy of the hammer is raised accordingly. High energy impacts can cause stresses close to the yield limit of the material especially at the pile head, increasing the risk of plastic deformations there.

Until recently, such plastic deformations were of little concern, since the pile head did not contribute to the bearing capacity of the pile due to the use of a grouted connection between the monopile and the superstructure (Jensen et al., 2018). However, more recently, the industry switched to a new connection between the monopile and the superstructure that relies on a bolted flange connection. This design change was necessary as undesired settlements of some grouted connections were registered (Chen et al., 2019; Dallyn et al., 2016). A flanged connection has the additional benefit that it reduces the total cost of wind turbine, as it requires less steel than the grouted version (Gollub et al., 2014). Nevertheless, it does require a perfect alignment between the pile head and the superstructure. Any plastic deformation of the pile head can potentially disturb this delicate alignment (Janele et al., 2015). Additionally, plastic deformation is unfavourable for the service life of the whole structure due to low-cycle fatigue, see Schijve (2009, pp. 161–167). Even when plastic

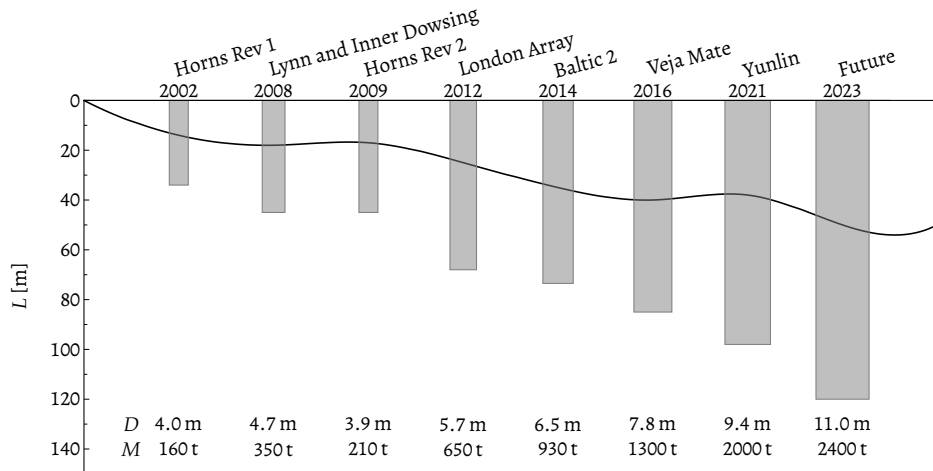


Figure 1.2: Increasing dimensions of monopile foundations for offshore wind over the past two decades. L represents the length of the pile, D denotes the outer diameter at the lower end of the pile and M is the mass of the pile in metric tons. Adapted from Niess (2013), Boskalis (2016) and Nordenham (2019, June 11).

deformations do not develop during the installation, a (significant) part of the structure's service life can be consumed by the application of repeated dynamic loads through high-cycle fatigue, see Schijve (2009, pp. 144–146). Hence, accurate measurement of the induced deformations and stresses during the installation is vital for the general assessment of the stress state and the associated fatigue damage during impact piling.

Next to inferring the stress state, monitoring the strains in the pile during installation provides the means to determine the dynamic response of the pile at the current penetration depth. Based on the estimated response, the hammer energy can be adjusted to maximise the penetration per hammer blow, and to simultaneously reduce the impact on the consumed fatigue life. Normally, the reduction in service life is computed based on measured strain signals in conjunction with a stress wave propagation model similar to the one proposed by Smith (1962). Consequently, it is common practice to measure strains and accelerations during *onshore* pile installations. From these measurements, which are taken a few meters below the pile head, the pile driving process is monitored (Rausche et al., 2009), the consumed fatigue life is estimated (Chung et al., 2013) and the bearing capacity is determined (Webster et al., 2008). Offshore, however, such sensors are rarely employed, as they are difficult to install en prone to damage (Wang et al., 2018a).

Ideally, measured strains and accelerations are used in real-time to assess the state of the support structure, a process called structural health monitoring (Deraemaeker and Worden, 2010). For the identification of structural damage, non-destructive evaluation methods have been developed over the years. In correspondence with the aim of monitoring and evaluation,

the following four stages of increasing accuracy and complexity are distinguished (Rytter, 1993):

1. **Detect** Based on the data, the presence of the quantity of interest is ascertained, yielding a binary result;
2. **Localise** The data provide the location of the quantity of interest;
3. **Quantify** The quantity of interest is quantified from the data;
4. **Prognosticate** The influence of the quantity of interest on the remaining life time of the structure is determined.

Of these stages, the first is purely qualitative, while the latter stages are increasingly quantitative. Ordinarily, these four stages pertain to identification methods for damage in a structure, e.g. a region of plastic deformation, a crack, a delamination, etc. However, one could apply these stages to study the elastic response of the structure, where the relevance of the third and fourth stage is the most apparent, since dynamic loads of small amplitude (i.e. resulting in elastic strains in the structure) can lead to failure of a structural element (high-cycle fatigue). Clearly, when the focus lies on elastic deformations, the first two stages seem trivial, unless one contemplates non-collocated measurements.

To measure a quantity of interest at a desired location, one must employ a sensor. Such a measurement can be classified based on the following three concepts:

- **Contact versus non-contact** The sensor is physically connected to the structure (contact) or not (non-contact);
- **Collocated versus non-collocated** The sensor is installed at the location of interest (collocated) or at a different location (non-collocated). These terms are regularly coined in control techniques (Preumont, 2018);
- **Direct versus indirect** The sensor measures the quantity of interest directly (direct) or a different quantity from which the quantity of interest can be inferred (indirect).

Figure 1.3 exemplifies the differences between the first two terms introduced above. Traditionally, a quantity is measured with a collocated contact measurement (Figure 1.3a), e.g. a strain gauge is glued to the surface of a structure to infer the strain at that location. One could typify such a measurement as classical, since this is the standard approach for measurements. Alternatively, when a sensor attached to the structure is employed to determine the strain at a different location, a non-collocated contact measurement is performed (Figure 1.3b). Finally, when a quantity is determined by a sensor that is not connected to the structure, one speaks of a non-collocated non-contact measurement (Figure 1.3c). By definition, a non-contact measurement is invariably non-collocated, thus, such a measurement can simply be referred to as non-contact. Contrary to classical measurements,

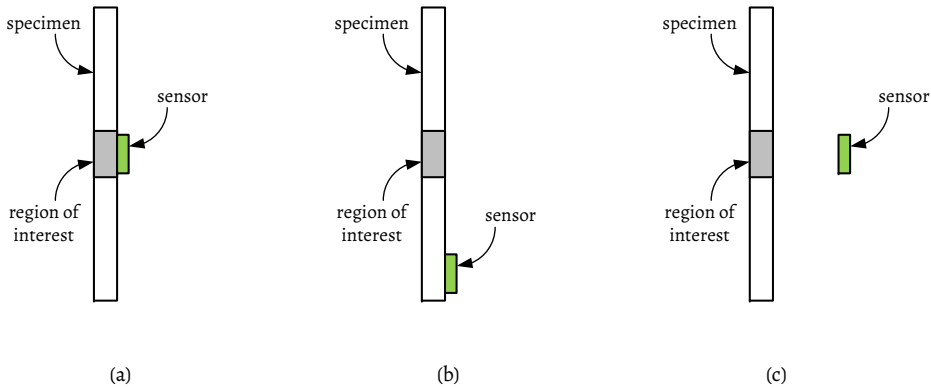


Figure 1.3: Three distinct measurement lay-outs. (a) Collocated contact measurement. (b) Non-collocated contact measurement. (c) Non-collocated non-contact measurement.

information regarding the quantity of interest needs to reach the sensor used during the non-collocated measurement. In case the quantity of interest is a field that persists outside of the structure, one can construct a direct non-contact measurement. However, as this thesis explores methods to infer the strain in a monopile generated by a hammer impact, and since the strain field does not exist outside of the structure, only indirect non-contact methods will be addressed.

1.2. Thesis objective

Offshore, continuous monitoring of the installation of a monopile would provide vital information about the (permanent) structural deformations, the pile penetration process and the bearing capacity (Seaway Heavy Lifting Engineering B.V., 2009; Wisotzki et al., 2019). However, attaching a sensor to the structure is onerous and time consuming, especially in the hostile marine environment (Anderson, 1987; Wang et al., 2018a). As a result, measurement devices are seldom employed during offshore pile driving. Moreover, to infer elastic strain and plastic deformation caused by a hammer blow with a collocated measurement, a sensor is required close to the pile head, where the largest strains are likely to occur. Unfortunately, these high strain levels can damage not only the pile itself, but also the sensors, making strain or acceleration measurements directly at the pile head infeasible during the piling process. Hence, a workable method to infer strains at the pile head should rely on non-collocated measurements. Furthermore, as connecting any sensor to the structure is a laborious process, a non-contact measurement device for impact-induced elastic strain has its own merits over currently used contact sensors.

Given the arguments above, the main objective of this thesis is to develop non-collocated measurement techniques to infer deformations, elastic as well as plastic, which are ap-

plicable to large-scale steel structures subjected to mechanical impact loads. Ideally, data obtained from a proposed non-collocated measurement technique should provide the means to infer elastic and plastic strain, creating a unified framework to simultaneously measure both deformation types. Additionally, the techniques proposed should also consider the difficulties associated with the harsh offshore environment when it comes to the practical issue of implementation of the sensors.

1.3. Scope of the research

A broad range of measurement techniques exists based on different physical aspects of the material or the structure, each of which could serve as a starting point for a non-collocated measurement technique to infer impact-induced deformation. To narrow the possibilities, a method should require as little additional external stimuli (e.g. an excitation signal) next to the sensor itself, since the deployment of supplementary devices in an offshore environment is undesirable. In this thesis, the scope is further limited to non-collocated methods using two distinct physical media: elastic and magnetic, yielding purely mechanical and magnetomechanical methods, respectively.

Purely mechanical methods are quite successful in detecting damage in large-scale structures. For example, Matlack et al. (2015) and Munoz et al. (2015) utilise ultrasonic harmonic waves to identify regions of plastic deformation and cracks by measuring the amplitude of the higher harmonics that are generated by the interaction of the incident waves and the defects, so called second harmonic generation measurements. Alternatively, Fan and Qiao (2011) localise defects based on the change of the structure's natural frequencies due to the apparent stiffness reduction. Unfortunately, both these acoustic approaches require an additional excitation signal to function. Therefore, such techniques will not be addressed further. However, a compelling base for a mechanical non-collocated method could be the propagation of elasto-plastic stress waves, which are generated in a monopile by each hammer blow.

Given the ferromagnetic nature of structural steel, a steel structure in the presence of the geomagnetic field is slightly magnetised, i.e. it has a magnetisation, which is (not exclusively) sensitive to elastic (Atherton and Jiles, 1983) and plastic deformation (Bozorth and Williams, 1945). The interactions between mechanical and magnetic quantities are colloquially known as the magnetomechanical effect. As the stray magnetic field generated by the structure's magnetisation permeates the space surrounding it, a magnetic field measurement in its vicinity could lead to a non-contact method to infer the structure's deformation. Although the origins of this effect—as all magnetic phenomena—are only correctly captured by quantum mechanics (Van Vleck, 1977, December 8), the discussion in this work is restricted to the essential features of the effect to describe and understand the behaviour of measurable macroscopic quantities. As most experimental research on the magnetomechanical effect has been performed on laboratory-scale specimens in well-controlled environments (Birss et al., 1971; Li et al., 2017a; Viana et al., 2011b; Yao et al., 2012),

little data is available on the in-situ magnetomechanical response of large-scale structures, especially under dynamic loading.

Relating to the aforementioned four stages of non-destructive evaluation, the fourth stage (prognosticate) is deemed too far from the state-of-the-art to be pursued in this research, as this requires the preceding three stages to be accomplished successfully. Although the research presented here aims for a non-collocated method to detect, localise and quantify impact-induced (permanent) deformations, this might not always be possible. In that case, a realistic estimate is made of the necessary additional developments.

The research approach in this thesis relies on modelling and collecting experimental data. The former entails models for three separate problems: the mechanical response (the dynamic response of a large-diameter thin-walled steel cylinder to an axial impact); the induced magnetic stray field (the magnetic field surrounding the structure generated by a known magnetisation state); and the magnetomechanical response (the strain-induced changes of the structure's magnetisation). Given the broad range of research fields spanned by these models, they are intended to be as simple as possible, while retaining the essential physical features to model the response of a large-scale structure. Preferably, the models can directly be applied to realistic monopile installation scenarios, which is the focal point in this thesis. Nonetheless, where possible, the application to other large-scale structures will be briefly touched upon.

Concretely, the research in this thesis involves the following steps. First, a model that described the deformations of a large-diameter monopile resulting from a hammer blow is developed, which serves a base for a non-collocated contact method to infer the development of plastic deformations in a monopile. Second, a laboratory-scale experiment is designed from which the impact-induced magnetic response of a thin-walled cylinder is measured in a magnetically uncontrolled environment. Third, the observed magnetic response is modelled to improve the understanding of the effect for large-scale structures. Fourth, an in-situ measurement campaign during an onshore monopile installation is performed to test whether the principles deduced from the laboratory-scale experiment are valid during a realistic installation scenario.

1.4. Thesis outline

This thesis is structured such that the topics relevant for the development of each non-collocated method are introduced in incremental steps. Consequently, each chapter builds upon the previously discussed subjects, which are divided into two parts: a purely mechanical and a magnetomechanical part.

Chapter 2 introduces the currently available models for pile driving. For the modelling of the pile, the starting point is the classical Donnell–Mushtari theory, which governs the motions of a cylindrical shell. This theory is deemed appropriate for the frequencies of interest and the wavelengths excited in the pile upon the hammer impact. A number of one-dimensional models, which include higher-order correction terms, is then examined. Based

on the wave dispersion characteristics, the range of applicability for each model is established, whereafter physical non-linear behaviour is included in one of the simplified models. The chapter concludes with a study that accounts for pile-soil interaction to determine the effect of stress wave dispersion on the driveability of large-diameter monopiles.

Based on the propagation of elasto-plastic stress waves, Chapter 3 describes a method to detect and quantify regions of plastic deformation resulting from an axial impact. This non-collocated contact method utilises energy fluxes measured with classical sensors, which occasionally are employed during monopile installations, providing a method that effortlessly could be applied to current installations.

Chapter 4 introduces the essentials of the magnetomechanical effect. With the main objective in mind, relevant quantities affecting the magnetisation are discussed in conjunction with state-of-the-art modelling approaches and common magnetic methods to infer deformation. From this literature review, the knowledge gaps in the available experimental data are identified which will be addressed in the laboratory experiment. The chapter closes with the derivation of a framework to compute the magnetic stray field around a thin-walled cylinder generated by a uniform external magnetic field, which serves as a basis for the magnetomechanical modelling in subsequent chapters.

Using data from the lab-scale experiment, Chapter 5 reports on the evolution of the remanent magnetic stray field in between impacts. To distinguish stray field changes due to elastic and plastic strain, these two loading regimes are assessed separately, leading to the formulation of a non-contact method to detect and localise a region of plastic deformation based on the remanent magnetic stray field of a steel structure.

As a natural continuation of the preceding chapter, Chapter 6 treats the transient strain-induced stray field measured during an impact. By means of the axi-symmetric mechanical model discussed in Chapter 2, the impact-induced strain field is simulated and validated against the measured strain data. By varying the impact energy and sensor position, the strain-induced magnetic field is analysed, and the correlation of the magnetic signals with the measured strain is determined. An extension of a state-of-the-art uniaxial magnetomechanical model is derived to model the observed stray field variation, and possible improvements to the model are identified.

In Chapter 7, the results of the in-situ measurement campaign are discussed, in which a more extensive sensor lay-out has been employed than in the laboratory experiment. The correspondence between the magnetic signals and the elastic axial strain is computed to determine whether the response observed in the laboratory experiment scales to large-scale structures in a more realistic environment. After the identification of possible sources of interference for the magnetic field measurements, the analysis of the collected data leads to two practical applications of magnetic field measurements during monopile installations: non-contact strain measurement and pile penetration monitoring.

Finally, Chapter 8 summarises the conclusions drawn from this research. Additionally, it outlines directions for future studies.

2

Pile driving dynamics

*And it hits me like a hammer
And I can't stop moving*

Drive Like Maria – Taillight

For the development of non-collocated methods to infer deformations in a pile during its installation, a sound understanding of the structural response to a hammer blow is essential. To this end, this chapter discusses several models describing the impact-induced elastic as well as plastic deformations, since both are relevant to ascertain the mechanical state of the pile during and after its installation. As the focus of this thesis is placed on the development of new non-collocated methods, the model for the structural deformations should be simple, but sufficiently accurate, while incorporating the relevant physical processes that occur during the installation of large-diameter monopiles, namely the stress wave dispersion and a non-linear constitutive relation (plastic deformation). In this thesis, structural deformations are assumed to be infinitesimal. Consequently, geometric non-linearities are not accounted for.

This chapter starts with an outline of the state of the art in modelling of the pile driving process, followed by a more in-depth discussion on modelling of the structural response to a hammer blow based on a cylindrical shell theory. Departing from the Donnell–Mushtari theory for cylindrical shells, several one-dimensional models with relevant higher-order corrections are derived using various justified assumption, ultimately retrieving the familiar

Parts of this chapter have been published in Meijers, Tsouvalas and Metrikine (2017), and Meijers, Tsouvalas and Metrikine (2018a).

one-dimensional wave equation, which is still the basis for models used in the industry. These simpler models are then extended by including physical non-linearity, i.e. plastic deformation. Since our main interest lies in the transient dynamic response to a hammer impact, soil-pile interaction is only briefly touched upon in the final section of this chapter. Ignoring the soil seems justified, as the highest strains are expected to be developed while the first group of stress waves propagates downwards along the pile (following the hammer impact); in this thesis, there is limited interest in the exact description of the strains developed upon wave reflection from the pile tip.

2.1. State of the art of pile driving modelling

The first author to recognise the importance of incorporating the dynamic response of a pile to an impact to correctly model the pile driving process has been Isaacs (1931), who applied the classical one-dimensional wave equation to the problem. He obtained a set of analytical solutions, which were limited in their applications, especially in view of the non-linear soil response. A real breakthrough has come with invention of digital computers, allowing for the numerical evaluation of the governing equations. Smith (1950, 1962) used a lumped mass model that includes soil resistance through the use of non-linear springs and dashpots to simulate the pile driving process. His model equations are identical to those obtained from discretising the classical one-dimensional wave equation. Due to its low complexity and resulting short computation times, his model still underlies most state-of-the-art computer software for pile driveability analyses, e.g. GRLWEAP (Rausche et al., 2004).

Later improvements to the modelling of pile driving have come from applying the Finite Element Method. In the works by Borja (1988) and Deeks (1992), the pile is treated as a rod, while the soil is regarded a continuum. The latter is also applied by Smith and Chow (1982) and Mabsout and Tassoulas (1994), although these authors treat the pile as an (axisymmetric) continuum. In these modelling approaches, it is common to only account for elastic deformations of the pile, since the plastic deformation of the soil around the pile is of greater concern for pile driving.

From a geotechnical vantage point, the validity of Smith's model is rightfully questioned by Wu et al. (1989), who examine the soil behaviour incorporated in the original Smith model. They conclude that the Smith's soil damping parameter depends on the duration of the force signal exerted by the hammer and cannot be regarded an intrinsic soil parameter. Alternatively, Randolph and Simons (1986) and Lee et al. (1988) derive expressions for the soil stiffness and damping from an elastic continuum description. Nonetheless, due to the complex behaviour at the soil-structure interface, pile driving models require a careful calibration to estimate the soil parameters (Masouleh and Fakharian, 2008a; Salgado et al., 2015).

An important adverse aspect of the installation of piles are soil vibrations, since they travel outwards from the pile towards neighbouring structures (Masoumi and Degrande, 2008; Ramshaw, 2002). A closely related subject is the generation of sound waves by a

hammer impact. Recently, parallel to the increasing number of large-diameter monopiles installed in marine environments, understanding anthropogenic noise generation and propagation during this process has become vital to limit the environmental impact of the construction of offshore wind farms (Tsouvalas, 2015; Tsouvalas, 2020). Since the produced sound waves span across a wide range of frequencies, more advanced structural models are essential to correctly predict the noise generation in these circumstances (Hall, 2015; Reinhall and Dahl, 2011; Tsouvalas and Metrikine, 2013, 2014). Note that to consider the noise generated during pile driving, the pile is assumed to be at a prescribed penetration depth, not advancing deeper into the soil. Hence, it suffices to describe the soil with a linear elastic constitutive relation in conjunction with a linear soil-structure interface, i.e. slip between the pile and the surrounding soil is not accounted for.

Some research has been devoted to the deterioration of the pile as a result of the driving process, which can be classified in two categories: fatigue and damage. Relating to the former, Priest and Large (1990) speculate that impact driving can have a beneficial effect with respect to the fatigue of the material. On the contrary, Rasmussen and Feld (1999) report the onset of damage in concrete pile due to pile driving fatigue. When a life-time extension of a pile foundation is considered, quantitative knowledge of the amount of fatigue damage induced during installation is crucial for the reassessment (Lotsberg et al., 2010a). Normally, the sustained fatigue damage is estimated based on the results of a driveability analysis with the use of one-dimensional models (Tang et al., 2005) and empirical S-N curves (Lotsberg et al., 2010b). The obtained results highly depend on the consulted standard (Chung et al., 2013), putting the applicability of these calculation schemes for fatigue into question.

While fatigue does not immediately render the pile useless, the second deterioration category, damage, is far more detrimental. Rausche and Goble (1979) describe a method to detect a crack in a concrete pile by analysing the travel time of the stress waves in the material, noticing that the crack acts as a reflective boundary. Therefore, the arrival of a reflected stress wave before the time moment expected from the pile's length indicates that a crack has formed. A second example of analysis of damage in a pile is reported by Aldridge et al. (2005), who state criteria for tip damage of steel cylindrical piles to develop.

From this literature review, the image emerges that, despite the availability of more accurate theoretical models, the one-dimensional model proposed in the 1950s still plays a pivotal role in the driveability analysis of piles in practice. This could be attributed to the higher computational cost of these advanced models compared to that of the wave equation model, while, at least for piles with limited radii, the accuracy improvements of prediction by the former are within engineering tolerances (Nath, 1990). An additional factor explaining the preference of the industry for the classical model might be that the soil parameter estimation is considerably simpler for these type of models (Masouleh and Fakharian, 2008b; Salgado et al., 2015). In the remainder of this chapter, the validity of applying the one-dimensional model, especially with respect to the large-diameter monopiles commissioned nowadays, is critically assessed.

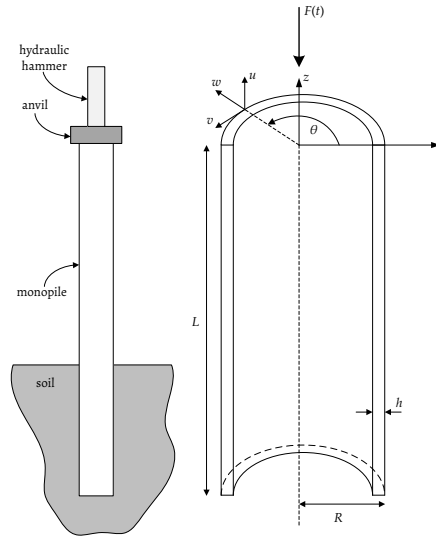


Figure 2.1: Schematic of the pile-hammer-soil system (left), and an overview of the thin-walled cylindrical shell structure used to derive the governing equations (right).

2.2. Governing equations for elastic deformation of a cylindrical shell

A schematic representation of the pile-hammer-soil system is shown in Figure 2.1, together with the cylindrical coordinate system that is used throughout this chapter. The axial, circumferential, and radial directions are denoted by z , θ and r , respectively. The monopile has outer radius R , wall thickness h , and length L . Initially, the traction of the surrounding soil with the shell's surface is ignored.

2.2.1. Donnell–Mushtari shell theory

The natural starting point for deriving the governing equations is a thin cylindrical shell theory, which is justified by the assumption that the pile's radius and length, and the excited wavelengths in the structure due to impact piling, are large compared to the wall thickness. By comparing exact theory and approximate thin shell theory, Greenspon (1961) shows that the latter is adequate for predicting the dynamical characteristics of a cylindrical shell structure with a diameter-to-wall-thickness ratio comparable to that of a monopile. Although there are many thin shell theories—each with its own complexity and range of applicability—they can be written in the operator form presented by Leissa (1973/1993):

$$\left(\mathcal{L}_{D-M} + \beta \mathcal{L}_{\text{mod}}\right) \bar{\mathbf{U}} = \mathbf{0}. \quad (2.1)$$

In this expression, $\bar{\mathbf{U}}$ is a vector containing the three dimensionless displacement components \bar{U} , \bar{V} , \bar{W} : the axial, circumferential, and radial displacements, respectively, which are functions of z , θ , and t .

The displacement components are made dimensionless upon division with the pile's radius, e.g. $\bar{U} = U/R$, in which bars indicate a non-dimensional quantity. In addition, the non-dimensional axial coordinate is defined as $s = z/R$, and the dimensionless time is $\tau = \omega_r t$ with

$$\omega_r = c_p/R \quad (2.2)$$

being the ring frequency in rad/s. Upon division with 2π , the ring frequency is expressed in Hz, i.e. $f_r = \omega_r/2\pi$. At the ring frequency, the breathing resonance of a ring with that radius occurs (Hodges et al., 1985). In the above, the plate velocity is

$$c_p = \sqrt{\frac{E}{\rho(1-\nu^2)}},$$

and it contains the linear elastic material properties: Young's modulus E , Poisson's ratio ν , and volumetric mass density ρ .

In Equation (2.1), the Donnell–Mushtari operator \mathcal{L}_{D-M} is the basis for all theories; other theories emerge by adding the modification operator \mathcal{L}_{mod} . The thickness-to-radius ratio $\beta \equiv h^2/12R^2$ determines the influence of this additional operator on the resulting theory. For a monopile, this ratio is much smaller than one, and the frequencies of interest are relatively low. Consequently, the modification term can be discarded altogether.

In terms of the dimensionless parameters, the nine components of the symmetric Donnell–Mushtari operator are (Leissa, 1973/1993):

$$\mathcal{L}_{D-M}^{11} = \frac{\partial^2}{\partial s^2} + \frac{1-\nu}{2} \frac{\partial^2}{\partial \theta^2} - \frac{\partial^2}{\partial \tau^2}, \quad (2.3a)$$

$$\mathcal{L}_{D-M}^{12} = \mathcal{L}_{D-M}^{21} = \frac{1+\nu}{2} \frac{\partial^2}{\partial s \partial \theta}, \quad (2.3b)$$

$$\mathcal{L}_{D-M}^{13} = \mathcal{L}_{D-M}^{31} = \nu \frac{\partial}{\partial s}, \quad (2.3c)$$

$$\mathcal{L}_{D-M}^{22} = \frac{1-\nu}{2} \frac{\partial^2}{\partial s^2} + \frac{\partial^2}{\partial \theta^2} - \frac{\partial^2}{\partial \tau^2}, \quad (2.3d)$$

$$\mathcal{L}_{D-M}^{23} = \mathcal{L}_{D-M}^{32} = \frac{\partial}{\partial \theta}, \quad (2.3e)$$

$$\mathcal{L}_{D-M}^{33} = 1 + \beta \left(\frac{\partial^4}{\partial s^4} + \frac{\partial^4}{\partial s^2 \partial \theta^2} + \frac{\partial^4}{\partial \theta^4} \right) + \frac{\partial^2}{\partial \tau^2}. \quad (2.3f)$$

Given the closed circumference of the structure, it is natural to assume that solutions to Equation (2.1) are periodic in the circumferential direction. By applying the principle of

separation of variables, the displacements are expressed as:

$$\bar{U}(s, \theta, \tau) = \sum_{n=-\infty}^{\infty} \bar{u}_n(s, \tau) e^{in\theta}, \quad (2.4)$$

where the lower case functions $\bar{u}_n(s, \tau)$ are complex-valued and n is an integer. As the displacements $\bar{U}(s, \theta, \tau)$ are necessarily real-valued, \bar{u}_n and \bar{u}_{-n} are complex conjugates. Substituting this assumed solution into the governing equations (2.1) and reversing the order of the summation and the differentiation, one obtains:

$$\sum_{n=-\infty}^{\infty} \mathcal{L}_n \bar{u}_n e^{in\theta} = \mathbf{0}. \quad (2.5)$$

This expression has to be satisfied for all s, θ and τ . Therefore, each contribution to the sum has to be zero individually, leading to the conclusion that the former expression for the governing equations can be written as:

$$\mathcal{L}_n \bar{u}_n = \mathbf{0}, \quad \forall n = 0, \pm 1, \dots, \pm \infty, \quad (2.6)$$

where the components of \mathcal{L}_n for each admissible value of n are:

$$\mathcal{L}_n^{11} = \frac{\partial^2}{\partial s^2} - \frac{(1-\nu)n^2}{2} - \frac{\partial^2}{\partial \tau^2}, \quad (2.7a)$$

$$\mathcal{L}_n^{12} = \mathcal{L}_n^{21} = \frac{(1+\nu)ni}{2} \frac{\partial}{\partial s}, \quad (2.7b)$$

$$\mathcal{L}_n^{13} = \mathcal{L}_n^{31} = \nu \frac{\partial}{\partial s}, \quad (2.7c)$$

$$\mathcal{L}_n^{22} = \frac{1-\nu}{2} \frac{\partial^2}{\partial s^2} - n^2 - \frac{\partial^2}{\partial \tau^2}, \quad (2.7d)$$

$$\mathcal{L}_n^{23} = \mathcal{L}_n^{32} = ni, \quad (2.7e)$$

$$\mathcal{L}_n^{33} = 1 + \beta \left(\frac{\partial^4}{\partial s^4} - 2n^2 \frac{\partial^2}{\partial s^2} + n^4 \right) + \frac{\partial^2}{\partial \tau^2}. \quad (2.7f)$$

The notation in Equation (2.6) enables one to approximate the governing equations by only selecting the desired circumferential mode numbers. For example, to correctly include an inclined hammer forcing on the pile into the model, one must at least include $n = 0$ and $n = \pm 1$ (Tsouvalas and Metrikine, 2013). For consistency, the initial and boundary conditions must be projected onto the selected circumferential modes. Therefore, the arbitrary functions describing the initial and boundary conditions are decomposed into their respective Fourier components along the θ -direction, which directly serves as an input for selecting the appropriate circumferential mode numbers n to approximate the given problem.

2.2.2. Governing equations for axi-symmetric deformation

Since the wave propagation caused by the hammer forcing is assumed to be predominantly axi-symmetric, the operator can be simplified further. By substituting $n = 0$ into Equation (2.7), the components of the axi-symmetric operator \mathcal{L}_0 yield

$$\mathcal{L}_0^{11} = \frac{\partial^2}{\partial s^2} - \frac{\partial^2}{\partial \tau^2}, \quad (2.8a)$$

$$\mathcal{L}_0^{12} = \mathcal{L}_0^{21} = 0, \quad (2.8b)$$

$$\mathcal{L}_0^{13} = \mathcal{L}_0^{31} = \nu \frac{\partial}{\partial s}, \quad (2.8c)$$

$$\mathcal{L}_0^{22} = \frac{1-\nu}{2} \frac{\partial^2}{\partial s^2} - \frac{\partial^2}{\partial \tau^2}, \quad (2.8d)$$

$$\mathcal{L}_0^{23} = \mathcal{L}_0^{32} = 0, \quad (2.8e)$$

$$\mathcal{L}_0^{33} = 1 + \beta \frac{\partial^4}{\partial s^4} + \frac{\partial^2}{\partial \tau^2}. \quad (2.8f)$$

The off-diagonal zeros in this operator, e.g. $\mathcal{L}_0^{12} = 0$, indicate that the torsional motions are now uncoupled from the radial-axial motions. For $n = 0$, the assumed solutions for the displacements in Equations (2.4) are real-valued for all θ , i.e. the imaginary part of $\bar{u}_0(s, \tau)$ equals zero. For conciseness, the subscript 0 will be omitted for the axi-symmetric displacements in the remainder of this chapter.

Since the axial motions are of major importance for pile driving, the two coupled equations are combined by eliminating the radial displacement, resulting in

$$\frac{\partial^4 \bar{u}}{\partial \tau^4} + \frac{\partial^2 \bar{u}}{\partial \tau^2} - \frac{\partial^4 \bar{u}}{\partial s^2 \partial \tau^2} - (1-\nu^2) \frac{\partial^2 \bar{u}}{\partial s^2} - \beta \left(\frac{\partial^6 \bar{u}}{\partial s^6} - \frac{\partial^6 \bar{u}}{\partial s^4 \partial \tau^2} \right) = 0. \quad (2.9)$$

Equation (2.9) can be further simplified by analysing the effect of the higher-order derivatives on the dispersion characteristics as discussed below.

2.2.3. Dispersion characteristics of axially symmetric shells

The frequency-wavenumber characteristics for the case $n = 0$ are expressed in terms of the dimensionless frequency $\Omega = \omega/\omega_r$ and the dimensionless wavenumber $\xi = kR$ by assuming harmonic solutions of the form $\bar{u} = \hat{u}e^{i(\Omega\tau + \xi s)}$. In these expressions, ω and k designate the frequency and wavenumber, respectively. Each further simplification of the equation of motion restricts the range of applicability in terms of these dimensionless quantities. Figure 2.2 presents the dispersion curves for four distinct models, which are computed with common values for steel monopiles: $\nu = 0.3$ and $\beta = 4.80 \cdot 10^{-5}$.

Due to the fourth-order time derivative in Equation (2.9), the frequency-wavenumber relation of the axi-symmetric shell (the grey dash-dotted line in Figure 2.2) has two branches. For ξ close to zero, i.e. large axial wavelengths, structural motions are mainly axial. However,

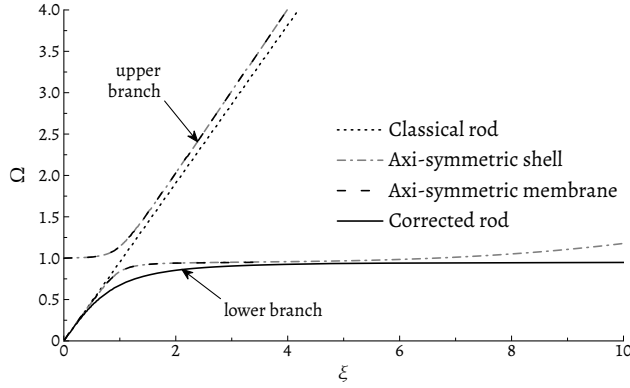


Figure 2.2: Dispersion curves for the considered theories computed with $\nu = 0.3$ and $\beta = 4.80 \cdot 10^{-5}$.

when the ring frequency ($\Omega = 1$) is approached, radial motions start to dominate, since the energy needed for in-surface shearing decreases (Bozich, 1967). When the wavenumber increases even further, axial bending energy eventually dominates the dispersion characteristics, causing the curve to bend back towards the infinite flat plate curve (Hodges et al., 1985).

Given that the lower branch of the full axi-symmetric shell theory only bends slightly upwards in the low-frequency, long-wavelength limit ($\xi > 6$), the first simplification is to neglect the bending behaviour in Equation (2.9). By discarding the β -terms in this equation, an axi-symmetric membrane theory emerges (Soedel, 2004, pp. 145–146):

$$\frac{\partial^4 \bar{u}}{\partial \tau^4} + \frac{\partial^2 \bar{u}}{\partial \tau^2} - \frac{\partial^4 \bar{u}}{\partial s^2 \partial \tau^2} - (1 - \nu^2) \frac{\partial^2 \bar{u}}{\partial s^2} = 0. \quad (2.10)$$

As the two branches of the dispersion relation of the membrane theory are indistinguishable from the shell theory for $0 \leq \xi \leq 6$, the axi-symmetric membrane theory is a good approximation of the shell theory for small wavenumbers. This observation holds for a wider selection of properties than the ones considered in this thesis.

Since the second branch only appears at frequencies above the ring frequency, an approximation of the lower branch would suffice to describe wave propagation in a monopile for waves that contain frequencies below this critical value, i.e. $\Omega = 1$. One obtains this approximation by omitting the fourth-order time derivative in the shell membrane equations (2.10) resulting in

$$\frac{\partial^2 \bar{u}}{\partial \tau^2} - \frac{\partial^4 \bar{u}}{\partial s^2 \partial \tau^2} - (1 - \nu^2) \frac{\partial^2 \bar{u}}{\partial s^2} = 0. \quad (2.11)$$

Because higher frequencies cannot propagate in this approximate theory, its range of applicability is limited to $0 \leq \xi \leq 6$ and $0 \leq \Omega < 1 - \nu^2$. This expression for the approximate lower branch resembles the Rayleigh–Love rod theory (Graff, 1975/1991, pp. 116–121), although

Table 2.1: Parameters for the installation process of a large-diameter steel monopile.

Parameter	Value	Parameter	Value
R	2.5 m	E	210 GPa
h	0.050 m	ν	0.3
L	33.9 m	ρ	7750 kg/m ³
a	9.0 m		

the coefficient of the mixed time-space derivative is adjusted here to approach the exact dispersion curves obtained with the shell theory. Therefore, this approximate theory is referred to as the corrected rod theory from here on.

As a reference, Figure 2.2 also shows the dispersion curve for the classic non-dispersive rod theory, which is the basis for Smith's pile driving model (Smith, 1962) commonly used in practice. In that case, the equation of motion simplifies further to

$$\frac{\partial^2 \bar{u}}{\partial \tau^2} - (1 - \nu^2) \frac{\partial^2 \bar{u}}{\partial s^2} = 0. \quad (2.12)$$

For low frequencies and wavenumbers ($0 \leq \xi \leq 0.5$ and $0 \leq \Omega \leq 0.5$), the lower branch of the axi-symmetric shell theories coincides with the one obtained from the non-dispersive theory, showing the validity of Smith's pile driving model when the frequency content of the hammer forcing is well below the ring frequency. However, when the forcing contains frequencies around the ring frequency, the effect of stress wave dispersion can no longer be neglected. This simple fact is very often overlooked in practice.

2.2.4. Comparison of the shell theories for a large-diameter monopile

To check the applicability of the simplified theories for the axial deformation of an axially symmetric cylindrical shell derived in the preceding section, the propagation of linear elastic waves in a large-diameter monopile is considered more closely. To this end, strain data recorded during the installation process of a monopile are analysed. The investigated pile can be considered to be large-diameter with a radius $R = 2.5$ m; nonetheless, piles with even larger diameters are currently commissioned (Igwemezie et al., 2019). The sketch previously presented in Figure 2.1 is applicable to the situation currently under investigation, with the pile's dimensions and material properties listed in Table 2.1. Using these quantities, the ring frequency is computed as: $f_r = 347$ Hz. During the driving of the pile, strain levels have been monitored with four sensors placed on a ring along the pile's circumference located 9.0 m below the pile head; this measurement plane is located at $z = -a$ in Figure 2.1. The measured data will be compared to the results of two linear elastic simulations—the corrected rod theory and the membrane theory—to determine which model is the most accurate for predicting the stress and strain levels at the sensor location.

As an input for the simulations, the measured stress signal resulting from a hammer impact is used (Figure 2.3a) of which Figure 2.3b shows the accompanying amplitude spectrum.

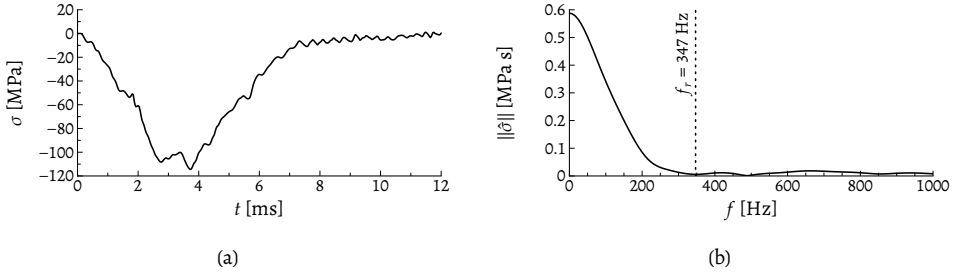


Figure 2.3: Hammer force used in the simulations of a large-diameter monopile installation. (a) Time signal of the stress level induced by the hammer force computed from measurements on the hammer casing. (b) Amplitude spectrum of the induced stress signal, where the dashed line indicates the pile's ring frequency.

The frequency content reveals that the hammer signal contains some energy at frequencies above the ring frequency of the shell. Therefore, it is expected that the corrected rod theory, Equation (2.11), will not accurately reproduce the measured signals, since energy contained above the ring frequency cannot propagate in that model. The simulations are performed with a finite element discretisation (Logg et al., 2012) and an explicit Newmark scheme (Newmark, 1959); the spatial resolution and time step are $\Delta z = 67.8 \cdot 10^{-3}$ m and $\Delta t = 1.0 \cdot 10^{-5}$ s, respectively.

Figure 2.4 shows the measured stress levels, computed as an average of the four measured strain signals, together with the results from a linear elastic simulation using the membrane theory and the corrected rod theory. The measured stress signal is relatively smooth for the first 5 ms, after which oscillations become more pronounced. This behaviour can be attributed to a number of factors. First, the input force itself is non-smooth due to the internal structure of the impact hammer. Stress pulses exerted by hammers are characterised by a relatively smooth ascending branch followed by several high-frequency oscillations that are caused by the dropping of the various smaller internal masses of the hammer on the top of the pile. Second, the shell itself is dispersive, and, therefore, the excited waves carrying energy at different frequencies arrive at the location of the sensors at different moments in time. Thus, even in the ideal case in which the input force is smooth, dispersion effects will tend to distort the original shape of the stress pulse. Third, the pile is never positioned totally vertically during installation, and the hammer-pile contact is, therefore, non-ideal, resulting in bending of the pile. Waves excited due to bending of the pile arrive at the location of the sensor at later moments in time.

As expected from the frequency restriction of the corrected rod theory, $0 \leq \Omega < 1 - v^2$, the high-frequency oscillations (above $f_{\max} = (1 - v^2) \cdot f_r = 315$ Hz) did not propagate, smoothing the signal considerably; nonetheless, the model is able to predict the peak stress. The results obtained with the membrane theory, however, correctly capture the main features of the measured stress pulse, showing the importance of the upper branch of the dispersion

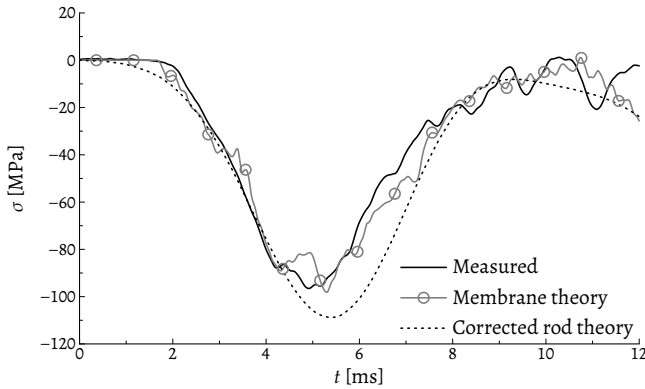


Figure 2.4: Stress levels at the sensor location ($z = -9.0$ m) for the large-diameter monopile.

relation for the stress wave propagation in large-diameter monopiles once frequencies close to, or above, the ring frequency are excited.

2.3. Inclusion of physical non-linearity

Up until now, only the propagation of elastic stress waves in the structure have been considered. However, to assess whether plastic deformation occurs in a pile during installation, a model which includes a non-linear constitutive relation needs to be considered. Plastic deformation is referred to as physical non-linearity, as the micro-structure of the material changes when plasticity forms. This is in contrast to geometric non-linearity, i.e. finite strains, which embodies large deformations of a structure, which can still be in the linear regime. The latter will not be considered in this thesis, because the small strain approximation is assumed to be sufficient to model the deformations of a monopile during driving.

2.3.1. Plastic deformation in metals

In the classical macroscopic description of plastic deformation—see e.g. Chakrabarty (2010, chap. 1) for an elaborate account of the subject—the material response to mechanical strain is reversible up to a certain strain magnitude: the yield, or elastic, limit. When the strain exceeds this limit, irreversible, or plastic, deformation starts to develop. A simple stress-strain diagram for this description of plastic deformation is shown in Figure 2.5a indicating the elastic limit with the yield strain ε_y and the yield stress σ_y . The slope of the elastic part of the curve is the Young's modulus E .

In the classical theory, a path with the same slope as the elastic loading is curved out in the $\sigma\varepsilon$ -space during unloading. The remnant strain is called the plastic strain ε_p . In the case of isotropic hardening, the material's yield limit is not constant, but increases with plastic strain, which is represented by the ascending line in the post-yielding regime in the graph.

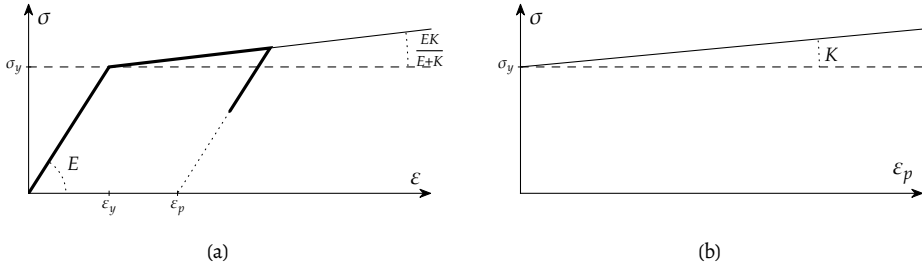


Figure 2.5: Stress strain diagram for a classical one-dimensional elasto-plastic material with linear isotropic hardening (Simo and Hughes, 1998, p. 14). (a) Stress versus total strain. (b) Stress versus plastic strain.

The plastic modulus K , shown in Figure 2.5b, quantifies the strength of the hardening with plastic strain. For metals, it is reasonable to assume identical stress-strain behaviour for tensile as well as compressive stresses.

Naturally, the material's behaviour at the macro scale is a manifestation of processes taking place at the micro scale. A detailed report on these processes, however, would be far beyond the scope of this thesis. Nonetheless, highlighting some basic principles will greatly improve the understanding of experimentally observed behaviour, especially when changes in the magnetic properties of the material are considered from Chapter 4 onwards. On the micro scale, elastic deformation results from the stretching and compressing of the atomic bonds in the crystal, i.e. no irreversible changes in the crystal structure are observed. As soon as plastic deformation starts to develop, permanent reorganisation of the crystal structure occurs as a result of the sliding of slip planes in this lattice. Sliding is possible due to the presence of dislocations, which are defects in the crystal structure (Honeycombe, 1968). During plastic deformation, the number of dislocations increases approximately linear with plastic strain, because new dislocations are generated in the deformation process (Gilman, 1968). Figure 2.6 presents the increased dislocation density after the plastic strain is doubled in a steel specimen subjected to a compressive impact load. With the increasing number of dislocations, interactions between the strain fields of adjacent dislocations become more apparent. Since these interactions impair the movement of the slip planes, a higher stress is required to allow for further sliding, explaining the aforementioned strain hardening effect observed at the macro scale (Honeycombe, 1968, chap. 5).

Over the years, advanced models for metal plasticity have been developed, e.g. multi-scale models, which incorporate the described processes at the micro scale. Roters et al. (2010) provide an extensive overview of these advanced modelling strategies. Nonetheless, the classical description for plastic deformation is employed in this work, since it captures the essential features of the macroscopic observations in very straightforward equations, ensuring that the models remain simple.

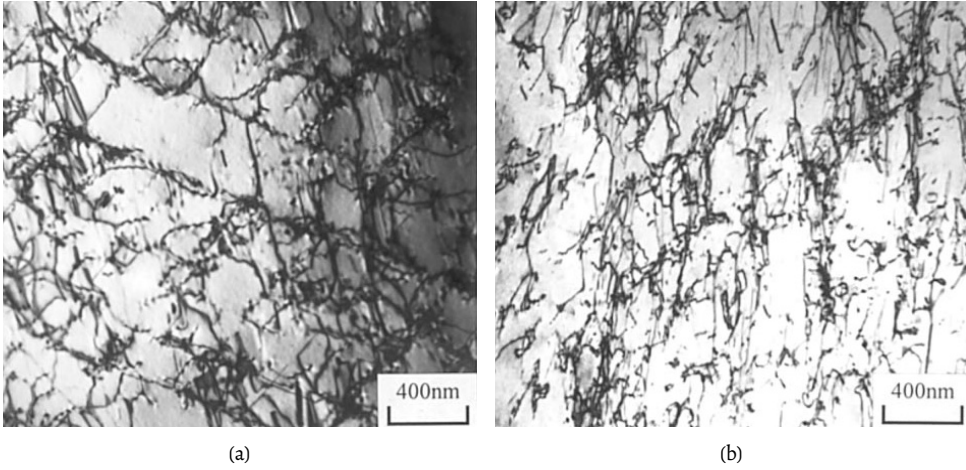


Figure 2.6: Micrographs obtained using a Transmission Electron Microscope of the evolution of the dislocation substructures in a steel specimen subjected to a compressive impact load. (a) $\epsilon_p = 0.05$. (b) $\epsilon_p = 0.10$. Reprint of Figures 9a–b from Lee and Lin (2001) with permission from Elsevier.

2.3.2. Components of the stress and strain tensors

To incorporate plastic deformations, the stress components of the plane stress state underlying the axi-symmetric membrane theory, Equation (2.10), are considered. By dividing each component by the Young's modulus E , the dimensionless version of the stress tensor is obtained, i.e.

$$(1 - \nu^2) \bar{\sigma}_s = \frac{\partial \bar{u}}{\partial s} + \nu \bar{w}, \quad (2.13a)$$

$$(1 - \nu^2) \bar{\sigma}_\theta = \bar{w} + \nu \frac{\partial \bar{u}}{\partial s}, \quad (2.13b)$$

$$(1 + \nu) \bar{\sigma}_{s\theta} = \frac{1}{2} \frac{\partial \bar{v}}{\partial s} = 0, \quad (2.13c)$$

in which $\bar{\sigma}_s$, $\bar{\sigma}_\theta$ and $\bar{\sigma}_{s\theta}$ are the axial, hoop and shear stress, respectively. The latter vanishes due to the assumption that the pile driving process causes no torsional motions in the structure, leaving only two non-zero stress components, i.e. Equations (2.13a) and (2.13b).

The relative importance of these components is frequency dependent, which is shown by expressing the dimensionless displacements in terms of the dimensionless frequency and wavenumber:

$$\bar{u} = \hat{u} e^{i(\Omega\tau + \xi s)},$$

$$\bar{w} = \hat{w} e^{i(\Omega\tau + \xi s)}.$$

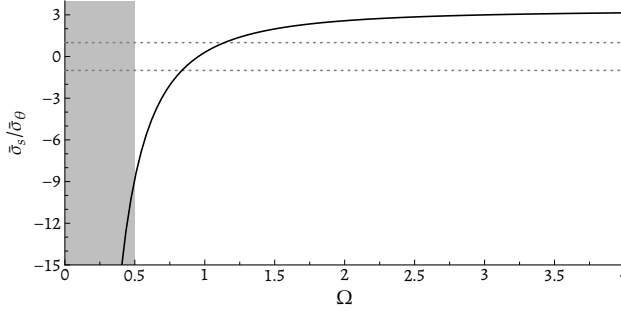


Figure 2.7: Ratio between the axial and the hoop stress versus frequency for $\nu = 0.3$. The ratio approaches $-\infty$ as Ω approaches zero. Dashed lines correspond to $\bar{\sigma}_s/\bar{\sigma}_\theta = \pm 1$. The low-frequency region ($\Omega < 0.5$) is shaded grey.

Utilising the operator for the axially symmetric case, Equations (2.8), and discarding the term associated with bending, the complex amplitude for the dimensionless radial displacement \hat{w} is

$$\hat{w} = \frac{iv\xi}{\Omega^2 - 1}\hat{u}.$$

By substituting these relations into Equations (2.13a) and (2.13b), the ratio between the axial and the hoop stress is

$$\frac{\bar{\sigma}_s}{\bar{\sigma}_\theta} = \frac{\Omega^2 - (1 - \nu^2)}{\nu\Omega^2}. \quad (2.14)$$

Figure 2.7 visualises Equation (2.14) for $\nu = 0.3$. Since $\bar{\sigma}_s/\bar{\sigma}_\theta$ tends to minus infinity when Ω approaches zero, the axial stress dominates the hoop stress at low frequencies ($\Omega < 0.5$). Therefore, it is reasonable to assume a uniaxial stress state in the low-frequency range. However, when the ring frequency is approached, the hoop stress is no longer negligible compared to the axial component, and a biaxial state needs to be considered. For simplicity, a uniaxial stress state will be used in the following, therefore restricting the applicability of the model to $\Omega < 0.5$.

A similar analysis can be applied to the components of the strain tensor, which in dimensionless form are:

$$\varepsilon_s = \frac{\partial \bar{u}}{\partial s}, \quad (2.15a)$$

$$\varepsilon_\theta = \bar{w}, \quad (2.15b)$$

$$\varepsilon_{s\theta} = \frac{\partial \bar{v}}{\partial s} = 0. \quad (2.15c)$$

In line with the shear stress, the shear strain also vanishes. By substituting the aforementioned displacements in terms of frequency and wavenumber into the equations above, the

two non-zero strain components are related by

$$\varepsilon_\theta = \frac{\nu}{\Omega^2 - 1} \varepsilon_z. \quad (2.16)$$

At low frequencies ($\Omega < 0.5$), $\varepsilon_\theta \approx -\nu\varepsilon_z$, which is to be expected in case the stress state is uniaxial.

2

2.3.3. One-dimensional physically non-linear theory

The membrane theory, Equation (2.10), is split into three expressions relating the axial displacement \bar{u} , the total axial strain ε , and the axial stress $\bar{\sigma}_s$, yielding:

$$\frac{\partial^2 \bar{u}}{\partial \tau^2} = (1 - \nu^2) \frac{\partial \bar{\sigma}_s}{\partial s}, \quad (2.17a)$$

$$\varepsilon = \frac{\partial \bar{u}}{\partial s}, \quad (2.17b)$$

$$\bar{\sigma}_s = \varepsilon + \frac{\partial^2 \bar{\sigma}_s}{\partial s^2} - \frac{\partial^2 \bar{\sigma}_s}{\partial \tau^2}. \quad (2.17c)$$

These three relations are the equilibrium, kinematic and constitutive equations for a linear elastic axi-symmetric membrane, respectively. First, by discarding the time derivative in the latter expression, the corrected rod theory, i.e. Equation (2.11), is retrieved. Second, the total axial strain is split into an elastic and a plastic part: $\varepsilon = \varepsilon_e + \varepsilon_p$. After inserting this expression in the constitutive equation and transforming the system back to dimensional quantities, the equations for the corrected rod including physically non-linear behaviour read

$$\rho \frac{\partial^2 u}{\partial t^2} = \frac{\partial \sigma}{\partial z}, \quad (2.18a)$$

$$\varepsilon = \frac{\partial u}{\partial z}, \quad (2.18b)$$

$$\sigma = E(\varepsilon - \varepsilon_p) + \underbrace{R^2 \frac{\partial^2 \sigma}{\partial z^2}}_{\text{Correction}}, \quad (2.18c)$$

in which σ denotes the axial stress. This set of equations closely resembles the model equations presented by DeVault (1965) based on the Rayleigh–Love rod theory. However, he considered a solid cylindrical rod with radius R , for which the expression for the axial stress becomes:

$$\sigma = E(\varepsilon - \varepsilon_p) + \underbrace{\frac{1}{2} \nu^2 R^2 \frac{\partial^2 \sigma}{\partial z^2}}_{\text{RL-correction}}. \quad (2.19)$$

It is important to note that the stress state in the Rayleigh–Love rod theory is always uniaxial, i.e. independent of frequency, whereas the stress state in the axi-symmetric membrane

theory becomes biaxial for $\Omega > 0.5$. In the corrected rod theory, the axial stress component is adjusted to account for the effect of dispersion.

Since the system of equations (2.18) is not yet complete, auxiliary relations for the plastic axial strain, $\varepsilon_p(z, t)$, are needed. Assuming uniaxial plasticity with linear isotropic hardening, one obtains (Simo and Hughes, 1998, pp. 9–14):

$$\frac{\partial \varepsilon_p}{\partial t} = \gamma \operatorname{sign}(\sigma), \quad (2.20a)$$

$$\frac{\partial \alpha}{\partial t} = \gamma, \quad (2.20b)$$

$$f(\sigma, \alpha) = \|\sigma\| - (\sigma_y + K\alpha), \quad (2.20c)$$

$$\gamma \geq 0, \quad f(\sigma, \alpha) \leq 0, \quad \gamma f(\sigma, \alpha) = 0, \quad (2.20d)$$

$$\gamma \frac{\partial f(\sigma, \alpha)}{\partial t} = 0 \quad \text{if } f(\sigma, \alpha) = 0, \quad (2.20e)$$

where γ is the magnitude of the plastic flow rate, α the hardening parameter, K the plastic modulus, $f(\sigma, \alpha)$ the yield function, and σ_y the yield stress of the material. This set of equations forms the basis for the discussion of a non-located method to detect and quantify plastic deformation resulting from an impact load which is presented in Chapter 3. It is important to note that the presented governing equations that include plastic deformation are only valid for a uniaxial stress state. Therefore, the non-linear corrected rod model can exclusively be applied when the loading of the hammer excites frequencies below $\Omega = 0.5$, since the stress state becomes essentially biaxial at higher frequencies.

2.4. Soil-structure interaction

In pile driving modelling, the interaction between the pile and the soil plays a pivotal role in the overall response of the hammer-pile-soil system. Valuable information retrieved from a driveability analysis is, for instance, the pile's settlement after a single hammer blow and the maximum stress induced during that impact. With these results, the number of hammer blows needed to drive the pile to its desired penetration depth can be estimated, which in turn, together with the predicted stress levels, serves as an input for fatigue calculations (Chung et al., 2013; Tang et al., 2005). As previously discussed in Sections 2.2 and 2.3, stress wave dispersion in large-diameter monopiles cannot be neglected, because the impact of the hammer inserts energy into the system at frequencies in which the waves become dispersive. Nonetheless, it remains unclear how this phenomenon affects the results of a driveability study. To this end, a dispersive term is added to the classical one-dimensional Smith model for pile driving (Smith, 1962), and, by means of a case study of piles with different radii, the possible implications of stress wave dispersion on the driveability are demonstrated.

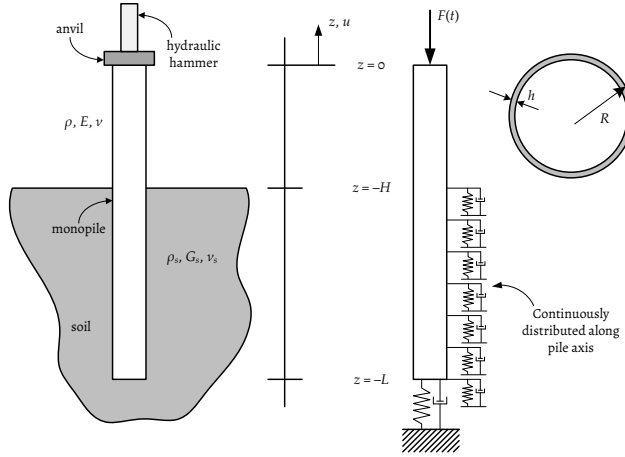


Figure 2.8: Sketch of the pile driving process (left) and the driveability model (right).

2.4.1. One-dimensional dispersive driveability model

A sketch of the pile driving process is shown in Figure 2.8, consisting of a linear elastic cylindrical hollow pile that is partially embedded into a uniform soil layer. The pile is considered to be thin-walled with outer radius R , wall thickness h and cross-sectional area $A \approx 2\pi R h$. The material properties of the pile are Young's modulus E , Poisson's ratio ν and density ρ , whereas the soil properties are similar but have the subscript s . To prevent soil plugging in the pile, which would complicate the analysis (Liyanapathirana et al., 2001), the tip of the pile is considered to be closed by a round plate. This latter assumption does not resemble a real situation as in most cases the pile tip is open. However, this is not expected to influence the conclusions drawn from this study which is to showcase the importance of the stress wave dispersion.

The axial displacement of the pile, $u(z, t)$, is assumed to be governed by the Rayleigh–Love rod theory (Graff, 1975/1991, pp. 116–121), which is an improvement of the classical rod theory that includes the effect of lateral inertia of the cross-section. The governing equation reads:

$$\rho A \frac{\partial^2 u}{\partial t^2} - EA \frac{\partial^2 u}{\partial z^2} + R_s - \left[\rho \nu^2 I_p \frac{\partial^4 u}{\partial t^2 \partial z^2} \right] = 0, \quad (2.21)$$

in which R_s is the non-linear resistance of the soil and I_p is the polar second moment of area of the cross-section. The term in square brackets is the additional Rayleigh–Love correction term, which is not included in the original wave equation model by Smith (1962). Please note that the dispersion characteristics for the Rayleigh–Love rod theory slightly differ from those of the membrane theory or the corrected rod theory; however, capturing the exact dispersion curve for this simplified case study is not essential to show the possible implications of stress wave dispersion on the results of a driveability analysis.

In Equation (2.21), the soil resistance along the pile shaft per unit length of the pile R_s is given by (Randolph and Simons, 1986)

$$R_s = \begin{cases} K_s u + C_s \frac{\partial u}{\partial t} & \text{when } \left\| K_s u + C_s \frac{\partial u}{\partial t} \right\| < 2\pi R q_u, \\ 2\pi R q_u & \text{otherwise,} \end{cases}$$

where the soil stiffness $K_s = 2.9G_s$ and the soil damping $C_s = 2\pi R \sqrt{G_s \rho_s}$, in which G_s is the soil's shear modulus and ρ_s denotes the density of the soil. The magnitude of the soil resistance is limited by the ultimate friction coefficient q_u of the soil multiplied by the circumference of the pile.

From the displacement $u(z, t)$, the axial stress $\sigma(z, t)$ in the pile is computed as:

$$\sigma(z, t) = E \frac{\partial u}{\partial z} + \left[\rho v^2 R_g^2 \frac{\partial^3 u}{\partial t^2 \partial z} \right],$$

in which $R_g = \sqrt{I_p/A}$ is the radius of gyration. Again, the term between square brackets emerges from the Rayleigh–Love theory and is neglected in classical wave equation approach. Regarding the initial conditions, at $t = 0$, the system is assumed to be at rest, and the boundary conditions are given by

$$\sigma(0, t) = F(t)/A, \quad (2.22a)$$

$$\sigma(-L, t) = P_s/A, \quad (2.22b)$$

where $F(t)$ is the hammer force and P_s the soil response at the pile tip, which is modelled as (Randolph and Simons, 1986):

$$P_s = \begin{cases} K_t u + C_t \frac{\partial u}{\partial t} & \text{when } \|K_t u\| < A_t P_s^{\max}, \\ A_t P_s^{\max} + C_t \frac{\partial u}{\partial t} & \text{otherwise,} \end{cases}$$

where $K_t = 4G_s R/(1 - \nu_s)$ and $C_t = 3.4R^2 \sqrt{G_s \rho_s}/(1 - \nu_s)$ with ν_s the Poisson's ratio of the soil. Furthermore, P_s^{\max} is the ultimate soil resistance and $A_t = \pi R^2$ is the cross-sectional area of the closed-off pile tip. The final set of the pile after one hammer blow is equal to the displacement of the pile head when the system is at rest again.

In the model equations, the soil is modelled by distributed non-linear springs and dashpots, following the classical approach of Randolph and Simons (1986). This model has been developed originally for piles of relatively small diameter and assumes a local reaction of the soil. For large-diameter piles, however, the soil reacts in a non-local manner (Versteijlen et al., 2016). Here, nonetheless, the local reaction is deemed sufficient for a demonstration of the effect of stress wave dispersion on the driveability.

Table 2.2: Pile and soil properties used for all cases.

Pile parameter	Value	Soil parameter	Value
E	210 GPa	G_s	24.25 GPa
ν	0.3	ν_s	0.48
ρ	7750 kg/m ³	ρ_s	1900 kg/m ³
L	58 m	H	23 m
		q_u	100 kN/m ²
		p_s^{\max}	900 kN/m ²

Table 2.3: Case specific parameters and values for the final set of the pile after a single hammer blow.

Case	R [m]	h [mm]	α [-]	f_r [Hz]	u_{CW} [mm]	u_{RL} [mm]	Δu [%]
1	0.4572	20	1.0	1900	5.57	5.55	-0.36
2	2.0	40	8.75	434	6.00	6.02	0.33
3	3.5	70	26.8	248	5.64	5.87	4.08

2.4.2. Case set-up

To analyse the effect of stress wave dispersion on the driveability parameters, predictions of a classical wave equation model are compared with the results of the dispersive model for three different cases. The cases consider piles of different radii while keeping the induced stress levels and the frequency content of the hammer force equal. Additionally, it is assumed that no plastic deformation is inflicted by the hammer blow. Table 2.2 lists the numerical values of the quantities common to all three cases, while Table 2.3 presents the case specific parameters and their respective values.

With the hammer model developed by Deeks and Randolph (1993), the hammer force $F(t)$ in Equation (2.22a) for Case 1 is generated with $m_r = 4000$ kg, $m_a = 1000$ kg, $c_c = 0$ Ns/m, $k_c = 3.5$ GN/m, $v_0 = 6.5$ m/s, $Z = A\sqrt{E\rho} = 2.3$ MNs/m. The resulting time signal is shown in Figure 2.9 together with the corresponding amplitude spectrum. In order to keep the frequency content of the hammer force equal for the three cases, only the amplitude of the force signal is scaled with scaling parameter α as presented in Table 2.3. The magnitude of α is chosen such that the axial stress induced at the pile head is equal for all cases.

As read from Equation (2.2), the ring frequency of the pile decreases with increasing radius. From the amplitude spectrum of the hammer force, it is clear that for Case 1 no energy is introduced in the vicinity of the ring frequency. On the contrary, for the remaining two cases, the hammer force contains a significant amount of energy around the ring frequency.

The pile driving problem defined above is solved numerically by means of the Finite Element Method using FEniCS (Logg et al., 2012) by dividing the pile into 250 linear elements along its axis, resulting in a spatial discretisation of $\Delta z = 0.232$ m. An explicit Newmark time marching scheme ($\beta = 0.25$ and $\gamma = 0.5$) with a time step of $\Delta t = 1 \cdot 10^{-5}$ s is chosen for the time integration of the governing equations (Newmark, 1959).

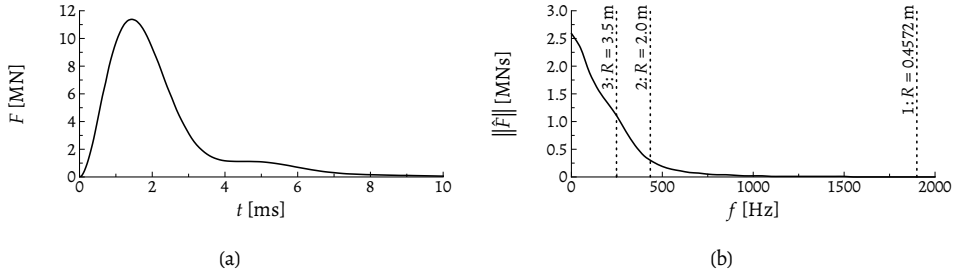


Figure 2.9: Hammer force $F(t)$ for Case 1 generated by the hammer-pile model developed by Deeks and Randolph (1993). (a) The simulated time signal of the force. (b) The corresponding amplitude spectrum with the ring frequencies for each case indicated by the dotted lines.

2.4.3. Influence of dispersion on the driveability

For the three cases, Figure 2.10 shows the axial stress distributions computed with the two pile driving models at two distinct time instances: $t = 0.10$ s (black lines), which is prior to the arrival of the stress wave front at the pile tip; and $t = 0.21$ s (grey), where the stress wave propagates upwards. In line with the analysis of the frequency content of the hammer force, the stress profiles for Case 1 predicted by both models coincide. For Case 2, the profiles start to differ: although their shape is similar, a time shift is observed. Due to the correspondence of stress wave shapes, fatigue predictions for Case 2 will not differ when the classical model or the proposed model is used, since the number of stress cycles remains equal. However, for the largest pile, the dispersion of the stress wave is no longer negligible. Careful examination of the stress wave profiles shows that the dispersion causes additional alterations of compressive and tensile stresses in the pile compared to the classical approach, resulting in an increase of the number of stress cycles. Therefore, predictions of consumed fatigue life of the pile based on the dispersive model will differ.

From a driveability study, a second quantity of interest is the penetration of the pile into the soil due to a single hammer blow, giving an indication of the total number of impacts needed to reach the desired penetration depth. Table 2.3 lists the final set of the pile from one hammer blow predicted by both models for each of the three cases. The difference between the predicted set of the classical model (u_{CW}) and of the dispersive model (u_{RL}) is given as a percentage of u_{CW} . When the shape of the stress wave is similar (Case 1 and 2), the models predict a comparable penetration. However, for Case 3, the difference between stress wave profiles predicted by both models becomes more pronounced, resulting in a set of the pile that differs almost 4%. Although this might not seem significant at first, one must bear in mind that the complete installation of a large-diameter pile demands several thousands of hammer blows. Due to this large number, these small differences add up to a rather significant difference in the predicted number of hammer blows required to reach the desired penetration depth between Case 3, and Cases 1 and 2.

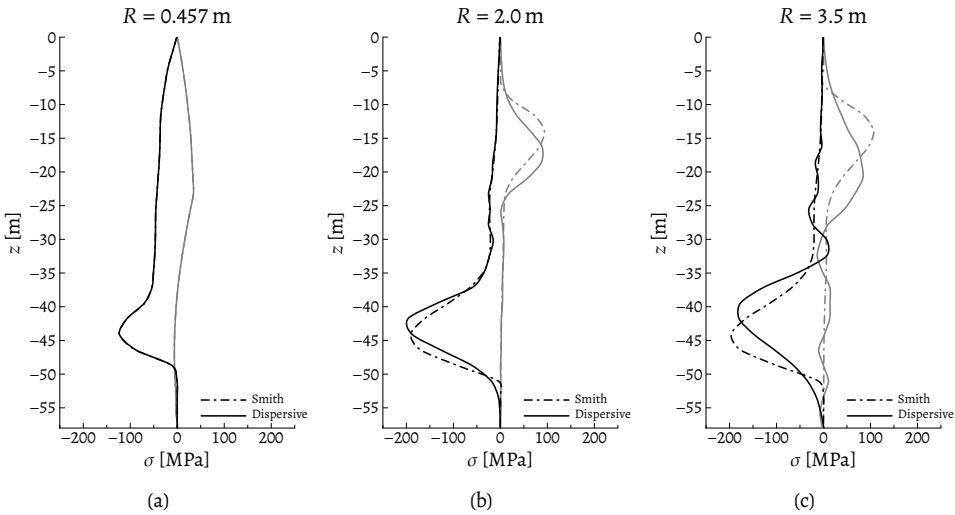


Figure 2.10: Axial stress distributions along the pile's axis at $t = 0.10$ s (black) and $t = 0.21$ s (grey) for different radii. The dashed lines (---) are the results from the classical wave equation model and the solid lines (—) the results from the dispersive model.

Although it is clear that stress wave dispersion has a pronounced influence on the outcomes of a driveability study, Section 2.2.4 showed that a membrane theory is the preferred option to model the stress wave propagation in a pile when the hammer force contains energy at frequencies above the ring frequency. Therefore, a real improvement for the one-dimensional driveability models when applied to large-diameter monopiles would come from using a membrane theory to model the deformations of the structure. Incorporating this theory—which is still one-dimensional, even though it has two degrees of freedom—into a driveability model is not completely straightforward, because, for an axi-symmetric cylindrical membrane, energy introduced around the ring frequency of the pile mainly excites radial motions of the pile (Bozich, 1967). Therefore, a driveability model that is based on the membrane equations (2.10) should include soil stiffness and damping in both the radial and the axial direction. Moreover, it is expected that, for a large-diameter piles, the soil-pile interaction is no longer governed by a local quantities, but by the global response of the soil (Versteijlen et al., 2018). This requires additional care in modelling the response of the soil. These recommended improvements of one-dimensional driveability models for large-diameter piles, which might significantly improve the predictions of the current models in these cases, are left for future research.

2.5. Conclusions

This chapter presented a short overview of the state-of-the-art modelling of the pile driving process. In the industry, one-dimensional models are still the preferred choice due to their

low computation cost. However, it is questionable whether these models are applicable to large-diameter monopiles currently commissioned. Several theories that govern axial displacements of a large-diameter pile have been derived from the Donnell–Mushtari theory for a cylindrical shell by applying justified assumptions, restricting their applicability in terms of frequency and wavelengths of the excited motions. In the low-frequency and long-wavelength limit, the classical wave equation is an appropriate approximation of the more complete theory. However, it has been shown that, when energy is introduced around the ring frequency of the pile, the effect of wave dispersion is no longer negligible. For excitations with frequencies close to the ring frequency, a more suitable theory is proposed: the corrected rod theory. However, strain data measured during the installation of a large-diameter monopile shows that, when sufficiently high frequencies are excited ($\Omega > 0.5$), only the axially symmetric membrane theory is capable of predicting the observed strain levels with satisfactory accuracy.

Analysis of results from a pile driving simulation shows that stress wave dispersion has a profound influence on the results of a driveability study for large-diameter piles. First, due to the dispersion, the predicted stresses display more undulations, which affect the estimated fatigue life of the structure. Second, the computed penetration depth for the dispersive model differs by about 4% compared to the currently used non-dispersive model. It is therefore recommended that this model should be improved by describing the deformations of the structure with the axi-symmetric membrane theory, while simultaneously introducing soil resistance in the radial direction.

An analysis of the stress tensor in terms of the dimensionless frequency indicates that, for $\Omega < 0.5$, the stress state in a cylindrical structure is essentially uniaxial. When higher frequencies are excited, the stress state becomes biaxial. Being uniaxial, yet dispersive, the corrected rod theory is altered to account for physical non-linearity, i.e. plastic deformations, enabling the theory to be used for the propagation of elasto-plastic stress waves, which serves as the basis for the derivation of a non-collocated technique to infer plastic deformation in the next chapter.

3

Quantifying physical damage with non-collocated contact measurements

*There'll be something missing
And now that you found it
It's gone*

Radiohead – *Nude*

During a monopile installation, a hammer blow can inflict plastic deformation at the pile head. As it is impossible to attach a classical strain gauge at the location of interest, a non-collocated method is needed to infer the development of such damage. In the previous chapter, the governing equations for elasto-plastic waves propagating in a monopile have been derived, resulting in a more accurate description of the behaviour of these waves, which is also valid for the large-diameter monopiles currently used by the offshore wind industry. This chapter develops a non-collocated contact method to detect and quantify these regions of plastic deformation by taking advantage of the propagation of elasto-plastic stress waves in the pile, which can be measured with strain gauges, which are mounted to the structure a certain distance below the impact location.

Parts of this chapter have been published in Meijers, Tsouvalas and Metrikine (2018a), and Meijers, Tsouvalas and Metrikine (2018b).

The propagation of elasto-plastic stress waves in solid metal cylinders has been studied already from the 1940s. Rate-independent theories based on the classical wave equation have been developed and validated against high-velocity impact experiments (Taylor, 1948; Von Karman and Duwez, 1950). More advanced models incorporate lateral inertia of the cross-section (DeVault, 1965) and rate dependency of the constitutive equation (Shea, 1968). Using these models, the dynamic properties of metals can be determined from experimental data (Kolsky and Douch, 1962). More recently, Khayer Dastjerdi et al. (2013) have reported an energy-based approach to study these impact tests.

Similar axial impact tests have been performed on hollow cylindrical shells (Murase and Jones, 1993; Ren et al., 1983). These thin-walled structures are used in the automotive industry as energy absorption devices, since the dynamic buckling of the cylinders removes energy from the system. Karagiozova et al. (2000), Karagiozova and Jones (2001) and Lepik (1999) show that the type of dynamic buckling and thus the deformed state of the cylinder after impact depends on the axial stress wave propagation. Moreover, Karagiozova and Jones (2000) report that for low-velocity (drop hammer) impacts, which resemble impact pile driving, most of the permanent deformation is concentrated in a small region at the impacted end of the cylinder. However, the use of non-collocated strain sensors mounted on the structure itself to quantify the amount of plastic deformation during the pile driving process has not been reported in literature so far.

Section 3.1 proposes a method to quantify plastic deformation based on non-collocated strain measurements and an energy balance. Section 3.2 presents a lab-scale experiment of a copper bullet hitting a solid rod (Kolsky and Douch, 1962), which allows one to validate the concept of the energy balance in a well-controlled environment. Hereafter, the applicability and the limitations of the method are discussed in Section 3.3, after which conclusions are drawn.

3.1. Method to quantify plastic deformation

When plastic deformations develop, stress waves inducing strains that exceed the yield limit can no longer propagate at the same velocity, affecting the shape of the original stress pulse. Due to this limit, a plateau in the stress signal appears, which results from the fact that a part of the energy contained in the stress wave is used to permanently deform the structure. This assertion is the basis for the method to detect and quantify plastic deformation.

The effect of the non-linear material behaviour on the shape of the stress wave is elaborated by considering simulated time signals of the axial strain in a small-diameter pile. Table 3.1 presents the considered parameters, while Figure 3.1 shows a sketch of the considered situation including the quantities mentioned in the aforementioned table. An elastic and an elasto-plastic simulation of the wave propagation in the pile are performed with the same force signal applied at $z = 0$ m, which is presented in the inset graph in Figure 3.2. The simulations differ exclusively in enforcing the yield limit: the elasto-plastic simulation imposes it, while the elastic neglects it.

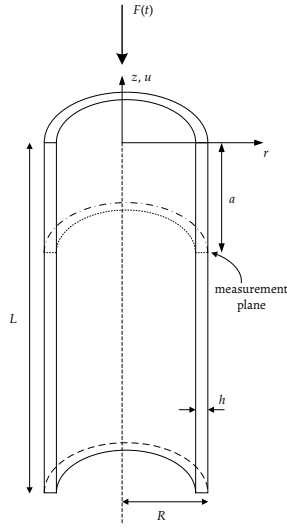


Figure 3.1: Schematic of a monopile subjected to an impact load at the top of the pile.

Table 3.1: Parameters for the simulations of stress wave propagation in a small-diameter steel monopile.

Parameter	Value	Parameter	Value
R	0.25 m	E	210 GPa
h	0.010 m	K	4.2 GPa
L	50 m	ν	0.3
a	3.0 m	ρ	7750 kg/m ³
		σ_y	235 MPa

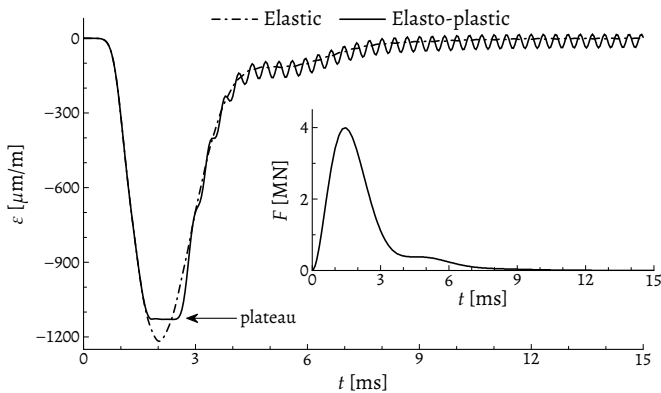


Figure 3.2: Strain signals at $z = -3.0$ m for an elastic and an elasto-plastic simulation of a small-diameter pile; the inset graph shows the force signal used in both cases.

Figure 3.2 shows the strain signals at $z = -3.0$ m resulting from the two simulations. In the elastic case, the shape of the signal is identical to that of the force signal. Note that the effect of dispersion is not visible for this exemplary small-diameter pile, as the forcing excites frequencies well below the ring frequency of the structure. However, in the elasto-plastic case, a plateau in the strain is visible, indicating that plastic deformation has occurred. Thus, by comparing the measured strain signal at a given location with the expected strain computed on the basis of an elastic model of the structure, one can draw some preliminary conclusions regarding the possible development of plastic deformation at cross-sections of the pile prior to the given location caused by the hammer impact.

To quantify this deformation, the following elementary energy balance is considered:

$$E_0 = E_w + E_p + E_{\text{loss}}, \quad (3.1)$$

in which E_0 denotes the input energy of the hammer, E_w the energy associated with the wave energy flux through the considered cross-section, E_p the energy spent to plastically deform the material, and E_{loss} the remaining losses, e.g. losses in sound radiation and material damping not associated with plastification. Below, each of the four contributions to the energy balance for a one-dimensional structure is elaborated.

First, the input energy E_0 represents the energy introduced into the considered section of the structure. Technically, its value could be measured by considering the energy flux through the cross-section. However, as plastic deformations are expected to develop at the impact location, this would entail a collocated measurement. Therefore, the input energy must be obtained from an alternative method, e.g. from a hammer model or by scaling the amplitude of the linear response of a low-energy impact that does not inflict plastic deformation in the pile.

Second, the energy E_w that passed through a cross-section is defined as the integral of the measured energy flux over a given time interval from $t = t_0$ to $t = t_1$:

$$E_w = \int_{t=t_0}^{t=t_1} \mathbf{F} \cdot \mathbf{v} \, dt, \quad (3.2)$$

where \mathbf{F} is the axial force and \mathbf{v} the velocity. The former quantity can be determined from a strain measurement and the latter can be measured with a separate acceleration sensor at the same location (cross-section of the pile). On its own, this integral is sufficient to quantify the energy associated with the passage of a stress wave, although the propagation direction of the stress wave must carefully be accounted for. However, for strictly one-dimensional stress wave propagation, it can be convenient to express the energy flux in terms of the axial strain, reducing the number of sensors required to obtain its value. In this one-dimensional case, the quantities of interest are co-directed, and the relations $F = A\sigma$, $\sigma = E\varepsilon$ and $v = \sigma/\sqrt{E\rho}$

are valid. With these expressions, the integral is rewritten in terms of the axial strain ε only:

$$E_w = \frac{AE^2}{\sqrt{E\rho}} \int_{t=t_0}^{t=t_1} \varepsilon^2 dt, \quad (3.3)$$

in which A is the area of the cross-section, ρ the density, and E without a subscript denotes Young's modulus.

Third, the plastic work E_p is equal to the mechanical dissipation due to plastification as defined in Simo and Hughes (1998, pp. 27–28) integrated over the region of interest Ω and over time:

$$E_p = \iint \mathcal{D}_{\text{mech}} d\Omega dt \quad (3.4)$$

For the one-dimensional case considered here, this is

$$E_p = A \int_{t=t_0}^{t=t_1} \int_{z=0}^{z=a} \left(\sigma \frac{\partial \varepsilon_p}{\partial t} - K\alpha \frac{\partial \alpha}{\partial t} \right) dz dt. \quad (3.5)$$

Using the auxiliary equations (2.20) for an elasto-plastic material with isotropic hardening and the fact that $\sigma \text{ sign}(\sigma) = \|\sigma\|$, the plastic work is rewritten as

$$E_p = A \int_{t=t_0}^{t=t_1} \int_{z=0}^{z=a} \left(\gamma [\|\sigma\| - \sigma_y - K\alpha] + \gamma \sigma_y \right) dz dt. \quad (3.6)$$

Since the term between square brackets is the yield function $f(\sigma, \alpha)$ and the auxiliary relations require that $\gamma f(\sigma, \alpha) = 0$, the expression reduces to

$$E_p = A\sigma_y \int_{t=t_0}^{t=t_1} \int_{z=0}^{z=a} \gamma dz dt. \quad (3.7)$$

The double integral of the plastic flow rate γ is an indicator of the amount of plastic deformation between the impact and sensor location; and it is henceforth referred to as a single quantity u_p : the permanent axial displacement. With this new quantity defined, the expression for the plastic work reduces to

$$E_p = A\sigma_y u_p. \quad (3.8)$$

Fourth, for the remaining losses in the pile E_{loss} , Tsouvalas and Metrikine (2014) show that the energy in the acoustic radiation is negligible for sensors positioned above the seabed. Therefore, provided that the other loss mechanisms are also small, E_{loss} can be altogether neglected for the first-order estimation of the amount of plasticity. By reordering the energy balance, u_p is expressed as

$$u_p = \frac{E_0 - E_w}{A\sigma_y}. \quad (3.9)$$

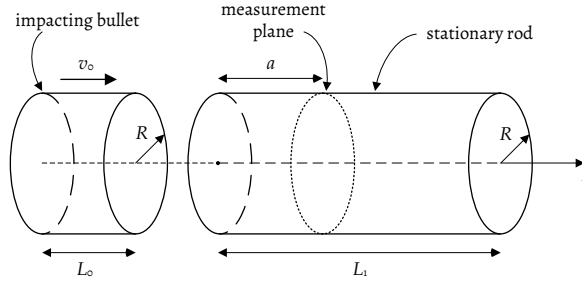


Figure 3.3: The modelled set-up of the lab-scale experiment of Kolsky and Douch (1962).

Equation (3.9) gives a simple relation to quantify the plastic deformation caused by an impact load based on a strain measurement at a certain distance from the impact point. Naturally, this expression will give an upper bound estimation of the expected plastic strain as E_{loss} is assumed equal to zero.

To summarise, the method to detect and quantify plastic deformations inflicted by a hammer blow relies on the following steps:

1. Measure the strain at a given location which allows the calculation of E_w by means of Equation (3.3). For more complicated structures one would need to measure both strains and accelerations in multiple directions to apply Equation (3.2); nonetheless, the approach remains essentially similar.
2. Calculate E_0 on the basis of the hammer characteristics or utilise the hammer input energy provided by the supplier.
3. Estimate the upper bound of the plastic deformation accumulated at the regions prior to the location of the sensor by applying Equation (3.9).

3.2. Validation against a lab-scale experiment

As an example, the proposed method is applied to the laboratory experiments of Kolsky and Douch (1962). In their paper, a solid cylindrical copper specimen of length L_0 (bullet) with initial velocity v_0 impacts a stationary solid cylindrical copper rod with length L_1 . The experiment is repeated with increasing initial velocities to show the effect of the yield limit on the shape of the induced stress pulse in the rod. Figure 3.3 shows a schematic of the experimental set-up. Both the specimen and the rod have radius R , which is listed in Table 3.2, together with the other dimensions and material properties. In this specific set-up, the initial energy E_0 follows directly from kinetic energy of the bullet. For an initial velocity $v_0 = 14.02 \text{ m/s}$ ($= 46 \text{ ft/s}$), it reads $E_0 = 1/2mv_0^2 = 36.8 \text{ J}$, in which m is the specimen's mass computed with the density and its volume.

Table 3.2: Parameters of the experiment of Kolsky and Douch (1962) on copper specimens.

Parameter	Value	Parameter	Value
L_0	0.1524 m	E	129.8 GPa
L_1	1.2192 m	K	1.298 GPa
R	9.525 mm	ν	0.34
a	0.548 m	ρ	8960 kg/m ³
		σ_y	210 MPa

In the original paper, only the oscillograph traces of the stress pulses are reported, see Figure 3.4. Since these traces lack a scale to quantify the actual stress levels, the measured wave energy E_w is computed by comparing the signals for two different impact velocities. Using the response of the low velocity impact, $v_0 = 8.53$ m/s (= 28 ft/s), which causes no plastic deformation in the rod, the wave energy for the impact of interest ($v_0 = 46$ ft/s) is estimated: $E_w = 24.6 \pm 3.8$ J. The uncertainty in the value results from the digitalisation of the oscillograph traces. By combining these two energies in Equation (3.9), the permanent axial deformation is estimated at

$$u_p = 0.20 \pm 0.06 \text{ mm.}$$

Note that the entire difference between the input energy and the measured wave energy is contributed to plastic deformation, as all other losses are assumed to be negligible.

To check whether this estimate is accurate, the high speed impact is also simulated using the stress wave propagation model introduced in Section 2.3.3. However, because these experiments concern a solid cylinder rather than a thin-walled cylindrical shell, the Rayleigh–Love correction term in the stress definition is used, i.e. Equation (2.19). Two simulations will be compared: a linear elastic simulation, which ignores the yield limit, and an elastic-plastic simulation, which enforces the yield limit. Only the latter simulation includes a loss mechanism, i.e. the plastic deformation; other loss mechanisms are not considered. From the elasto-plastic simulation, it is possible to determine the amount of plastic deformation in the rod, which is then compared to the estimate obtained from the measurements.

For the simulations, the model equations (2.18) are spatially discretised with the Finite Element Method in FEniCS (Logg et al., 2012), and an explicit Newmark scheme (Newmark, 1959) is used for the time integration. The spatial resolution and time step are $\Delta z = 2.74 \cdot 10^{-3}$ m and $\Delta t = 1.0 \cdot 10^{-7}$ s, respectively. A return mapping algorithm (Simo and Hughes, 1998) ensures that the auxiliary constitutive equations (2.20) are all satisfied.

Figure 3.5 shows the time traces of the total axial strain at the sensor location ($z = 0.548$ m) for the two simulations, while the axial plastic strain along the rod's axis for the elasto-plastic simulation is presented in Figure 3.6. The latter figure shows that the plastic strain is zero at the sensor location, which actually means that the total strain in Figure 3.5 is equal to the elastic strain. In line with the observations by Kolsky and Douch (1962), the stress wave at

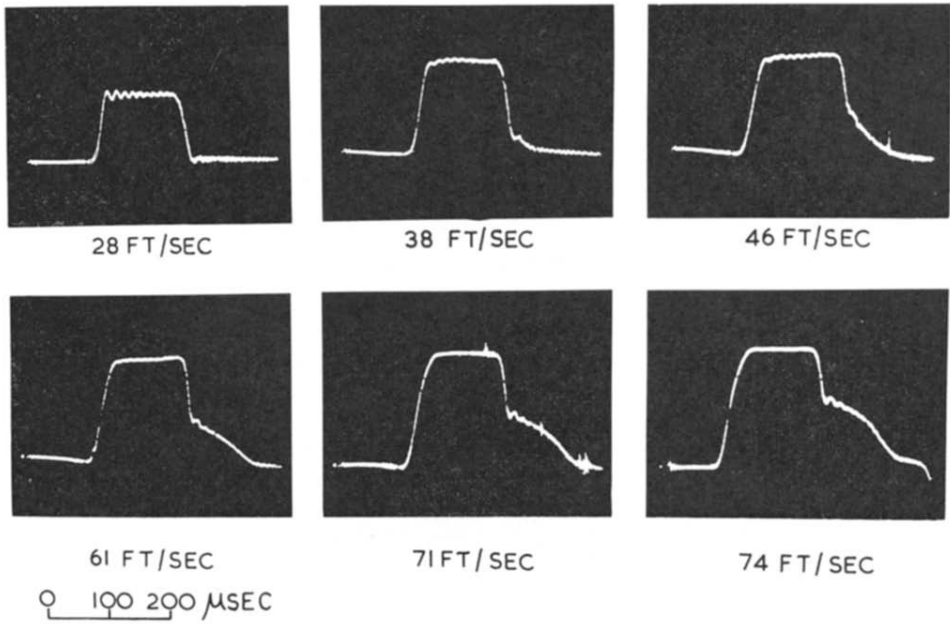


Figure 3.4: Oscillograph traces of copper on copper impacts. Reprint of Figure 19 from Kolsky and Douch (1962) with permission from Elsevier.

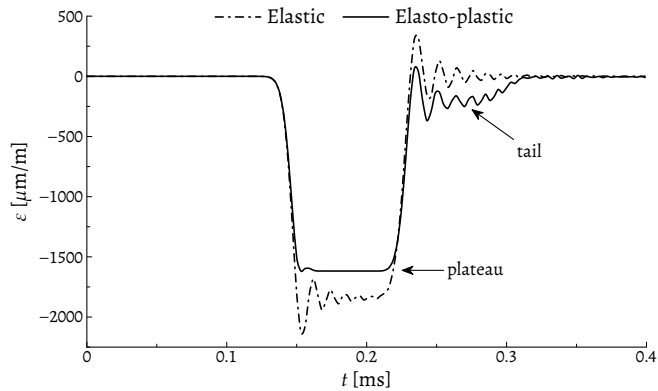


Figure 3.5: Simulated total strain signals at $z = 0.548$ m for the elastic and the elasto-plastic rod after impact with $v_0 = 14.02$ m/s (= 46 ft/s).

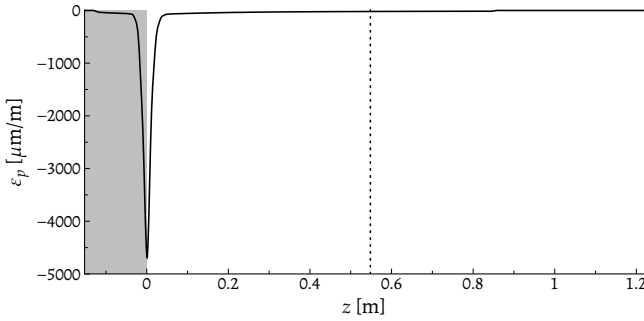


Figure 3.6: Plastic axial strain from the elasto-plastic simulation along the length of the rod. The shaded grey area is the length of the impacting bullet L_0 . The dashed line indicates the location of the strain gauge.

the sensor displays a plateau and a tail for the elasto-plastic case as result of the yield limit. The shape of the tail, however, differs from the experimental one. This difference can be attributed to the simple hardening law used in the presented model; in reality, the material response is more complex.

The observed distortion of the stress wave indicates that plastic deformation has developed, which is also clear from the plastic strain profile presented in Figure 3.6. With the simulated data, the permanent axial deformation can be computed in two different ways: either by applying the procedure outlined in Section 3.1 to the strain signal read from Figure 3.5, or by integrating the plastic strain along the length of the rod up to the location of the sensor. The latter approach yields:

$$u_p = \int \varepsilon_p dz = 0.13 \text{ mm.}$$

Since no other loss mechanisms are considered in the simulations, the former approach is equivalent to the latter and results in the same value of u_p . However, if one would consider additional loss mechanisms in the simulations, the predicted strains at the location of the sensor for the elasto-plastic case would have been lower, resulting in a higher value for u_p when Equation (3.9) is applied. The plastic strain profile, however, would remain unaffected by these additional loss mechanisms. Given this reasoning and the fact that the predicted plastic deformation u_p is lower than the measured one, it can be concluded that the other loss mechanisms in the experiment are non-negligible. Nevertheless, the permanent deformation predicted by the model does confirm that the estimate by the experimental data is an accurate upper bound for the amount of plastic deformation in the rod.

3.3. Generalisation and limitations

The method to quantify plastic deformation presented above has been derived from, and applied to, a problem pertaining a one-dimensional stress state. However, as seen in the

previous chapter, the stress state for a large-diameter monopile is essentially biaxial when frequencies are introduced above $\Omega = 0.5$. Therefore, the currently presented method cannot readily be applied to that situation. In this more general case, all components of the stress and strain tensor have to be incorporated into the expression for the mechanical dissipation, Equation (3.8). Moreover, the energy flux in Equation (3.2) should contain all non-zero structural velocities and strains. To this end, multi-axial strain and acceleration sensors have to be employed on the analysed structure.

3

Since the proposed method depends on an elementary energy balance, and the energy is a positive scalar quantity in the derived uniaxial case, only the magnitude of the permanent axial deformation is identified. As a result, the direction of this irreversible deformation, i.e. extension or compression, remains unknown, although for a one-dimensional case it can easily be deduced from the sign of the measured strain. In the multi-axial extension of the method, the direction of plastic flow is ambiguous based on the energy alone. Similar to the one-dimensional case, the sign of the deformation can be ascertained from the measured strain.

When the strain gauges are positioned relatively far from the pile head, i.e. the impact location, reflections from the seabed and the pile toe, i.e. stress waves travelling back up the pile, can contaminate the measured strain signal, obscuring the information about plastic deformation contained in the signal. A possible remedy could be installing the sensors closer to the impact location, or by using strain gauges located at different cross-sections along the pile's axis, enabling one to deduce in which direction different wave components travel.

Up to now, the plastic deformation has been assumed to form between the impact location and the measurement plane. The proffered method, however, can be applied to much more general cases. As long as one carefully tracks the stress wave energy flowing into and out of the region of interest, the method could immediately be applied. This means that both E_0 and E_w are determined from the energy flux based on Equation (3.2). Gómez et al. (2018) employ a similar concept to estimate the structural damping in high-rise buildings, where the energy deficit is attributed to damping rather than to plastic work.

3.4. Conclusions

The discussion in this chapter has shown that plastic deformations at the top of a foundation pile can be detected and quantified using non-collocated strain measurements. With an elementary energy balance, an upper bound for the amount of plastic deformation sustained between the impact and sensor location is found by comparing the energy contained in the measured strain pulse to the expected strain signal, which is computed with a linear elastic model of the structure. The proposed method to quantify plastic deformation is based on a uniaxial stress state, and it gives an adequate estimation when it is applied to a lab-scale experiment, where this stress state is valid.

Although the method relies on non-collocated measurements, it still requires data to be recorded with contact sensors. In an ideal non-collocated method to infer deformations in

a structure, the need for contact between the structure and the sensor is completely eliminated. To develop such a non-contact method, the scope of the research will be expanded to include the interaction between mechanical strain and the structure's magnetisation, i.e. magnetomechanics. The subsequent chapters will introduce the fundamental concepts of this field and demonstrate how these principles can be used to infer deformations in a structure in a non-contact manner.

4

Magnetomechanics of steel cylinders

*And if I need to rearrange my particles
I will for you*

Nothing But Thieves – Particles

After focussing on the strain field to convey the information pertaining the deformation of the structure towards a non-located sensor, this chapter focusses on an alternative medium: the magnetic field. In the following, the phenomena related to the interaction between the mechanical strain in a steel cylindrical structure and its magnetisation are discussed. In line with previous chapters, the physical quantities are treated as continuous macroscopic field variables, and the discussion only briefly touches upon the magnetic processes at the micro-scale. To frame the deliberation to our purpose, i.e. the development of non-located methods to infer deformations in a steel monopile during its installation, the following conditions apply:

- (i) the external magnetic field is weak, time- and space-invariant; e.g. the omnipresent geomagnetic field with a magnitude in the range $30\text{--}70\ \mu\text{T}$ is such a weak field (Cullity and Graham, 2009, p. 341);
- (ii) the dimensions of the cylindrical structure are large, especially relative to specimens used in laboratory testing.

In the case of impact pile driving in particular, the following additional conditions apply (Chapter 2):

- (iii) high compressive strains are induced upon the hammer impact;
- (iv) a biaxial stress state develops when energy is introduced in the vicinity of the ring frequency of the pile;
- (v) a broad range of frequencies is excited;
- (vi) the impact load is repeated hundreds or thousands of times during the installation of a single pile.

4

With these conditions in mind, first, the physics of a ferromagnetic materials is shortly introduced. Second, the interaction between mechanical strain and the magnetisation is deliberated. Third, an overview of relevant techniques for non-destructive evaluation of ferromagnetic materials based on the magnetomechanical effect is presented. Fourth, several types of models describing this effect are discussed. Fifth, a framework is explicated to compute the magnetic stray field around a thin-walled steel cylinder subjected to a known external background field. Finally, conclusions are drawn with respect to the usability of the magnetomechanical effect to infer deformations of a steel structure with non-collocated sensors.

4.1. Physics of ferromagnetic materials

Ferromagnetic materials react strongly to an external magnetic field as a result of the presence of spontaneous magnetisation (Chikazumi and Graham, 1997, chap. 6). Iron is the most famous example, providing the phenomenon with its name. The spontaneous magnetisation is caused by the parallel alignment of the spin of unpaired electrons in the outer shells of the iron atoms. However, in order to minimise the magnetostatic energy in a material, regions with aligned spin form, the so-called magnetic domains (Jiles, 2015, p. 142). The arrangement of these domains determines the observed magnetic behaviour at the macro-scale.

4.1.1. Magnetic domains

A magnetic domain is bounded by a domain wall, a relatively small region where the spin of one domain gradually transits to the spin on the neighbouring domain (Kittel, 1949).^{*} Figure 4.1a presents a simplified image of a small collection of adjacent domains when the material is demagnetised, i.e. it has no net magnetisation. Since the electron spins in a magnetic domain are aligned, each domain has an associated magnetic moment—indicated by the arrows, which is proportional to the size of the domain. The directions of the magnetic

^{*}For an extensive account on the subject, the reader is referred to Craik and Tebble (1961), Hubert and Schäfer (1998) and Kittel (1949).

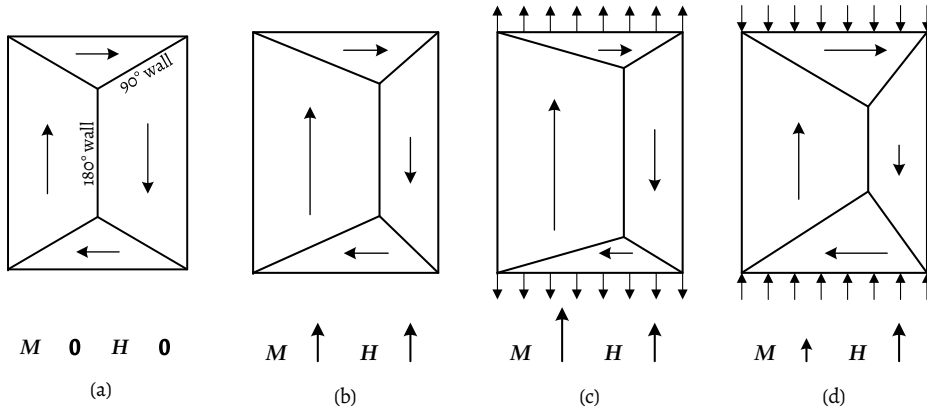


Figure 4.1: Simplified domain configuration based on Schneider et al. (1992) for four distinct scenarios. Arrows below indicate the magnitude of the applied external auxiliary field H and the resulting bulk magnetisation M . (a) Demagnetised state. (b) External field only. (c) External field and tensile strain. (d) External field and compressive strain.

moments in the neighbouring domains characterise the domain wall. When the magnetic moments on each side of the wall are anti-parallel, the wall is called a 180° domain wall; the other type of wall is designated a 90° wall, since the domains moments are orthogonal.

When energy is added to the system, e.g. a change is effectuated in the external magnetic field or the application of a mechanical strain, the magnetic ordering alters accordingly to minimise the total energy in the new situation. Effectively, magnetic domains change their size by the motion of the domains walls. Figure 4.1b shows the newly attained domain arrangement after the application of an external field, resulting in an aligned net magnetisation. In the figure, the external field H is prescribed, and the resulting magnetisation M is merely the sum of the contributions of magnetic moments of the individual domains, i.e. the arrows in the four regions. All domain wall types are sensitive to changes in the external field; domains with a moment aligned with the external field grow at the expense of those that oppose it. However, for an applied strain, only 90° walls are sensitive to this external impetus (Bulte and Langman, 2002). Figure 4.1c displays the redistribution due to a uniaxial tensile strain, resulting in an increase of the magnetisation. In contrast, when the specimen is subjected to compressive strain, the magnetisation decreases, which is clear from the domain configuration in Figure 4.1d. Note that in both cases, only the 90° walls have shifted under influence of the strain.

In the above simplified situation, the domain walls can move unimpeded. However, most engineering materials have a large number of impurities at the micro-scale: inclusions of different types of atoms, dislocations in the crystal lattice and similar defects. These crystallographic defects generate a local strain field in the lattice (Honeycombe, 1968), which acts as a barrier for the domain walls. Consequently, domain walls are pinned to these

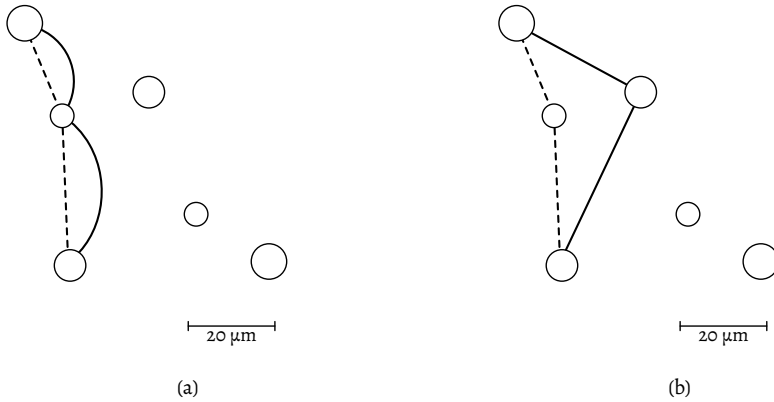


Figure 4.2: Two domain wall processes. Dashed lines signify the initial domain wall position, while the solid lines represent the new location of the wall resulting from an external stimulus. (a) Reversible domain wall bowing. (b) Irreversible domain wall movement.

imperfections, which are called pinning sites (Jiles and Atherton, 1984) and play a pivotal role in the magnetic behaviour of ferromagnetic materials subjected to external loads. For low-energy disturbances, the main mechanism for domain wall movement is bowing, i.e. the domain wall only bulges while it is kept in place by the pinning sites (Figure 4.2a). This process is reversible: when the external stimulus is removed, the original situation is recovered. However, when sufficient energy is added to the system, the domain wall can overcome a pinning site and move until a stronger pinning site is encountered (Figure 4.2b). This process is irreversible: upon removal of the external force, the domain wall remains pinned at its new location, permanently changing the configuration of the magnetic domains in the material.

4.1.2. Macroscopic description of ferromagnetism

Since a steel structure contains a vast amount of magnetic domains, its magnetic behaviour is more commonly described in terms of the bulk magnetisation M , which is acquired by spatial averaging of the magnetic moments of the constituent magnetic domains. Inside a magnetised material, the magnetic field B , also referred to as the magnetic flux density, and the bulk magnetisation are related by (Griffiths, 1999, p. 629):

$$\mathbf{B} = \mu_0 (\mathbf{H} + \mathbf{M}), \quad (4.1)$$

in which μ_0 is the magnetic constant ($\approx 4\pi \cdot 10^{-7}$ H/m), and \mathbf{H} denotes the magnetic field strength, also called auxiliary magnetic field. Each bold letter represents a vector containing the spatial components of the respective fields. Typically, the magnetic field \mathbf{B} is expressed in tesla (T), while the auxiliary field \mathbf{H} and the magnetisation \mathbf{M} are given in ampere per

metre (A/m). In the absence of a material, the magnetic field is proportional the auxiliary field, since in that case $M = \mathbf{0}$ by definition. A material is characterised by its dependence of M on H :

$$M = \chi H, \quad (4.2)$$

in which χ is the magnetic susceptibility tensor. For an isotropic material, the tensor reduces to a scalar. The magnetic susceptibility is related to the relative magnetic permeability μ_r , which relates the magnetic field and the auxiliary field in the isotropic case:

$$B = \mu_0 \mu_r H, \quad (4.3)$$

in which $\mu_r = \chi + 1$. Both quantities represent the same physical process, hence, the terms, can be interchanged. Throughout this thesis, the susceptibility will be used to quantify the relation between the magnetisation and the auxiliary field.

In a paramagnetic material, which is characterised by a positive susceptibility, the auxiliary field and magnetisation increases concurrently; while when the magnetisation opposes the magnetising field, the material is called diamagnetic, and it has a negative susceptibility. For a ferromagnetic material, the magnetic susceptibility is a non-linear function of the magnetising field, which is characterised by magnetisation curves.

4.1.3. The magnetisation curve

A magnetisation curve plots the magnetisation changes resulting from a varying external factor (Stoner, 1950). Commonly, such a curve is determined on a rod-like specimen enclosed by two coils: one generating the external magnetic field, which is coaxial with the specimen, and one measuring the induced magnetic field, which is directly related to the induced magnetisation (Jiles et al., 1984). When the external magnetic field is varied in the vicinity of a ferromagnetic specimen, a typical magnetisation curve as shown in Figure 4.3 is obtained. Starting at the origin (indicating that no net magnetisation is present, i.e. the material is demagnetised), the external field is first increased until the curve flattens. Thereafter, the field is diminished until the curve levels for negative field values, after which the loop is closed by increasing the field again. It is clear that the curve is not single-valued due to hysteresis.

Each curve contains notable characteristic quantities. First, the saturation magnetisation M_s quantifies the maximum magnetisation a material can attain, in which case all magnetic domains are completely aligned with the external field. The numerical value for the saturation magnetisation M_s of a material is determined from a relatively simple experiment, see Purcell and Morin (2013, pp. 565–566). Second, the remanent magnetisation or the remanence M_r represents the magnetisation in the absence of an external field, which is of particular interest to quantify the strength of a permanent magnet (Chikazumi and Graham, 1997). Third, the coercive field H_c is the field strength that eliminates the magnetisation in

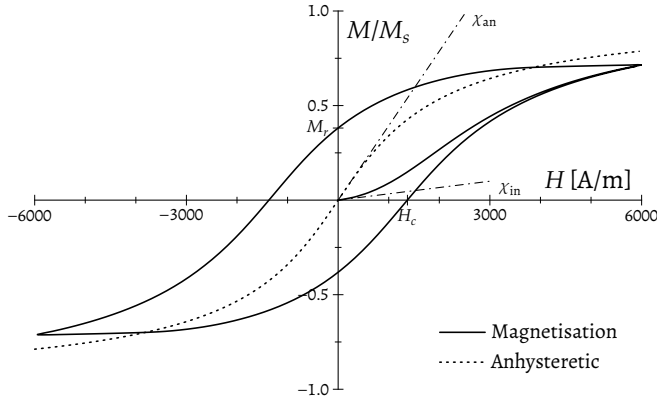


Figure 4.3: Magnetisation curve for a varying external magnetic field.

a material. Fourth, the initial differential susceptibility χ_{in} is defined as the slope of the magnetisation curve at the origin.

4.1.4. Anhysteretic magnetisation

Figure 4.3 contains an additional magnetisation curve: the anhysteretic magnetisation curve. This curve, occasionally referred to as the ideal magnetisation curve, is obtained by applying a decaying alternating field on top of a static bias field (Bozorth, 1951/1993, p. 8). As its name implies, this special curve displays no hysteresis, because it represents a statistical distribution of the magnetic domains that corresponds to the minimal energy state of the material, while neglecting any sources impeding the motion of the domain walls (Jiles and Atherton, 1986). However, in reality, these disturbances are present in a steel specimen, in which case the anhysteretic describes the global magnetic equilibrium state of the material for a given external field (Tebble and Craik, 1969, p. 401).

A common way to mathematically describe the anhysteretic magnetisation curve is based on the thermodynamic equilibrium of a distribution of typical magnetic domains (Jiles and Atherton, 1986). Appendix A treats this derivation, which results in the following expression for an isotropic three-dimensional solid (Raghunathan et al., 2009):

$$M_{an} = M_s \mathcal{L}\left(\frac{H_e}{a}\right), \quad (4.4)$$

in which M_s is the aforementioned saturation magnetisation and

$$\mathcal{L}(x) = \coth(x) - \frac{1}{x} \quad (4.5)$$

is the modified Langevin equation. In Equation (4.4), H_e is the effective field and a denotes a parameter inversely proportional to the strength of the magnetic moment of a typical

magnetic domain (Sablík et al., 1993). Consequently, the latter is regarded a model parameter to obtain the desired magnetisation. Note that the strength of the magnetic moment of a typical domain depends on the magnetic domain configuration; hence, its value can change whenever that configuration irreversibly changes, e.g. due to the formation of additional pinning sites or when domain walls break away from their respective pinning sites. Therefore, a cannot be considered a material constant.

Ordinarily, the effective field is derived from the Helmholtz free energy density A , which is given by (Sablík et al., 1988):

$$A = \frac{1}{2}\alpha\mu_0 M^2 - TS + \mu_0 HM, \quad (4.6)$$

in which μ_0 is the magnetic constant, M the bulk magnetisation, T the absolute temperature, S the entropy, H the auxiliary field, and α a coefficient to quantify the coupling between the domain's magnetic moment and the bulk magnetisation (Jiles and Atherton, 1986). Subsequently, by taking the derivative of A with respect to the magnetisation M under constant temperature, the effective field is obtained:

$$H_e = \frac{1}{\mu_0} \left(\frac{\partial A}{\partial M} \right)_T = H + \alpha M. \quad (4.7)$$

The expression describing the anhysteretic magnetisation above is acquired assuming that the bulk magnetisation and the external field are uniaxial and parallel. However, more generally, it is reasonable to expect that the anhysteretic magnetisation is a vector quantity. For an isotropic material, Leite et al. (2004) presents a vectorial generalisation of the modified Langevin equation:

$$M_{\text{an}} = M_s \mathcal{L} \left(\frac{H_e}{a} \right) \frac{H_e}{H_e}, \quad (4.8)$$

in which $H_e = \|\mathbf{H}_e\|$ is the L_2 -norm of the effective field vector.

For our specific purpose, i.e. the magnetic response of a structure in the presence of a weak external field, it is safe to assume that the effective field is also relatively weak. As a result, the anhysteretic magnetisation curve is approximated for low effective field values. By considering the first order Maclaurin series of the modified Langevin function, Equation (4.5), one obtains:

$$\mathcal{L}(x) = \mathcal{L}(0) + \left. \frac{d\mathcal{L}(x)}{dx} \right|_{x=0} x + O(x^2) \approx \frac{x}{3}. \quad (4.9)$$

Applying this result to the expression for the anhysteretic, Equation (4.4), yields:

$$M_{\text{an}} \approx \frac{M_s}{3a} H_e. \quad (4.10)$$

This implies that, for low effective field values, the anhysteretic magnetisation is linearly related to the effective field. A similar result is obtained for the vectorial expression:

$$\mathbf{M}_{\text{an}} \approx \frac{M_s}{3a} H_e \frac{\mathbf{H}_e}{H_e} = \frac{M_s}{3a} \mathbf{H}_e. \quad (4.11)$$

By applying the low-field approximation and substituting the effective field, the anhysteretic magnetisation can be expressed directly in terms of the external field H , yielding

$$M_{\text{an}} = \frac{M_s}{3a} H_e = \frac{M_s}{3a} (H + \alpha M_{\text{an}}) = \chi_{\text{an}} H \quad (4.12)$$

in which the anhysteretic susceptibility χ_{an} is given by (Jiles et al., 1992):

$$\chi_{\text{an}} = \frac{M_s}{3a - \alpha M_s}, \quad (4.13)$$

which is the slope of the anhysteretic at the origin, see Figure 4.3. Due to the presence of pinning sites, the amplitude of initial magnetisation curve always lies below the anhysteretic magnetisation, hence $\chi_{\text{in}} < \chi_{\text{an}}$.

4.2. Magnetomechanical effects

So far, the discussion has focused on the change of the magnetisation caused by a varying external field. However, next to that, mechanical strain can influence the magnetisation significantly (Bozorth and Williams, 1945). Strain-induced magnetisation changes are collectively known under the term magnetomechanical effect, which encompasses the magnetisation changes in a material due to both elastic and plastic deformations. Lee (1955) gives an extensive account on the different manifestations of the magnetomechanical effect, noting that all of them are related to the same physical processes: magnetostriction and its inverse.

Magnetostriction[†] refers to the strain induced in a ferromagnetic specimen when it becomes magnetised, which has first been observed by Joule (1847). The magnitude of the magnetostrictive strain is normally in the order of 10^{-5} m/m for magnetically saturated specimens, which is rather insignificant compared to the observed elastic strain levels in steels, which are 10^{-3} m/m or higher. Hence, the magnetostrictive contribution to the mechanical strains is normally negligible.

Villari (1865) has been the first to describe the converse of magnetostriction. Hence, it is referred to as the Villari effect or, more commonly, inverse magnetostriction. It encompasses the change of the magnetisation in a ferromagnetic material due to a change in the applied

[†]Magnetostriction is not be confused with piezomagnetism. According to Cullity (1971), a piezomagnetic material can attain a net magnetisation when strained in the absence of an external field. However, no ferromagnetic material is known to be piezomagnetic. For magnetisation changes due to strain to occur in a ferromagnetic material, a non-zero magnetisation is required (Bulte and Langman, 2002). Therefore, when discussing magnetisation changes due to strain in a ferromagnetic material, e.g. steel, one must refrain from using the term piezomagnetism.

strain. Most authors relate the magnetisation changes to the stress rather than to the strain, even though one would expect that, considering the term inverse magnetostriction, strain drives the magnetisation changes analogously to normal magnetostriction, in which magnetisation induces strain. Fortunately, in the elastic range, stress and strain can be interchanged by applying the proper (mechanical) constitutive equation. However, when plastic deformation develops, the one-to-one correspondence between strain and stress ceases to exist, yielding a situation in which the change in magnetisation is described in terms of elastic stress and plastic strain. In this thesis, magnetisation changes are related to the strain field, except when citing previous work of other authors who refer to stress in order to keep the notation consistent with their work. Please note that in those cases, stress and strain can be interchanged freely, keeping in mind the correct conversion factors, since elastic stresses are considered.

While studying the magnetomechanical effect, two parameters can independently be varied: the external magnetic field and the strain field. Hence, two magnetisation scenarios can be distinguished (Jiles, 2015, pp. 423–427):

1. **Isostrain** Magnetisation changes due to a varying external magnetic field under a constant strain level—*isostress* is an equivalent term;
2. **Isofield** Magnetisation changes due to a varying strain in a steady external field.

The former focuses on the influence of strain on the defining characteristics of the magnetisation curve, which are listed in Section 4.1.3. Determining these magnetisation parameters involves generating and controlling a high-strength—preferably spatially homogeneous—external magnetic field, which is difficult to achieve in situ for large-diameter monopiles. As the external field during a monopile installation is the time- and space-invariant geomagnetic field, the latter magnetisation scenario is a natural starting point to study the magnetomechanical behaviour of such a structure. Factors influencing the isofield magnetomechanical response are categorised as follows:

- (i) external magnetic field;
- (ii) elastic and plastic deformation;
- (iii) history of magnetic and mechanical loading;
- (iv) demagnetising field caused by the structure's geometry;
- (v) strain rate.

Each of these factors is elaborated upon in the following sections, after which a conclusion is drawn pertaining the knowledge gaps for the magnetomechanical response of large-scale structures under dynamic loading.

4.2.1. External magnetic field

Although the external magnetic field is the most obvious trigger for the magnetisation changes under applied strain, the available experimental data imply that no straightforward relation between strain and applied external field exists. Data for demagnetised samples subjected to a single strain cycle in a weak field presented by Birss et al. (1971) indicate that the amplitude of the magnetisation changes increases with increasing external field. However, for stronger magnetic fields, Atherton and Jiles (1986) observe that the magnetisation change caused by a strain cycle is proportional to the difference between the magnetisation before the strain is applied and the anhysteretic magnetisation value associated with the current field strength. This indicates that strain-induced magnetisation cannot be evaluated solely based on the external magnetic field, but rather that the complete magnetic and mechanical loading history must be accounted for.

4.2.2. Elastic and plastic deformation

For initially demagnetised samples, Craik and Wood (1970) and Birss et al. (1971) report isofield magnetisation curves for tensile and compressive loads that remain in the elastic regime. They observe a distinct asymmetry in the magnetic response with compressive and tensile strain. During the release of the strain, the magnetisation does not follow that same path as before, indicating that, just as for a varying external field, hysteresis is present (Craik and Wood, 1970). A further sign of the hysteretic nature of the magnetomechanical effect is that, after a full strain cycle, the magnetisation at zero strain has irreversibly changed. The hysteresis results from the domain wall movement due to the added strain energy overcoming the pinning sites in the material (Atherton et al., 1988) as described in Section 4.1.1. Jiles and Atherton (1984) notice that a complete strain cycle pushes the magnetisation towards the anhysteretic magnetisation curve, a phenomenon called the law of approach (Jiles, 1995). The experimental data of Pitman (1990) confirm this hypothesis, which highlights the importance of this global magnetic equilibrium.

Regarding the influence of plastic strain, Bozorth and Williams (1945) report a marked irreversible decrease of the magnetisation due to tensile strain as soon as plastic deformation develops. More recently, Lazreg and Hubert (2012) describe a similar degradation of the magnetic behaviour due to plastic tensile strain. For compressive strain, this reduction of the magnetic properties is confirmed by Jiles (1988a), who presents a range of magnetic properties obtained from magnetisation curves, each displaying a decline for increased levels of plastic strain. For the rod-shaped specimens, the changes in susceptibility appear to be related to the residual stress (Jiles, 2015, p. 425). Most commonly, the observed behaviour is attributed to the increase in dislocation density, which accompanies the development of plastic deformation (Gilman, 1968). The newly formed pinning sites fragment the domain structure, i.e. the number of domains increases, which, in turn, leads to a reduction of the bulk magnetisation.

4.2.3. Loading history

The previous section considered only a single strain cycle, in which the load is applied and removed once, while in practice more complex loading histories occur. When a strain cycle is repeated, the resulting magnetisation changes differ from the previous cycle (Bozorth, 1951/1993, pp. 600–601). After a few cycles, however, the response stabilises, indicating only reversible magnetisation changes to occur (Atherton and Jiles, 1986; Guo and Atherton, 1995). This behaviour is explained by the domain walls breaking away from their pinning sites aided by the provided strain energy until they reach stronger pinning sites which prevent the wall from moving further. After a sufficient number of load cycles, all domain walls are pinned to the stronger pinning sites, and the domain wall's response to strain is restricted to reversible domain wall bowing during subsequent cycles. However, as soon as more strain energy is introduced, i.e. a strain cycle that exceeds the previous peak strain, the stronger pinning sites are also conquered, resulting in an irreversible magnetisation change towards a new equilibrium (Li et al., 2017a). When a subsequent strain cycle remains below the previously sustained peak strain, only reversible changes are observed. The attained equilibrium after multiple strain cycles is not necessarily the global magnetic equilibrium, but rather a local or meta-stable equilibrium (Makar and Atherton, 1995; Maylin, 1994; Maylin and Squire, 1993a).

Figure 4.4 shows an illustrative example of the change of magnetisation with five uniaxial compressional strain cycles for an initially demagnetised sample. During the first cycle, the magnetisation is irreversibly pushed towards the first magnetic equilibrium \bar{M}_1 . Note that the magnetic equilibrium is defined in an unstrained situation. Subsequent load cycles with the same peak strain display an identical magnetic response. However, when a new peak strain is introduced, the magnetisation permanently moves to \bar{M}_2 , since the higher strain energy supplied to the specimen enable the domain walls to break away from their respective pinning sites. A successive load cycle with an amplitude below the previous peak strain (between t_4 and t_5) causes only reversible changes in the magnetisation returning to \bar{M}_2 when the strain equals zero.

4.2.4. Demagnetising field

When a ferromagnetic specimen is placed in a uniform external field, the resulting magnetisation is inhomogeneous as a result of magnetic self-interaction (Beleggia et al., 2009). Due to the specimen's geometry, the magnetisation of the entire structure influences the local value of the auxiliary field through this non-local interaction. In that case, the auxiliary field H consists of the external field H_0 and the so-called demagnetising field H_d as follows:

$$H = H_0 + H_d = H_0 - \mathbf{NM}. \quad (4.14)$$

The demagnetising field is related to the induced magnetisation through the demagnetisation tensor \mathbf{N} , which is a function of the geometry and magnetic susceptibility (Parq, 2017).

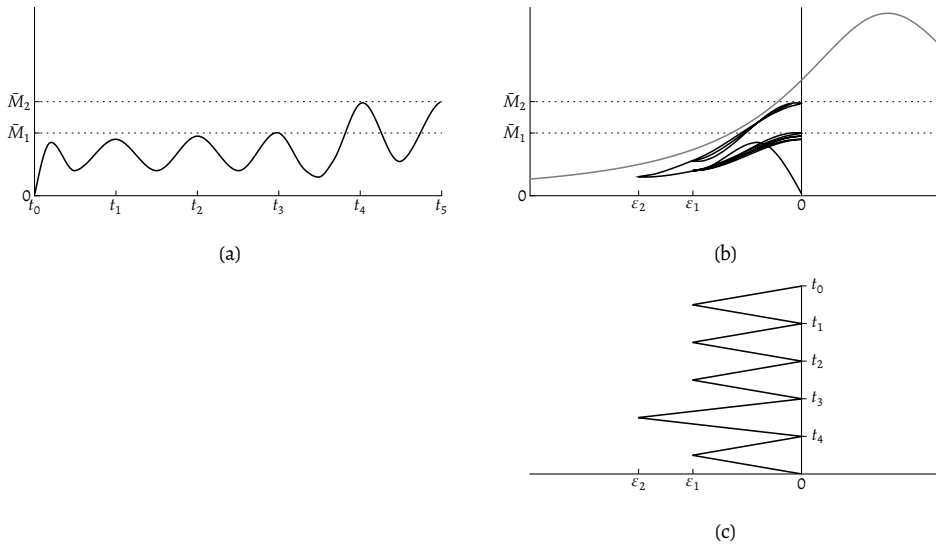


Figure 4.4: Illustrative example of magnetisation versus uniaxial compressive strain based on data from Atherton and Szpunar (1986). (a) Time trace of the evolution of the magnetisation, starting from a demagnetised state. (b) Evolution in the strain-magnetisation plane with the anhysteretic magnetisation curve indicated by the grey line. (c) Time trace of the compressive strain cycles.

Only for a select number of simple geometries, e.g. ellipsoids, closed form expressions exist (Chen et al., 1991). Consequently, the demagnetisation tensor for other geometries has to be approximated with numerical methods.

For the majority of reported experiments on the magnetomechanical effect, the demagnetising field of the specimen is negligible due to their rod-like shapes. In those experiments, a search coil surrounding the specimen is deployed to infer its magnetisation (Jiles et al., 1984). However, for a large-scale structure, such an approach is not only impractical, but it also obscures the delicate variations in the surrounding magnetic field, since a search coil gives an average of the magnetic field encompassed by the coil's windings. Hence, points measurements of the magnetic field are required, for which magnetometers based on other magnetic principles, e.g. fluxgate magnetometers (Ripka, 1992), can be used. In that case, the position of the sensor relative to the structure becomes an important parameter in the analysis of its magnetisation.

Viana et al. (2010) show that the influence of the demagnetisation resulting from the non-local interaction of the magnetisation is considerable for large ferromagnetic structures. In the same measurement campaign, they observed that, just as for the small specimens, the magnetisation approaches the anhysteretic magnetisation curve when the structure is subjected to cyclic tensile strain (Viana et al., 2011b). This suggests that the principles

derived from the small-scale specimens can readily be applied to a large-scale structure as long as the demagnetising field is properly accounted for.

A final note on the influence of the demagnetising field pertains the dearth of magnetic data under compressive loading. To prevent buckling of a specimen subjected to a compressive load, a specimen must have a certain thickness to length ratio. Birss et al. (1971) indicate that specimens with a sufficient value of this ratio have an appreciable demagnetising factor, complicating the analysis significantly. Therefore, at present, most experiments are performed with tensile strain, especially for high strain levels.

4.2.5. Strain rate

Since most experimental work on the magnetomechanical effect reported in literature consider quasi-static loads, not much is known regarding the influence of the strain rate on the magnetic response of a material. On one hand, Bao et al. (2017b) report measurable differences in the stray field changes after systematically varying the loading speed, even though the strain rate in their work is several orders of magnitude smaller than the strain rate induced by an impact load. They suggest that the strain rate must be included in a more accurate magnetomechanical model for such loading conditions. On the other hand, Crum et al. (2017) and Domann et al. (2015) report magnetisation changes in Galfenol under impact loads, which is a material that exhibits significantly stronger magneto-elastic interactions than steel. Based on their experiments, these authors conclude that the magneto-elastic coupling is insensitive to strain rates up to 33 s^{-1} . Altogether, these contradicting findings illustrate that the influence of the strain rate on strain-induced magnetisation changes is an open academic issue.

4.2.6. Discussion

From the above, it is clear that the isofield magnetic response for small-scale specimens under repeated loading is thoroughly researched. The available data show that the magnetisation is pushed towards the anhysteretic magnetisation due to an elastic load. Additionally, the magnetisation reaches a meta-stable equilibrium due to repetition of an identical load. When a new peak strain is introduced, the magnetisation is pushed towards a new equilibrium. As soon as plastic deformation develops, the magnetic properties deteriorate significantly. The dislocation density and magnetic domain configuration in the material explain this observed behaviour.

For large-scale structures, e.g. a monopile, the effect of the demagnetising field is substantial, complicating the analysis as the magnetisation due to a space-invariant external field is non-uniform. At present, the available magnetomechanical data for these structures are limited to static tensile loads. Since an impact hammer induces high-frequency compressive strains, it is uncertain if the observations above will hold during these loading conditions. Thus, an experimental set-up must be designed that explicitly accounts for these factors to fill the raised knowledge gaps.

4.3. Applications of the magnetomechanical effect

Before focusing on models for the experimentally observed effects, this section presents an overview of applications of the magnetomechanical effect to infer deformations of a material by means of non-destructive magnetic methods. Depending on the control of the external magnetic field, the applications are categorised into two groups: active and passive methods. As the name suggests, in the former, the external field is varied, similar to the isostrain magnetisation scenario, while in the latter, the external field is not controlled.

4.3.1. Active methods

A wide variety of active magnetic methods for non-destructive evaluation has been developed over the years (Jiles, 1988b, 1990), which share the requirement of a controllable external magnetising field. The differences between the methods arise from the measured quantities. Three distinct active methods are discussed below.

The first group of methods rely on the strain-dependency of the magnetic susceptibility χ to infer the strain by constructing isostrain magnetisation curves (Langman, 1981; Makar and Atherton, 1994). For example, Garikepati et al. (1988) determine the elastic strain from the change in the anhysteretic susceptibility χ_{an} , and Takahashi et al. (2017) utilise a similar approach to infer plastic deformation and cracks.

The second group of methods measures the intensity of sudden jumps during the isostrain magnetisation process; i.e. the magnetic Barkhausen effect (Maylin and Squire, 1993b). These discontinuities in the magnetisation curve are caused by the sudden movement of domain walls due to the changing external field. As a result, the intensity of the Barkhausen count reflects the micro-structure of the material (Kleber and Vincent, 2004). Consequently, this method is predominantly applied to infer plastic deformations.

The last group of methods (Magnetic Flux Leakage (MFL) methods) utilises the magnetic stray field surrounding a specimen, which is generated by its magnetisation. To amplify the signals, the specimen is normally magnetised to saturation (Wang et al., 2018b). Due to changes in the geometry (e.g. a crack) or variations in the magnetic susceptibility (e.g. plastic deformation), the demagnetising field H_d (Equation (4.14)) changes locally, creating a pronounced disturbance in the magnetic stray field in the vicinity of the defect (Babbar et al., 2005). Due to its high sensitivity to the presence of such defects, this technique has successfully been applied to large-scale structures, especially when visual inspection is impossible, e.g. for pipe lines (Atherton and Teitsma, 1982; Ege and Coramik, 2018; Li et al., 2017b) or for wire ropes used in suspension bridges (Christen et al., 2009).

4.3.2. Passive methods

Contrary to the active methods, passive magnetic methods do not require a controlled excitation signal to infer deformations in a structure. These methods rely on the magneto-mechanical response of the specimen in the ambient magnetic field, e.g. the geomagnetic field.

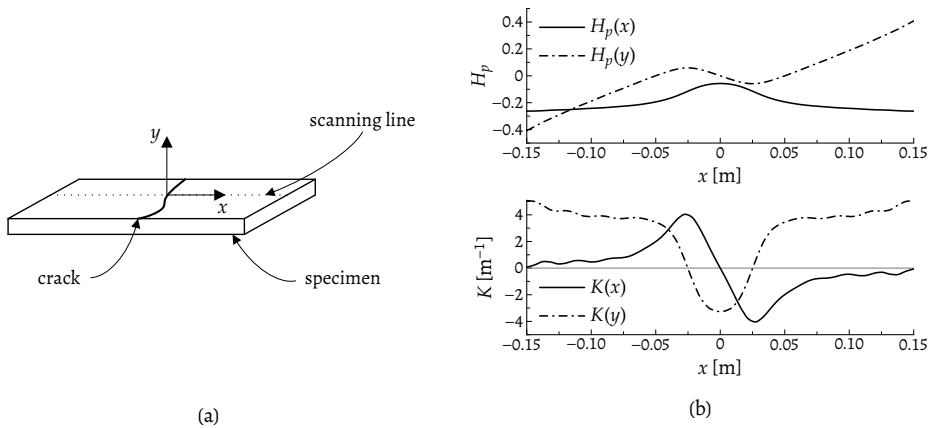


Figure 4.5: Example of an MMM evaluation of a cracked ferromagnetic specimen. (a) Schematic of the specimen and the scanning line. (b) Stray field signals in the normal ($H_p(y)$) and tangential ($H_p(x)$) direction and the corresponding gradients along the scanning line.

Metal Magnetic Memory

A passive magnetic technique that has received considerable attention in the past two decades is the Metal Magnetic Memory (MMM) method, which is first described by Dubov (1997). Similar to the active MFL technique, the magnetic stray field of the specimen is mapped using a magnetometer. It has been successfully used as a qualitative inspection technique to locate stress concentration zones, cracks and regions of plastic deformation (Bao et al., 2020). According to the developers, the method is based on the observation that in cyclically strained areas, e.g. stress concentration zones, the magnetisation will keep increasing until failure. By detecting anomalies in the stray field, which are generated by the accumulated magnetisation, critical areas in a structure can be identified (Wilson et al., 2007).

Figure 4.5 presents a schematic representation of MMM's *modus operandi*. During an MMM evaluation, two components of the stray field are recorded: the normal component $H_p(y)$ (y is normal to the surface), and the tangential component $H_p(x)$ (x is along the scanning line). Based on the gradients of these quantities along the scanning line ($K(y)$ and $K(x)$), the location of plastic deformation (Dong et al., 2009) and cracks (Chen et al., 2017) can be determined, which presents itself as a peak in $K(y)$ in conjunction with a zero crossing for $K(x)$ (Figure 4.5b). Note that these detection criteria are qualitative and do not entail quantitative information about the defect.

In the MMM technique, the remanent magnetic field is commonly measured when the strain has been released (En et al., 2007; Li and Xu, 2012). Additionally, the specimen is demagnetised before a load is applied to erase the magnetic history, as the presence of an initial magnetisation frustrates the detection of defects (Guo et al., 2011; Leng et al., 2012; Ren et al., 2019). Gorkunov (2014) states that, without properly accounting for the magnetic

history, MMM cannot be used to reliably assess a specimen, since a multitude of factors result in an identical remanent stray field.

The MMM method is not without criticism. First, Augustyniak and Usarek (2015) argue whether the method can be applied for purposes beyond the qualitative assessment of damage in specimens, because a measured stray field value is not necessarily one-to-one related to the current (plastic) strain value, preventing one to formulate an inverse description of the problem. Second, Li et al. (2017a) investigate the accumulation of magnetisation in stress concentration zones, which is the physical foundation of the method according to Dubov (1997). They conclude that the magnetisation process under cyclic strain is in accordance with the data from Robertson (1993), where a cyclic load pushes the magnetisation towards a magnetic equilibrium state, which differs from the usual physical explanation underlying the MMM method. Nonetheless, this conclusion does not compromise MMM's ability to detect stress concentration zones, it only asserts that the physical process differs.

4

SQUID magnetometry

Other research groups use highly sensitive SQUID magnetometers (Buchner et al., 2018) to infer defects in steel specimens. As the method uses the gradients of the stray field of the specimen (Banchet et al., 1995; Mignogna et al., 1993), it can be regarded as MMM *avant la lettre*. More recently, Bonavolontà et al. (2007) detected a region of localised plastic deformation using this method. Since mapping the stray field in real-time is not possible with a SQUID magnetometer, Bonavolontà et al. (2009) concurrently deploy a fluxgate sensor to measure the stray field changes during loading. They successfully detect a stress concentration zone in a notched sample based on both the SQUID and fluxgate signals.

Real-time passive methods

In the passive magnetic methods above, measurements of the magnetic stray field in the geomagnetic field are made after applying a full strain cycle and are used to infer stress concentration zones and regions of plastic deformation. However, to infer the current deformation state of the material, the stray field has to be measured concurrently with the application of the external mechanical strain. Viana et al. (2011b) record strain-induced stray field changes while increasing the pressure in a steel cylinder. Subsequently, an analytic expression is determined for the stray field variations with applied pressure based on the measured data. Staples et al. (2013) pursue an identical approach, albeit for a smaller specimen in a test machine. For plastic deformation, Bao et al. (2016) measure the stray field in real-time, in which a dog-bone specimen is loaded beyond the yield limit while simultaneously the stray field changes are monitored.

4.3.3. Discussion

Although successful in determining strains and defects, all active methods have the disadvantage of the need to control an external magnetic field, which is not practical during

a monopile installation. Next to that, to determine the magnetic properties of interest with an active method, the strain has to remain constant during the construction of the magnetisation curve. For rapid variations of the strain field, this might be problematic, as the swift application of a full magnetisation signal generates eddy currents in a conducting material (Jiles, 1994b; Scheidler and Dapino, 2016). Therefore, active magnetic methods do not qualify as workable non-contact magnetic methods to infer deformation during a monopile installation.

Naturally, a passive method does not exhibit these disadvantages, enabling real-time measurements of the deformations. The passive methods above are relatively similar to each other, since they all measure the magnetic stray field. Consequently, the observations made with MMM are an essential starting point for a method to infer deformations based on magnetic field measurements. Nonetheless, the name MMM will not be used in this thesis, since it reflects the false assumptions regarding the underlying physical process. In current passive methods, the initial magnetic state is a major obstruction in their successful application. Therefore, in a newly proposed method, the influence of the initial state should be carefully considered.

4.4. Magnetomechanical models

To model the magnetomechanical effect, one should account for the influences discussed in Section 4.2 in the modelled magnetisation M . A generic model for the bulk magnetisation takes the following form:

$$M = f(B, \varepsilon, M) \quad (4.15)$$

where B denotes the local magnetic field, which is reciprocally influenced by the magnetisation of the entire structure through the demagnetising field; ε represents the total strain tensor, which includes the mechanical loading history; and M is the local magnetisation which encompasses the magnetic history.

4.4.1. Particle models

A classical approach to model the magnetomechanical effect is to divide the bulk material into elementary magnetic particles. Originally developed for a single magnetic domain, the summed contribution of a distribution of these particles enables one to model the bulk magnetic behaviour of a multi-domain specimen. Liorzou et al. (2000) reviews three of these particle methods (Preisach, modified Globus, and Stoner–Wohlfarth). Although each model has its own range of application, they all include anhysteretic magnetisation behaviour, stressing the importance of this ideal magnetisation curve in the magnetisation process. Another common feature of the particle methods is the necessity of a distribution function for the particles, which Everett (1955) proposes. To determine the particle distribution, several full magnetisation curves have to be determined (Benabou et al., 2003).

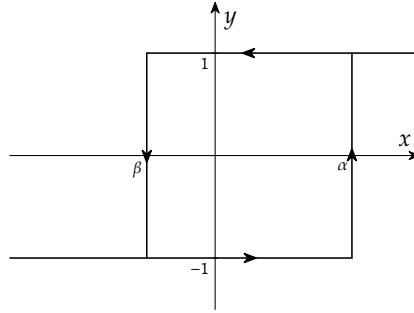


Figure 4.6: The relay hysteron, the fundamental building block of the Preisach model for ferromagnetic hysteresis (Ruderman, 2015).

4

At first, particle model have been developed to model hysteretic magnetisation curves in the absence of applied strain. Later, two models have been proposed to include strain in an isostrain scenario: the Preisach model (Bergqvist and Engdahl, 1991), and the Stoner–Wohlfarth model (Xu et al., 2015). To the best of the author’s knowledge, no particle method applicable to an isofield magnetisation scenario exists.

Particle methods are generalised by the concept of hysterons, which are elementary hysteretic functions (Bobbio et al., 1997). As an example, Figure 4.6 shows the relay hysteron, which is the fundamental building block of the Preisach model, in which x represents the magnetising field and y the magnetisation. Starting at $y = -1$ and increasing x , this value is retained until $x > \alpha$. If the magnetising field is then reduced, the magnetisation switches back only when $x < \beta$. Clearly, this simple process creates hysteresis. More advanced types of hysterons exist and have been used to model isostrain magnetisation curves (Bergqvist, 1997; d’Aquino et al., 2003; Lin et al., 2014; Sixdenier et al., 2016). However, a hysteron approach for isofield magnetisation is not reported in literature at present.

4.4.2. Multi-scale models

In a multi-scale approach, the material is modelled at three separate length scales: domain, grain and macro scale (Hubert, 2019). Naturally, this division reflects the structures found in a real polycrystalline ferromagnetic material. To convey the results from a smaller scale to a larger scale, a process called homogenisation is applied. Since the material model is constructed from the smaller scales, a broad range of effects can be incorporated in a simple manner, e.g. crystalline anisotropy (Vanoost et al., 2016) and plastic deformation (Hubert and Lazreg, 2017). Most importantly, these models treat the physical quantities in their full tensorial forms (Daniel et al., 2008), which is normally not the case in phenomenological models.

A disadvantage of the multi-scale models is the relatively high computational cost, since a considerable amount of domains and grains have to be considered in a computation to

yield reliable results. Consequently, simplified versions of the full multi-scale models for the magnetomechanical effect have emerged to reduce the computational time. One simplification approach replaces the domain scale by the response of single average domain (Aydin et al., 2017; Daniel et al., 2015) by introducing additional model parameters. Another strategy to simplify a multi-scale model is to assume the material consists of six domains, each with a magnetic moment aligned to the positive and negative directions of an orthogonal coordinate system (Bernard et al., 2011). Despite the reduced range of application, the resulting model equations have analytical solutions as a consequence of the simple domain configuration (Daniel, 2013, 2018).

4.4.3. Jiles–Atherton models

A phenomenological approach to model the magnetomechanical effect has been developed over the years for isostrain magnetisation by Jiles and Atherton (1986) and subsequently for isofield magnetisation by Jiles (1995). Therefore, these models and derived extensions are collectively referred to as Jiles–Atherton (J–A) models. At the heart of the theory is the anhysteretic magnetisation curve, which, as mentioned before, represents the magnetisation with a global energy minimum for a given external field.

Strain dependency of the anhysteretic magnetisation

The anhysteretic magnetisation curve depends on externally applied strain (Dobranski et al., 1985), which is accounted for by including a stress-induced term into the effective field, Equation (4.7):

$$H_e = H_0 + \alpha M + H_\sigma. \quad (4.16)$$

This additional term stems from the magnetoelastic energy stored in the material, which is (Sablik and Jiles, 1993)

$$E_{me} = \frac{3}{2} \lambda \sigma, \quad (4.17)$$

where σ is the applied uniaxial stress, and λ denotes the magnetostriction coefficient. By adding this energy to the free energy and taking the derivative with respect to the magnetisation, the stress-induced effective field H_σ yields (Sablik et al., 1988)

$$H_\sigma = \frac{1}{\mu_0} \left(\frac{\partial E_{me}}{\partial M} \right)_T = \frac{3\sigma}{2\mu_0} \frac{\partial \lambda}{\partial M}. \quad (4.18)$$

As the magnetostriction coefficient is a symmetric function of the magnetisation (Bozorth, 1951/1993, chap. 13), it is usually modelled as (Jiles, 1995):

$$\lambda = \sum_i^{\infty} (\gamma_i + \sigma \gamma'_i) M^{2i}, \quad (4.19)$$

where the γ coefficients are constants to be determined from experimental data. In the above, the stress is considered uniaxial and aligned with the auxiliary field. By substituting the effective field, Equation (4.16), into Equation (4.4), the stress-dependent anhysteretic magnetisation M_{an} is obtained:

$$M_{\text{an}} = M_s \mathcal{L}\left(\frac{H_e}{a}\right), \quad (4.20)$$

in which

$$H_e = H_0 + \alpha M + \frac{3\sigma}{2\mu_0} \frac{\partial \lambda}{\partial M} \quad (4.21)$$

represents the stress-dependent effective field.

4

The law of approach for isofield magnetisation

Jiles and Atherton (1984) observe that the magnetisation in an isofield experiment moves towards the anhysteretic magnetisation under the influence of applied strain. Subsequently, Jiles (1995) derives an expression to model this so-called law of approach. Based on available experimental data, he remarks that the observed shift towards the anhysteretic is independent of the sign of the applied load, but rather depends on a related quantity: the elastic energy per unit volume, which, for a one-dimensional elastic stress state, reads

$$W = \frac{1}{2} \sigma \varepsilon = \frac{\sigma^2}{2E}, \quad (4.22)$$

in which ε is the strain and E denotes Young's modulus. Next, the change of the magnetisation M with respect to a change in elastic energy W is

$$\frac{\partial M}{\partial W} = \frac{1}{\xi} (M_{\text{an}} - M) + c \frac{\partial M_{\text{an}}}{\partial W}, \quad (4.23)$$

where M_{an} is the strain-dependent anhysteretic magnetisation, ξ and c are model parameters. The first term in this expression signifies that the magnetisation change is proportional to the distance of the magnetisation to the anhysteretic, while the second term is related to the stress dependency of the anhysteretic magnetisation. Often, the relation is rewritten in terms of stress using $dW = (\sigma/E) d\sigma$, yielding

$$\frac{\partial M}{\partial \sigma} = \frac{\sigma}{\xi E} (M_{\text{an}} - M) + c \frac{\partial M_{\text{an}}}{\partial \sigma}. \quad (4.24)$$

With this expression, the resulting magnetisation due to an applied stress is easily computed for a given initial magnetisation. Jiles (1995) shows that this model equation replicates the available experimental data of Craik and Wood (1970) rather well, where a steel specimen is subjected to a single load cycle.

In Equation (4.24), the first term on the right-hand side gives rise to irreversible changes of the magnetisation, which result from the permanent displacement of the magnetic domain walls. As soon as the magnetisation M equals M_{an} , this term vanishes, and no further irreversible changes occur, which is in accordance with the definition of the anhysteretic magnetisation. The latter term on the right-hand side signifies the reversible magnetisation changes due to the exerted mechanical strain, i.e. the bowing of domain walls, and it is the only source of strain-induced magnetisation changes when the magnetisation equals the anhysteretic magnetisation.

Improvements to the original J–A model

Over the years, many improvements to the model described above have been proposed to account for several additional external influences, of which two are discussed here. First, due to cyclic loading, the magnetisation reaches a magnetic equilibrium state (Atherton and Szpunar, 1986). However, Sablik et al. (2000) show that the model above does not display this behaviour after consecutive application of a load cycle, and they propose to add a so-called turning point stress into the model formulation to capture the observed behaviour. A different approach to address the same deficiency of the original model is presented by Xu et al. (2012a), who introduce a local equilibrium state M_0 in accordance with the experimental data of Maylin and Squire (1993a).

Second, Sablik et al. (2004) include plastic deformation into the model. They attribute two types of changes to the development of plastic deformation: an increase in dislocation density and the appearance of residual stress. A slightly different approach is reported by Wang et al. (2011), in which the effective field is augmented with a term related to the amount of plastic strain in the material. In the end, plastic deformation reduces the effective magnetic susceptibility in the both formulations, which is in line with the expected reduction of the magnetic properties due to the increased number of pinning sites.

4.4.4. Discussion

Despite their successful application for isostrain magnetisation scenarios, the particle and hysteron models for the magnetomechanical effect have not yet been developed further to apply to isofield magnetisation procedures, which is essential to the use of a passive magnetic method. Moreover, it might be cumbersome to determine the distribution function for the constituent particles experimentally. Hence, this modelling strategy does not appear to be a practical path to model the magnetomechanical effect during monopile installations.

Due to their requirement to estimate the domain distribution, the full multi-scale models share this disadvantage with the particle methods. Furthermore, the computational cost of the approach is high, possibly prohibiting a real-time evaluation of the measured signals. This is unfortunate, since these models are able to account for a large range of relevant processes in a natural manner, e.g. the full tensor expressions of the physical

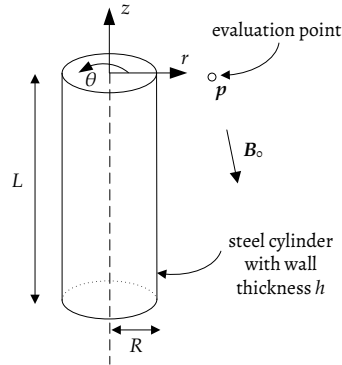


Figure 4.7: Schematic to determine the magnetisation and the resulting magnetic stray field of a thin-walled steel cylinder due to the presence of an external magnetic field.

quantities. Consequently, some concepts from the multi-scale models might be useful to incorporate in the phenomenological models.

From the three discussed modelling classes, the phenomenological J–A models seem to be the most promising to model strain-induced magnetisation changes, since they have successfully been applied to the isostrain scenario and are relatively simple to implement and calibrate due to their limited number of parameters. For reversible magnetisation changes, the law of approach suggests that only the strain-dependency of the magnetic equilibrium has to be analysed. At present, J–A models are derived under the assumption that the magnetisation and the auxiliary field are coaxial and that the applied load is uniaxial, resulting in scalar expressions involving the quantity’s magnitudes. Due to the demagnetising field, this assumption is not expected to hold in large-scale structures. Thus, the aforementioned models should be carefully extended to incorporate stress states that are multi-dimensional to successfully apply the phenomenological modelling approach in the case of monopile installation, which is of our interest in this work.

4.5. Modelling of the magnetic stray field of a thin-walled steel cylinder

In order to model the magnetic response of a thin-walled steel cylinder in the presence of a time- and space-invariant external field B_0 , the situation sketched in Figure 4.7 is considered. The origin of the cylindrical coordinate system is at the top of the cylinder along its axis of symmetry, in which r , θ and z define the radial, circumferential and axial directions, respectively. The thin-walled cylinder has length L , outer radius R and wall thickness h . The volume of the structure is designated by Ω , in which r denote all points within that spatial region. Additionally, p indicates an evaluation point, which may lie within or outside of the structure.

In the following sections, starting with Maxwell's equations, a magnetostatic framework is developed to calculate the magnetisation and resulting magnetic stray field of a cylinder induced by a given external magnetic field. With the framework in place, the fields generated by two particular external field configurations are analysed, culminating in a set of recommendations for the sensor placement in the experiments.

4.5.1. Magnetostatic equations

Electromagnetism in matter is governed by Maxwell's equations, which are (Griffiths, 1999, pp. 328–333):

$$\nabla \cdot \mathbf{D} = \rho_f, \quad (4.25a)$$

$$\nabla \cdot \mathbf{B} = 0, \quad (4.25b)$$

$$\nabla \times \mathbf{E} = -\frac{\partial \mathbf{B}}{\partial t}, \quad (4.25c)$$

$$\nabla \times \mathbf{H} = \mathbf{J}_f + \frac{\partial \mathbf{D}}{\partial t}, \quad (4.25d)$$

in which ρ_f is the free charge density, and \mathbf{J}_f is the free current. The auxiliary fields \mathbf{D} and \mathbf{H} are related to the electric field \mathbf{E} and magnetic field \mathbf{B} as:

$$\mathbf{D} = \varepsilon_0 \mathbf{E} + \mathbf{P}, \quad (4.26a)$$

$$\mathbf{H} = \frac{\mathbf{B}}{\mu_0} - \mathbf{M}, \quad (4.26b)$$

in which \mathbf{P} and \mathbf{M} are the polarisation and magnetisation per unit volume, respectively. In addition, the expression contains the electric constant ε_0 and the magnetic constant μ_0 .

Since it is reasonable to assume that the air surrounding a monopile is a non-conducting linear isotropic medium, the dispersion equation for an electromagnetic plane wave is (Griffiths, 1999, pp. 382–395):

$$\omega = ck, \quad (4.27)$$

in which c is the speed of light, ω is the frequency and k is the wavenumber. Recalling from Chapter 2 that a hammer blow excites frequencies up to 1 kHz in a large-diameter monopile, the lower limit for the wavelength $\lambda = 1/k = 47$ km. Substituting such a value into Equation (4.25c) shows that the term on the right-hand side of the equation with the time derivative of the magnetic field has negligible contribution, since the spatial variation of the electric field is large. In a monopile, no free currents are present, therefore, the same argument is applied to Equation (4.25d), demonstrating that the temporal variation of \mathbf{D} can be neglected. Consequently, Maxwell's equations are simplified by eliminating the time derivatives and the contributions of the free current, resulting in the following set of

homogeneous partial differential equations:

$$\nabla \cdot \mathbf{D} = 0, \quad (4.28a)$$

$$\nabla \cdot \mathbf{B} = 0, \quad (4.28b)$$

$$\nabla \times \mathbf{E} = \mathbf{0}, \quad (4.28c)$$

$$\nabla \times \mathbf{H} = \mathbf{0}, \quad (4.28d)$$

In this particular case, the relations above indicate that the magnetic and electric fields are decoupled, i.e. the two fields can be analysed independently. For the magnetic field, the governing equations read:

$$\nabla \cdot \mathbf{B} = 0, \quad (4.29a)$$

$$\nabla \times \mathbf{H} = \mathbf{0}. \quad (4.29b)$$

These relations are known as the magnetostatic equations (Griffiths, 1999, p. 232), in which the aforementioned relation between the magnetic field and the auxiliary field holds:

$$\mathbf{B} = \mu_0 (\mathbf{H} + \mathbf{M}). \quad (4.30)$$

4.5.2. The magnetic scalar potential

As Equation (4.29b) implies that the auxiliary field \mathbf{H} is irrotational, a scalar magnetic potential $\varphi(\mathbf{p})$ exists such that

$$\mathbf{H}(\mathbf{p}) = -\nabla_p \varphi(\mathbf{p}), \quad (4.31)$$

in which ∇_p is the gradient at point \mathbf{p} . As the potential φ is similar to the electric potential V , the expression for the scalar potential φ for a single magnetic dipole \mathbf{m} is (Griffiths, 1999, pp. 166–168):

$$\varphi(\mathbf{p}) = \frac{1}{4\pi} \frac{\mathbf{s} \cdot \mathbf{m}}{s^3}, \quad (4.32)$$

where $\mathbf{s} = \mathbf{p} - \mathbf{r}$ is the separation vector, and $s = \|\mathbf{s}\|$ is its magnitude. The bulk magnetisation $\mathbf{M}(\mathbf{r})$ is defined as a volume distribution of dipoles, hence, $\mathbf{m} = \mathbf{M}(\mathbf{r}) \, d\Omega$. When all contributions of $\mathbf{M}(\mathbf{r})$ are summed over the volume accordingly, one obtains:

$$\varphi(\mathbf{p}) = \frac{1}{4\pi} \int_{\Omega} \frac{\mathbf{s} \cdot \mathbf{M}(\mathbf{r})}{s^3} \, d\Omega, \quad (4.33)$$

in which \mathbf{r} denotes all points in the structure's volume Ω . An alternative expression for this potential is retrieved by rewriting the former equation using the identity

$$\frac{\mathbf{s}}{s^3} = \nabla_r \frac{1}{s}.$$

Subsequently, by integrating by parts and invoking the divergence theorem, one obtains

$$\varphi(\mathbf{p}) = \frac{1}{4\pi} \oint_{\Gamma} \frac{\mathbf{M}(\mathbf{r}) \cdot \mathbf{n}}{s} d\Gamma - \frac{1}{4\pi} \int_{\Omega} \frac{\nabla_r \cdot \mathbf{M}(\mathbf{r})}{s} d\Omega, \quad (4.34)$$

in which \mathbf{n} is the outward pointing vector of Ω . The former integral can be thought of as an equivalent surface charge distribution, and the latter as a volume charge distribution.

Since $\varphi(\mathbf{p})$ cannot be measured instantly, it is convenient to express the potential due to the magnetisation in terms of $\mathbf{H}(\mathbf{p})$, which is, in the absence of any material, related to the directly measurable magnetic field $\mathbf{B}(\mathbf{p})$:

$$\mathbf{B}(\mathbf{p}) = \mu_0 \mathbf{H}(\mathbf{p}). \quad (4.35)$$

This relation is only valid outside of Ω . Inside the structure's volume, the magnetisation $\mathbf{M}(\mathbf{p})$ should be included in this expression.

Two distinct, yet equivalent, expressions for the auxiliary field $\mathbf{H}(\mathbf{p})$ can be derived. First, Equation (4.33) is substituted into Equation (4.31):

$$\begin{aligned} \mathbf{H}(\mathbf{p}) &= -\frac{1}{4\pi} \int_{\Omega} \left[\mathbf{s} \cdot \mathbf{M}(\mathbf{r}) \nabla_p \left(\frac{1}{s^3} \right) + \nabla_p (\mathbf{s} \cdot \mathbf{M}(\mathbf{r})) \frac{1}{s^3} \right] d\Omega \\ &= \frac{1}{4\pi} \int_{\Omega} \left[\frac{3(\mathbf{s} \cdot \mathbf{M}(\mathbf{r})) \mathbf{s}}{s^5} - \frac{\mathbf{M}(\mathbf{r})}{s^3} \right] d\Omega. \end{aligned} \quad (4.36)$$

Second, using Equation (4.34) and the fact that

$$\nabla_p \frac{1}{s} = -\frac{\mathbf{s}}{s^3},$$

the boundary and volume integrals become:

$$\mathbf{H}(\mathbf{p}) = \frac{1}{4\pi} \oint_{\Gamma} \mathbf{M}(\mathbf{r}) \cdot \mathbf{n} \frac{\mathbf{s}}{s^3} d\Gamma - \frac{1}{4\pi} \int_{\Omega} \nabla_r \cdot \mathbf{M}(\mathbf{r}) \frac{\mathbf{s}}{s^3} d\Omega. \quad (4.37)$$

Equation (4.36) has the advantage that the auxiliary field is expressed without derivatives of the magnetisation, while Equation (4.37) conveniently separates the influence of the magnetisation into a boundary term and a volume term. This division is used in the next section to discretise the integrals, while simultaneously removing the singularity that exists when $s = 0$.

4.5.3. Discretisation of the thin-walled structure

For a monopile, the wall thickness h is small compared to the structure's other dimensions. Hence, in accordance with the mechanical description of the problem, it is reasonable to assume that the pile is approximately a shell. In that case, the magnetisation component along the thickness, the radial component M_r , can be neglected, since the magnetisation

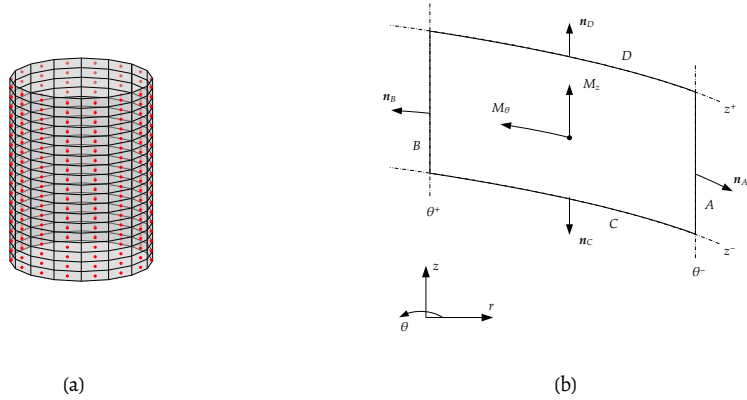


Figure 4.8: Schematics of a discretised cylinder. (a) Discretisation of a thin-walled cylinder into $N = N_\theta N_z$ elements. (b) Element i .

is necessarily tangential to the plate due to the demagnetising field in the normal direction (Chadebec et al., 2000; Viana et al., 2011a). Then, the magnetisation $\mathbf{M}(\mathbf{r})$ expressed in cylindrical coordinates reads

$$\mathbf{M}(\mathbf{r}) = \mathbf{M}(\theta, z) = \begin{bmatrix} 0 \\ M_\theta(\theta, z) \\ M_z(\theta, z) \end{bmatrix}_{r\theta z}. \quad (4.38)$$

Note that $\mathbf{M}(\theta, z)$ is only a function of θ and z .

To approximate the integrals in Equation (4.37), the structural domain Ω is discretised by evenly subdividing the volume into N_θ elements in the circumferential and N_z elements in the axial direction. The total number of elements is $N = N_\theta N_z$. Figure 4.8a shows an example of a discretised cylinder, and Figure 4.8b presents one of these elements. As a result of dividing the computational domain, the auxiliary field is expressed as the sum of each integral over all elements:

$$\mathbf{H}(\mathbf{p}) = \frac{1}{4\pi} \sum_{i=1}^N \oint_{\Gamma_i} \mathbf{M}(\mathbf{r}) \cdot \mathbf{n}_i \frac{\mathbf{s}}{s^3} d\Gamma_i - \frac{1}{4\pi} \sum_{i=1}^N \int_{\Omega_i} \nabla_r \cdot \mathbf{M}(\mathbf{r}) \frac{\mathbf{s}}{s^3} d\Omega_i. \quad (4.39)$$

In the above, $d\Gamma_i$ and $d\Omega_i$ represent the boundary and the volume of each element i , respectively, and \mathbf{n}_i is the outward-pointing normal to boundary $d\Gamma_i$. To simplify this expression, $\mathbf{M}(\mathbf{r})$ is assumed to be constant inside each element. Consequently, the volume integral vanishes, since $\nabla_r \cdot \mathbf{M}(\mathbf{r}) = 0$, reducing the former relation to

$$\mathbf{H}(\mathbf{p}) = \frac{1}{4\pi} \sum_{i=1}^N \oint_{\Gamma_i} \mathbf{M}(\mathbf{r}) \cdot \mathbf{n}_i \frac{\mathbf{s}}{s^3} d\Gamma_i. \quad (4.40)$$

In this formulation, a singularity arises when the evaluation point \boldsymbol{p} coincides with an integration point \boldsymbol{r} , which occurs when the magnetic field inside the structure is determined. To avoid this unphysical behaviour, $\boldsymbol{M}(\boldsymbol{r})$ is assumed to be located in the barycentre of the element \boldsymbol{r}_i , while the integration is performed along the element's boundaries (Chadebec et al., 2006).

After evaluating the integrals, the auxiliary field at the evaluation point \boldsymbol{p} can be expressed in terms of the following summation over all elements:

$$\boldsymbol{H}(\boldsymbol{p}) = \sum_{i=1}^N \mathbf{G}_i \boldsymbol{M}(\boldsymbol{r}_i), \quad (4.41)$$

where \mathbf{G}_i is a 3×2 matrix that contains the coefficients resulting from the integrals. Expressed in their respective components, the above expression reads:

$$\begin{bmatrix} H_r \\ H_\theta \\ H_z \end{bmatrix} = \sum_{i=1}^N \begin{bmatrix} G_{r\theta} & G_{rz} \\ G_{\theta\theta} & G_{\theta z} \\ G_{z\theta} & G_{zz} \end{bmatrix}_i \begin{bmatrix} M_\theta \\ M_z \end{bmatrix}_i, \quad (4.42)$$

in which $(G_{r\theta})_i$ represents the influence of the circumferential magnetisation component of element i to the auxiliary field in the radial direction, etc. The exact expressions for each entry of \mathbf{G}_i are presented in Appendix B. By rewriting the summation over the elements, a more concise expression for $\boldsymbol{H}(\boldsymbol{p})$ is

$$\boldsymbol{H}(\boldsymbol{p}) = \mathbf{G}_p \boldsymbol{M} \quad (4.43)$$

in which \boldsymbol{M} is a vector that contains the $2N$ magnetisation components, and \mathbf{G}_p denotes a $3 \times 2N$ matrix that collects the contributions of each \mathbf{G}_i .

When the magnetisation of the discretised structure \boldsymbol{M} is known, the magnetic stray field $\boldsymbol{B}(\boldsymbol{p})$ can be determined at any point outside the cylinder by applying Equation (4.43):

$$\boldsymbol{B}(\boldsymbol{p}) = \mu_0 \boldsymbol{H}(\boldsymbol{p}) = \mu_0 \mathbf{G}_p \boldsymbol{M}. \quad (4.44)$$

Subsequently, in the absence of other magnetisable materials, the total magnetic field $\boldsymbol{B}_t(\boldsymbol{p})$ is then

$$\boldsymbol{B}_t(\boldsymbol{p}) = \boldsymbol{B}(\boldsymbol{p}) + \boldsymbol{B}_0. \quad (4.45)$$

However, the magnetisation due to an external field is generally not known a priori. Fortunately, the same expressions enable one to compute the magnetisation based on a given constitutive equation.

4.5.4. Magnetisation of a cylinder induced by an external field

For the magnetisation at the barycentre of element i , a general constitutive relation is

$$\mathbf{M}(\mathbf{r}_i) = \chi \mathbf{H}_i(\mathbf{r}_i), \quad (4.46)$$

in which χ is the magnetic susceptibility, and $\mathbf{H}_i(\mathbf{r}_i)$ denotes the total auxiliary field at the barycentre, which is

$$\mathbf{H}_i(\mathbf{r}_i) = \mathbf{H}_0 + \mathbf{H}(\mathbf{r}_i). \quad (4.47)$$

The first term in the sum is the external auxiliary field \mathbf{H}_0 , which is proportional to the time- and space-invariant magnetic field \mathbf{B}_0 :

$$\mathbf{H}_0 = \frac{\mathbf{B}_0}{\mu_0}. \quad (4.48)$$

The second is the auxiliary field generated by the entire structure as given by Equation (4.41). Substitution of that relation into the constitutive equation gives the following implicit expression for the magnetisation at the barycentre of an element:

$$\mathbf{M}(\mathbf{r}_i) = \chi \left(\mathbf{H}_0 + \sum_{j=1}^N \mathbf{G}_j \mathbf{M}(\mathbf{r}_j) \right). \quad (4.49)$$

In the above, no assumptions have been made about the susceptibility, which generally is a tensor that depends on time, space, strain and the auxiliary field. However, for a homogeneous isotropic material, a constant scalar is adequate to model the magnetic behaviour. As a result of this assumption, $\mathbf{M}(\mathbf{r})$ and the local value of the auxiliary field $\mathbf{H}_i(\mathbf{r})$ are coaxial.

For the discretised structure, it is possible to rewrite the implicit relation, Equation (4.49), explicitly in terms of \mathbf{H}_0 only. Recalling that the radial component of the magnetisation is zero, the magnetisation is represented by a vector \mathbf{M} containing $2N$ unknowns. Then, Equation (4.49) becomes

$$\mathbf{M} = \chi (\mathbf{H}_0 + \mathbf{G}_r \mathbf{M}), \quad (4.50)$$

in which \mathbf{G}_r is a $2N \times 2N$ matrix representing the non-local interaction of the structure's magnetisation, which is obtained by substituting $\mathbf{p} = \mathbf{r}_j$ into Equation (4.43). Under the assumption that χ is not a function of the magnetisation itself, rearranging the former relation yields

$$\mathbf{M} = \mathbf{X} \mathbf{H}_0, \quad (4.51)$$

where

$$\mathbf{X} = \chi (\mathbf{I} - \chi \mathbf{G}_r)^{-1},$$

in which \mathbf{I} is the $2N \times 2N$ identity matrix and $(\cdot)^{-1}$ denotes the matrix inverse.

From Equation (4.51), it is clear that this formulation cannot account for the magnetisation history, since the magnetisation vanishes when \mathbf{H}_0 reduces to zero. Generally, only

the anhysteretic magnetisation curve displays this behaviour. Using the low-field approximation of the anhysteretic magnetisation, Equation (4.11), an explicit expression for the anhysteretic magnetisation of a steel cylinder is obtained by rewriting the effective field H_e . For simplicity, the strain dependency of the anhysteretic magnetisation is neglected, resulting in the following expression for the effective field:

$$H_e = H_0 + \alpha M + \mathbf{G}_r M. \quad (4.52)$$

The latter term on the right hand side is added to include the magnetic self-interaction of the structure. After some manipulations, the anhysteretic magnetisation in a weak external field can be written as

$$M_{\text{an}} = \mathbf{X}_{\text{an}} H_0, \quad (4.53)$$

in which

$$\mathbf{X}_{\text{an}} = \frac{M_s}{3a} \left(\left(1 - \frac{M_s}{3a} \alpha \right) \mathbf{I} - \frac{M_s}{3a} \mathbf{G}_r \right)^{-1}$$

denotes the anhysteretic susceptibility accounting for the non-local magnetic interaction, in which M_s is the saturation magnetisation, a is a parameter proportional to the initial domain density and α is the domain coupling factor (Jiles et al., 1992). When the geometry of a structure is such that the influence of the non-local magnetic interaction is negligible, i.e. $\mathbf{G}_r = \mathbf{0}$, the expression reduces to the scalar susceptibility presented in Equation (4.13).

4.5.5. Magnetisation and magnetic stray field due to particular external fields

For a thin-walled cylinder with a constant radius and its axis of rotation parallel to the z -axis, a time- and space-invariant Cartesian external field B_0 can be split into a vertical (\parallel) and a horizontal (\perp) field:

$$B_0 = B_0^{\parallel} + B_0^{\perp}. \quad (4.54)$$

The vertical field is simply the z -component of B_0 , while the horizontal field consists of the components in the xy -plane, which corresponds to the $r\theta$ -plane in cylindrical coordinates. According to Equation (4.51), the magnetisation and the external field are linearly related. Hence, the magnetic response of the structure to each of the two contributions can be analysed separately. This analysis is performed on a simple test case of a cylinder with a constant scalar magnetic susceptibility. Table 4.1 lists the numerical values of the relevant parameters, whereas Figure 4.7 shows their definitions. The vertical magnetic field is considered first, whereafter the horizontal field is discussed.

Table 4.1: Parameters of the steel cylinder used to simulate the magnetisation induced by the vertical and horizontal components of the external field.

Parameter	Value	Parameter	Value
R	0.5 m	N_θ	32
h	0.001 m	N_z	40
L	10.0 m	χ	1000

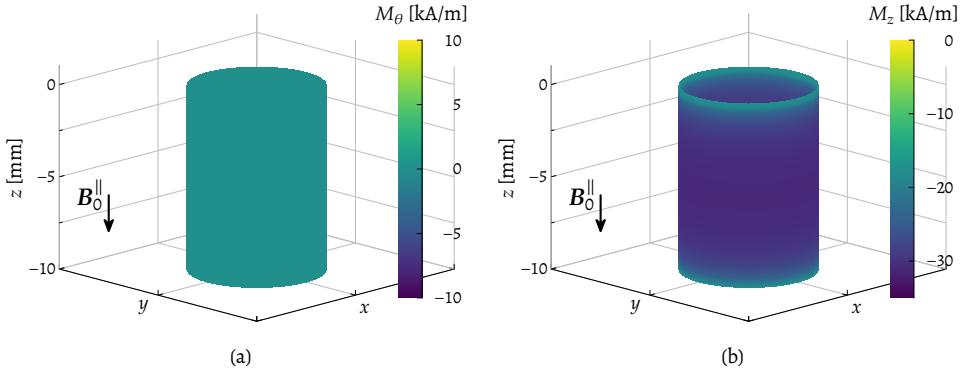


Figure 4.9: Magnetisation resulting from a vertical magnetic field. (a) Circumferential component. (b) Axial component.

Vertical external field

Since the geomagnetic field points predominantly downwards in the Northern hemisphere (Thébault et al., 2015), the following vertical external field is considered:

$$\mathbf{B}_0^{\parallel} = \begin{bmatrix} 0 \\ 0 \\ B_z^0 \end{bmatrix} = \begin{bmatrix} 0 \\ 0 \\ -40 \end{bmatrix} \mu\text{T}. \quad (4.55)$$

By subsequently substituting this vector into Equations (4.48) and (4.51), the magnetisation of the cylinder is obtained, which is presented in Figure 4.9. Due to the rotational symmetry about the z -axis, the induced magnetisation is symmetric, and the circumferential component M_θ is zero everywhere. The axial component M_z is aligned with the external field, albeit that it is not uniform even though the external field is. The magnitude of M_z reduces towards the edges as a result of the magnetic self-interaction.

The stray field induced by the magnetisation at the top edge of the cylinder is visualised in Figure 4.10. To improve the appearance, the field vectors are normalised; hence, the arrows indicate the direction, and their colour signify the magnitude of the vector. Note that the stray field is the total magnetic field with the external field subtracted. It is clear that the stray field at the top edge points towards the cylinder, displaying maximum strength at the edge itself.

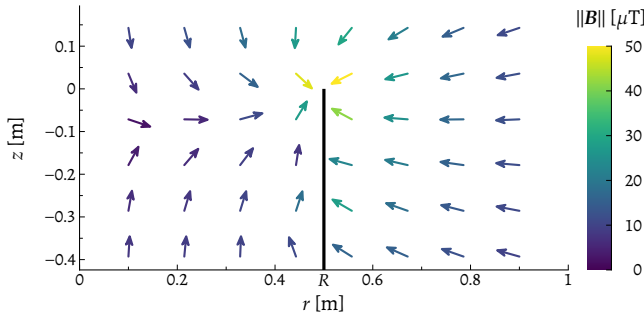


Figure 4.10: Magnetic stray field surrounding the top of the cylinder resulting from a vertical external field. The line at $r = 0.5$ m indicates the position of the cylinder.

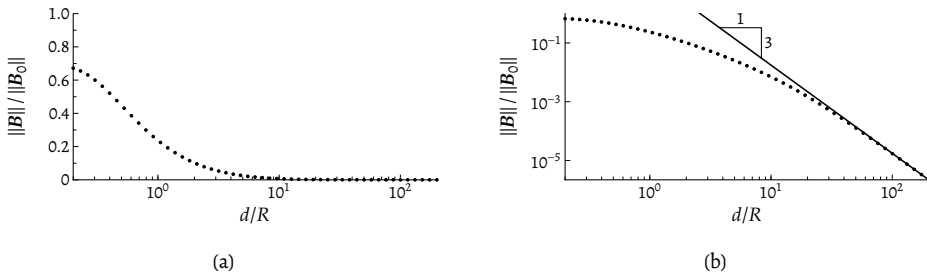


Figure 4.11: Attenuation of the magnitude of the magnetic stray field with increasing distance d from the surface of the cylinder resulting from a vertical external field at $\theta = 0^\circ$ and $z = -0.125$ m. (a) Log-linear scale. (b) Log-log scale.

Outside of the cylinder ($r > R$), the decay of the stray field with distance is evident from the graphs shown in Figure 4.11, which presents the magnitude of the stray field as a fraction of the magnitude of the external field with increasing distance d from the surface of the cylinder at $z = -0.125$ m. For $d/R < 1$, the stray field’s strength is a considerable portion of the external field; however, for larger distances, the stray field diminishes quickly. Close to the surface of the structure, the stray field contains a number of contributions from a multipole expansion, i.e. the near field. Since the high-order contributions decay faster with distance, eventually, for $d/R > 10$, the dipole contribution starts to dominate, which decays with r^{-3} as indicated by the solid line in the log-log plot (Figure 4.11b).

Horizontal external field

Contrary to a magnetic field aligned with the cylinder’s axis, a horizontal field does not share a symmetry with the cylinder, resulting in a more complex magnetisation field inside the structure. A horizontal field in Cartesian coordinates, which is aligned with the x -axis

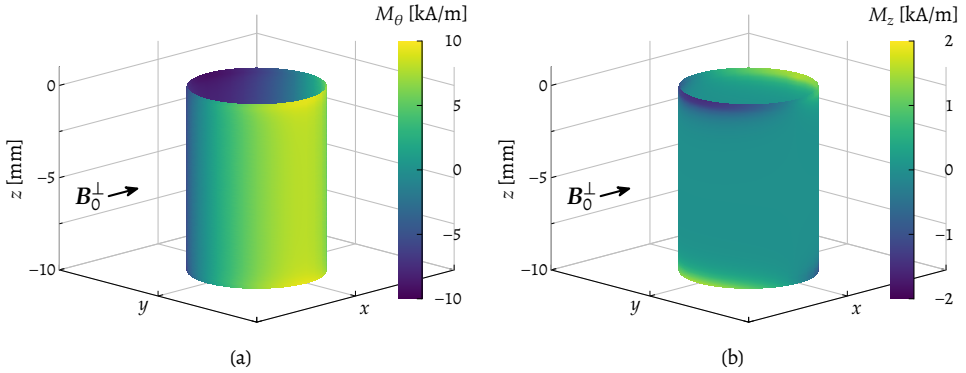


Figure 4.12: Magnetisation resulting from a horizontal magnetic field. (a) Circumferential component. (b) Axial component.

4

in this particular case, reads:

$$\mathbf{B}_0^\perp = \begin{bmatrix} B_x^0 \\ B_y^0 \\ 0 \end{bmatrix} = \begin{bmatrix} 20 \\ 0 \\ 0 \end{bmatrix} \mu\text{T}. \quad (4.56)$$

However, expressed in cylindrical coordinates, the external field is a function of the circumferential coordinate θ :

$$\mathbf{B}_0^\perp(\theta) = \begin{bmatrix} B_r^0 \\ B_\theta^0 \\ 0 \end{bmatrix} = \begin{bmatrix} \cos(\theta) B_x^0 + \sin(\theta) B_y^0 \\ -\sin(\theta) B_x^0 + \cos(\theta) B_y^0 \\ 0 \end{bmatrix}. \quad (4.57)$$

After inserting these values in Equations (4.48) and (4.51), Figure 4.12 presents the induced magnetisation. The circumferential magnetisation component M_θ is aligned with the circumferential external field B_θ^0 : it is zero at $\theta = 0^\circ$ and $\theta = 180^\circ$, and it has a maximum at $\theta = 90^\circ$ and $\theta = 270^\circ$. More interestingly, due to the geometry of the structure, a substantial axial magnetisation component M_z appears at the edges of the cylinder, of which the maximum occurs at 90° relative to the maximum of the circumferential component M_θ .

For three circumferential positions, the stray field generated by the magnetisation is shown in Figure 4.13. At $\theta = 0^\circ$, the stray field radiates outwards in the $r\theta$ -plane with the circumferential component B_θ equal to zero. Moving 45° further along the θ -axis, the radial and axial components diminish, while B_θ increases pointing in the positive θ -direction. Continuing to $\theta = 90^\circ$, only the circumferential component of the stray field remains. Therefore, contrary to the axial external field, the generated stray field is a function of θ .

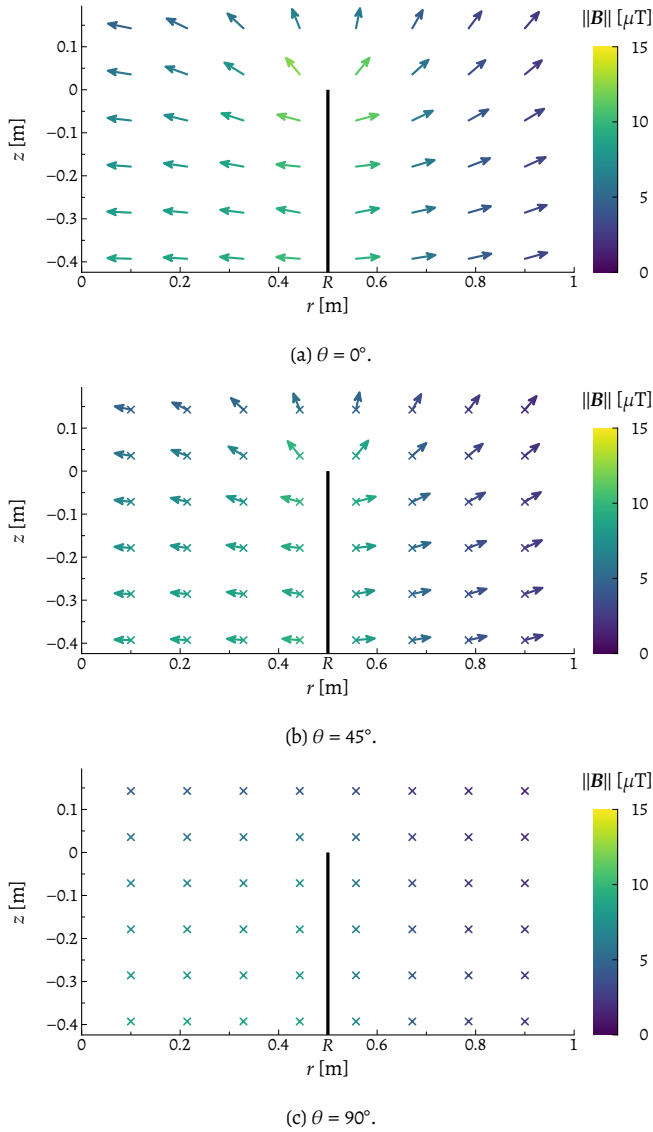


Figure 4.13: Magnetic stray field surrounding the top of the cylinder resulting from a horizontal external field. The line at $r = 0.5$ m indicates the position of the cylinder. The direction of the circumferential stray field component is indicated with \times (into the paper) or \circ (out of the paper).

4.5.6. Discussion

The simulated stray field data determine the optimal positioning of the sensors for the experiment needed to fill the knowledge gaps identified earlier. In the preferred magnetically-uncontrolled set-up, both a vertical and a horizontal external field are present. To obtain the full picture of the magnetisation and stray field in that case, the contribution from the external field components should simply be added together. The magnitude of the magnetisation and the stray field generated by the vertical field is much larger than the one induced by the horizontal field. Therefore, it is expected that the radial and axial components of the stray field will show the most pronounced changes when the structure is strained, since these directions dominate the approximately axially symmetric stray field.

Due to the horizontal field, the magnetisation and stray field are not completely axially symmetric: the direction of the external field in the xy -plane is easily distinguishable in the circumferential magnetisation component and by the appearance of slight aberrations at the cylinder's edges in the axial magnetisation. In the resulting stray field, a similar asymmetry occurs in all three stray field components. Consequently, sensors should be placed at different angles with respect to the horizontal external field in the experimental set-up.

Regarding the distance of a magnetometer to the surface of the structure, the sensor should be employed within one radius distance to obtain a significant signal compared to the external field, given the decay of the magnitude of the stray field with distance. Naturally, this separation value is an upper limit; more pronounced signals can be measured when the sensor is located closer to the surface, especially given that the changes in the magnetisation due to strain might be only a fraction of the remanent magnetisation.

4.6. Conclusions

In this chapter, the basic principles behind ferromagnetic materials and the magnetomechanical effect have been presented, which are a direct result of the presence of magnetic domains and the motion of domain walls. Data from small-scale experiments indicate that elastic strain irreversibly pushes the magnetisation towards a global magnetic equilibrium, by permanently moving the domain walls. Additionally, plastic deformation causes a significant deterioration of a material's magnetic properties due to the increased dislocation density. However, the currently available strain-induced magnetisation data for large-scale structures, which have a substantial demagnetising field, are limited to static tensile loads. Therefore, to get a complete insight into the magnetic response of a monopile to a hammer blow, data for a structure subjected to impact loads have to be gathered from new experiments.

Given the impracticality of imposing a strong (uniform) external magnetic field near a large-scale structure, a non-collocated method to infer deformation in such structures needs to be based on a passive magnetic method, which relies solely on the ambient magnetic field. Surrounding a ferromagnetic structure, a magnetic stray field is present, which is generated

by the structure's magnetisation. Passive methods analyse this field to infer deformations or the presence of defects. Since the initial magnetic state influences the success rate of passive methods significantly, the initial state should be carefully considered in a newly proposed passive method to infer deformations.

In terms of modelling the strain-induced magnetisation changes for a large-scale structure, the phenomenological J–A models seem to be the most promising candidates, since they are relatively simple to implement and to calibrate due to their limited number of parameters. For reversible magnetisation changes, the law of approach suggests that only the strain-dependency of the magnetic equilibrium has to be considered. At present, J–A models are derived under the assumption that the magnetisation and the auxiliary fields are coaxial and that the applied mechanical load is uniaxial. It is anticipated that these assumptions are not valid for large-scale structures. Thus, a magnetomechanical model should necessarily treat the physical quantities as tensors, for which some aspects of multi-scale models might be of importance.

In the final section of this chapter, a magnetostatic framework has been introduced to compute the stray field of a thin-walled steel cylinder, incorporating the demagnetising field. Subsequently, the stray field induced by a vertical and a horizontal external magnetic field has been simulated and analysed to deduce the optimal positions of a magnetic field sensor in the required experimental set-up. From the results, the radial and axial components of the stray field are expected to display the most pronounced changes when the structure is strained, since these directions dominate the approximately axi-symmetric stray field. Due to the horizontal external field, the magnetisation and stray field are not completely axi-symmetric. Consequently, sensors should be placed at different angles with respect to the horizontal component of the external field to capture the possible effects of this asymmetry in the magnetisation. Furthermore, a sensor is ideally employed within one radius distance to the cylinder's surface to obtain a significant signal compared to the external field.

Given the theoretical framework discussed in this chapter, a novel experimental set-up is presented in the subsequent chapters, in which a steel cylinder is impacted by a free-falling mass. In the design, the above conclusions and recommendations are incorporated to collect unique magnetic data of a steel structure subjected to repeated dynamic compressive loads. From the results, new passive magnetic methods are proposed to infer elastic and plastic deformations using non-contact sensors.

5

The remanent magnetic stray field and its sensitivity to physical damage

*Yes I'm changing
Can't stop it now*

Tame Impala – *Yes I'm changing*

In the previous chapter, it has been demonstrated that the magnetic stray field is a suitable candidate for a method to infer deformation in a structure using non-collocated measurement points, since this field permeates the space around the structure. This chapter focuses on the remanent magnetic stray field, i.e. the stray field measured when the structure is no longer subjected to an external mechanical load, to detect and localise regions of plastic deformation once they have developed. Contrary to the method to detect plastic deformation presented in Chapter 3, the sensors do not need to be attached to the structure, designating the method proposed here besides non-collocated also non-contact.

To date, all methods used to identify whether an irreversible change in the magnetisation is caused by elastic or plastic strains are developed in well-controlled environments in which the location of the plastic deformation is known a priori and the loading is introduced

Parts of this chapter have been published in the MSc thesis by Chris Jolink (2018) and are intended to be published in a manuscript prepared for the *International Journal of Mechanical Sciences* (Meijers, Jolink, Tsouvalas and Metrikine, 2021a).

gradually (Bao et al., 2017a; Li et al., 2017a). For large-scale structures, however, this is generally not the case, prohibiting the application of the current methods. To develop a method that is applicable in a realistic setting, a laboratory-scale impact experiment is reported in this chapter, providing data on strain-induced magnetisation changes in a less-controlled environment.

First, irreversible magnetisation changes due to elastic and plastic deformations are revised, which reveals the need to distinguish between these two causes. Second, the set-up of the impact experiment on a steel cylinder is presented. Third, the evolution of the remanent stray field with elastic strain cycles is discussed after which a method to detect and localise plastic deformations is introduced. Afterwards, the influence of the initial magnetic state on the results obtained from the proposed method is carefully considered, and the generalisation and limitations of the method are discussed. Finally, conclusions are drawn.

5.1. Irreversible changes of the magnetic stray field

Similar to the passive methods described in Section 4.3.2, the magnetic stray field is investigated, which surrounds a steel structure (Figure 5.1a) and is solely generated by its magnetisation. This field is related to the total magnetic field $B_t(\boldsymbol{p})$ at point \boldsymbol{p} through

$$B_t(\boldsymbol{p}) = \boldsymbol{B}(\boldsymbol{p}) + B_0. \quad (5.1)$$

In the above, the latter represents the background field B_0 , e.g. the geomagnetic field, which is assumed to be spatially-uniform and time-invariant for the length- and time-scales relevant to this work. The former, the stray field $\boldsymbol{B}(\boldsymbol{p})$, is determined by the structure's magnetisation $\boldsymbol{M}(\boldsymbol{r})$, since these two quantities are related as follows (Equation (4.36)):

$$\boldsymbol{B}(\boldsymbol{p}) = \frac{\mu_0}{4\pi} \int_{\Omega} \left[\frac{3(\boldsymbol{M}(\boldsymbol{r}) \cdot \boldsymbol{s})\boldsymbol{s}}{s^5} - \frac{\boldsymbol{M}(\boldsymbol{r})}{s^3} \right] d\Omega, \quad (5.2)$$

in which \boldsymbol{r} are all points within the structure's volume Ω , $\boldsymbol{s} = \boldsymbol{p} - \boldsymbol{r}$ denotes the separation vector with corresponding magnitude $s = \|\boldsymbol{s}\|$, and μ_0 is the magnetic constant. To analyse the irreversible change of the stray field due to impact loads, it is convenient to consider the stray field when the structure is unloaded: the so-called remanent stray field, which is denoted by $\bar{\boldsymbol{B}}(\boldsymbol{p})$. Given the direct relation between the structure's magnetisation and the stray field, the evolution of the remanent field $\bar{\boldsymbol{B}}(\boldsymbol{p})$ will reflect the impact-induced irreversible changes in the magnetisation, which result from two different physical processes.

First, elastic strain can permanently alter the magnetisation of a material (Brown, 1949). As mentioned in Section 4.2.3, for strains below the elastic limit, the strain energy supplied by the load enables magnetic domain walls to move towards a magnetic equilibrium by overcoming pinning sites which originally impeded their motion (Atherton et al., 1984; Makar and Atherton, 1995). Thereafter, consecutive load cycles of the same magnitude do not alter the magnetisation further (Atherton and Szpunar, 1986). However, when a new loading

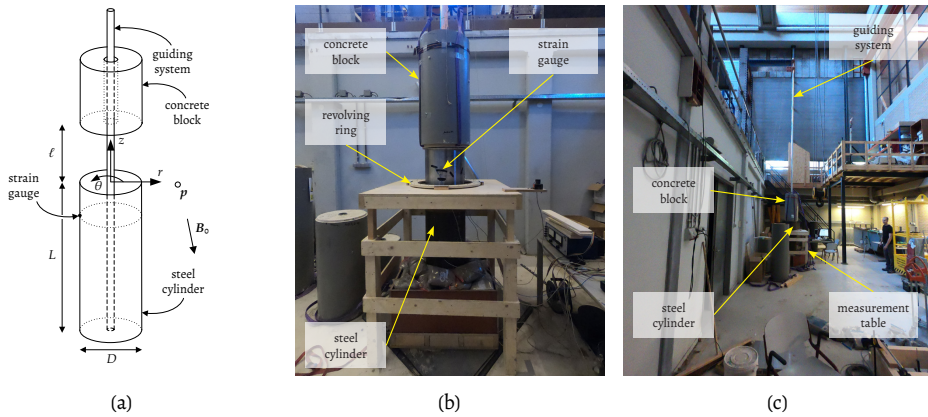


Figure 5.1: (a) Schematic of the set-up of the thin-walled cylinder, including the background field B_0 . (b) Photograph of the set-up and the measurement table. (c) Side-view of the set-up, which shows the support structure for the guiding system.

cycle induces strains that surpass the previously endured peak strain, an irreversible change occurs towards a new magnetic equilibrium state (Li et al., 2017a). Note that these processes, although related to the elastic regime, may cause irreversible changes in the magnetisation.

Second, as soon as plastic deformation develops in the structure, the dislocation density increases locally (Gilman, 1968). These newly formed dislocations are additional pinning sites for magnetic domain walls, impeding their motion. Moreover, the plastic deformation introduces residual strains in the material. Both these effects resulting from plastic deformation contribute to irreversible changes in the structure's magnetisation (Sablík et al., 2004). As a first load cycle that exceeds the material's yield limit simultaneously introduces a new peak strain, both aforementioned irreversible changes of the magnetisation occur in conjunction. In the following, based on the data from a laboratory experiment, a method is developed to distinguish between the two causes of permanent changes in the magnetic stray field, which in essence allows one to separate plastic from elastic deformations in the structure through measurements of the magnetic stray field.

5.2. Laboratory-scale experiment

Due to the lack of experimental data of magnetisation changes of a steel cylinder due to strain induced by an impact load in an uncontrolled environment, a unique axial drop-weight experiment has been designed. The general set-up is introduced first, and the employed sensors and measurement phases are described subsequently.

5.2.1. Experimental set-up

Figure 5.1a presents a schematic of the set-up, which indicates the cylindrical coordinate system and the relevant structural dimensions. The axial, circumferential and radial direc-

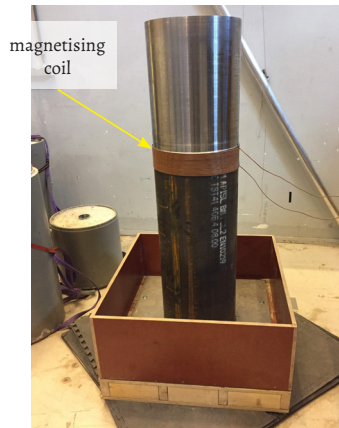


Figure 5.2: Photograph of the cylinder showing the thinner top part of the cylinder and the magnetising coil.

5

tion are denoted by z , θ and r , respectively. Moreover, the cylinder has length $L = 1500$ mm, and its outer diameter equals $D = 406.4$ mm. To increase the impact-induced strain at the top of the cylinder, the wall thickness h is not uniform along the cylinder's axis: for the lower part of the cylinder $h = 8$ mm, while $h = 2.5$ mm for $z > -0.5$ m. A 403 kg concrete mass, which can fall freely along an aluminium guiding system from different heights ℓ , provides the means to introduce an axial impact of varying amplitude to the structure. To spread the energy of the impact as evenly as possible without cracking the concrete, a stainless steel plate is attached directly underneath the mass. The photograph shown in Figure 5.1b shows the concrete mass, which is enclosed by a PVC casing. Furthermore, Figure 5.1c shows the guiding system in conjunction with the crane, which is used to lift the mass to the desired height.

Due to the size of the set-up, the external magnetic field in the test area is not controlled, which would require magnetising coils in three perpendicular directions surrounding the entire structure. Such a device to control the magnetic field is unfeasible on this scale, not to mention the scale encountered during a monopile installation in practice. However, on the laboratory scale, it is possible to control the cylinder's initial magnetisation. To this end, the structure can be demagnetised with a hand-held degaussing coil, forcing the magnetic ordering to a more or less random state, effectively reducing the bulk magnetisation. Nevertheless, due to the presence of the external field, the magnetisation will not be completely reduced to zero. The effect of this imperfect demagnetisation on the validity of the results and the proposed method for plasticity detection is addressed later in this chapter.

After demagnetisation, a part of the cylinder can be remagnetised using a coil of 32 windings located at $z = -0.5$ m, which is shown in Figure 5.2. The strength of the auxiliary field

generated by a solenoid is given by (Jiles, 2015, p. 18)

$$H = \frac{NI}{L_c}, \quad (5.3)$$

where N is the number of windings, I is the applied current and L_c denotes the axial length of the solenoid. In this case, $N = 32$, $I = 10$ A, and $L_c = 0.13$ m, resulting in an auxiliary field strength $H = 41.6$ A/m. Depending on the direction of the current, which can be reversed if required, the magnetising field points either up or down along the z -axis. Together with the demagnetising device, this coil allows the creation of different, yet consistent and repeatable, initial magnetic states of the cylinder. After the initial magnetic state has been established, the magnetising current is ceased; therefore, besides the geomagnetic field, no additional field is present during the impacts.

5.2.2. Sensor description

To measure the axial deformation induced by an impact, two axial strain gauges (type: UFLA-5-11) are diametrically attached to the cylinder's surface at $z = -200$ mm. From the measured axial strain ε_z , the impact-induced stress components can be determined by applying the theory presented in Chapter 2.

For the magnetic field measurements, a choice has to be made from the plethora of available types of magnetometers (Ripka, 2000). Based on the results presented in Section 4.5.5, it is expected that the magnitude of the stray field at the top of the cylinder is of the same order as that of the geomagnetic field. Furthermore, it is expected that the remanent stray field does not change in the absence of an external mechanical load. With these two notions in mind, a triaxial fluxgate magnetometer is selected, due to its high accuracy in the anticipated magnetic field range (Ripka, 1992). The selected sensor (type: FLC3-70) has a measuring range of ± 200 μ T, a sensitivity of 0.035 μ T/mV, a noise density of 120 pT/ $\sqrt{\text{Hz}}$ at 1 Hz, and a bandwidth ranging from 0 to 1 kHz.

In between impacts, the total magnetic field B_i at the top of the cylinder is measured with the triaxial magnetometer, which is mounted on a specially designed wooden table. This measurement table contains a ring that can rotate (Figure 5.1b), and it can be positioned at various heights and offsets relative to the structure. Figure 5.3 shows the selected heights and offsets d , which form measurement rings RO1 to R12. Additionally, the grey area in the figure indicates the position of the magnetising coil. By revolving the sensor around the cylinder during a measurement and subsequently applying Equation (5.1), a spatial map of the magnetic stray field is constructed.

5.2.3. Sources of error

Naturally, the measurements of the stray field will contain certain errors. Normally, the measurement errors are categorised into systematic errors and random errors (Bevington and Robinson, 2003, pp. 3–4). The former is partially determined by the employed fluxgate

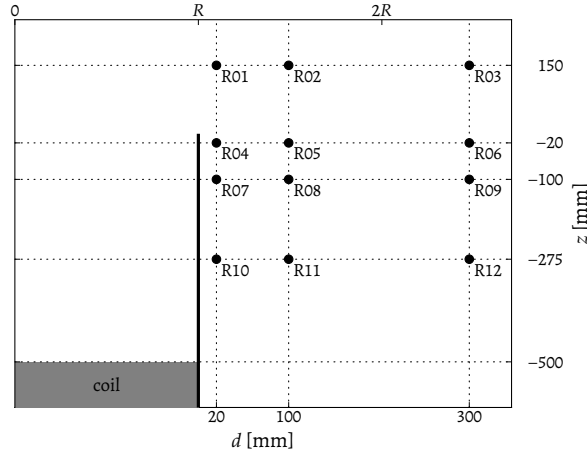


Figure 5.3: Position of the twelve measurement rings relative to the cylinder's surface to map the magnetic stray field around the top of the cylinder. The black solid line represents the surface of the cylinder and the location of the magnetising coil is indicated by the grey area.

5

sensor, which has an accuracy of $\pm 0.5 \mu\text{T}$ at 20°C . Additionally, the precision of the sensor adds to the systematic error. Given the sensor's sensitivity ($0.035 \mu\text{T/mV}$) and the accuracy of the 16-bit data acquisition system (*National Instruments USB-6343*), the sensor's precision is negligible compared to the overall accuracy of the magnetometer. However, another major contribution to the precision of the magnetic field measurement is the relative position to the structure (Szulim et al., 2015). In the presented setup of the experiment, the measurement table is not connected to the pile. Consequently, small deviations in the offset d of the magnetometer are possible, which are estimated to be $\pm 1 \text{ mm}$. To determine the error in the measured magnetic field caused by the uncertainty in the position, the sensitivity of the field's magnitude with respect to the sensor position \boldsymbol{p} , i.e. $\Lambda = \frac{\partial}{\partial \boldsymbol{p}} \|\boldsymbol{B}(\boldsymbol{p})\|$, is computed using the framework derived in Chapter 4. From the analysis, the dominant error is approximately 2% of $\|\boldsymbol{B}(\boldsymbol{p})\|$ per mm in the r -direction. It is expected that the latter term is the dominant source of error in the stray field measurements.

Next to the error in measurement of the magnetic field components, there is an uncertainty in the value of the drop height ℓ . Given the set-up, which required manual operation of the crane to lift the impacting mass to the desired height, the error in the drop height is estimated to be $\pm 10 \text{ mm}$. This error influences the induced strain levels. In the remainder of this chapter, the uncertainty in the value for ℓ is not explicitly shown to create a more concise notation.

Table 5.1: Detailed description of the five tests of phase A in consecutive order. M_{in} is the initial magnetic state, and ℓ_1 and ℓ_2 represent the initial and the increased impact height, respectively.

id	M_{in}	ℓ_1 [mm]	ℓ_2 [mm]
A1	A	500	1000
A2	B	500	1000
A3	C	500	1000
A4	C	1000	-
A5	B	1000	-

5.2.4. Measurement phases

Since elastic and plastic deformation can cause strain-induced irreversible magnetisation changes, the experiment is split into two phases: Phases A and B. During the former, the impact height of the impacting mass is restricted such that only elastic deformations develop in the structure, allowing one to analyse the behaviour of the magnetisation caused by elastic strain alone. On the contrary, in the latter phase, the impact height ℓ is gradually increased until visible plastic deformation develops. The data collected in both phases provide the opportunity to distinguish the cause of the irreversible changes in the remanent magnetisation.

5.3. Evolution of the remanent stray field in the elastic regime

In this first phase of the experiment, the impacts are selected such as to generate only elastic deformations in the structure. To quantify the influence of the initial magnetisation, the structure is magnetised to distinct initial magnetic states.

5.3.1. Measurement procedure

Table 5.1 summarises the measurement procedure for phase A, which consist of five tests. Before each test, the cylinder is demagnetised and then remagnetised to a specific initial magnetic state using the magnetising coil. In initial states A and B, the generated auxiliary field counteracts the external field, whereas in initial state C, the auxiliary field enhances the external field. State A and B only differ in the applied strength of the current passed through the solenoid.

During a test, the cylinder is repeatedly impacted from an identical height ℓ_1 until the remanent stray field measured on ring R10 at $\theta = 0^\circ$ no longer changes significantly. The criterion for convergence is based on the moving standard deviation computed using the trailing five values; the stray field has converged when twice the standard deviation is less or equal to the positioning error (2% of $\|B\|$, which is $\pm 0.68 \mu\text{T}$ for this particular sensor location).

In the first three tests, the drop height is subsequently increased to ℓ_2 , and the mass is dropped again until no further changes are observed in the stray field using the same

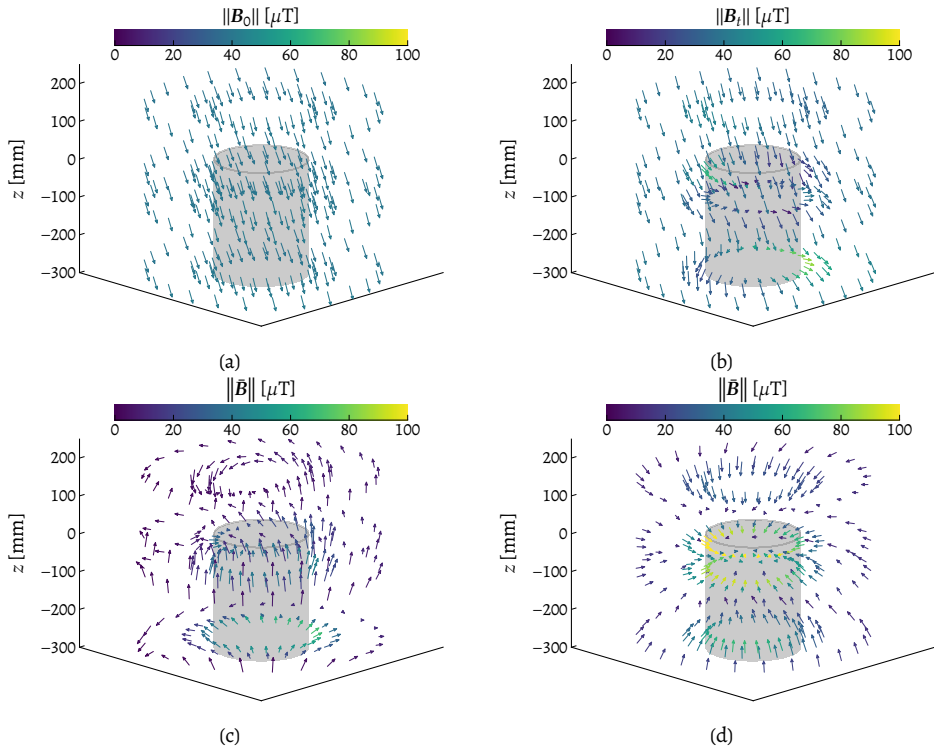


Figure 5.4: Measured magnetic field around the top of the cylinder. (a) The background field B_0 . (b) The total magnetic field of the cylinder in initial magnetic state B . (c) The magnetic stray field of the cylinder with initial magnetic state B . (d) The remanent stray field after five impacts with $l = 1000$ mm.

criterion as before. Note that the cylinder is only demagnetised at the start of a test; when the impact height is increased from l_1 to l_2 , no further actions are taken in this respect.

5.3.2. Results

Before the cylinder is placed into the set-up, the external field B_0 is measured by revolving the fluxgate sensor around the specified rings. Figure 5.4a shows the field components, which are normalised in size for clarity with their colour indicating the magnitude of the field. In line with the aforementioned assumption, the geomagnetic field is space-invariant and points predominantly in the negative z -direction. To exemplify the stray field generated by the cylinder, Figure 5.4b shows the total magnetic field just before the start of test A5 (initial magnetic state B). It is clear that the field is slightly perturbed by the presence of the cylinder. However, greater detail is obtained by subtracting the uniform external field, leaving the magnetic stray field. As indicated by the dark blue colours in Figure 5.4c, the stray field is very weak at the rings most distant from the structure, which is not surprising given that a demagnetising procedure has been applied. Close to the magnetising coil,

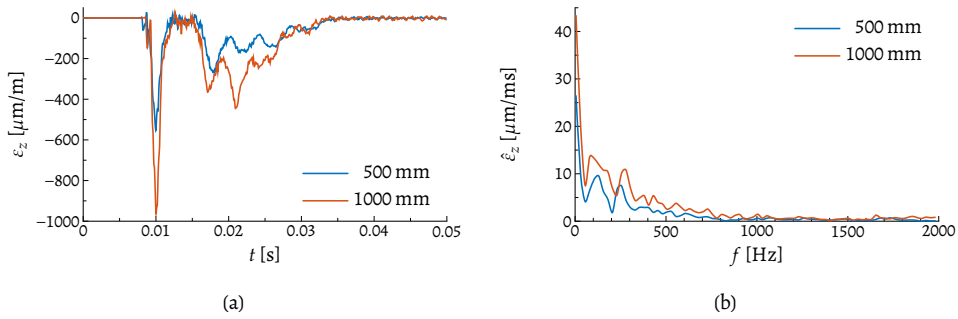


Figure 5.5: Impact-induced axial strain measured during impacts from $\ell = 500$ mm and $\ell = 1000$ mm. (a) Time series. (b) Amplitude spectra.

the stray field is more pronounced pointing upwards and away from the surface of the cylinder. This behaviour results from initial magnetic state \mathbb{B} , which is directed towards the positive z -axis. After five impacts from $\ell = 1000$ mm, the remanent stray field exhibits a radical transformation. The influence of the cylinder's magnetisation is visible on every measurement ring with the field pointing towards the top of the cylinder, indicating that the magnetisation has attained a large component along the negative z -direction, i.e. coaxial with the external field.

Time series of typical axial strain signals measured during impacts from $\ell = 500$ mm and $\ell = 1000$ mm are presented in Figure 5.5a, which indicate that each impact induces only compressive axial strain. Furthermore, the signals demonstrate two compression stages: a sharp initial peak which contains the maximum induced strain and a wider second peak of lower amplitude. This behaviour stems from the interaction between the cylinder and the impacting mass. During the first peak, the top mass exerts a large force on the top of the cylinder; as a result, the latter accelerates and separates from the falling mass. The two objects reconnect during the second stage, where energy is transferred back to the top mass, eventually pushing it back upwards. Since the duration of this interaction is primarily governed by the stiffness and damping contained in the complete structure-mass system, the signals for the two impact heights mainly differ in amplitude and not in duration.

Normally, the second peak described above is not observed during pile driving by means of a hydraulic impact hammer, since the length of a typical monopile is much larger than the length of the cylinder in the presented laboratory experiments. This additional length allows for stress waves to develop and propagate downwards transporting energy away from the impacted end towards the soil, where this energy allows the structure to overcome the soil resistance. Hence, little energy reaches the impacted end after reflection. In contrast, in the described experiment, virtually all energy reflects back to the impacted end due to the absence of a damping mechanism at the lower end that is similar to soil, allowing for the interaction between the impacting mass and structure as described above. Despite this difference, the range of excited frequencies in the laboratory experiment does not differ

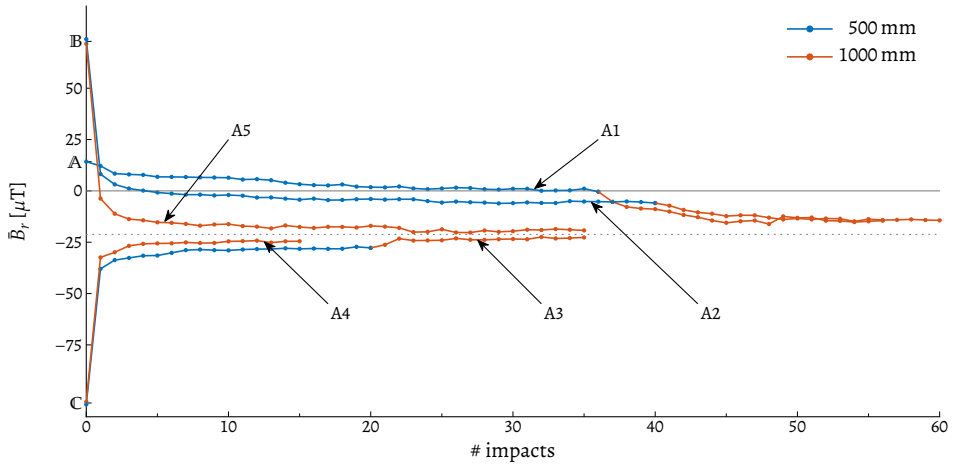


Figure 5.6: The evolution of the radial component of the magnetic stray field with repeated impacts measured on ring R10 at $\theta = 0^\circ$.

5

significantly from that observed in the full scale. Figure 5.5b shows that the lab-scale signals contain frequencies up to 1000 Hz. This range corresponds well to the frequency range excited by an impact hammer during a monopile installation (Chapter 2). Therefore, although the precise interaction between the impacting mass and structure differs in the two cases, the dynamics in terms of excited frequencies is comparable.

To avoid the time-costly process of measuring the full stray field after each impact, a single sensor position is selected to track the evolution of the stray field for test A1 to A5: ring R10 at $\theta = 0^\circ$. The use of a single measurement point for these static measurements has been verified by comparing the stray field at several unique locations in between impacts in the exploratory phase prior to the experiments reported here. Furthermore, that preliminary research demonstrated that the three components of the stray field exhibit similar behaviour as result of the impacts; hence, for conciseness, only the field component with the largest amplitude is presented: the radial component \bar{B}_r .

Figure 5.6 shows the measured evolution of \bar{B}_r , from which it is clear that the field converges towards a consistent value as long as the impact height is kept constant. However, as soon as a higher peak strain is introduced, the field moves towards a new equilibrium level, which stabilises after a few repetitions of the same load. Note that the structure's magnetisation does not always reach the same value, e.g. A1 and A2 appear to end at a similar level, while A5, which started with the same magnetisation as A2, ends at a different value.

5.3.3. Discussion

The observed magnetic behaviour can be explained by the movement of magnetic domain walls. When sufficient energy is introduced in the material, these walls break away from their pinning sites, eventually settling to a new wall configuration. Overcoming these new pinning sites requires additional energy, which can only be provided by introducing strain energy that surpasses the previously sustained level (Jiles and Atherton, 1984). Ultimately, the ideal—anhyseretic—magnetisation state should be attained (the law of approach (Jiles, 1995)), which represents the global magnetic equilibrium given an external field and pinning site distribution (Tebble and Craik, 1969, p. 401).

The data presented in Figure 5.6 implies that the magnetisation asymptotically approaches some common ideal value, which would be in between the final values obtained in tests A3 and A5. Whether this value corresponds to the (ideal) anhyseretic magnetisation state is unknown; this would require generating a decaying alternating external field using magnetising coils that completely surround the structure (Bozorth, 1951/1993, p. 8), which have already been dismissed as impractical at this scale. Similar to Maylin and Squire (1993a), the test data indicates that local magnetic equilibria are reached due to repeated loading. The exact numerical value of the acquired equilibrium is difficult to predict and differs even for tests starting at seemingly identical initial magnetisation states, e.g. tests A2 and A5. As soon as the magnetisation reaches a certain local equilibrium, the induced strains cause only reversible magnetisation changes; these reversible transient strain-induced magnetisation changes are discussed in Chapter 6.

When a new peak strain is introduced, the magnetisation's evolution displays a conspicuous approach towards a new magnetic equilibrium (Figure 5.6). The model equations for irreversible magnetisation changes due to strain as proposed by Jiles (1995) and the extension of Xu et al. (2012b) could in principle be applied to this situation, which would also show a comparable decay. Unfortunately, it is expected that, for each new equilibrium, a new set of coefficients has to be determined, limiting this modelling approach solely to academic purposes.

5.4. Detecting and localising regions of plastic deformation

In this section, the focus is placed on the investigation of the relation between plastic deformations and the measured remanent stray field. The aim is to develop a method to effectively discriminate between the two different causes of irreversible magnetisation changes.

5.4.1. Measurement procedure

Analogous to the final test in phase A, the cylinder is prepared magnetically such that it resides in initial magnetic state \mathbb{B} , which opposes the geomagnetic field. Starting from a drop height of $\ell = 1000$ mm, the cylinder is repeatedly impacted until the remanent

Table 5.2: Detailed description of the tests in phase B in consecutive order. Suffixes i, e and p denote initial state, elastic and plastic deformation, respectively. The drop height is represented by ℓ , the (average) measured peak strain is ϵ_z and the number of impacts needed to reach a magnetic equilibrium is denoted by #.

id	ℓ [mm]	ϵ_z [$\mu\text{m}/\text{m}$]	#
B1i	-	-	-
B2e	1000	832	5
B3e	1500	1200	5
B4e	2000	1510	8
B5p	2500	1574	1
B6p	2500	1550	1
B7p	2500	1544	1

stray field stabilises. Thereafter, the impact height is increased by 500 mm, repeating the procedure until visible plastic deformation develops.

5

5.4.2. Results

An overview of the performed tests in phase B is summarised in Table 5.2, which includes the measured peak strain (ϵ_z) averaged over the number of impacts needed to reach a magnetic equilibrium (#). During test B5p, visible plastic deformation developed at the top of the cylinder; this location of the damaged zone is in accordance with damage reported in other low-velocity drop mass experiments (Karagiozova and Jones, 2000). A close-up of the sustained damage is presented in Figure 5.7a, which shows a so-called elephant foot buckle: a localised protrusion close to the impacted end. To accommodate such a pronounced permanent change in the geometry of the structure, substantial plastic deformation has developed in the material. Initially, the plastic zone is confined between $\theta = 270^\circ$ and $\theta = 360^\circ$. Subsequently, it progresses in the positive θ -direction during test B6p and B7p, as indicated in Figure 5.7b.

Three-dimensional map of the stray field

After each test, the magnetic stray field in the vicinity of the top of the cylinder is mapped using the procedure described in Section 5.2.2. Figures 5.8a, 5.8b and 5.8c present the stray field measured after test B3e, B4e and B5p, respectively. It is clear that the global shape of the field is preserved in between tests. However, in accordance with Phase A, the stray field does evolve with increasing impact height, which becomes apparent by considering the difference field $\Delta\vec{B}$. When the induced strains remain in the elastic regime (i.e. from B3e to B4e), the shape of the difference field resembles that of the total stray field (Figure 5.8d), which indicates that structure's magnetisation increases in magnitude while retaining its direction. However, after the plastic deformation developed (i.e. from B4e to B5p), the change in the stray field is no longer uniform, but depends on the circumferential coordinate (Figure 5.8e). Most of the change is directed towards the cylinder (similar to the elastic case),

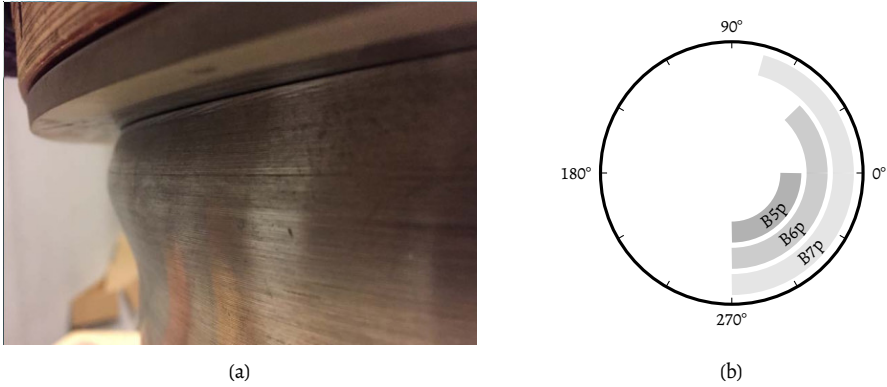


Figure 5.7: Developed visible plastic deformation and progression with subsequent tests. (a) Close-up of the induced visible plastic deformation at the top of the cylinder inflicted during test B5p. (b) Circumferential location of the plastic region sustained during test B5p, B6p and B7p.

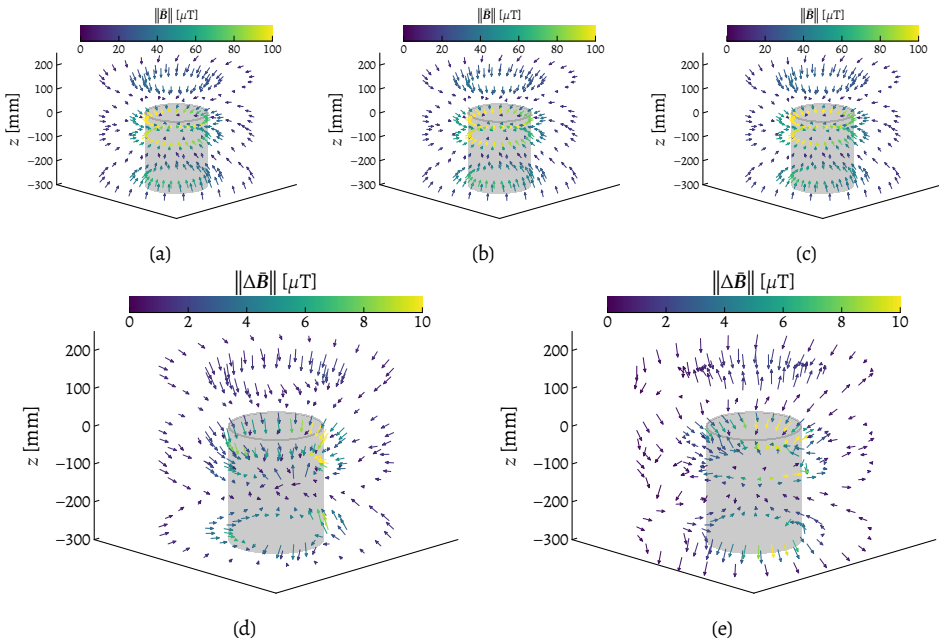


Figure 5.8: Three-dimensional map of the magnetic stray field in the vicinity of the top of the cylinder. (a) B3e. (b) B4e. (c) B5p. (d) $\Delta\vec{B}$ between B3e and B4e. (e) $\Delta\vec{B}$ between B4e and B5p.

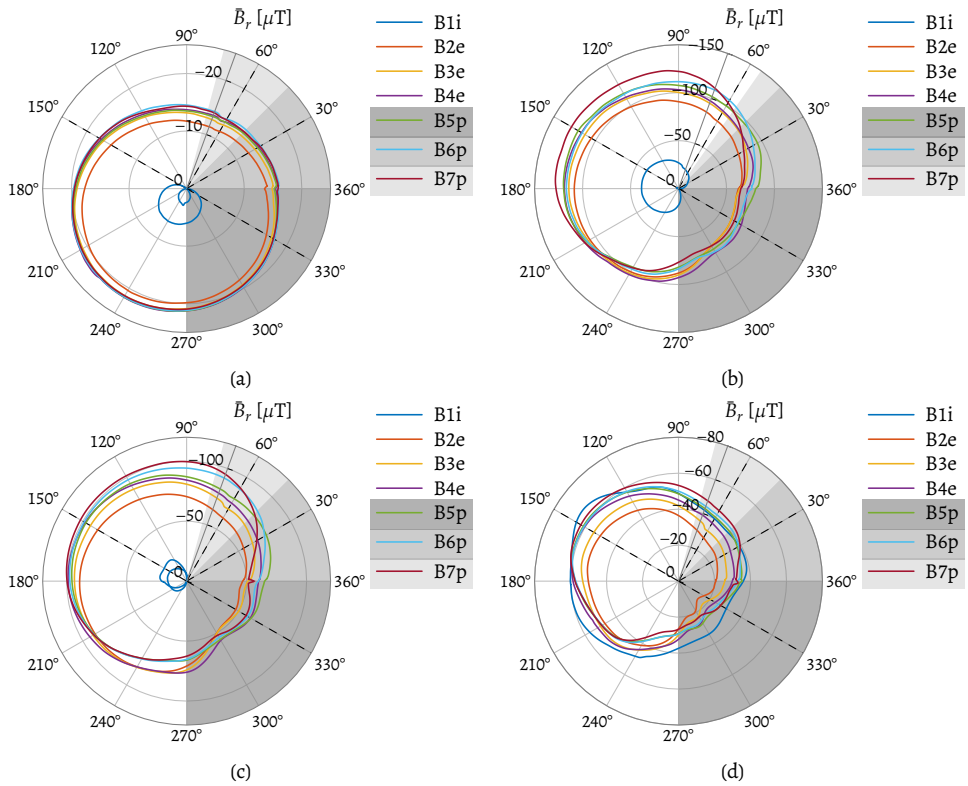


Figure 5.9: Circumferential profile of the radial component of the magnetic stray field \bar{B}_r , measured on rings with $d = 20$ mm. Grey areas indicate regions where visible plastic deformation developed; darker shaded regions were inflicted earlier. (a) RO1, $z = 150$ mm. (b) RO4, $z = -20$ mm. (c) RO7, $z = -100$ mm. (d) RO10, $z = -275$ mm.

while at some locations the change is directed outwards. This behaviour is most pronounced on measurement ring RO4, which is the closest to the top edge of the cylinder.

Circumferential profiles of the radial stray field component

Given the abundance of information contained in Figure 5.8, it is difficult to use the three-dimensional data to detail the irreversible changes due to the impacts. To explicate these changes, circumferential profiles of the radial component of the stray field \bar{B}_r are presented in Figures 5.9 and 5.10, which correspond to data obtained on a single measurement ring. The radial component is selected as it dominates the field at the top of the cylinder, especially in the difference field $\Delta\bar{B}$. Since the stray field is determined by the magnetisation of the entire structure, the profiles are shown for two sets of measurement rings, which provides the means to determine how localised the influence of the damage is on the stray field. First, Figure 5.9 shows the circumferential data with a constant offset $d = 20$ mm at four distinct axial rings: RO1, RO4, RO7 and RO10. Second, Figure 5.10 displays the data from three rings

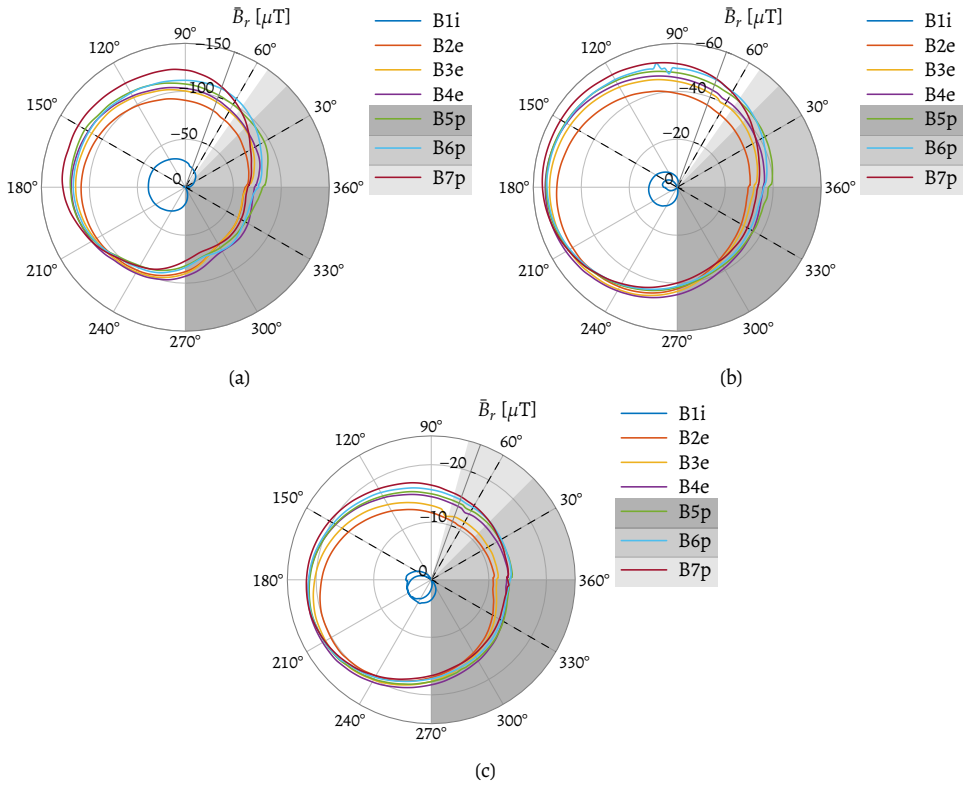


Figure 5.10: Circumferential profile of the radial component of the magnetic stray field \vec{B} , measured on rings with $z = -20$ mm. Grey areas indicate regions where visible plastic deformation developed; darker shaded regions were inflicted earlier. (a) RO4, $d = 20$ mm. (b) RO5, $d = 100$ mm. (c) RO6, $d = 300$ mm.

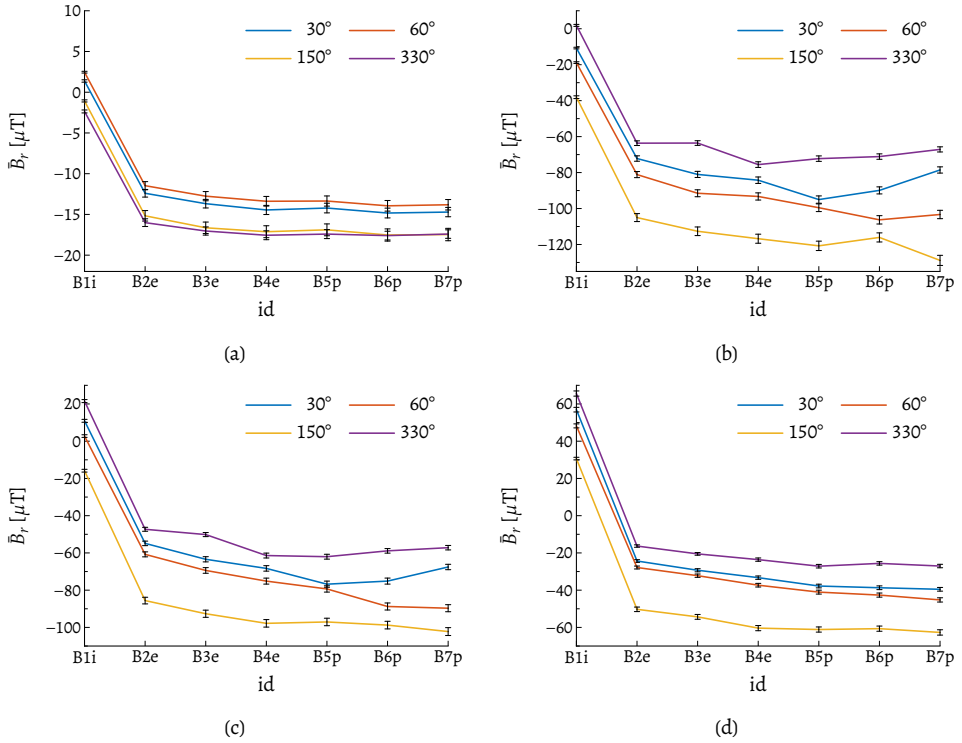


Figure 5.11: Evolution of \bar{B}_r in between tests at four selected circumferential positions with $d = 20$ mm. (a) RO1, $z = 150$ mm. (b) RO4, $z = -20$ mm. (c) RO7, $z = -100$ mm. (d) RO10, $z = -275$ mm.

with increasing offset in which the axial position remains constant at $z = -20$ mm: RO4, RO5 and RO6. In the circumferential profiles, four distinct regions are shaded conform the colours introduced in Figure 5.7, indicating where and when visual plastic deformation developed.

Evolution of the stray field at selected circumferential positions

To further clarify the effect of the increased impact heights on the remanent stray field and the progression of the damage, the stray field at four circumferential positions is presented: $\theta = 150^\circ$ (no plastic deformation), $\theta = 330^\circ$ (B5p), $\theta = 30^\circ$ (B6p) and $\theta = 60^\circ$ (B7p). For each of these regions, Figures 5.11 and 5.12 show the evolution of \bar{B}_r with each test. In the figures, the error bars indicate the uncertainty in the measured value corresponding to 2% of $\|\mathbf{B}\|$. Similar to the results of Phase A, the evolution of the remanent stray field displays a tendency to converge towards a constant value during the increase of the impact height. However, as soon as the reported damage has developed, a deviation from this trend is observed, e.g. Figure 5.11b. In the ensuing discussion, this behaviour is further analysed.

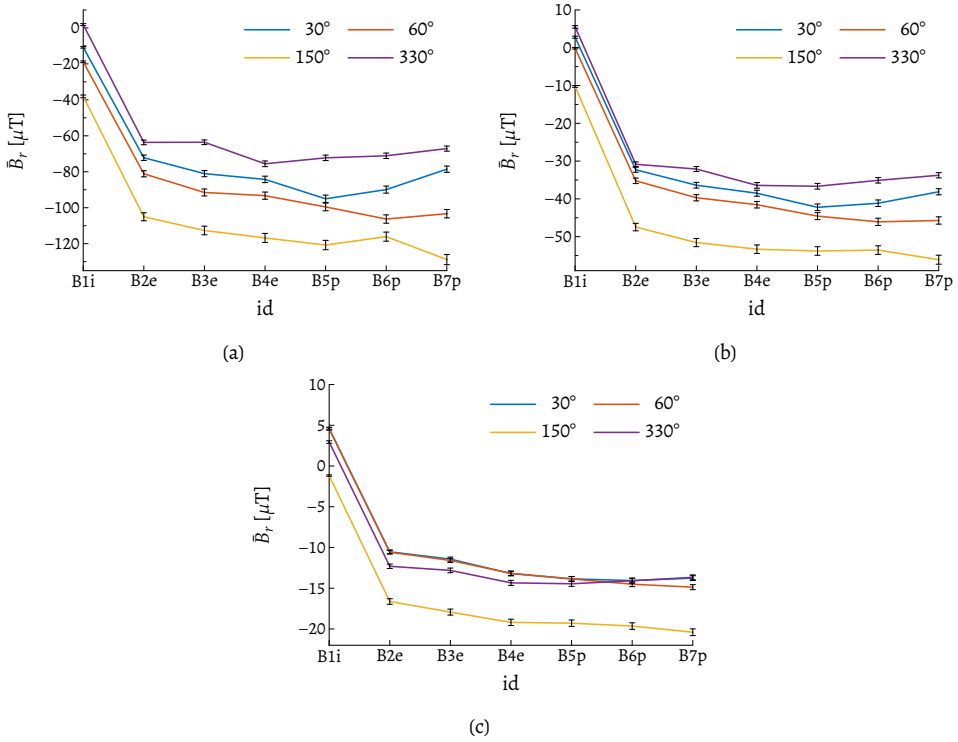


Figure 5.12: Evolution of \bar{B}_r in between tests at four selected circumferential positions with $z = -20$ mm. (a) RO4, $d = 20$ mm. (b) RO5, $d = 100$ mm. (c) RO6, $d = 300$ mm.

5.4.3. Discussion

Below, the discussion on the reported stray field measurements is split into three topics: the initial magnetic state, the elastic regime and the plastic regime.

The initial magnetic state

Initially (test B1i), the structure's magnetisation is in initial state B, in which the magnetisation is non-zero and is directed upwards close to the magnetising coil, i.e. R10; this results in an outwards pointing (positive) radial stray field (Figure 5.11d). However, the magnetisation at the top of the cylinder is close to the demagnetised state (see e.g. the circumferential profiles in Figure 5.9). Due to the presence of the external geomagnetic field, the weak remaining magnetisation in the structure adheres to the direction of the external field, resulting in the measured inhomogeneous initial stray field profiles for \bar{B}_r . The observed skewness of the initial (and subsequent) profiles (Figures 5.9 and 5.10) stems from the geometry-induced demagnetising field caused by the horizontal component of the geomagnetic field, which points approximately towards $\theta = 325^\circ$.

5

Elastic regime

Subsequently, the axial impacts introduce sufficient energy to magnetise the structure further; its magnetisation aligns with the external field B_0 . Naturally, this observation is completely in line with the results discussed previously for the elastic loading in Phase A. Due to the increasing strain energy supplied to the structure, the magnetisation progressively tends towards the global magnetic equilibrium (anhysteretic magnetisation). In the circumferential profiles, the gradual expansion of the profile measured after test B2e with each test illustrates this tendency. Since this behaviour is apparent in all profiles along the axial line with $d = 20$ mm (Figure 5.9) and the line with increasing offset (Figure 5.10), it is reasonable to assume that the increase of the magnetisation is uniformly occurring throughout the structure.

In Figures 5.11 and 5.12, the evolution of the stray field (and consequently the magnetisation) resembles the lines measured during Phase A presented in Figure 5.6. The large difference between the initial state (B1i) and the stray field after 5 impacts of 1000 mm (B2e) stems from the fact that the initial state is noticeably different from the global magnetic equilibrium. For the subsequent tests within the elastic regime, the differences between successive stray field values are smaller but significantly larger than the measurement error in most cases. An exception to this trend appears between B2e and B3e at $\theta = 330^\circ$ for R04 (Figure 5.11b) and R07 (Figure 5.11c). However, this difference lies within the error margin; hence, the converging trend appears to continue as well at these locations.

Plastic regime

In contrast, as soon as plastic deformation develops, e.g. test B5p at $\theta = 330^\circ$, the evolution of the stray field deviates from the aforementioned converging trend (Figure 5.11b). This

is a consequence of the deterioration of the magnetic properties due to the formation of additional pinning sites and residual strain (Jiles, 1988a), which results in a reduction of the magnetisation in the affected area. Since ring R04 is the closest to the damaged area, Figure 5.11b shows the break of the trend most clearly. For circumferential positions where no visible damage developed in test B5p ($\theta = 30^\circ$, $\theta = 60^\circ$ and $\theta = 150^\circ$), the trend towards global equilibrium simply continues until plastic deformation does develop, i.e. during test B6p and B7p at $\theta = 30^\circ$ and $\theta = 60^\circ$, respectively. Therefore, it seems that the departure from this trend permits not only detecting, but also localising the damage.

Since the stray field is generated by the magnetisation of the entire structure, it is important to check up to which distance from the damaged region the deviation from the tendency towards global equilibrium is significantly measurable. Naturally, it is to be expected from a non-contact method to infer plastic deformation that the magnetisation reduction is noticeable at several offsets from the structure's surface—in this case, different measurement rings. Figure 5.11b demonstrates that for R04 (directly next to the damaged area), the deviation is most pronounced. At R07 (Figure 5.11c), the effect of the plastic region is significant at $\theta = 330^\circ$ and $\theta = 30^\circ$. However, no effect of the development of plastic deformation is visible for the two rings further from the top edge of the cylinder, i.e. R01 (Figure 5.11a) and R10 (Figure 5.11d). Similarly, for increasing distance from the cylinder's surface, R05 (Figure 5.12b) displays the same behaviour as on R04 (Figure 5.12a), albeit less pronounced. For R06 (Figure 5.12c), the deviation is only visible at $\theta = 330^\circ$ and $\theta = 30^\circ$. From this data, one can conclude that the stray field measurements enable one to localise a region of plastic deformation.

During the development of plastic deformation, the remanent stray field irreversibly changes as a result of three physical processes of which the effects are superimposed:

- (i) deterioration of magnetic properties due to the formation of plastic deformation. This always results in a local decrease of strength of the magnetisation, and reciprocally a demise of the stray field's amplitude in the vicinity of the damage;
- (ii) irreversible domain wall motion due to energy provided by elastic deformation (Section 5.3.3). For the presented results, this constitutes to a relatively small increase of the magnitude of the magnetisation, which is clear from the evolution of the stray field during tests B2e to B4e;
- (iii) permanent change in the geometry due to the damage, which brings the surface of the cylinder closer to the sensor (Figure 5.7a). Normally, the strength of the measured stray field increases when a ferromagnetic material comes closer to a magnetic field sensor.

Of these three processes, only the first reduces the stray field's magnitude. The latter two increase the measured strength of the stray field. Given that, due to the development of the plastic zone, the amplitude of the measured stray field still diminished, one is inclined to conclude that the sustained damage significantly reduced the local magnetisation, and

that this decline can only be attributed to the development of a region of substantial plastic deformation.

5.5. Limitations of the method to detect plastic zones

To successfully ascertain the cause of the irreversible magnetisation changes—and thus to detect and localise plastic deformation when that develops—using the observation discussed above, certain conditions have to be met, limiting the direct application of this method. These limitations are addressed below.

5.5.1. The initial magnetic state

Although the magnetisation's tendency towards a global equilibrium state resulting from elastic load cycles is pronounced, the experimental data show that the exact value of this magnetic equilibrium state cannot easily be determined a priori. Fortunately, an exact value is unnecessary to detect and localise plastic deformation, since the development of permanent strain violates the trend. However, for some initial magnetic states, this transgression is not observed when plastic deformation forms, which becomes clear by a closer examination of the local equilibrium positions of the magnetisation, which govern the observed behaviour.

Figure 5.13 presents a simplified representation of the energy E associated with each value of the structure's magnetisation M . In reality, the line is a hypersurface, which depends on a plethora of parameters: external field strength and orientation, elastic strain, temperature, and, most importantly, the distribution of pinning sites for the magnetic domain walls. The (local) minima of the hypersurface, indicated the vertical dotted lines, are the admissible values for the structure's magnetisation. According to its definition (Tebble and Craik, 1969, p. 401), the anhysteretic magnetisation M_{an} for the given field strength, dislocation distribution and strain is represented by the global minimum of the hypersurface.

Assuming that the dislocation distribution does not change significantly due to induced elastic strains, the additional strain energy introduced by a new peak strain provides the system with sufficient energy to overcome the barrier that originally prevented it from reaching a lower energy state. Hence, induced elastic strain ε_e moves the magnetisation closer to the anhysteretic state, which is illustrated by the arrows at the top of Figure 5.13. When plastic strain ε_p develops, the dislocation density increases. These newly-formed pinning sites disintegrate the existing magnetic domains, reshaping the hypersurface, and shifting the global minimum towards zero magnetisation. The direction of the magnetisation change caused by plastic deformation is marked by the arrow below the figure.

When the structure's initial magnetic state is in the grey-shaded area shown in Figure 5.13, the remanent stray field displays the behaviour described above: the deviation from the trend allows one to discriminate between the two causes for irreversible magnetisation changes. Nonetheless, for an initial magnetisation in the unshaded area, both elastic and plastic strain tend to decrease the magnetisation, obscuring the cause of the permanent

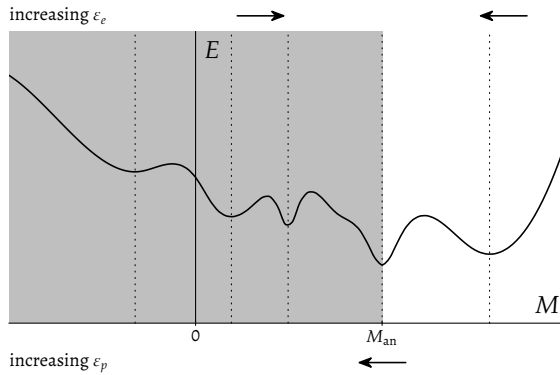


Figure 5.13: Simplified representation of the energy E associated with the attained magnetisation M , in which the global minimum corresponds to the anhysteretic magnetisation M_{an} .

shift in the magnetisation. Hence, to successfully identify the source of an irreversible magnetisation change, the initial magnetic state of the structure must lie within the shaded area. This can be achieved by magnetically preparing the structure's area of interest in one of the two following ways: demagnetising or magnetising with a magnetising field that opposes the local geomagnetic field. The former is simpler to accomplish in a practical situation as the structure does not have to be fully demagnetised; therefore, a hand-held device—as used in the reported experiment—already suffices.

Since the hypersurface contains all relevant information to determine the magnetic state of a structure in case the external stimuli change, an expression for that surface would provide an extremely useful insight into the dynamics of the magnetomechanical response of a structure. Unfortunately, deriving such an expression is an immense exercise, which requires detailed inputs, e.g. the domain and dislocation distributions. These quantities are difficult to determine experimentally, especially for large-scale structures. Therefore, the derivation of such an expression is left out of the scope in this thesis.

5.5.2. Application of the load

Since the direction of change of the remanent magnetic stray field towards the new equilibrium state is initially ambiguous, the load should be introduced gradually to reveal the trend towards the global equilibrium. Fortunately, the hammer energy is incrementally introduced when a monopile is driven, since the soil resistance is lower during the initial stages of installation. Hence, during a typical monopile installation, the requirement of the gradual introduction of the load is automatically satisfied.

5.5.3. Sensor position

Since the changes of the remanent stray field are relatively small, not only the use of a high-accuracy magnetometer is advisable, but also the placement of the sensor should be considered with care in order to reduce the possibility of a false positive. Due to the geometry of the structure, the stray field is not uniform. Consequently, an accidental shift of the sensor's position relative to the pile results in a permanent change in the measured stray field that is indistinguishable from deformation-induced irreversible changes. Hence, to successfully detect and localise regions of plastic deformation in the structure, the sensor should retain its position with respect to the structure in between load cycles. Future research should be devoted to finding practical solutions to preserve the sensor's position or correcting for the effects of relative displacements if they occurred. Additionally, as Equation (5.2) relies explicitly on the distance between the measurement point and the structure, further research should be devoted to determining the optimal distance at which plastic deformation reliably can be identified in a structure subjected to dynamic loading.

5

5.6. Generalisation of the proposed method

In this section, various aspects relevant to generalising and improving the proposed method are treated.

5.6.1. Quantifying the plastic strain

Based on the presented data, quantifying the plastic deformation is not possible at present. However, by including a dependency on plastic strain in a model for the magnetisation $M(r)$ in Equation (5.2), this should ultimately be realisable. Sablik et al. (2004) and Wang et al. (2011) have presented phenomenological models that account for the development of plastic deformation. Once such a description is included in the modelling framework presented in Chapter 4, the amount of plastic deformation can be estimated. However, at present, it is still unknown whether the parameters encountered in current models that allow the modelling of plastic strains are structure-dependent or not. Additional experimental research should shed light on this aspect. Most probably, quantitative prediction of the induced plastic deformation entails a calibration step, which is a topic of future investigation.

5.6.2. Pure tensile loads

In the presented experiment, the measured irreversible magnetisation changes result from compressional load cycles, and the stray field reaches an equilibrium after a few cycles. However, ferromagnetic materials display an asymmetric response to compressive and tensile strain in isostrain scenarios (Craik and Wood, 1970). Fortunately, experimental data from small-scale steels specimens subjected to purely tensile load cycles are available. Bao et al. (2010) present graphs of the magnetic field against the applied strain, which show that the magnetic field returns to its initial value after removal of the load, indicating that

the specimen's magnetisation is at an equilibrium. Furthermore, visual analysis of the data presented in Figure 4 of Bao et al. (2016) indicates that the measured remanent magnetic field initially increases with increasing elastic strain until a yield limit is reached. At that point, the amplitude of the magnetic field decreases with the development of plastic deformation. For other specimens reported in the same work, changes in the magnetic field do not exhibit this behaviour, which can be explained by the fact that the specimens are not demagnetised prior to loading. Thus, the initial magnetisation for these specimens could be such that the effects of elastic and plastic deformations reinforce each other. All in all, these other experiments are compelling evidence that the method introduced in this chapter is also valid for structures loaded purely in tension when the specimen has an appropriate initial magnetic state.

5.6.3. Other load types

Next to load cycles in pure compression or tension, a structure can also be loaded in an alternating fashion: a compression-tensile cycle. Most experimental data of strain-induced magnetisation changes for specimens repeatedly subjected to such oscillating cycles pertain to low-cycle fatigue experiments, in which considerable plastic deformation is inflicted during each cycle (Bao and Gong, 2012; Erber et al., 1997). Ruuskanen and Kettunen (1991) report reversible magnetisation changes due to sinusoidal loading with varying amplitude, which remain in the elastic regime. Unfortunately, it is difficult to determine from their data if the measured magnetisation returns to the same value when the specimen is unstrained. Moreover, the authors examine a rod surrounded by a search coil, which is a configuration in which the effect of the demagnetising field is negligible. Consequently, a dedicated experiment should be conducted to demonstrate whether the magnetisation of a more complex structure attains a magnetic equilibrium due to alternating cyclic loading. If this turns out to be the case, detecting and localising plastic deformation using the remanent stray field could also be applied in this loading scenario.

Contrary to the experiments cited above, which are performed with quasi-static loads ($f < 50$ Hz), a broad range of frequencies is excited by the impact in the reported dynamic experiment ($f < 1000$ Hz, see Figure 5.5b). Experiments with high-frequency magnetic loading have shown that the loading frequency influences the induced magnetisation curves due to the generation of eddy currents in the material (Jiles, 1994a,b). However, the remanent magnetisation—i.e. the magnetisation in absence of an external field—appeared to be invariant to the loading frequency. At present, it is unknown whether these conclusions are equally valid for the remanent magnetic field resulting from high-frequency mechanical loading.

5.6.4. Fatigue damage

To detect and estimate fatigue damage, another relevant type of damage in dynamically loaded structures—e.g. monopile foundations during operational conditions subjected to

wind and wave loads—future research should be dedicated to magnetisation changes in case of high-cycle fatigue loading. Potentially, continuous non-contact monitoring of the structure's magnetic stray field could lead to a more accurate estimate of the remaining life time of the support structure.

5.7. Conclusions

In this chapter, data is presented from a unique magnetomechanical experiment, in which a steel cylinder is subjected to axial impacts from various heights. Due to repeated impacts that induce elastic strains, the remanent magnetisation converges to a magnetic equilibrium state. When the cylinder is subsequently repeatedly impacted with an increased drop height, the magnetisation quickly settles at a new magnetic equilibrium. The exact value of these equilibria is difficult to predict. Nonetheless, the data suggest that the magnetisation approaches the global magnetic equilibrium: the anhysteretic magnetisation.

When plastic deformation is inflicted by an impact, careful analysis of the measured remanent magnetic stray field demonstrates that irreversible changes in the structure's magnetisation caused by plastic deformation can be distinguished from irreversible changes due to elastic deformation. The former changes result in a deviation from the tendency of the magnetisation to converge towards the global equilibrium. Moreover, this behaviour due the plastic deformation, of which the exact circumferential location is unknown a priori, is solely observed in the proximity of the affected area, enabling one to localise the damaged region.

Elastic deformation irreversibly pushes the magnetisation towards the global equilibrium, while plastic deformation tends to reduce the value of this magnetic equilibrium towards zero. For most initial magnetic states, these two processes counteract each other, manifesting the deviation of the trend towards this global equilibrium. However, for some initial magnetic states, this identification procedure is not possible. To guarantee that the initial magnetic state is at the correct position relative to the global magnetic equilibrium so that the proposed method is effective, the structure should be demagnetised.

In the current experiment, each impact generates only compressive structural strains. An analysis of magnetic data induced by tensile loads reported in literature indicate that the structure's magnetisation attains a magnetic equilibrium when subjected to these repeated loads. Moreover, for demagnetised samples, plastic deformation leads to a reduction of the remanent magnetisation. Hence, the presented method seems similarly applicable in that case. However, for alternating compression and tension cycles, it remains uncertain whether a magnetic equilibrium is reached by repetition of the load or not.

After focussing on the irreversible changes of the remanent magnetic field here, the next chapter is devoted to the reversible strain-induced stray field changes during an impact.

6

Strain-induced transient components of the magnetic stray field

*Alles läuft perfekt, schon seit Stunden
Wissenschaftliche Experimente*

Peter Schilling – Major Tom

To infer when and where regions of plastic deformation develop as a result of an axial impact, the previous chapter has focussed on the evolution of the remanent stray field in between impacts. However, during loading, the stray field has an additional strain-induced component, which is related to the transient elastic deformation of the structure. This chapter analyses the strain-induced components of the magnetisation in order to investigate whether stray field measurements can be used as a non-contact alternative to traditional strain gauges.

Thus far, experiments aiming to detect impact-induced strain in steel specimens through magnetic field measurements have been performed with a split-Hopkinson bar in which a steel rod is impacted by a striker bar. In the reported literature, a search coil that completely surrounds the specimen is employed to record the varying magnetic field (Belahcen et al.,

Parts of this chapter are intended to be published in a manuscript under preparation for the *Journal of Sound and Vibration* (Meijers, Tsouvalas and Metrikine, 2021c).

2014; Hecker and Schulz, 1997; Hubert and Rizzo, 2008; Kim et al., 2003; Lolloz et al., 2006; Peussa and Belahcen, 2015). Given the geometry and size of the specimens, the effect of the demagnetising field is negligible, and consequently, the quantities of interest are approximately uniaxial and parallel. However, for a slightly more complex geometry, e.g. a cylinder, this is no longer the case. To illustrate that, the strain-induced transient stray field measured during the experiment described in Chapter 5, which exhibits a significant demagnetising field, is examined by placing the magnetometer at different circumferential positions.

First, the strain field during an impact is examined in detail to unveil the dominant components of the strain tensor. To this end, the deformation field is modelled with an axially symmetric elastic shell theory, which has previously been introduced in Chapter 2. Second, the magnetic stray field variations measured during several impacts are presented and discussed with the emphasis being placed on the similarity between the strain signal and the stray field components. This is essential in order to infer the elastic strain from the recorded stray field alone. Third, a magnetomechanical model for the reversible strain-induced magnetisation is developed assuming isotropic magnetic material properties. Simulated results obtained from the model are compared with the measured data, and the sources for the observed discrepancies are highlighted. Fourth, the general applicability of the method to large-diameter monopiles and its possible limitations are discussed. Finally, the chapter is concluded with a summary of the most important findings.

6.1. Transient strain field generated by an axial impact

In this section, the measured axial strain is analysed using data collected during the experiment described in Chapter 5, of which Figures 6.1a and 6.1b present the set-up. Subsequently, a mechanical model of a thin-walled cylinder impacted by a free-falling mass is developed using the axially symmetric elastic theory, which has been introduced in Chapter 2. Although the model is applied to describe the structural response in a lab-scale experiment, the same model is considered to be applicable to large-diameter monopile installations by means of a hydraulic hammer.

6.1.1. Measured impact-induced axial strain

The set-up of the experiment in which a steel cylinder is repeatedly impacted by a free-falling concrete mass has been described in detail in Section 5.2. During each impact from a variable height ℓ , two axial strain gauges (type: UFLA-5-II) measure the axial strain ε_z . These devices are diametrically attached to the cylinder's surface at $z = -200$ mm (Figure 6.1b), and signals are sampled with a frequency of 50 kHz.

Figures 6.2a and 6.2b show the time-frequency plots of the registered axial strain ε_z resulting from an impact with $\ell = 500$ mm and $\ell = 1500$ mm, respectively. Clearly, only compressive axial strain is generated in the cylinder by the impact. The amplitude spectra for these signals indicate that the energy is contained in a frequency range up to 2 kHz. Moreover,

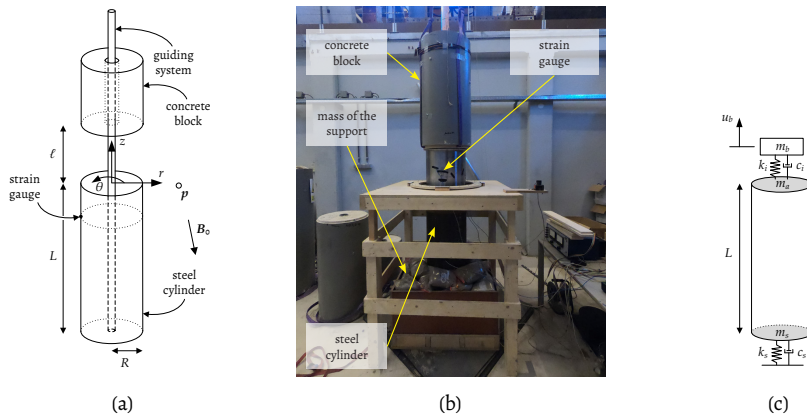


Figure 6.1: The experimental set-up. (a) Detailed schematic representation. (b) Annotated photograph of the set-up. (c) Simplified schematic representation replacing the concrete block by a point mass m_b .

the time series can be split into two distinct strain pulses with different duration: the short primary strain pulse ($t_1 = 0 \geq t \geq 5$ ms), and the secondary strain pulse ($t_2 = 5 \geq t \geq 40$ ms), which has a lower frequency content than the former. These two time intervals are indicated in Figure 6.2. Even though the impact from $\ell = 1500$ mm introduced significantly more energy into the system than the impact from $\ell = 500$ mm, the frequency content of the strain signals appears approximately equal. Only the amplitude of the signals differs. Using the results from the model to simulate the experiment developed hereafter, the observed behaviour of the strain is explained later in this chapter.

6.1.2. Governing equations for an axially symmetric cylinder

The data collected at a large-diameter monopile installation (Section 2.2.4) have shown that the axi-symmetric membrane theory is adequate to predict elastic deformations induced by a hammer blow, since the dispersion characteristics of stress waves propagating in the pile are captured correctly in the frequency range of interest. In the lab-scale experiment, the impact is generated by a free-falling concrete block, which is modelled as a point mass m_b moving in the gravitational field along the z -axis (Figure 6.1c). The mass interacts with the cylinder at $z = 0$ through a non-linear spring and dashpot. When an additional mass m_a is located at the top of the pile (representing the anvil of a hydraulic hammer), the system is equivalent to the hammer-pile interaction model examined by Deeks and Randolph (1993).

Thus, the mechanical model outlined hereafter can be applied to predict elastic strains during the installation of large-diameter monopiles. To accommodate the more complex behaviour of hydraulic impact hammers, the single mass m_b could be replaced by multiple masses. However, for the current laboratory set-up, a single impacting mass is assumed to be sufficient. Additionally, in reality, soil resistance will be present at the lower end of the pile. In the model described below, the distributed stiffness and damping (Section 2.4) is omitted

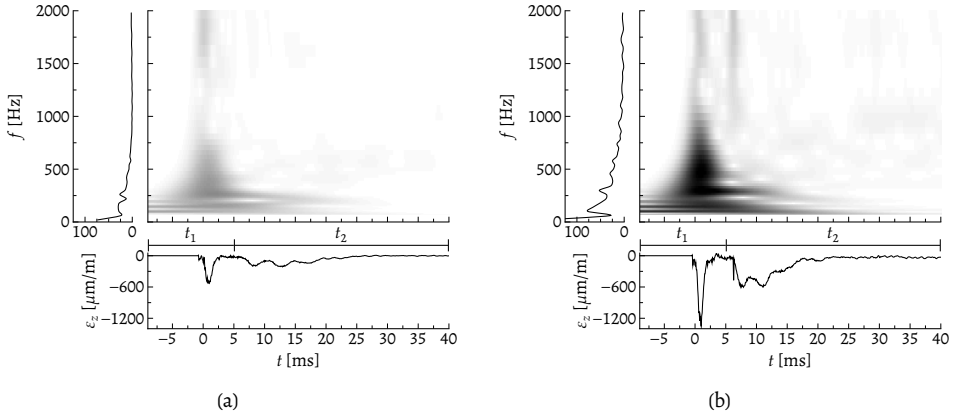


Figure 6.2: Time-frequency analysis of the axial strain ε_2 measured at $z = -200$ mm. (a) Impact with $\ell = 500$ mm. (b) Impact with $\ell = 1500$ mm.

due to their absence in the set-up studied here. Only tip resistance is incorporated through a mass, damping and stiffness term, which are represented by m_s , c_s and k_s , respectively (Figure 6.1c). It is expected that the model without the axially-distributed soil resistance gives a fair prediction of the first downwards propagating stress wave in a pile.

6

Axially symmetric membrane equations

To model the deformation of the cylinder, the axially symmetric membrane theory is employed, which is obtained by considering only the $n = 0$ circumferential mode in the Donnell–Mushtari operator for a cylindrical shell, while simultaneously neglecting bending of the shell’s surface. Due to these assumptions, the circumferential deformations decouple from the two other displacements: the axial $u(z, t)$ and radial $w(z, t)$ displacements, in which the θ -dependency is discarded due to symmetry. Once the axi-symmetric operator (Equation (2.8)) has been transformed into dimensional form, the governing equations for the two displacement components read:

$$\rho A \frac{\partial^2 u}{\partial t^2} = \frac{EA}{1-\nu^2} \left(\frac{\partial^2 u}{\partial z^2} + \frac{\nu}{R} \frac{\partial w}{\partial z} \right), \quad (6.1a)$$

$$\rho A \frac{\partial^2 w}{\partial t^2} = -\frac{EA}{1-\nu^2} \left(\frac{\nu}{R} \frac{\partial u}{\partial z} + \frac{w}{R^2} \right), \quad (6.1b)$$

in which $A = 2\pi Rh$ denotes the cross-sectional area of the cylinder, R is the radius, h represents the wall thickness, and L is the cylinder’s length. The material properties are the density ρ , Young’s modulus E , and Poisson’s ratio ν .

Equation of motion of the impacting block

The impacting concrete block has a mass m_b and is modelled by a simple one-degree-of-freedom system, in which its motion $u_b(t)$ is governed by

$$m_b \ddot{u}_b = -m_b g + F_i(t), \quad (6.2)$$

where a dot above a quantity represents the ordinary derivative with respect to time, g is the gravitational acceleration and $F_i(t)$ denotes the non-linear interface force as defined below.

Interface condition at $z = 0$

At the interface of the cylinder and the block ($z = 0$), the two boundary conditions for the membrane equations are

$$F_i(t) = -\frac{EA}{1-\nu^2} \frac{\partial u}{\partial z} - m_a \frac{\partial^2 u}{\partial t^2}, \quad (6.3a)$$

$$w = 0, \quad (6.3b)$$

in which m_a represents the anvil mass. The latter expression implies that the radial displacement remains zero for all t , while the former relation relates the axial force in the membrane to the aforementioned interface force, i.e.:

$$F_i(t) = \begin{cases} k_i [u(0, t) - u_b(t)] + c_i [\dot{u}(0, t) - \dot{u}_b(t)] & \text{if } u_b(t) < u(0, t), \\ 0 & \text{otherwise.} \end{cases} \quad (6.4)$$

The description above ensures that only when the block and the cylinder are in contact a force is activated. The stiffness and damping of the interface element are labelled k_i and c_i , respectively.

Boundary condition at $z = -L$

At the lower end of the cylinder ($z = -L$), the following boundary conditions apply:

$$F_s = \frac{EA}{1-\nu^2} \frac{\partial u}{\partial z} = k_s u + c_s \frac{\partial u}{\partial t} + m_s \frac{\partial^2 u}{\partial t^2}, \quad (6.5a)$$

$$w = 0, \quad (6.5b)$$

in which m_s denotes the mass of the support structure. Again, the radial displacement is zero, while the axial membrane force is proportional to the displacement and velocity of the structure at the same location through the stiffness k_s and damping c_s , respectively.

Initial conditions at $t = 0$

Initially, the cylinder is at rest. Instead of prescribing the impact height ℓ of the concrete block explicitly, the velocity reached during a free fall from that height is imposed. Therefore,

the initial conditions for the impacting mass are given by

$$u_b(0) = 0, \quad (6.6a)$$

$$\dot{u}_b(0) = -\sqrt{2g\ell}. \quad (6.6b)$$

The sign in the velocity term is negative to account for the downward acceleration experienced by the block due to gravity. These initial conditions ensure that the impacting block and the cylinder are directly in contact at $t = 0$.

Extracting the strain components

Once the displacement fields $u(z, t)$ and $w(z, t)$ have been determined, the non-zero components of the strain tensor $\varepsilon(z, t)$ are easily computed using the dimensional form of Equation (2.15):

$$\varepsilon_z = \frac{\partial u}{\partial z}, \quad (6.7a)$$

$$\varepsilon_\theta = \frac{w}{R}, \quad (6.7b)$$

in which ε_z and ε_θ represent the axial and the circumferential strain, respectively. Note that the shear strain $\varepsilon_{z\theta}$ is equal to zero due to the absence of the torsional motions in the structure.

Solution strategy

As the system of governing equations described above is non-linear, a numerical solution strategy is employed. Spatially, the cylinder is discretised with linear finite elements using FEniCS (Logg et al., 2012) with $\Delta z = 15.2$ mm. For the time resolution, an adaptive Runge-Kutta 4–5 time marching scheme (Fehlberg, 1969) is used. Table 6.1 lists the numerical values for the model parameters. For the stiffness and damping coefficients at the interface and the support, no values are known a priori. Consequently, these values are obtained with an identification procedure, in which the amplitude and the frequency content of the axial strain at $z = -200$ mm for the primary and secondary pulse of the simulated time series is matched to the measured signal. For three impacts height, Table 6.2 presents the calibrated parameters.

6.1.3. Simulated impact-induced strain field

Figures 6.3a, 6.3b and 6.3c compare the measured and simulated axial strain for a sensor located at $z = -200$ mm induced by an impact with $\ell = 500$ mm, $\ell = 1000$ mm and $\ell = 1500$ mm, respectively. For clarity, the presented signals have been filtered by a low-pass filter with a cut-off frequency of 2 kHz. In all cases, the model predicts the shape and amplitude of the primary strain pulse very well, while the correspondence with the secondary strain

Table 6.1: Parameters to model the dynamic response of a cylinder impacted by a free-falling mass.

Parameter	Value	Parameter	Value	Remark
g	9.81 m/s ²	R	203.2 mm	
ρ	7850 kg/m ³	h	2.5 mm	$z \geq -500$ mm
E	210 GPa	h	8.0 mm	$z < -500$ mm
ν	0.3	m_b	400 kg	
L	1500 mm	m_a	0 kg	
		m_s	350 kg	

Table 6.2: Estimated stiffness (k) and damping (c) parameters. Suffixes i and s indicate the interface between the impacting mass and the cylinder, and the support, respectively.

Parameter	Values	ℓ [mm]
k_i	[170, 250, 450] MN/m	[500, 1000, 1500]
c_i	[80, 50, 50] kNs/m	[500, 1000, 1500]
k_s	[18, 18, 18] MN/m	[500, 1000, 1500]
c_s	[50, 50, 120] kNs/m	[500, 1000, 1500]

pulse is inferior, but still adequate. Despite this mismatch, this relatively simple model is able to predict the strain induced in the cylinder by an impact.

From the simulated impacts, one can understand the interaction between the impacting block and the cylinder, and how that yields the distinct shape of the measured strain signal. To this end, the mean displacement of the cylinder $u_c(t)$ and the position of the mass $u_b(t)$ for an impact with $\ell = 1500$ mm are analysed, which are shown in Figure 6.3d. The initial impact accelerates the cylinder downwards, while simultaneously decelerating the mass. In effect, the cylinder moves away from the mass, even resulting in a short period where no contact exists between the two objects. However, the support pushes the cylinder up, and the block continues to move down due to the experienced gravitational pull. Consequently, they come in contact again introducing compressional strain (the secondary strain pulse), while moving upwards together. At $t \approx 30$ ms, the concrete mass disconnects from the cylinder, and the strain reduces to zero.

A further point of interest is the spatial distribution of the non-zero components of the strain tensor: the circumferential strain ε_θ and the axial strain ε_z . Figure 6.4 presents the simulated time series at $z = -200$ mm for both strain components. Additionally, the strain distribution over the cylinder's length is presented for six time instances, which are indicated in the time series by points with corresponding colours. Except for the points in the ascending branch of the primary strain pulse, the strains are relatively uniformly distributed along the z -axis, which indicates that the cylinder is compressed equally over its length, effectively acting as a spring. This response is a consequence of the excited wavelengths, which are much longer than the length of the cylinder. Only during the ascending branch of the primary strain pulse, wavelengths are excited that are shorter than the structure's

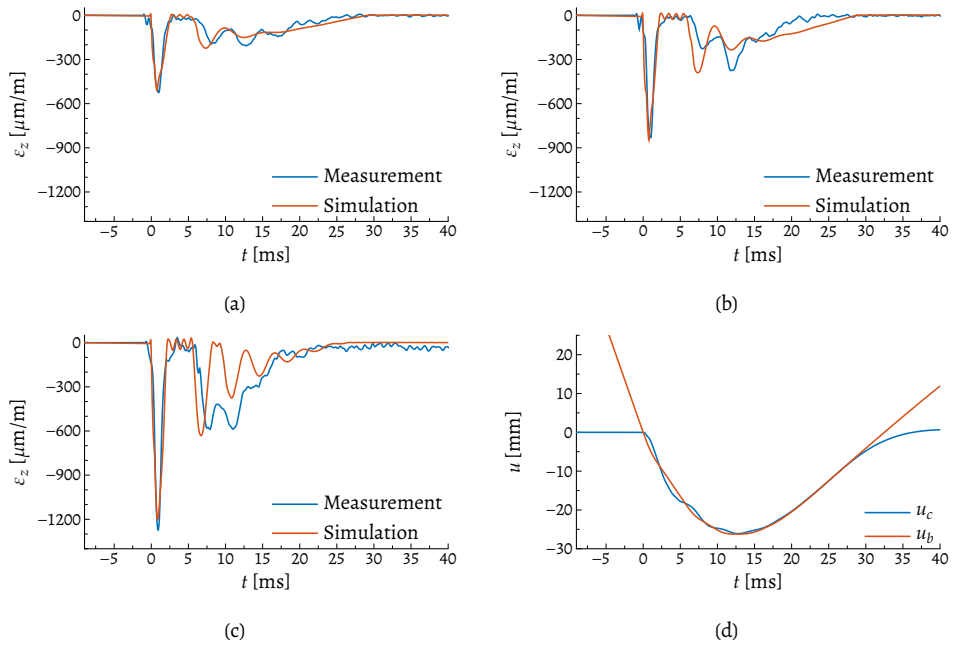


Figure 6.3: Mechanical quantities from a modelled impact with different drop heights ℓ . (a) Modelled and measured axial strain at $z = -200$ mm for $\ell = 500$ mm. (b) Modelled and measured axial strain at $z = -200$ mm for $\ell = 1000$ mm. (c) Modelled and measured axial strain at $z = -200$ mm for $\ell = 1500$ mm. (d) Simulated mean displacement of the cylinder u_c and modelled displacement of the impacting mass u_b for $\ell = 1500$ mm.

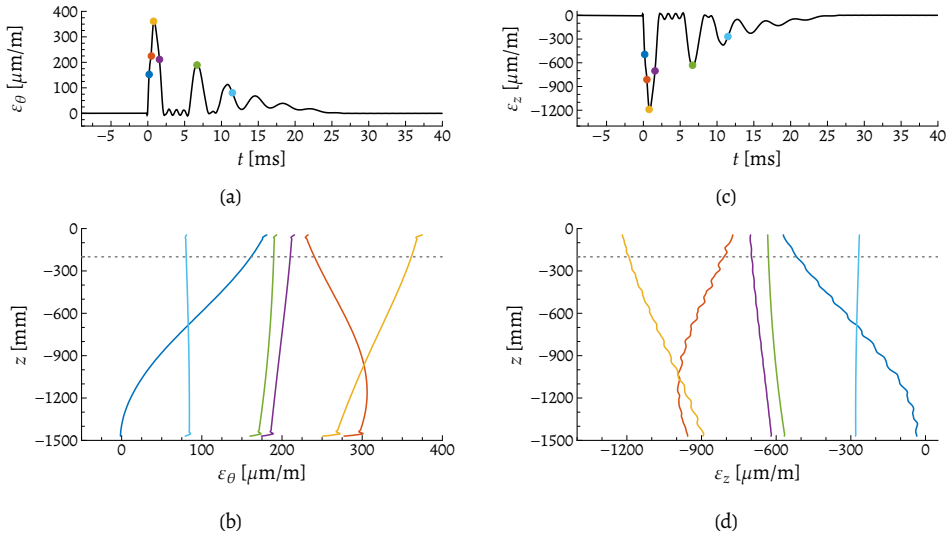


Figure 6.4: Simulated strain signals for an impact with $\ell = 1500$ mm. (a) Circumferential strain registered by a virtual strain gauge at $z = -200$ mm. (b) Spatial variation of the circumferential strain at selected time moments, in which the dashed grey line indicates the position of the virtual strain gauge. (c) Axial strain registered by a virtual strain gauge at $z = -200$ mm. (d) Spatial variation of the axial strain at selected time moments, in which the dashed grey line indicates the position of the virtual strain gauge.

length, indicated by the non-uniform variation of the strain along the z -axis—the wave front can be distinguished in that case.

The graphs in Figure 6.4 also indicate that the shape of the axial distribution of the circumferential strain is approximately identical to the one of the axial strain. This is not surprising, since the excited frequencies f are well below the ring frequency of the structure ($f_r = 4.2$ kHz). As seen in Section 2.3.2, the axial and circumferential strains are related by

$$\varepsilon_\theta = \frac{\nu}{\Omega^2 - 1} \varepsilon_z, \quad (6.8)$$

in which $\Omega = f/f_r$. Given that $f < 2$ kHz, it is easily verified that $\varepsilon_\theta \approx -\nu\varepsilon_z$, which is confirmed by comparing the amplitudes of the two strain signals. For this small value of Ω , the stress state in the cylinder is essentially uniaxial with only one non-zero component σ_z .

6.2. Analysis of the transient magnetic stray field

After examining the dynamic strain field, the focus is shifted to the effect of elastic deformations on the structure's magnetisation. Given the expected frequency content (identical to that of the induced strains, i.e. up to 2 kHz) and the anticipated amplitude of variation in the measured magnetic field (0.1–10 μT), an appropriate magnetometer is selected to capture the strain-induced stray field.

6.2.1. Sensor selection and positioning

As seen in Chapter 5, a triaxial fluxgate magnetometer is the optimal choice to measure the remanent magnetic stray field due to its high sensitivity. Unfortunately, the operating frequency range of this specific magnetometer type is restricted to 1 kHz. For the static remanent field, this is sufficient; but not for the dynamic signals, since a minimum sampling frequency of 4 kHz (twice the maximum frequency of interest) is required to prevent aliasing (Shin and Hammond, 2008).

A common magnetometer type that can be sampled with a tolerable rate relies on the Hall effect. Based on the graph displaying the sensitivities of different magnetometer types by Edelstein (2007), nonetheless, it is concluded that this type of sensor is also not suitable for the current purpose, because the lower limit of its sensitivity range coincides with the magnitude of the geomagnetic field. Given its apparent simplicity and sensitivity range, the next alternative is to employ a dedicated search coil in each orthogonal direction to capture the fluctuating magnetic field in the vicinity of the pile. However, such search coils are notoriously difficult to use as they have to be specifically designed for the magnitude of the magnetic field and frequency range of interest (Ripka, 2000, chap. 2). Hence, this type of magnetometer is discarded at this point.

In the end, the preferred magnetometer type is an Anisotropic Magnetoresistive (AMR) sensor, in which the electrical resistance of a material changes in the presence of an external magnetic field (Jogschies et al., 2015). The employed biaxial sensor (type: HMC1052L) has a measuring range of $\pm 600 \mu\text{T}$, a sensitivity of $20 \mu\text{T}/\text{mV}$ ($V_{\text{bridge}} = 5 \text{ V}$), and a noise density of $1 \text{ nT}/\sqrt{\text{Hz}}$ at 1 kHz. Most importantly, the magnetic field can be sampled at a sufficient rate due its bandwidth, which ranges from 0 to 5 MHz. Before the magnetic signal is recorded by a data acquisition system, the signal is amplified by a factor thousand. While a triaxial sensor would have provided a complete image of the transient components of the stray field, it proved difficult to acquire one within the time frame of the experiment. Consequently, a biaxial sensor has been selected that monitors the two dominant components of the magnetic stray field: the radial and axial components.

Both the strain and magnetic field are measured with a sampling rate $f_s = 50 \text{ kHz}$ using a 16-bit data acquisition system (*National Instruments* USB-6343). Given the required frequency range based on the frequency content of the strain signal, this might appear to be an unnecessary high rate. However, one must bear in mind that the frequencies excited by the impact were unknown before the experiment was conducted. Thus, the sampling rate has been selected with a large safety factor.

To fairly compare the strain and magnetic field signals, the magnetometer is placed at a distance $d = 20 \text{ mm}$ from the cylinder's surface in the same plane from the top of the cylinder as the classical strain gauges ($z = -200 \text{ mm}$). Given that the magnetisation induced in the cylinder by the horizontal component of the geomagnetic field is inhomogeneous (Section 4.5.5), two distinct sensor positions relative to the external field are considered. Figure 6.5 presents a top view of the cylinder with these positions: A at $\theta = 210^\circ$, in which

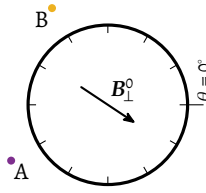


Figure 6.5: Top view of the cylinder indicating two positions of the AMR sensor relative to the direction of the horizontal component of the external magnetic field B_{\perp}^0 .

the measured radial component is perpendicular to the external field vector in the xy -plane; and B at $\theta = 120^\circ$, in which the radial component is approximately coaxial with the direction of external magnetic field. Simultaneous measurement of the strain-induced magnetic field changes at both locations is unfortunately not possible with the current set-up, as only a single AMR sensor is available for this experiment.

6.2.2. Processing the measured quantities

To simplify the analysis of the raw data, auxiliary magnetic quantities are defined. Furthermore, two mathematical tools which aid the analysis of the transient components of the stray field are introduced: namely, the normalised correlation coefficient (to quantify the similarity of two time signals) and the principle component analysis (to redefine the basis vectors of the dynamic components of the stray field based solely on the measured data).

Definition of auxiliary magnetic quantities

During the experiment, the AMR sensor at point p registers the total magnetic field $B_t(p, t)$, which can be decomposed into two separate fields as follows:

$$B_t(p, t) = B(p, t) + B_0, \quad (6.9)$$

in which $B(p, t)$ denotes the structure's magnetic stray field at point p and B_0 represents the time- and space-invariant external field. Since the cylinder does not experience an external mechanical load before it is impacted by the mass at $t = 0$, the remanent stray field \bar{B} prior to each impact is defined by

$$\bar{B} = B(p, 0). \quad (6.10)$$

Note that the remanent field is determined prior to each impact. As seen in Chapter 5, the remanent field can change during an impact, even if the induced strains remain in the elastic regime. By subtracting the remanent stray field from the time signal of the stray field, the magnetic variation is obtained:

$$\Delta B(p, t) = B(p, t) - \bar{B}. \quad (6.11)$$

This quantity provides the means to fairly compare magnetic signals with different remanent fields. Additionally, the magnetic variation is equal to zero at $t = 0$ conform the axial strain.

Normalised correlation coefficient

Since the goal of the dynamic experiment is to examine whether the magnetic stray field varies in correspondence with the induced strain, the similarity of the time signals of the strain and stray field components must be determined. To quantify this, the normalised cross-correlation coefficient is computed. For two real valued functions $u(t)$ and $v(t)$, the normalised correlation function is defined as (Shin and Hammond, 2008, pp. 227–229):

$$\rho_{uv}(t) = \frac{1}{\sqrt{E_u E_v}} \int_{-\infty}^{\infty} u(\tau - t) v(\tau) d\tau, \quad (6.12)$$

in which

$$E_u = \int_{-\infty}^{\infty} u(\tau)^2 d\tau, \quad E_v = \int_{-\infty}^{\infty} v(\tau)^2 d\tau, \quad (6.13)$$

are the expected values for the two functions. When the function $u(t)$ and $v(t)$ are only defined on a finite time interval, as is the case for the magnetic and strain signals, the integration limits are equal to the bounds of the chosen time interval. The normalised correlation function is a function of a time shift, and it takes a maximum value when the time-shifted version of $u(t)$ matches $v(t)$. Consequently, a useful parameter to quantify the correlation is the normalised correlation coefficient:

$$c_{uv} = \max(\|\rho_{uv}(t)\|). \quad (6.14)$$

When $c_{uv} = 1$, the signals are perfectly correlated; when the time series are completely dissimilar, $c_{uv} = 0$. If $u(t)$ and $v(t)$ are two distinct realisations of the same quantity, the resulting coefficient c_{uv} is normally referred to as the auto-correlation coefficient, while the term cross-correlation coefficient applies to comparing two realisations of different quantities. In case $u(t)$ and $v(t)$ are perfectly correlated, $u(t) = \alpha v(t)$, i.e. $v(t)$ is a scaled version of $u(t)$, and α is a scalar proportionality constant. The latter incorporates the sign difference between the amplitudes of the signals, hence the absolute value of $\rho_{uv}(t)$ suffices in Equation (6.14). Note that, in case $c_{uv} = 1$, the two signals have an identical frequency content as well, since they only differ in amplitude.

Principle component analysis

The biaxial magnetometer registers the radial and axial component of the stray field, i.e. B_r and B_z , respectively. However, it is unlikely that the variability of the strain-induced stray field is solely directed along one of these two directions. Hence, the strain should be analysed in relation to both stray field components. To simplify this comparison, the magnetic signal is projected onto its principle axes. Given the two measured components, the principle

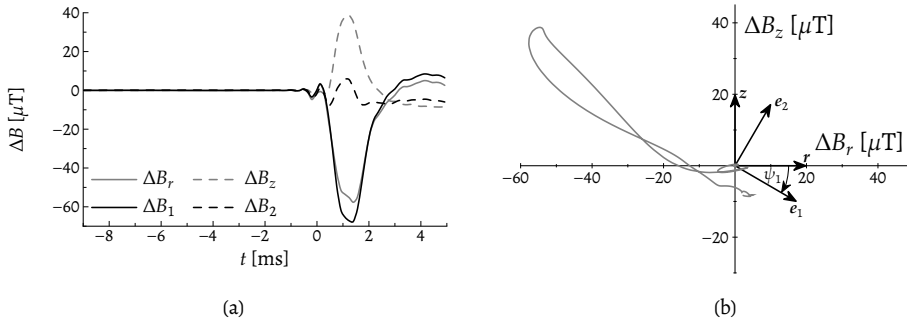


Figure 6.6: Magnetic variation ΔB induced by the primary strain pulse generated by an impact with $\ell = 1500$ mm. (a) Time signals of the measured components ΔB_r and ΔB_z , and the components along the principle axes ΔB_1 and ΔB_2 . (b) Vector space representation in which r and z denote the unit vectors of the respective measured radial and axial components of ΔB . Unit vectors e_1 and e_2 are directed along the major and minor principle axis, respectively. ψ_1 represents the angle between e_1 and the $r\theta$ -plane.

components decomposition of the magnetic variation $\Delta B(t)$ is as follows:

$$\Delta B(t) = \Delta B_r(t) \mathbf{r} + \Delta B_z(t) \mathbf{z} = \Delta B_1(t) \mathbf{e}_1 + \Delta B_2(t) \mathbf{e}_2, \quad (6.15)$$

in which \mathbf{r} , \mathbf{z} , \mathbf{e}_1 and \mathbf{e}_2 represent the unit vectors along the radial, the axial, the major principle and the minor principle axes, respectively. Along each of these directions, $\Delta B_r(t)$, $\Delta B_z(t)$, $\Delta B_1(t)$ and $\Delta B_2(t)$ denote the respective variations of the stray field.

To illustrate the decomposition, Figure 6.6b shows $\Delta B(t)$ induced by the primary strain pulse measured during an impact with $\ell = 1500$ mm in the vector space spanned by \mathbf{r} and \mathbf{z} . Figure 6.6a presents the corresponding components in the time domain. It is easily verified that the maximum variability is directed along the major principle axis \mathbf{e}_1 , which is the essence of the principle component analysis (PCA) (Jolliffe and Cadima, 2016). Thus, by re-expressing the dynamic stray field along the principle axes, only the first principle component has to be considered to analyse the dynamic magnetomechanical response of the structure. Next to the dimensional reduction of the data, the PCA removes the aforementioned ambiguity regarding the orientation of the transient stray field. The latter is unknown a priori; nevertheless, it is expected to spatially vary in conjunction with the remanent magnetisation of the structure. As the PCA is completely data driven (Jolliffe and Cadima, 2016), it provides an objective way to extract a single magnetic variable that captures the desired dynamic response regardless of the dominant measured component.

The necessity to consider the principle components of $\Delta B(t)$ in the first place accentuates the novelty of the present experimental set-up with respect to those reported in literature (Belahcen et al., 2014; Hecker and Schulz, 1997; Hubert and Rizzo, 2008; Kim et al., 2003; Lolloioz et al., 2006; Peussa and Belahcen, 2015). Since these experiments concern the impact-induced dynamical magnetomechanical response of a small-diameter steel rod, all relevant physical quantities—strain, external magnetic field, magnetisation and stray

field—are coaxial and oriented along the rod's axis, i.e. they are essentially one-dimensional. In that case, the major principle axis coincides with the axis of the rod, and the measured quantities can be directly compared. However, in the current experiment, the stray field of the cylinder exhibits a considerable spatial variation (Chapter 5), creating the need to redefine the magnetic signals along the dominant axis. Fortunately, the strain tensor is fully defined by a single component due to the fact that the excited frequencies are relatively low compared to the ring frequency of the structure (Section 6.1.3). Consequently, the first principle component of the strain ε_1 is directly proportional to the axial strain ε_z , and it suffices to consider the axial strain itself to characterise the impact-induced strain. Thus, in this case, the PCA provides a way to fairly compare the dynamic stray field to the strains, by analysing these time signals along their major principle axis.

6.2.3. Evolution of the stray field towards a magnetic equilibrium

In Chapter 5, it was shown that the measured remanent stray field of a structure approaches a magnetic equilibrium after a few consecutive identical impacts (Figure 5.6). Naturally, the structure's magnetisation does not reach this equilibrium in a discontinuous fashion, rather, it moves along with the strain when that quantity reaches a new peak value. The time resolution of the AMR sensor enables one to resolve this evolution in time. Figure 6.7 shows the time series of the strain and the radial component of the stray field during the first three impacts from $\ell = 500$ mm after an initial magnetic state—state B (Chapter 5)—has been established, which opposes the geomagnetic field. The presented signals have been filtered with a low-pass filter with a cut-off frequency of 2 kHz, since most energy is contained below this value. In the figure, the colours indicate the three consecutive impacts; the solid lines designate the primary strain pulse; and the dashed-dotted lines represent the secondary strain pulse.

From the time trace of the radial component of the magnetic stray field, it is clear that primary strain pulse induced by the first impact leads to the largest irreversible change in the stray field and thus in the structure's magnetisation. Subsequent impacts slightly alter the remanent field, but it undoubtedly tends towards an equilibrium. Note that a careful analysis of high-speed images of the impact reveals that there is minor relative motion of the cylinder with respect to the sensor, for which the presented data are not corrected, since the mean displacement of the cylinder is not measured by independent means. The relative movement might explain the difference in the remanent stray field as measured directly before and after the primary strain pulse during the third impact (solid yellow line). If the cylinder is stationary with respect to the magnetic sensor, the stray field directly after the primary strain pulse should have been equal to the remanent value just before the impact. Since this is not the case, it is clear that the cylinder has moved with respect to the sensor. This relative movement is only temporary, as it is caused by the mean displacement of the cylinder along the z-axis (Figure 6.3d).

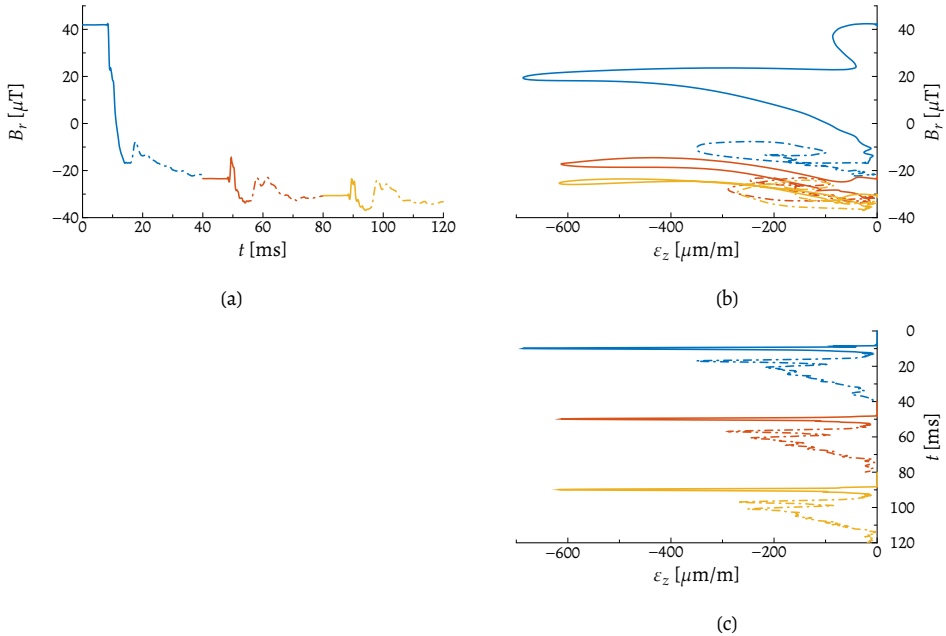


Figure 6.7: The evolution of the radial component of the magnetic stray field for three consecutive impacts with $\ell = 500 \text{ mm}$ measured at position B ($\theta = 120^\circ$). The solid and dashed-dotted lines denote the primary and secondary strain pulse, respectively. (a) Time series of the radial component. (b) The radial component versus strain. (c) Time series of the strain.

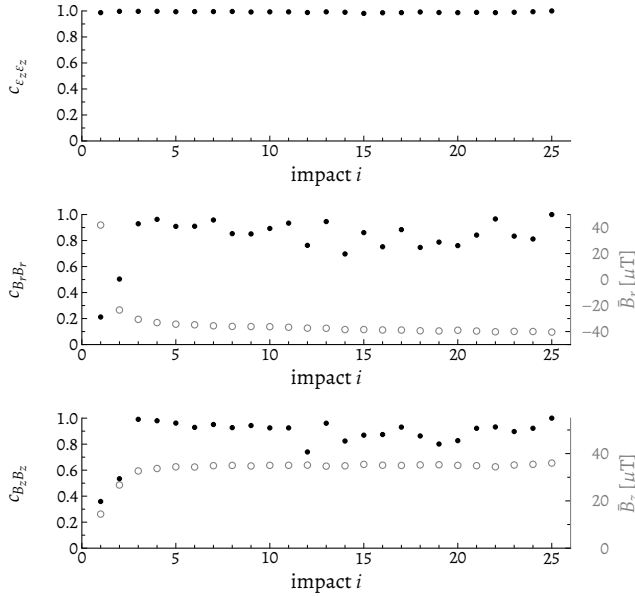


Figure 6.8: Auto-correlation of the measured signals during 25 consecutive impacts from $\ell = 500$ mm. For each signal, the correlation is computed with respect to the signal of that quantity measured during impact 25.

6

6.2.4. Consistency of the measured signals

With the magnetisation at an equilibrium, the question remains whether the obtained signals become reproducible for successive impacts from identical height. To address this, the auto-correlation coefficients for the three measured quantities (strain and two stray field components) are determined for 25 consecutive impacts from $\ell = 500$ mm with impact 25 as the reference event. Hence, the auto-correlation coefficients are equal to one by definition for impact 25. Figure 6.8 shows the calculated coefficients (black dots) in conjunction with the radial component of the remanent stray field \bar{B}_r prior to each impact (grey circles). In this figure, impacts 1–3 correspond to the three impacts discussed in the previous section (Figure 6.7).

From the top graph of Figure 6.8, it is clear that the strain signals for the consecutive impacts are almost identical, since the normalised auto-correlation coefficient $c_{\epsilon_z \epsilon_z}$ is close to one. On the contrary, the correlation coefficients for the stray field components show different behaviour for the first two impacts, where the correlation coefficients are 0.5 or lower. From impact 3 onwards, the auto-correlation becomes close to unity, indicating that the magnetic stray field components are almost proportional to the reference signal. In the same graphs, the remanent magnetic field shows that the magnetisation reaches an equilibrium after impact 2. Thus, when the magnetisation is at an equilibrium, the subsequent impacts display reproducible behaviour, signalling that the magnetisation induced by elastic strain is then fully reversible.

Table 6.3: The six selected impacts with three different impact heights ℓ and two circumferential sensor locations θ .

Impact	ℓ [mm]	θ [°]
1A	500	210
2A	1000	210
3A	1500	210
1B	500	120
2B	1000	120
3B	1500	120

6.2.5. Influence of impact height and sensor position

In this section, the influence of increasing the impact height and varying the sensor position is analysed by selecting a representative impact for each possible combination of parameters. To this end, for each sensor position, three impacts with increasing impact heights, which yield solely elastic strains, have been selected, which are listed in Table 6.3. Figure 6.9 presents the measured quantities for the selected impacts. Based on the data, the following observations are made:

- (i) The magnitude of the compressive strain increases for more energetic impacts. Visual comparison of the lines suggests that the frequency content of the impact-induced strains is similar for each impact height. This assertion is confirmed by the normalised correlation coefficients for the axial strain, which are close to unity (Tables 6.4a and 6.4b for the primary and secondary pulse, respectively).
- (ii) When the measured radial component is perpendicular to the external field (position A, $\theta = 210^\circ$), the magnetic deviations ΔB_r and ΔB_z (Figure 6.9a) indicate that their amplitudes increase with increasing impact height during the primary strain pulse. However, for this location, the response to the secondary strain pulse is less pronounced in the magnetic stray field.
- (iii) At position B ($\theta = 120^\circ$), in which B_r is parallel to the external field vector, the transient stray field shows both impact-induced pulses (Figure 6.9b), albeit that the amplitude of the radial component ΔB_r during the primary strain pulse is lower than during the secondary strain pulse. The axial component ΔB_z displays remarkable behaviour: for $\ell = 500$ mm, the deviation during the primary strain pulse is positive, while it is negative for the secondary pulse.

Figure 6.10 provides a shift of perspective on the transient behaviour of the magnetic stray field by presenting the components in the measured vector space. For clarity, the full signals are split into separate figures for the two pulses and the two circumferential positions. At position A, amplitude of the stray field during the primary pulse (Figure 6.10a) increases, although the difference between impact 2A and 3A is small. Moreover, the angle of the major principle axis ψ_1 is approximately constant. For the secondary pulse (Figure 6.10b), the stray field's behaviour is not as pronounced as for the primary pulse. The corresponding

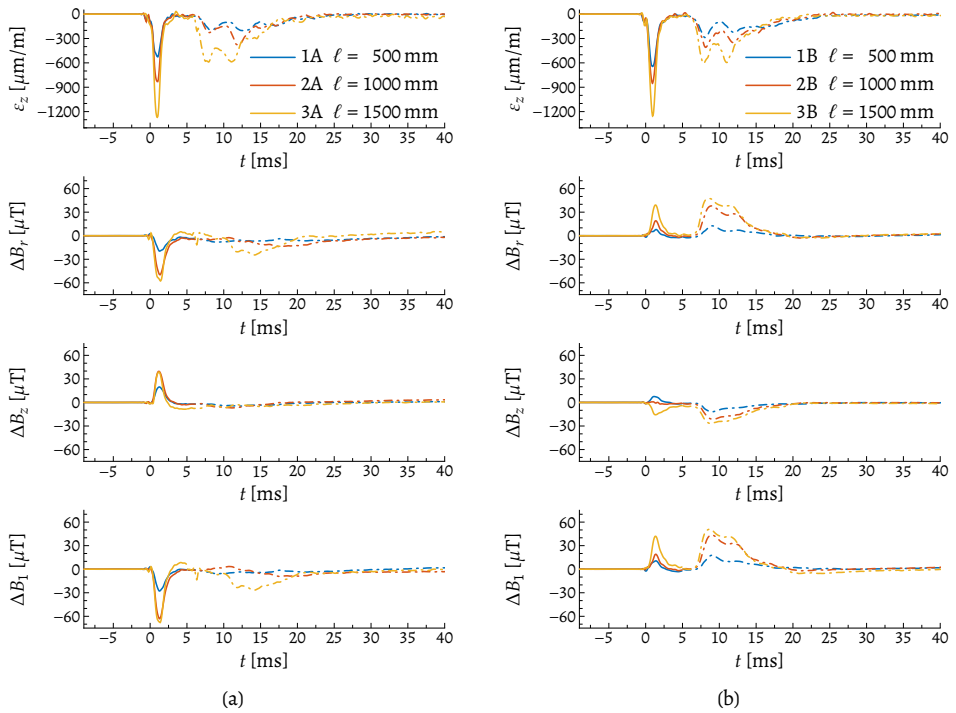


Figure 6.9: Time series for the measured axial strain ε_z and magnetic stray variation $\Delta B(t)$ for increasing impact height ℓ . Solid and dashed-dotted lines represent the primary and second pulse, respectively. (a) AMR sensor at position A ($\theta = 210^\circ$). (b) AMR sensor at position B ($\theta = 120^\circ$).

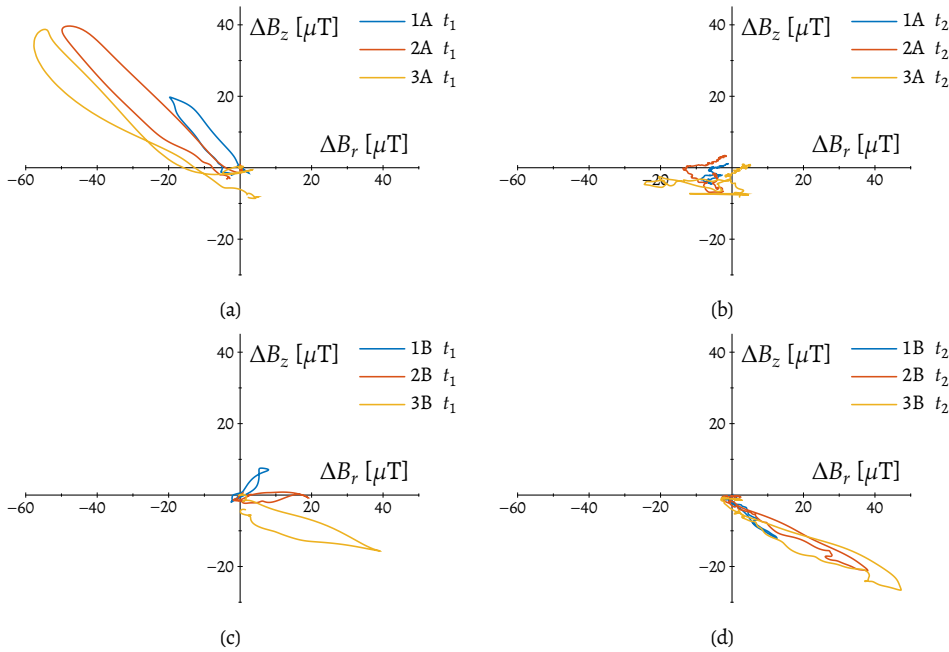


Figure 6.10: Vector space representation of the stray field variation ΔB of the six impacts. (a) ΔB induced by the primary strain pulse at position A. (b) ΔB induced by the secondary strain pulse at position A. (c) ΔB induced by the primary strain pulse at position B. (d) ΔB induced by the secondary strain pulse at position B.

variation in the principle axis ΔB_1 is shown in the lower graph of Figure 6.9a. Note that ψ_1 differs for the primary and secondary pulse. At position B, the stray field during the primary pulse (Figure 6.10c) exhibits an increase in amplitude and a rotation of the major principle axis with more energetic impacts. On the contrary, for the secondary pulse (Figure 6.10d), ψ_1 remains constant. The lower graph of Figure 6.9b presents the major principle component of the dynamic magnetic response.

By considering the transient stray field in principle components, Tables 6.4c and 6.4d quantify the correspondence between these signals for the selected impacts for the primary and secondary pulses, respectively. Similar to the graphical representation in Figure 6.9, the coefficients for the primary pulse imply that the shape of the signals remains identical with an increase of the impact height or change in sensor position ($c_{B_1 B_1} \approx 1$). However, for the secondary pulse, the correlation between corresponding impact heights for the two sensor locations (the nine entries in the top right of Table 6.4d) is less ($c_{B_1 B_1} \approx 0.8$). Visually, this difference is shown in Figure 6.11, where the measured quantities for an impact with $\ell = 1500$ mm at position A and B are superimposed. A noticeable feature of the magnetomechanical response is that the sign of each component of the transient magnetic stray field is opposite for sensors positioned at a 90° angle from each other.

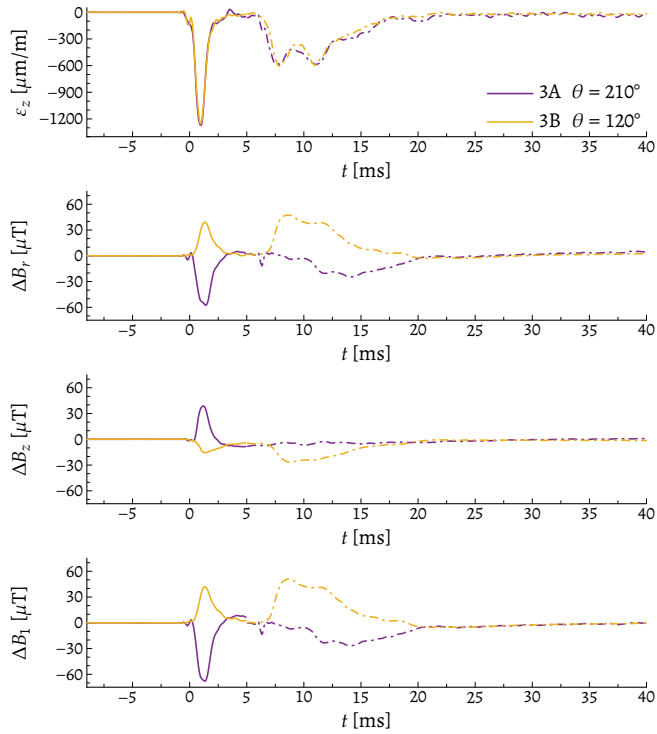


Figure 6.11: Magnetomechanical response to two impacts from $\ell = 1500$ mm measured at different circumferential sensor positions. Solid and dashed-dotted lines represent the primary and secondary pulse, respectively.

Table 6.4: Normalised correlation coefficients for the six selected impacts. (a) Axial strain during the primary pulse. (b) Axial strain during the secondary pulse. (c) Major principle component of the magnetic stray field for the primary pulse. (d) Major principle component of the magnetic stray field for the secondary pulse.

(a)							(b)						
$c_{\varepsilon_z \varepsilon_z}$	1A	2A	3A	1B	2B	3B	$c_{\varepsilon_z \varepsilon_z}$	1A	2A	3A	1B	2B	3B
1A	1	0.99	0.98	0.99	0.99	0.99	1A	1	0.96	0.92	0.98	0.96	0.90
2A		1	1.00	0.99	0.99	0.99	2A		1	0.95	0.94	0.97	0.94
3A			1	0.99	0.99	1.00	3A			1	0.92	0.98	0.99
1B				1	1.00	0.99	1B				1	0.96	0.90
2B					1	1.00	2B					1	0.97
3B						1	3B						1

(c)							(d)						
$c_{B_1 B_1}$	1A	2A	3A	1B	2B	3B	$c_{B_1 B_1}$	1A	2A	3A	1B	2B	3B
1A	1	1.00	0.97	0.91	0.98	0.99	1A	1	0.92	0.89	0.80	0.75	0.69
2A		1	0.97	0.91	0.98	0.99	2A		1	0.91	0.82	0.79	0.71
3A			1	0.97	0.98	0.95	3A			1	0.93	0.93	0.90
1B				1	0.94	0.88	1B				1	0.98	0.94
2B					1	0.97	2B					1	0.99
3B						1	3B						1

To check the correspondence between the strain and the stray field during each impact, the cross-correlation coefficients $c_{\varepsilon_z B_1}$ are computed and presented in Figure 6.12. For the primary pulse (Figure 6.12a), the cross-correlation coefficients are almost one, indicating that the impacts excite the same frequencies in the strain and the stray field signals. Note that the angle ψ_1 is not identical for the impacts, which signals that relative importance of the two measured stray field component (B_r and B_z) varies with impact height and circumferential sensor position. For the secondary pulse (Figure 6.12b), the similarity between the strain and the stray field signals is slightly less $c_{\varepsilon_z B_1} > 0.8$. Moreover, the value of ψ_1 fluctuates for each test, especially at position A, which reflects the change of the dominant measured stray field component.

6.2.6. Discussion

As seen from the presented data, the magnetomechanical response of the cylinder becomes consistent when the structure's magnetisation has attained a magnetic equilibrium, which is the case after the application of a few identical impacts. The fact that the magnetisation is at an equilibrium implies that no irreversible domain wall motions occur due to the induced elastic strains. Hence, the observed strain-induced transient stray field results from a fully reversible magnetic process. For the weak magnetic field under consideration, a realistic candidate for this reversible mechanism is the bulging of the domain walls under strain.

Next to being reversible, the magnetic response shows a distinct spatial variation; i.e. depending on the measurement point, the sign of the dynamic stray field is either positive

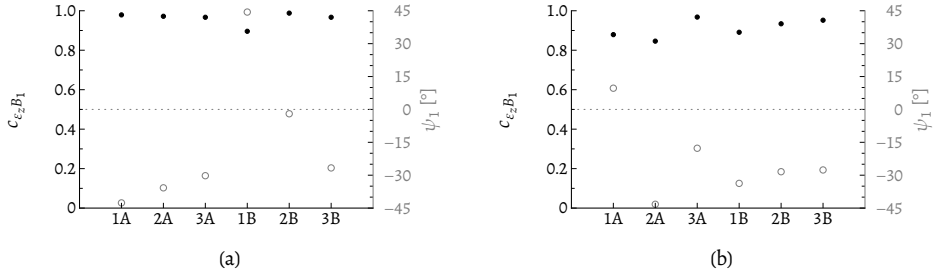


Figure 6.12: Cross-correlation coefficients between the axial strain and the major principle component for the six impacts in conjunction with the angle of the major principle axis ψ_1 . (a) Coefficients for the primary pulse. (b) Coefficients for the secondary pulse.

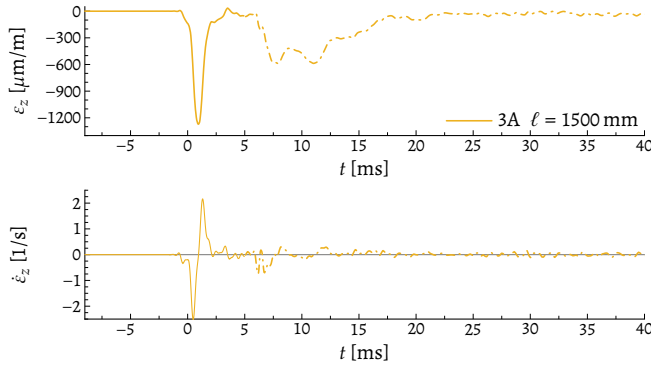


Figure 6.13: Measured strain signal ε_z and computed strain rate $\dot{\varepsilon}_z$ for impact 3A ($\ell = 1500$ mm).

or negative. This is illustrated by the graphs in Figure 6.11, which presents the magnetomechanical data for two sensors that are placed 90° apart. Assuming that the induced strain field is essentially axially symmetric, the observed stray field variations must result from the inhomogeneous magnetisation distribution caused by the non-local magnetic interaction of the structure's geometry (i.e. the demagnetising field), which, in turn, is a result of the horizontal component of the external field B_\perp^0 .

Further analysis of the magnetic response shows that the amplitude ratio between the magnetisation changes caused by the primary and the secondary strain pulses differs from the amplitude ratio of the strain signals itself. This disagreement might be attributed to the sustained strain rate during each pulse, of which the influence on the magnetomechanical effect remains obscured (Section 4.2.5). Figure 6.13 shows the measured axial strain and computed strain rate $\dot{\varepsilon}$ (the dot denotes the time derivative) of impact 3A. During the primary strain pulse (solid lines), the magnitude of the strain rate is 2 s^{-1} , while significantly lower values are recorded throughout the secondary strain pulse (dashed-dotted lines). Given that measured transient stray field does not exhibit any of the characteristics of the strain rate, this does not appear to be the most probable explanation for the observed

differences. Another, more plausible, reason for the disparity of the amplitude ratios is that the magnetomechanical coupling is non-linear in relation to the applied strain.

The normalised cross-correlation coefficients for the magnetic stray field measurements and the strain (Figure 6.12) are nearly one for the primary and the secondary pulse, which implies that one could relate the two quantities by means of a scalar coefficient. Once this proportionality constant is determined by applying a calibration procedure, the strain generated by subsequent impacts could simply be inferred by multiplying the recorded stray field with the identified coefficient. However, given the variation in ψ_1 between the pulses and the sensor positions, a proportionality coefficient is required for each pulse as well as each sensor position. In fact, constructing such an empirical relation between the stray field and the strain obscures the physical processes that govern the magnetomechanical response of the structure to an impact. An accurate magnetomechanical model can resolve this problem by describing the relation between the strain field and the magnetisation.

6.3. Modelling the strain-induced transient magnetisation

In the previous section, the necessity for an accurate magnetomechanical model has been highlighted. To simplify this complex task, only the reversible strain-induced magnetisation is considered. This implies that the magnetisation is assumed to be at a metastable equilibrium, which, in turn, is taken to be close to the anhysteretic magnetisation. Furthermore, attention is placed on a rate-independent model, since it is questionable whether the strain rate affects the magnetic behaviour under the current loading conditions. Most importantly, the proposed model must account for the tensorial nature of the physical quantities involved, which is, to the best of the author's knowledge, not considered in magnetomechanical models that describe the magnetisation of a steel structure subjected to dynamic mechanical loads. The tensorial nature is twofold: First, the magnetisation is a spatially-varying first-order tensor field. Second, strain is a second-order tensor—albeit that in the described experiment, it is fully determined by only one independent component, ε_z . Consequently, the common assumption that the loading direction, external field and magnetisation are coaxial, is not justified in this more complex geometry.

Here, the main challenge is to develop a magnetomechanical model to describe the reversible strain-induced magnetisation that is applicable to a polycrystalline material, while accounting for the spatial variation of the magnetisation and strain tensors. As the structure's magnetisation is not directly measurable, the computed transient magnetisation is translated to the stray field at the sensor position using the framework introduced in Chapter 4.

6.3.1. Vectorial effective field for an isotropic magnetoelastic solid subjected to uniaxial stress

After a few repeated impacts, the structure's magnetisation reaches a magnetic equilibrium, and subsequent impacts only induce reversible variations in the magnetisation—i.e. the remanent magnetisation is not altered. The law of approach (Jiles, 1995) states that the magnetisation of a material tends towards the global—anhysteretic—magnetic state due to external straining. As the name implies, this ideal magnetic state does not display hysteresis, i.e. it is fully reversible. Thus, this state is a convenient starting point to derive a magnetomechanical model for the reversible strain-induced magnetisation changes.

To recapitulate, in an isotropic solid, the anhysteretic magnetisation for a weak effective field is (Equation (4.11))

$$\mathbf{M}_{\text{an}} = \frac{M_s}{3a} \mathbf{H}_e, \quad (6.16)$$

in which M_s is the saturation magnetisation, and a is a model parameter. Since the effective field is derived from the free energy density, the definition of the latter (Equation (4.6)) is adapted accordingly to accommodate the physical quantities in tensorial form:

$$A = \frac{1}{2} \alpha \mu_0 \mathbf{M} \cdot \mathbf{M} - TS + \mu_0 \mathbf{H} \cdot \mathbf{M} + E_{\text{me}}, \quad (6.17)$$

in which μ_0 is the magnetic constant, T represents the absolute temperature, S is the entropy, E_{me} is the magnetoelastic energy, and α denotes a coupling coefficient. Subsequently, by taking the derivative of A with respect to the magnetisation \mathbf{M} while keeping the temperature constant, the effective field vector is obtained:

$$\mathbf{H}_e = \frac{1}{\mu_0} \left(\frac{\partial A}{\partial \mathbf{M}} \right)_T = \mathbf{H} + \alpha \mathbf{M} + \frac{1}{\mu_0} \left(\frac{\partial E_{\text{me}}}{\partial \mathbf{M}} \right)_T. \quad (6.18)$$

where the latter term is the so-called stress-induced effective field vector:

$$\mathbf{H}_\sigma = \frac{1}{\mu_0} \left(\frac{\partial E_{\text{me}}}{\partial \mathbf{M}} \right)_T. \quad (6.19)$$

One can easily verify that these expressions reduce to the scalar relation in Equation (4.16), when the magnetisation and external field are coaxial.

Magnetoelastic energy

So far, the magnetoelastic energy has not been specified in this chapter, even though this quantity governs the strain-induced changes of the magnetisation. In the general case, this energy density is (Daniel and Hubert, 2009)

$$E_{\text{me}} = \boldsymbol{\sigma} : \boldsymbol{\varepsilon}^{\mu}, \quad (6.20)$$

where σ is the stress tensor, ε^H represents the magnetostrictive strain tensor, and the colon denotes the double contraction of the second order tensors. Note that the applied stress is easily expressed in terms of the applied strain by using the proper mechanical constitutive equation, as only elastic deformation is considered here. Assuming that the magnetostriction is isotropic and isochoric, i.e. the material's volume is preserved, the magnetostrictive strain tensor is (Federico et al., 2019):

$$\varepsilon^H = \frac{3}{2}\lambda \left(\mathbf{m} \otimes \mathbf{m} - \frac{1}{3}\mathbf{I} \right) \quad (6.21)$$

in which $\mathbf{m} = \mathbf{M}/M$ is a unit vector in the magnetisation direction with $M = \|\mathbf{M}\|$, \otimes denotes the dyadic product, \mathbf{I} is the second order identity tensor, and λ represents the scalar magnetostriction coefficient. Substituting Equations (6.20) and (6.21) into Equation (6.19), the stress-induced effective field yields:

$$\mathbf{H}_\sigma = \frac{3}{2\mu_0} \frac{\partial \lambda}{\partial M} \left(\sigma : \left[\mathbf{m} \otimes \mathbf{m} - \frac{1}{3}\mathbf{I} \right] \right) + \frac{3}{\mu_0} \frac{\lambda}{M} (\mathbf{m} \cdot \sigma \cdot [\mathbf{I} - \mathbf{m} \otimes \mathbf{m}]). \quad (6.22)$$

The latter term on the right-hand side is proportional to the component of the traction $T = \sigma \cdot \mathbf{m}$ that is perpendicular to \mathbf{m} , while the former is proportional to the magnitude of the normal stress in the direction of \mathbf{m} .

Uniaxial stress state

No assumptions have been made yet about the nature of the stress tensor. Provided that in the described experiment only frequencies below the ring frequency are excited, the stress state is essentially uniaxial. By means of a spectral decomposition of the stress tensor (Itskov, 2019, pp. 111–113), a uniaxial stress with magnitude σ_0 can be expressed as:

$$\sigma = \sigma_0 \mathbf{n} \otimes \mathbf{n}, \quad (6.23)$$

in which \mathbf{n} is the unit vector in the direction of the applied stress.* Substituting this expression into Equation (6.22) and applying the identity $\mathbf{n} \cdot \mathbf{m} = \cos \varphi$ leads to the following expression for the stress-induced effective field vector:

$$\mathbf{H}_\sigma = \frac{3\sigma_0}{2\mu_0} \left[\frac{\partial \lambda}{\partial M} \left(\cos^2 \varphi - \frac{1}{3} \right) + 2 \frac{\lambda}{M} (\cos \varphi \mathbf{n} - \cos^2 \varphi \mathbf{m}) \right], \quad (6.24)$$

*Another commonly encountered stress state is hydrostatic stress, for which the stress tensor simply reads

$$\sigma = \sigma_0 \mathbf{I}.$$

By substituting this form into Equation (6.22), it is clear that $\mathbf{H}_\sigma = \mathbf{0}$, indicating that hydrostatic stress does not contribute to the magnetomechanical effect when the magnetostriction is isotropic and isochoric, see Daniel (2013) and Sablik et al. (1994).

in which φ is the angle between the magnetisation and the uniaxial stress. In case the effective field and the magnetisation are assumed to be coaxial, an expression for an effective stress is derived based on the relation above in Appendix C, comparing this new effective stress formulation to a commonly used alternative expression.

Scalar magnetostriction coefficient

For an isotropic polycrystalline material, the scalar magnetostriction coefficient in Equation (6.24) is not a material constant, but rather a structure-sensitive parameter (Cullity, 1971). Additionally, it depends on the magnetisation and stress. Hence, in the coaxial case, the following model is commonly employed (Jiles, 1995):

$$\lambda = \sum_{i=1}^{\infty} (\gamma_i + \sigma \gamma'_i) M^{2i}, \quad (6.25)$$

in which γ_i and γ'_i are model constants, and σ is the applied uniaxial stress. Based on current literature, the value of the latter is ambiguous when the stress is not aligned with the magnetisation. To account for the three-dimensional nature of the quantities involved, the following model for the magnetostriction coefficient is proposed:

$$\lambda = \sum_{i=1}^{\infty} \gamma_i (\mathbf{M} \cdot \mathbf{M})^i + \gamma'_i (\mathbf{M} \cdot \boldsymbol{\sigma} \cdot \mathbf{M})^i, \quad (6.26)$$

which reduces to the uniaxial expression, when the magnetisation and the uniaxial stress are coaxial, and only $i = 1$ is considered. By substituting the uniaxial stress tensor (Equation (6.23)), the former expression is rewritten as

$$\lambda = \sum_{i=1}^{\infty} \gamma_i (M^2)^i + \gamma'_i (\sigma_0 \cos^2 \varphi M^2)^i. \quad (6.27)$$

This expression naturally resolves the ambiguity of the stress value by explicitly stating the angle between the uniaxial stress and the magnetisation.

Analysis of the effective field vector

In the following, the higher order components of the magnetostriction model ($i > 1$) are discarded for simplicity. Then, substitution of Equation (6.27) into Equation (6.24) yields the following stress-induced effective field:

$$\begin{aligned} \mathbf{H}_\sigma = \frac{3\sigma_0 M}{\mu_0} & \left[\gamma_1 \left(\cos \varphi \mathbf{n} - \frac{1}{3} \mathbf{m} \right) \right. \\ & \left. + \gamma'_1 \sigma_0 \left(\left(2 \cos^3 \varphi - \frac{1}{3} \cos \varphi \right) \mathbf{n} - \cos^4 \varphi \mathbf{m} \right) \right], \end{aligned} \quad (6.28)$$

which is a quadratic function of the applied uniaxial stress. The formulation above reflects two characteristics of the magnetomechanical effect. First, when no stress is present ($\sigma_0 = 0$), the stress-induced effective field is zero. Second, in the absence of magnetisation ($M = 0$), stress alone cannot generate an effective field and reciprocally induce magnetisation.

In Equation (6.28), the stress-induced effective field has components that are aligned with the magnetisation and with the stress. The behaviour of this expression for varying φ is analysed by letting $\mathbf{n} = [\cos \varphi \ \sin \varphi]^T$ and $\mathbf{m} = [1 \ 0]^T$, which represents the vector quantities in two dimensions to aid the visualisation. Figure 6.14 shows the components of \mathbf{H}_σ parallel (\parallel) and perpendicular (\perp) to \mathbf{m} resulting from a tensile stress applied along \mathbf{n} for $\varphi = -\pi/2 \dots \pi/2$. This range covers the complete spectrum of possible angles, since larger angles correspond to the application of a compressive stress along a line with $\varphi \pm \pi$. Figure 6.14a shows the individual behaviour of the components that are proportional to γ_1 , and Figure 6.14b maps those components onto the two-dimensional plane. Figure 6.14c and Figure 6.14d display the same for components proportional to γ'_1 . In case the magnetisation and the stress are coaxial ($\varphi = 0$), the effective field naturally only has a component in that direction. When the stress is applied perpendicular to the magnetisation ($\varphi = \pm\pi/2$), all terms vanish except $-\gamma_1/3 \mathbf{m}$, which results from the isochoric nature of the selected magnetostrictive strain tensor. For intermediate angles, the effective field has a component perpendicular to the magnetisation, of which the largest contribution occurs when the stress is applied at an acute angle of $\pi/4$ (proportional to γ_1) or smaller (proportional to γ'_1). In the latter case, the contributions diminish quickly for larger angles. All in all, this indicates that the effective field is anisotropic due to the stress (stress-induced anisotropy), which is a direct consequence of the introduction of a preferred direction by the uniaxial stress.

6.3.2. Computation of the impact-induced transient stray field

With the derived vectorial description of the effective field, the strain-induced magnetisation can be simulated. To this end, conform the procedure outlined in Section 4.5, the structure is discretised in N_θ and N_z elements in the circumferential and axial direction, respectively; the total number of element is $N = N_\theta N_z$. In each element, the magnetisation is assumed to be constant and concentrated at the element's barycentre \mathbf{r}_i . Due to the small wall thickness in comparison to the other dimensions, the radial component of the magnetisation is assumed negligible. Consequently, each element has two non-zero magnetisation components: M_θ and M_z , which are the circumferential and the axial magnetisation, respectively. Collecting these unknown components for all elements yields the magnetisation vector $\mathbf{M}(t)$ with $2N$ entries. Assuming the transient magnetisation is proportional to the effective field vector $\mathbf{H}_e(t)$, the following constitutive equation is employed:

$$\mathbf{M}(t) = \chi \mathbf{H}_e(t), \quad (6.29)$$

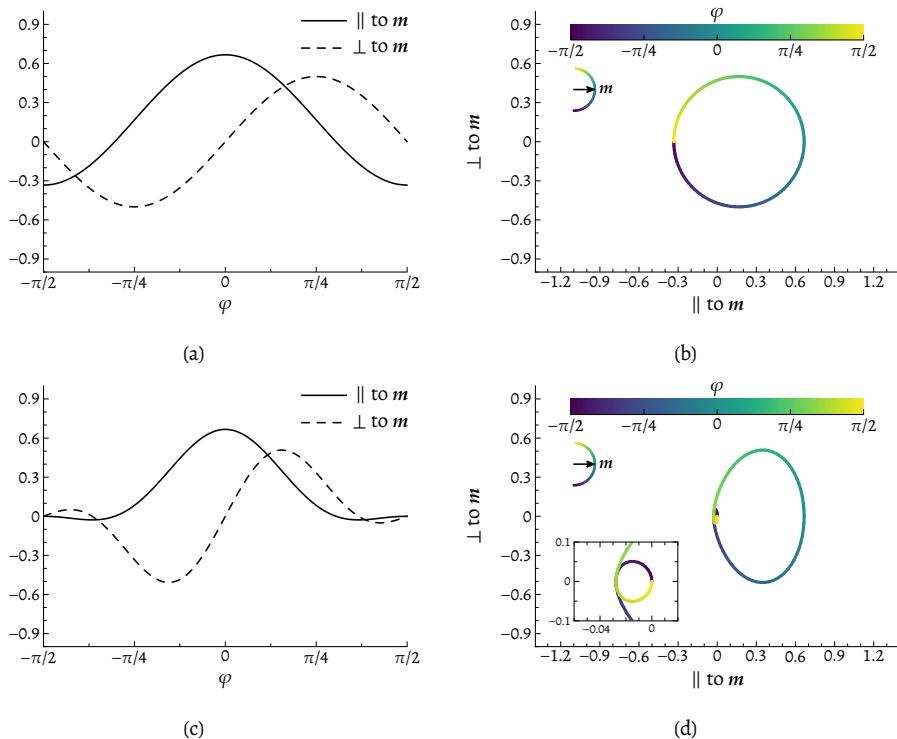


Figure 6.14: Variation of the coefficients in the stress-induced effective field given by Equation (6.28). (a) & (b) Components proportional to γ_1 . (c) & (d) Components proportional to γ'_1 . The inset graph shows a close-up of the behaviour near the origin.

Table 6.5: Parameters to model the dynamic magnetic response of a cylinder impacted by a free-falling mass.

Parameter	Value	Parameter	Value	Remark
N_θ	64	α	0 A/m	
N_z	80	γ_1	$2.0 \cdot 10^{-18} \text{ A}^{-2} \text{ m}^2$	Jiles (1995)
χ	900	γ'_1	$-1.5 \cdot 10^{-26} \text{ A}^{-2} \text{ m}^2 \text{ Pa}^{-1}$	Jiles (1995)

in which χ is a scalar magnetic susceptibility and

$$\mathbf{H}_e(t) = \mathbf{H}_0 + \mathbf{G}_r \mathbf{M}(t) + \alpha \mathbf{M}(t) + \mathbf{H}_\sigma(t). \quad (6.30)$$

In this expression, the latter two terms have been introduced in the previous section, $\mathbf{H}_0 = \mathbf{B}_0 / \mu_0$ denotes the auxiliary external field, and \mathbf{G}_r is a $2N \times 2N$ matrix. The term $\mathbf{G}_r \mathbf{M}(t)$ represents the demagnetising field resulting from the structure's geometry (Section 4.5.4). In magnetomechanical models reported so far in literature, the demagnetising field is not included, since it is insignificant for the geometries investigated therein. Viana et al. (2010) note that the influence of the demagnetising field is substantial for a cylindrical structure; nonetheless, they do not attempt to include it in their models. Here, on the contrary, this field is incorporated.

In Equation (6.29), apart from the external field, each contribution of the effective field is a function of the magnetisation, making it an implicit function of $\mathbf{M}(t)$. Since $\mathbf{H}_\sigma(t)$ is a non-linear function of the magnetisation (Equation (6.28)) and an explicit function of the applied stress (or strain), it is linearised to avoid inverting a matrix in each time step. To this end, the magnetisation computed in the previous time step is substituted into the formulation in Equation (6.28), which is justified by the fact that the strain increments in between modelled time steps are relatively small. Ultimately, the magnetisation is determined by

$$\mathbf{M}(t) = \mathbf{X} (\mathbf{H}_0 + \mathbf{H}_\sigma(t)), \quad (6.31)$$

in which

$$\mathbf{X} = \chi \left[(1 - \chi \alpha) \mathbf{I} - \chi \mathbf{G}_r \right]^{-1},$$

where \mathbf{I} is the $2N \times 2N$ identity matrix, and $(\cdot)^{-1}$ denotes a matrix inversion. Note that, throughout the computation, the influence of the magnetisation on the total strain is neglected. Therefore, the strain-induced magnetisation in each time step is completely determined by the strain computed with the model introduced in Section 6.1.3.

To complete the set-up of the simulation, Table 6.5 lists the numerical values for the model constants, and the external field is $\mathbf{B}_0 = [B_0^x \ B_0^y \ B_0^z]^T = [14.3 \ -9.5 \ -35.3]^T \mu\text{T}$. In Section 6.1.3, it was concluded that the impact-induced stress is uniaxial with $n = z$, i.e. along the axis of the cylinder. After the magnetisation has been calculated for each time

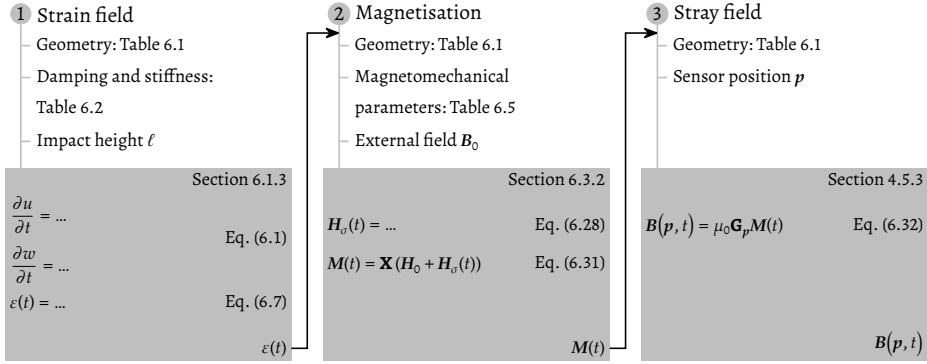


Figure 6.15: Flow chart for the consecutive computation steps to simulate the magnetomechanical response of a cylinder subjected to an impacting mass.

step, the stray field $B(p, t)$ at sensor positions A and B can be determined with:

$$B(p, t) = \mu_0 \mathbf{G}_p M(t), \quad (6.32)$$

in which \mathbf{G}_p is a matrix that maps the structure's magnetisation to the stray field at point p (Section 4.5.3). Subsequently, the stray field variation $\Delta B(p, t)$ is defined by

$$\Delta B(p, t) = B(p, t) - \bar{B}(p), \quad (6.33)$$

in which $\bar{B}(p)$ denotes the computed remanent stray field at $t = 0$.

To summarise the steps to determine the magnetomechanical response of a cylinder to an impact generated by free-falling mass, Figure 6.15 presents a flow chart of the three consecutive computation steps: the strain field, the structure's magnetisation, and the stray field. In the figure, the required input parameters are listed per step; the grey boxes contain the fundamental expressions together with a reference to the section in which these equations are discussed.

6.3.3. Simulated transient stray field

For an impact with $\ell = 1500$ mm, Figure 6.16 presents the modelled and measured stray field variation $\Delta B(p, t)$ at position A and B. At position B (Figure 6.16b), the direction of the modelled stray field variation corresponds to the measured one. Nonetheless, the amplitude of the simulated stray field differs significantly. Specifically, the amplitude ratio between the primary and secondary pulse is not captured by the proposed model. For the response at position A (Figure 6.16a), the direction of modelled stray field is completely opposite to the measured behaviour. Actually, the modelled stray field at the two sensor positions is practically indistinguishable, which indicates that the pursued modelling strategy is unable

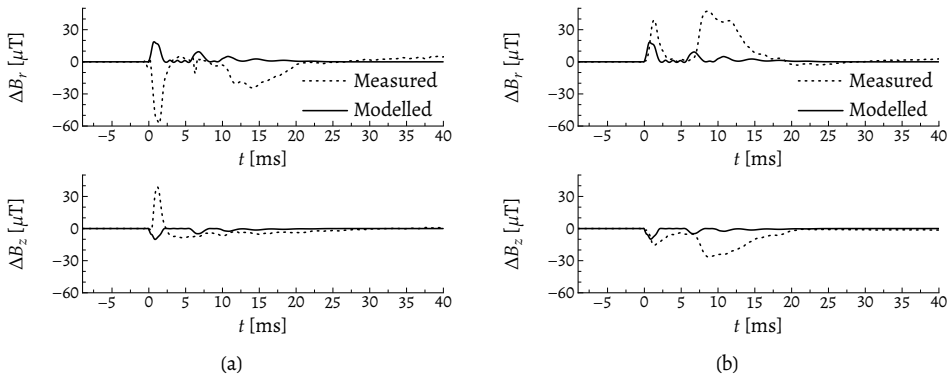


Figure 6.16: Comparison between the modelled and the measured strain-induced magnetisation changes. (a) AMR at position A ($\theta = 210^\circ$). (b) AMR at position B ($\theta = 120^\circ$).

to replicate the observed behaviour for sensors that have a different position with respect to the horizontal component of the external magnetic field. It was expected that the spatial distribution of the magnetisation caused by the demagnetising field would have created at least some spatial variation in the stray field for different circumferential sensor positions, which is clearly not the case in the modelled results.

6.4. Analysis of the modelling discrepancies

In this section, some possible explanations for the modelling discrepancies of the previously described magnetomechanical model are discussed. First, the influence of circumferential spatial variation of the magnetisation is analysed. Second, the isotropic assumption of the model is questioned by considering sources of magnetic anisotropy. Third, the significance of the magnetic history—represented by the irreversible magnetisation—is discussed.

6.4.1. Contributions of circumferential magnetic modes

As the measured data implies that the relative position of the sensor with respect to the horizontal component of the external field is of importance for the direction of the stray field changes, this section is devoted to a more in-depth analysis of the influence of the individual magnetisation components (M_θ and M_z) on the stray field at the sensor locations. By considering a prescribed increment of each of the independent components, the main contributions to the observed changes can be identified. Due to the presence of the horizontal component of the external field (Section 4.5.5), some of the physical quantities involved in the magnetomechanical effect have a $\cos(\theta)$ circumferential dependency (e.g. B_0^\perp), while others are distributed almost evenly along the cylinder's circumference (e.g. ϵ). A full list of the relevant quantities and their respective distributions is given in Table 6.6. To determine which distribution contributes to the stray field changes, the magnetisation

Table 6.6: Circumferential distribution of the quantities relevant for the magnetomechanical response of an impacted cylinder expressed in the circumferential mode number n .

$n = 0$	$n = 1$	$n = 2$
M_z, M	M_θ	M
B_z	B_θ^\perp	
ε		
σ		

increments are imposed using the following spatial distribution, which can be regarded as circumferential magnetic mode shapes.

$$\Delta M_\theta = C (\cos(n\theta) + \sin(n\theta)) \theta, \quad (6.34a)$$

$$\Delta M_z = C (\cos(n\theta) + \sin(n\theta)) z, \quad (6.34b)$$

in which C is the predefined amplitude, n represents circumferential mode number, and θ and z denote the unit vectors in the circumferential and axial direction, respectively. Along the axial direction, the magnetisation increment is uniformly distributed.

Table 6.7 presents the direction of the stray field changes induced by magnetisation increments with $C = 1$ kA/m in conjunction with the corresponding circumferential mode shapes. The sensor is located at $d/R = 0.050$ from the cylinder's surface, corresponding to the offset used in the experiment. Moreover, the stray field data is simulated at four positions in the axial plane with $z/R = -1.0$, which is also in accordance with the reported set-up. Based on the measured data (Figure 6.16), the amplitude ratio between the sensor locations for both components of the stray field is negative. Hence, magnetisation increments that generate stray field changes with opposite signs for position A and B are of interest.

For the axi-symmetric mode $n = 0$, it is clear that, on one hand, an increase in the circumferential magnetisation component cannot generate a stray field change, since the contributions from each part of the cylinder cancel perfectly. On the other hand, the axial magnetisation does generate stray field changes, which are (obviously) axi-symmetric. Thus, purely axi-symmetric magnetisation changes cannot account for the observed strain-induced stray field changes, indicating that they result from higher-order circumferential spatial distributions. For $n = 1$, a circumferential magnetisation increase generates the measured amplitude ratio. Moreover, the desired behaviour appears for both increments in case $n = 2$.

Nonetheless, the direction of the stray field variations alone is insufficient to fully characterise them. Figure 6.17 presents the stray field changes for a normalised distance below the top of the cylinder. The graphs indicate that the largest variation of stray field occurs in the vicinity of the top of the cylinder. One radius below the cylinder's top, the amplitudes of most changes are nearly zero. Regarding the correct amplitude ratio, only three increments result in opposing stray field changes for sensors A and B: ΔM_θ with $n = 1$ and $n = 2$, and

Table 6.7: Direction of stray field changes at four distinct sensor locations resulting from a magnetisation increment distributed with circumferential mode n . Data generated at $d/R = 0.05$ and $z/r = -1$.

		$n = 0$				$n = 1$				$n = 2$			
		A	B	A'	B'	A	B	A'	B'	A	B	A'	B'
ΔM_θ	ΔB_r	0	0	0	0	-	+	+	-	+	-	+	-
	ΔB_z	0	0	0	0	-	+	+	-	+	-	+	-
ΔM_z	ΔB_r	+	+	+	+	+	+	-	-	+	-	+	-
	ΔB_z	-	-	-	-	+	+	-	-	+	-	+	-

ΔM_z with $n = 2$. However, the latter does not contribute significantly in the measurement plane ($z/R = -1$). Consequently, the observed ΔB_r most probably results from ΔM_θ .

The measured stray field data in Figure 6.16 support this conclusion. At position B, the circumferential magnetisation induced by the external field is close to zero as a result of the geometry of the cylinder. Therefore, the stray field at this location is governed by the axial magnetisation, which is directed along the negative z -axis to adhere to the external field. Since compressive stress tends to reduce the magnetisation, it is expected that the strain-induced magnetisation change is pointing towards the positive z -axis, which corresponds to a positive value for C. Hence, the direction of resulting stray field changes are identical to the direction due to a positive ΔM_z (Figure 6.17b). This explains the correspondence between the modelled and measured stray field at this location. On the contrary, at position A ($\theta = 210^\circ$), the circumferential magnetisation is non-zero. Since an identical stray field response as registered at location B can be expected due the axial magnetisation, the observed stray field must be generated by the circumferential magnetisation. This implies that the contribution of the latter not only nullifies the axial contribution but it even completely reverses the signs. Consequently, in this specific case, the stray field due to a change in the circumferential magnetisation must be roughly twice as large as one due to the axial magnetisation. This indicates that there is a preferred direction for the strain-induced magnetisation, i.e. the magnetic response of the material is anisotropic.

6.4.2. Magnetic anisotropy

Magnetic anisotropy emerges due to several external factors. One of these, stress-induced anisotropy, has already been encountered in the formulation of the stress-induced effective field. It is a result of the preferential direction introduced by the uniaxial applied stress. However, this is not the sole source of anisotropy in ferromagnetic materials. The magnetisation in a single metal crystal naturally has preferred directions due to the ordering of

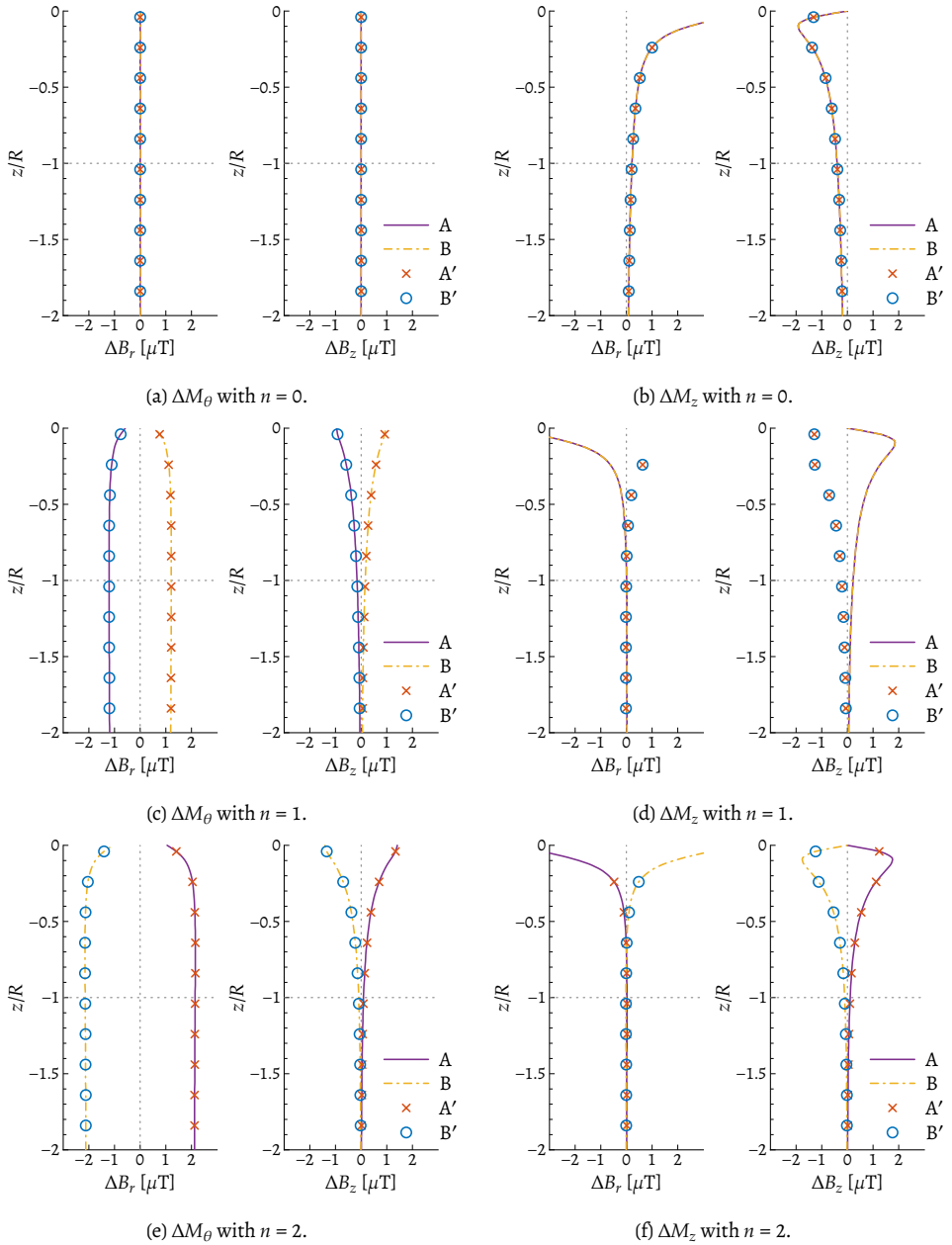


Figure 6.17: Stray field changes along the normalised axial position z/R generated by a magnetisation increment of 1 kA/m applied with several circumferential mode shapes. Data simulated at four positions separated by a 90° angle with $d/R = 0.050$.



Figure 6.18: The two cylinders used in the laboratory experiments.

the atoms in the crystal, so-called magnetocrystalline anisotropy (Chikazumi and Graham, 1997, pp. 249–256). Despite the fact that one might expect that due to averaging the bulk behaviour is isotropic in polycrystalline materials, this is rarely the case in reality (Cullity and Graham, 2009, pp. 229–230). In that case, the anisotropy stems from the formation process of the material. For example, a sheet material has a rolling direction, to which the constituent grains (and crystals) align to on average.

Moreover, the shape of a specimen alone (even if averaging the orientation of the grains results in isotropic conditions) can lead to another type of anisotropy: shape anisotropy (Cullity and Graham, 2009, p. 234). In the formulation to compute the cylinder's magnetisation, shape anisotropy is accounted for by assuming that the out-of-plane component (M_r) is zero. Additionally, the local auxiliary field in each element is influenced by the geometry of the entire structure through the matrix \mathbf{G}_r .

Since shape anisotropy is accounted for in the developed magnetomechanical model, the discrepancy between the modelled and measured stray field could be attributed to the crystalline anisotropy, which results from the forming process of the cylinder. To investigate this premise, the magnetomechanical response of cylinders with different formation processes are compared. Up to now, the measured stray field changes have only been reported from a single cylinder (specimen C2). However, in the initial stage of the experiment, another cylinder (specimen C1) has been subjected to identical axial impacts. The main difference between the two specimens is their wall thickness: C1 has a uniform wall thickness $h = 5.0$ mm, while the wall thickness of the upper part of C2 has been machined down to $h = 2.5$ mm. Figure 6.18 shows both cylinders.

Figure 6.19 shows the measured magnetomechanical response for impacts that induced similar strain levels in the structure ($\ell = 1500$ mm for C1 and $\ell = 500$ mm for C2), which is verified by the time traces of the axial strain. The presented data have been measured by a magnetometer at position A (Figure 6.5), of which the radial component is perpendicular to

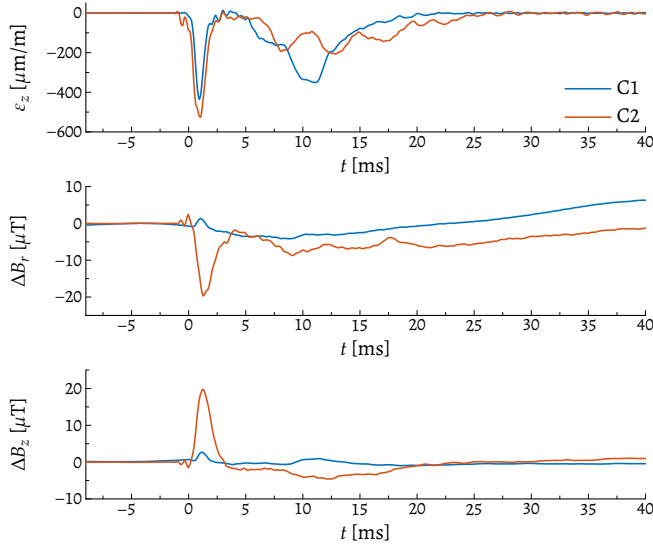


Figure 6.19: Measured magnetomechanical response of two different cylinder with comparable induced strain levels at the same sensor location $\theta = 210^\circ$ (position A).

6

the horizontal external field. Even though the wall thickness of C1 is twice that of C2, the amplitude of the strain-induced transient stray field in the former is much smaller than the latter. Furthermore, the signs of the radial components are opposite, which indicates that the strain-induced magnetisation cumulate to other behaviour in the two instances.

In both cases, the cylinder is constructed by rolling a flat sheet into the required circular shape. Therefore, the rolling direction of the cylinders coincides with the circumferential coordinate, which acts as a preferred direction. To reduce the wall thickness of C2, the top of that cylinder has been machined down, which is achieved by carefully grinding off some of the material. During this process, the cylinder is rotated around its axis of symmetry. Hence, the grinding occurs along the circumferential direction, enhancing the anisotropy along the rolling direction. This might (partially) explain the increased amplitude measured for C2, even though it has half the wall thickness of C1.

To account for this type of anisotropy in the model equations, two quantities that thus far have been assumed to be isotropic must be altered to incorporate the influence of the rolling direction: the magnetic susceptibility χ and the magnetostrictive strain tensor ε^H . The former could be altered in a straight-forward manner by applying a separate susceptibility in each direction, since the rolling direction coincides with one of the coordinates. To modify the latter, a suitable anisotropic magnetostrictive strain tensor should be selected, e.g. from Federico et al. (2019). Naturally, the number of free parameters in an anisotropic model will increase, and, consequently, the model calibration will be more elaborate.

6.4.3. Irreversible magnetisation

In the current model equations, the strain-induced magnetisation is essentially proportional to the external field B_0 , which is clear from Equation (6.31). This implies that, when the external field is reduced to zero, the structure's magnetisation is zero as well; and, as a result, the strain-induced changes are zero as well. However, this would conflict with the presence of the magnetic domain structure inside the ferromagnetic material, as only a portion of the magnetisation is expected to disappear when the external field is removed. To represent this fact, the total magnetisation is often split (Jiles and Atherton, 1984):

$$\mathbf{M} = \mathbf{M}_{\text{rev}} + \mathbf{M}_{\text{irr}}, \quad (6.35)$$

in which \mathbf{M}_{rev} and \mathbf{M}_{irr} denote the reversible and the irreversible part of the magnetisation, respectively. The latter remains when external stimuli are removed, while the former diminishes in that case. Therefore, the irreversible magnetisation can be associated with the magnetic domain structure, i.e. the position of the domain walls and the orientation of the magnetisation within the domain. Changes in the irreversible magnetisation are related to permanent movement of these walls, which requires a sufficient amount of energy to be supplied to the material by an external factor, i.e. strain or an external magnetic field. This effect has been discussed in more depth in Chapter 5. In the above decomposition, the reversible magnetisation can be identified as the contribution due to domain wall bowing, which does not permanently change the position of the domain wall.

Given this premise, the irreversible magnetisation becomes insensitive to strain variations when the strain remains below or equals the previously endured peak strain as soon as the magnetisation has reached a metastable magnetic equilibrium—which is not necessarily equal to the anhysteretic magnetisation (Makar and Atherton, 1995). When this is the case, strain-induced magnetisation is solely due to changes of the reversible magnetisation, i.e. domain wall bowing.[†] However, whether a domain wall bows due to the action of strain is determined by the type of wall: only 90° walls are mobilised, while 180° walls are immobile in that case (Bulte and Langman, 2002). Consequently, the strain-induced magnetisation depends on the current domain wall configuration, i.e. the number of stress-active walls (Schneider et al., 1992), which is determined by the complete magnetic history of the specimen.

Experimentally determining the domain configuration in a sample of sufficient size is currently practically impossible. As a result, modelling the strain-induced magnetisation based on domain wall bowing alone is a daunting task. In theory, one could incorporate domain wall processes into particle methods (Section 4.4.1) or multi-scale models (Section 4.4.2), although it might be expected that this would result in a computationally

[†]The reversible magnetisation is also determined by the rotation of the magnetisation within each domain due to an external magnetising field. However, as this effect only becomes apparent for external fields with a substantially greater magnitude than the geomagnetic field, this contribution to the reversible magnetisation is neglected in the present discussion.

expensive model. Alternatively, the decomposition of the magnetisation in Equation (6.35) could be substituted into the derived model equations, yielding

$$\mathbf{M}_{\text{rev}}(t) = \mathbf{X}(\mathbf{H}_0 + \mathbf{G}_r \mathbf{M}_{\text{irr}} + \alpha \mathbf{M}_{\text{irr}} + \mathbf{H}_\sigma(t)). \quad (6.36)$$

In the above, \mathbf{M}_{irr} is assumed to have become strain-invariant as a metastable equilibrium state has been attained. This additional vector field, which is present in the entire volume of the structure, is unknown a priori. Therefore, it must be determined from experimental data, e.g. via inverse modelling. All the possible improvements of the magnetomechanical modelling proposed in this section are left for future research.

6.5. Generalisation and limitations

The aim of the laboratory experiment discussed in this chapter has been to demonstrate whether the impact-induced strain can be inferred from non-contact measurements of the transient magnetic stray field. To this end, a promising correlation between the strain and stray field changes has been found, especially for the primary strain pulse. However, to generalise this principle to a workable method to infer elastic deformation during a monopile installation using non-contact sensors, additional steps are required.

First, to assure consistency of the measured strain-induced stray field, the structure's magnetisation must reach a magnetic equilibrium to accommodate only reversible magnetisation changes during dynamic loading. A structure attains this state after several impacts that induce an identical peak strain. Fortunately, a typical monopile installation consists of several thousands of hammer blows. It is therefore expected that, during the bulk of the administered hammer blows, the magnetisation resides at such an equilibrium, and the measured stray field variations reflect the impact-induced elastic strain.

A relevant parameter is the relative position of the magnetic field sensor with respect to the structure. As seen from the data in Figure 6.17, an increment of each of the magnetisation components leads to different measured stray field changes depending on the axial and circumferential position of the sensor. Consequently, an identical strain pulse might result in a decrease of the measured stray field at a certain axial position, while at a lower axial position it might generate an increase in the registered stray field. Therefore, the sensor preferably retains its position relative to the structure throughout the installation.

Even though reproducing the measured strain-induced stray field with a magneto-mechanical model is an open challenge, some aspects of the modelling for large-diameter monopiles have been addressed. Since the ring frequency for large-diameter piles lies within the frequency range excited by impact hammers, the stress state in these structures is biaxial. Provided that the material reacts isotropically, the effective field vector (Equation (6.22)) can be employed in conjunction with the model for the magnetostriction coefficient (Equation (6.26)), as these expressions naturally incorporate the tensorial nature of the relevant quantities. Whether the magnetic properties of a large-diameter monopile are isotropic

is unknown at present. However, in the laboratory set-up, the magnetic anisotropy is enhanced by the grinding process used to reduce the wall thickness. Perhaps large-diameter monopiles are approximately magnetically isotropic, since no grinding process is applied during their fabrication.

To accurately infer the deformation based on the measured stray field at a certain sensor location, calibration is inevitable, even when a suitable magnetomechanical model is available, since the model parameters are not necessarily material constants, but rather structure-dependent coefficients. When such a model is unavailable, an appropriate calibration still enables one to infer the current strain level from magnetic stray field measurements, given the excellent similarity between the strain and the major principle component of the stray field, especially for the primary strain pulse. Hence, the magnetic signals can be calibrated with measured strain signals from, for example, a strain gauge, which is temporarily attached to the structure. Preferably, this calibration is performed when the pile is at the installation site, since the local external magnetic field partially determines the induced magnetisation. Presently, it is clear that more research into this calibration procedure, and other aspects mentioned in this section, is required. The following chapter will treat some of the aforementioned points by considering the results from an in-situ measurement campaign during the installation of a monopile.

6.6. Conclusions

This chapter treated the results of a laboratory experiment of a steel cylinder subjected to axial impacts to investigate the possibility to use the measured transient magnetic stray field to infer the induced strain in a non-contact manner. In the beginning of the chapter, the impact-induced strain field has been analysed by means of a simulation of an impact using an axially symmetric mechanical model. This model has been developed such that it can be applied to the simulation of large-diameter monopile installations by hydraulic impact hammers. From the simulated strain data, it has become apparent that an impact induces a uniaxial stress state, since the excited frequencies are well below the ring frequency of the structure.

For repeated impacts, analysis of the measured stray field indicated that the magnetic response becomes consistent (i.e. repeatable) when the structure's magnetisation has reached a magnetic equilibrium, i.e. the remanent magnetisation does not change when the load is repeated. Using the principle component analysis, the dynamic stray field is expressed along its principle axes. For the primary strain pulse, the correlation between the strain and the major principle component of the stray field for impacts from different heights is excellent ($c_{\varepsilon_z B_1} > 0.9$). However, the direction of principle axes depends on the sensor's circumferential position and the impact height. To appreciate the actual physical processes governing the magnetomechanical behaviour, a new magnetomechanical model has been developed.

Given the observation that the transient stray field becomes fully reversible as soon as the magnetisation is at an equilibrium, a reversible model for the magnetisation is developed along the lines of the anhysteretic magnetisation. Assuming isotropic material behaviour, a vectorial expression for the strain-induced magnetisation is derived. Subsequently, the expression is simplified by substituting the stress tensor representing a uniaxial stress state. An important new aspect that is incorporated into the model is the effect of the demagnetising field generated by the geometry of the cylindrical structure. A comparison between the simulated and measured strain-induced stray field and a subsequent analysis of the stray field's response to distinct magnetisation increments show that the newly proposed magnetomechanical model is insufficient to predict the observed stray field variations. Inclusion of anisotropy and accounting for the irreversible magnetisation have been identified as promising directions for improvements to the magnetomechanical model.

From the discussion in this chapter, it has become clear that in order to infer the elastic deformation in a structure resulting from an impact load using non-contact sensors, additional research is required into the specifics of the calibration procedure, the role of material's anisotropy and the magnetic loading history. Nonetheless, the data obtained from the laboratory experiment does provide a valuable basis for a non-contact method to infer the current strain level provided that a proper calibration procedure is applied. In the subsequent chapter, results from an in-situ measurement campaign are discussed, which is conducted during the onshore installation of a medium-sized monopile.

7

In-situ magnetomechanical response of a steel monopile during pile driving

*And now I can consider
Now there is this distance*

Interpol – PDA

Until now, the main discussion of this thesis has concerned lab-scale experiments to demonstrate non-contact methods to infer structural deformations by considering the magnetic stray field. Although the experimental set-up discussed in the previous chapters is novel, it still differs significantly from a full-scale offshore monopile installation in terms of scale and controllability of the external factors. To date, limited data have been published on the in-situ magnetomechanical response of large-scale steel structures in a weak ambient magnetic field. In fact, they focus solely on statically loaded steel pipelines for inspection (Atherton et al., 1983, 1984). More recently, the bending strength of corroded reinforced concrete beams was determined with a method that employs the structure's magnetic stray field (Qiu et al., 2020). However, all the aforementioned examples from literature pertain quasi-static loading conditions, which are incomparable to the dynamic loadings

Parts of this chapter have been published in Meijers, Tsouvalas and Metrikine (2021b) and in Meijers, Tsouvalas and Metrikine (2020).

encountered during monopile installations. Therefore, the measurement campaign treated in this chapter is designed to demonstrate the practical feasibility of utilising non-contact measurements to infer impact-induced elastic deformations during a realistic monopile installation.

First, the set-up of the measurement campaign is presented including the sensor lay-out. Second, the data processing algorithm is described, which is used to analyse the recorded data from several thousand hammer blows. Third, the processed measurement results are treated, with an emphasis on the similarity of the magnetic signals recorded during each impact and the correlation between the stray field and the strain. Fourth, sources of error and other disturbances which might interfere with soundness of the magnetic measurements are examined and mitigation strategies are suggested. Fifth, two practical applications of the magnetic stray field measurements are discussed. Finally, the conclusions from this chapter are summarised.

7.1. Set-up of the measurement campaign

In July 2019, a steel cylindrical pile was installed at the new yard of IHC-IQIP in Sliedrecht, the Netherlands. This so-called test pile is used for performance tests of hydraulic impact hammers. The full test pile assembly consists of two steel piles: an outer and an inner pile. The former surrounds the latter and serves as isolation to prevent vibrations from spreading into the surrounding soil when a hammer exerts an impact on the inner pile. With the aid of an IHC-IQIP S350 hydraulic hammer, which is capable of delivering a blow with an impact energy up to 350 kJ, the inner pile has been driven to the desired depth. The installation site at Sliedrecht comprises a small area next to the Beneden-Merwede river, which is indicated in the aerial view shown in Figure 7.1.

A schematic of the pile during installation is presented in Figures 7.2a and 7.2b, which indicates the two coordinate systems used throughout this chapter: a Cartesian and a cylindrical. In the latter the radial, circumferential and axial directions are designated as r , θ , and z , respectively. The former is useful to describe the external field, while the latter is convenient to define the sensor positions and the measured magnetic field components. Additionally, the schematics indicate the direction of the geomagnetic field \mathbf{B}^0 , which is—as in previous chapters—considered to be time- and space-invariant. At the installation site, the measured components of \mathbf{B}^0 in the Cartesian xyz -coordinate system are:

$$\begin{bmatrix} B_x^0 \\ B_y^0 \\ B_z^0 \end{bmatrix} = \begin{bmatrix} 15 \\ 10 \\ -40 \end{bmatrix} \mu\text{T}. \quad (7.1)$$

Clearly, the z -component of the geomagnetic field dominates, i.e. the magnetic field points strongly downwards. In the top view of the pile (Figure 7.2b), the angle between the geomagnetic field vector and the x -axis is $\beta \approx 33^\circ$.



Figure 7.1: Aerial view of the yard of IHC-IQIP in Sliedrecht, the Netherlands, in which the installation site is encircled (Google Maps, n.d.).

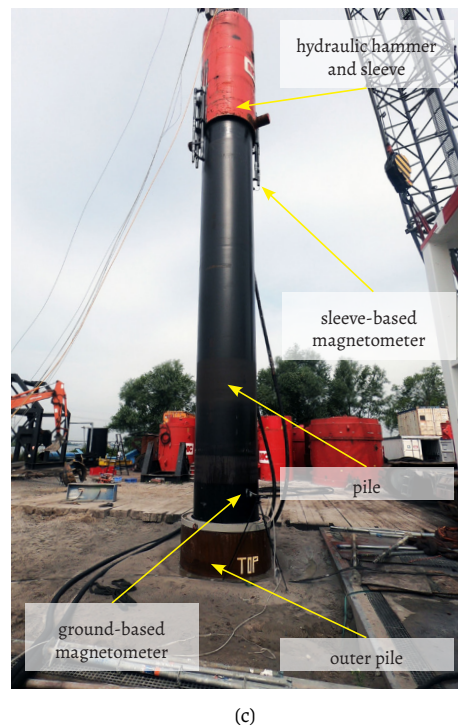
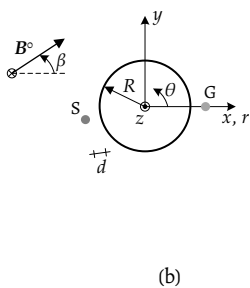
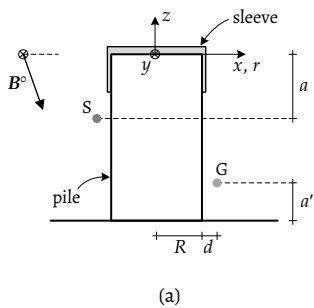


Figure 7.2: Overview of the measurement system during installation of the inner pile. The two distinct magnetic sensor configurations are indicated with S (sleeve-based) and G (ground-based). (a) Schematic side view. (b) Schematic top view. (c) Annotated photograph of the installation.

Table 7.1: Dimensions and material properties of the steel monopile installed during the in-situ measurement campaign in Sliedrecht, the Netherlands.

Parameter	Value	Parameter	Value
L	62.0 m	E_p	210 GPa
R	0.6096 m	ρ_p	7850 kg/m ³
h	0.050 m	ν_p	0.3

The installed pile is composed of cylindrical steel sections with a height of 3 m each, which are stacked on top of each other using circumferential welds. Before installation, the pile has been coated for corrosion protection, obscuring the exact locations of the welds. The dimensions and material properties of the installed pile are summarised in Table 7.1, in which L denotes the length of the pile, R is the outer diameter, and h represents the wall thickness. Moreover, E_p is Young's modulus, ρ_p denotes the density and ν_p is Poisson's ratio. Although this specific pile has a rather small radius compared to monopiles currently installed offshore (Igwemezie et al., 2019), the main elements of pile driving dynamics, i.e. stress wave propagation and pile penetration, are present. Consequently, it provides a more realistic scenario than the previously discussed controlled lab-scale experiment (Chapter 6). It is important to note that, prior to installation, the pile was not subjected to any magnetic treatment, i.e. no (de)magnetisation procedure of the structure was performed. Employing such a process is not feasible in an offshore environment (or even in an onshore setting given the large scale), as it requires the generation of carefully controllable magnetic fields by means of magnetising coils. Nevertheless, based on the results from the lab-scale experiments, it is expected that the structure's magnetisation attains a magnetic equilibrium quite rapidly as a result of the repeated loading by the hammer.

7

7.1.1. Sensor description and positioning

For the simultaneous measurement of the strain-induced magnetic stray field changes in the vicinity of the structure at different locations, a dedicated measurement system was developed to support several biaxial magnetometers. Each sensor (type: HMC1022) had a measuring range of $\pm 600 \mu\text{T}$, a sensitivity of $20 \mu\text{T/mV}$ ($V_{\text{bridge}} = 5 \text{ V}$), a noise density of $960 \text{ pT}/\sqrt{\text{Hz}}$ at 1 Hz, and a bandwidth ranging up to 5 MHz. The measurement system was specifically designed to transmit the measured magnetic field data using cables of considerable length: 100 m in this specific case. Furthermore, each channel was sampled with a frequency of 50 kHz.

Each biaxial magnetic sensor was placed at a certain distance d (indicated in Figures 7.2a and 7.2b) from the surface of the pile. Additionally, two different configurations for positioning of the magnetometers were employed: sleeve-based (S) and ground-based (G). In the former configuration, the sensor is attached to a PVC frame which is directly connected to the sleeve of the hammer (Figure 7.2c). Due to the frame, the sleeve-based sensors retain their relative position a (Figure 7.2a) with respect to the pile head during the tests. In the

Table 7.2: Overview of the three days of the measurement campaign which summarises the deployed sensors, the measured pile penetration $\Delta\zeta$, the number of recorded hammer blows N_i and the index i used to reference these hammer blows.

	Day 1	Day 2	Day 3
System	Reduced	Reduced	Full
Sensors	2×S, 1×G	2×S, 1×G	4×S, 4×G, 2×PDA
$\Delta\zeta$	7.4 m	8.6 m	-
N_i	2174	3459	141
Index	i_1	i_2	i_3

other configuration, the sensors are mounted on top of non-magnetic tripods which are placed directly on the ground. As a result, the relative position between the sensor and the pile changed when the pile penetrated further into the soil. For these ground-based sensors, the axial position a' was measured relative to the ground (Figure 7.2a).

Next to the magnetic stray field measurement, strains in the structure were recorded by means of a Pile Driving Analyser (PDA), which was directly attached to the pile surface using an adhesive. Such a sensor consists of a strain measurement device (type: TML FLA-2.350-11) and an accelerometer (type: Endevco 7270A) to measure the strain and acceleration in the axial direction, i.e. along the z -axis. Moreover, during installation, an optical sensor, which was bolted to the sleeve, recorded the penetration of the pile using the time-of-flight principle.

7.1.2. Measurement systems

The entire experiment on the inner pile lasted for three days with a different number of sensors deployed on each day. Table 7.2 presents an overview of these three days with the deployed sensors, the measured pile penetration $\Delta\zeta$, the number of recorded hammer blows N_i and the index i used to reference the hammer blows of each day. On the first two days, the pile was not fully instrumented. Only three biaxial magnetometers (two sleeve-based and one ground-based) were installed. Unfortunately, one of the magnetometers failed early on the first day; the defective sensor was replaced before the installation continued on the subsequent day. Therefore, data from the first campaign day is not discussed in depth in the remainder of this chapter. As only magnetometers were deployed, the measurement system on the initial two days is referred to as the reduced measurement system. Despite the absence of classical strain measurements, the obtained results are still very valuable, since the observed penetration of the pile $\Delta\zeta$ was considerable. This provides a record of the magnetic stray field while the pile is moving relative to the sensor, an aspect that was not included in the lab-scale experiment (Chapter 6). On the third day of the installation, all sensors described above were employed; hence, on the final day, data was collected with the full measurement system, which includes classical strain measurements to fully characterise the magnetomechanical response of the structure. At the beginning of each section with measured results, the exact measurement system is detailed.

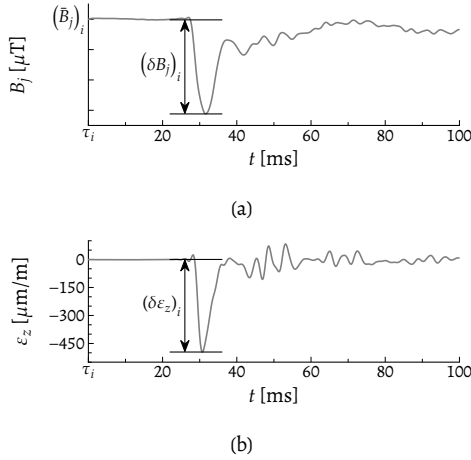


Figure 7.3: Exemplary time signals of (a) a component of the magnetic stray field and (b) the axial strain ε_z measured during a single hammer blow i with three relevant characteristic parameters indicated: the remanent stray field value $(\bar{B}_i)_i$, the maximum magnetic variation from the remanent field $(\delta B_i)_i$, and the peak strain $(\delta \varepsilon_z)_i$.

7.1.3. Data processing

Given the broad variety of the measured quantities, direct comparison of the raw data does not provide a feasible framework to analyse the magnetomechanical response of the system during pile driving. Thus, the full time signals are reduced to a selected number of characteristic parameters for each individual hammer blow, which can be regarded as a discrete event in the full data set. For impact i , the hammer registers the impact time τ_i , which is the time instance the ram of the hammer is released at, the supplied hammer energy E_i and the current penetration depth ζ_i . Figure 7.3 shows typical signals of the magnetic stray field and the axial strain directly after $t = \tau_i$. Using τ_i , a time interval t_i ensuing the impact is defined as follows:

$$t_i = [\tau_i, \tau_i + \Delta t], \quad (7.2)$$

in which Δt is a time interval which is approximately twenty times the duration of the initial strain pulse, i.e. $\Delta t = \pm 100$ ms for the case study here.

Figure 7.3a shows the axial component of the full magnetic field vector $B(t)$. Note that, even in the absence of mechanical loading, the magnetic field in the vicinity of the pile is non-zero, since the structure's magnetisation generates a magnetic stray field that permeates the region around it. Assuming that at $t = \tau_i$ the structure is unloaded (the static load caused by the mass of the impact hammer resting on the pile is assumed to be negligible), the remanent stray field value \bar{B}_i is equal to the magnetic field in the unloaded state:

$$\bar{B}_i = B(\tau_i). \quad (7.3)$$

On the vertical axis of Figure 7.3a, this remanent value is marked. As a result of strain-driven reordering of the internal magnetic domains, the remanent stray field value could change in between impacts when sufficient energy is supplied to the system (Chapter 5). Additionally, external factors, e.g. a steel object temporarily approaching the sensor, can further alter this value.

During a hammer blow, the generated strain pulse changes the structure's magnetisation through the magnetomechanical effect. The resulting variations in the magnetic stray field are small compared to the remanent field. Hence, it is useful to separately define the magnetic field variation $\Delta B(t_i)$ as follows:

$$\Delta B(t_i) = B(t_i) - \bar{B}_i. \quad (7.4)$$

Similar to the analysis of the transient response of the lab-scale experiment (Chapter 6), this quantity can be rewritten using the Principle Component Analysis as (Section 6.2.2):

$$\Delta B(t_i) = \Delta B_r(t_i) \mathbf{r} + \Delta B_z(t_i) \mathbf{z} = \Delta B_1(t_i) (\mathbf{e}_1)_i + \Delta B_2(t_i) (\mathbf{e}_2)_i, \quad (7.5)$$

in which \mathbf{r} , \mathbf{z} , $(\mathbf{e}_1)_i$ and $(\mathbf{e}_2)_i$ represent the unit vectors along the radial, the axial, the major principle and the minor principle axis, respectively. Along each of these directions, $\Delta B_r(t_i)$, $\Delta B_z(t_i)$, $\Delta B_1(t_i)$ and $\Delta B_2(t_i)$ denote the respective variations of the stray field. The angle between \mathbf{r} and $(\mathbf{e}_1)_i$ is defined as $(\psi_1)_i$. Note that the principle components are determined for each impact separately, as indicated by the subscripts i .

The magnetic field variation describes the deviations of the stray field from the unstrained state of the system, and, consequently, it is expected to reflect solely the strain-induced magnetisation changes. Given the clear peak in the magnetic signal in Figure 7.3a, it is natural to define the maximum deviation from the remanent value as a new quantity: the maximum deviation from the remanent field δB_i . Note that, for example, a compressive strain—i.e. negative strain—does not necessarily cause a negative magnetic field change. Thus, to correctly capture the extreme value of the magnetic field variation, one needs to consider the largest deviation from the remanent field (either positive or negative):

$$(\delta B_j)_i = \max \left(\left\| (\Delta B_j)_i(t_i) \right\| \right) \text{signum} \left((\Delta B_j)_i(t_i) \right) \quad (7.6)$$

in which j specifies the vector component, which is collinear either with the measurement directions ($j = r, \theta, z$) or the principle directions ($j = 1, 2$). The above expression ensures that the largest deviation from the remanent field is selected while retaining its sign. As an example, Figure 7.3a indicates $(\delta B_j)_i$ for a hammer blow.

Similar quantities can be defined to characterise the strain signal $\varepsilon_z(t_i)$. Assuming no permanent structural deformation at the location of the strain sensor, the structure is unstrained before each impact, eliminating the need to specify the remnant strain value for

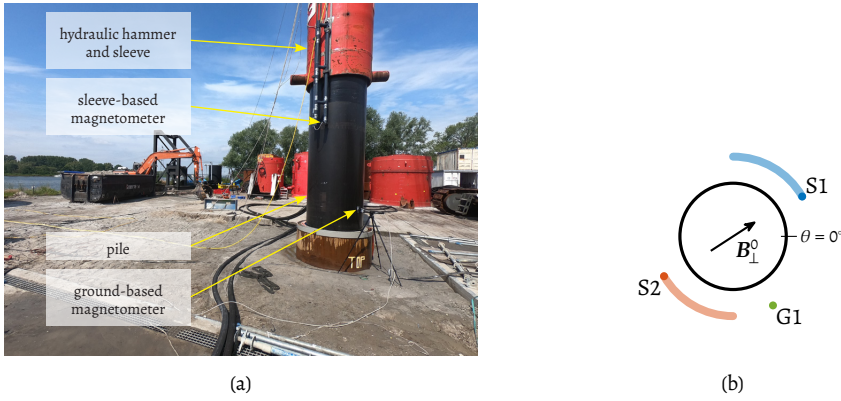


Figure 7.4: The reduced measurement system. (a) Annotated photograph of the set-up. (b) Schematic top view indicating the direction of the horizontal component of the geomagnetic field B_{\perp}^0 and the circumferential positions of the magnetometers.

each hammer blow. By applying an expression similar to Equation (7.6) to $(\varepsilon_z)_i$, the peak of the strain signal $(\delta\varepsilon_z)_i$ is obtained as shown in Figure 7.3b.

To summarise, for each impact i , the following impact characteristics are considered:

- (i) impact energy E_i ;
- (ii) penetration depth ζ_i ;
- (iii) peak strain $(\delta\varepsilon_z)_i$;
- (iv) angle between the major principle axis and the $r\theta$ -plane $(\psi_1)_i$;
- (v) maximum deviation from the remanent field $(\delta B_j)_i$.
- (vi) remanent magnetic field \bar{B}_i ;

Note that the latter two quantities are determined for each component of the stray field. For brevity, the subscripts i are dropped in the sequel, keeping in mind that the impact characteristics above are examined at discrete time moments.

7.2. Analysis of data collected by the reduced measurement system

Figure 7.4a presents the reduced measurement system used on the second installation day, which consists of three biaxial magnetometers: one ground-based sensor and two diametrically placed sleeve-based sensors. Table 7.3 lists the positions and the measurement directions of each sensor. Note that the circumferential position of the sleeve-based sensors are given as a range, because the hammer and sleeve slowly rotate with respect to the pile

Table 7.3: Overview of the reduced measurement system deployed on the second day. For each sensor, the measured quantities are listed; θ and a are the circumferential and axial positions, respectively; the distance from the pile surface is denoted by d .

Sensor	Measurement	θ [°]	a [m]	d [m]
S1	B_z, B_r	[30, 90]	3.50	0.20
S2	B_z, B_r	[210, 270]	3.50	0.20
G1	B_z, B_r	300	1.10	0.20

during the installation process. Figure 7.4b visualises these ranges in a schematic top view. Since this gradual hammer rotation is not recorded in real-time during the campaign, data from non-consecutive impacts should be compared with care.

A total of 3459 impacts were recorded with the reduced measurement system on the second installation day. Figure 7.5 presents an overview impact characteristics extracted from the full time signals. As a result of the hammer blows, the pile penetration was $\Delta\zeta = 8.6$ m. Based on the hammer energy E (which was rather constant throughout the process) and the recorded pile penetration ζ (Figure 7.5e), it is clear that the penetration speed was variable, which is a result of the varying soil resistance that the pile experienced at different penetration depths. Throughout the day, the installation was stopped and restarted several times. During a hammer restart, the energy is introduced in gradual steps to avoid damage to the hammer, which appears as a distinct pattern of increasing hammer energy.

Regarding the magnetic quantities, the characteristics extracted from the measurements by the ground-based sensor (G1) shows significantly more variation than those determined for the sleeve-based sensors (Figures 7.5a–7.5d). The difference is attributed to the relative motion of the pile to the sensor in the former configuration. Given the different responses for the sensor configurations, each sensor lay-out is discussed separately hereafter.

7.2.1. Response of the sleeve-based sensors

For S1 and S2, the axial component of the remanent field \bar{B}_z remains constant up to impact $i_2 \approx 2400$, after which a slight reduction is observed (Figure 7.5b); whereas the radial component \bar{B}_r shows more variation over the considered impact range (Figure 7.5a). The latter behaviour can most probably be attributed to the rotation of the hammer-sleeve assembly, which might also explain the variation in the maximum deviation from the remanent field (Figure 7.5d). Most noticeable in the presented data is the change in the angle of the major principle component ψ_1 that occurs after impact $i_2 = 2400$ (Figure 7.5c), which is a result of the sensors approaching the outer pile (Figure 7.2c). The latter has a significant remanent field of its own, which locally alters the external field. Naturally, this additional stray field also causes the observed change in the remanent stray field.

To eliminate the effect of the rotation of the hammer from the analysis, the evolution of the impact characteristics is examined for a shorter time interval, which contains all the facets of interest. The selected interval comprises the first 294 hammer blows. Figure 7.6

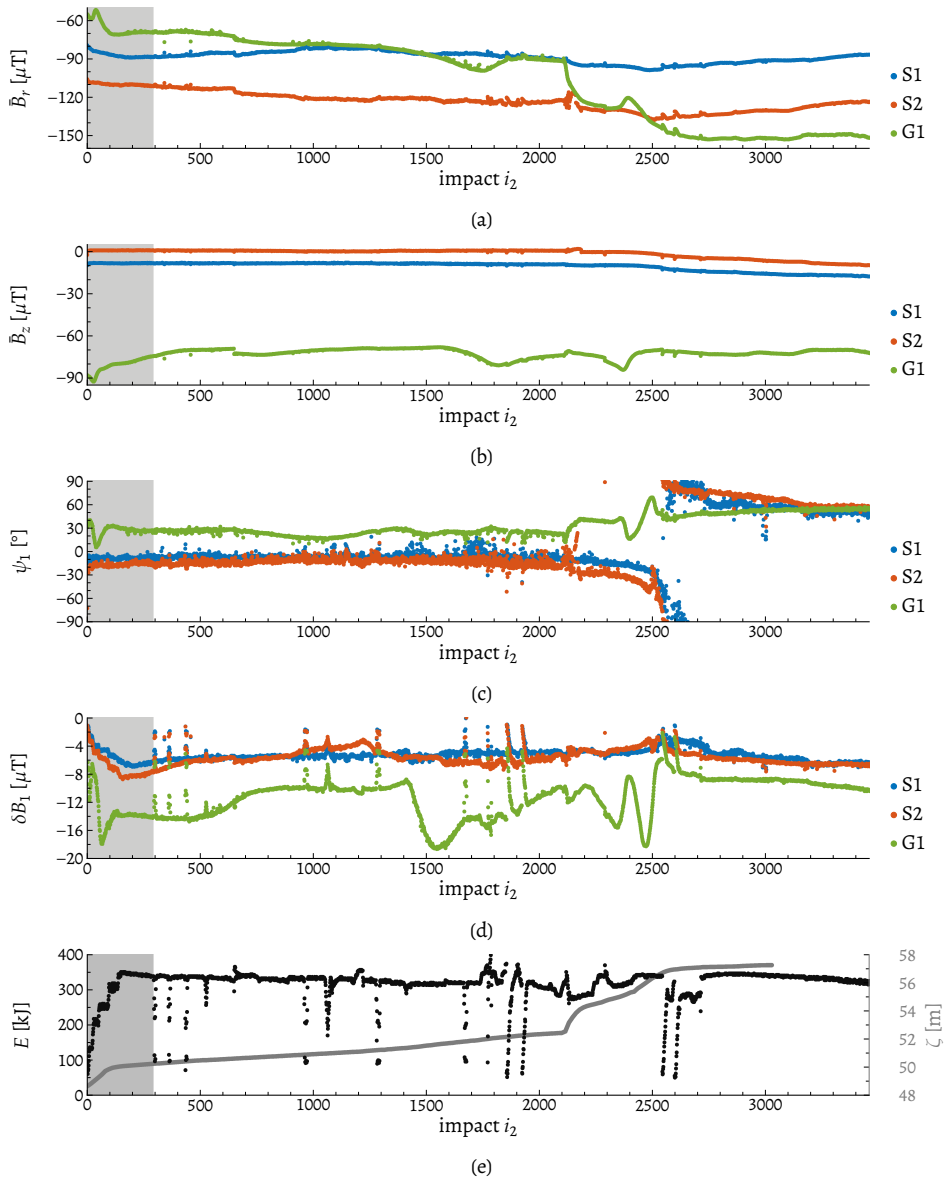


Figure 7.5: Overview of the impact characteristics measured with the reduced measurement set-up on the second installation day. The grey shaded area indicates the initial phase. (a) Radial component of remanent stray field. (b) Axial component of remanent stray field. (c) Angle of the major principle component with respect to the $r\theta$ -plane. (d) Maximum deviation from the remanent stray field. (e) Hammer energy (black) and pile penetration (grey).

presents the impact characteristic for the sleeve-based sensors during $i_2 = [1, 294]$, which is also indicated by the grey area in Figure 7.5. During this interval, the hammer energy was increased in steps of 50 kJ until the maximum hammer energy of 350 kJ was reached. Initially, the pile penetrated the soil by 2 m; however, when the maximum hammer energy was reached, the pile did not significantly progress into the soil (Figure 7.6e). For S1 and S2, the remanent magnetic field \bar{B} and the angle of the major principle component ψ_1 did not considerably change due to the impacts.

Figure 7.6d presents the magnetic deviation from the remanent field δB_1 , which evidently follows a trend similar to the one displayed by the hammer energy E . According to the elastic theory of impacting bars (Timoshenko and Goodier, 1951, pp. 438–452), the peak strain $\delta\epsilon_z$ is expected to be proportional to the square root of the impact energy E . This assertion will be critically assessed later in this chapter, when strain measurements are available. To determine the exact relation between the two quantities, δB_1 is plotted against the square root of the impact energy E in Figure 7.7. The distribution of the data suggests that the quantities are related via a polynomial expression, namely:

$$\delta B_1 \approx \alpha_2 E + \alpha_1 \sqrt{E}, \quad (7.7)$$

in which α_1 and α_2 are calibration constants which are determined by means of polynomial regression, the results of which are presented in Figure 7.7. Clearly, a quadratic relation exists between the hammer-induced peak strain and the resulting stray field variation. Note that the values of the calibration constants are only valid for these particular sensor locations, since the remanent stray field determines the actual magnetomechanical response.

7.2.2. Response of the ground-based sensor

For the ground-based sensor, the impact characteristics show a large variation over the course of reported impact range, which is a direct result of the pile moving relative to the sensor due to the pile penetrating the soil. For example, the remanent stray field changes substantially when the pile progresses further into the soil (Figures 7.5a and 7.5b). This is a direct consequence of the inhomogeneous distribution of the magnetisation of the structure, which, in turn, is a result of the presence of the circumferential welds.

Considering the characteristics associated with the transient response of the pile, δB_1 measured by G1 shows a less regular pattern than obtained by its sleeve-based counterparts. Even though the hammer restarts are visible in Figure 7.5d (signalling a dependency on the hammer-induced strain), the amplitude of δB_1 deviation also varies with the remanent stray field. Although this complicates the applicability of a ground-based sensor as a non-contact strain measurement device, it does confirm that the local magnetisation level determines the magnetomechanical response of the structure.

A different perspective of the ground-based sensor data is obtained by considering the evolution of the magnetic characteristics with increasing penetration depth as presented

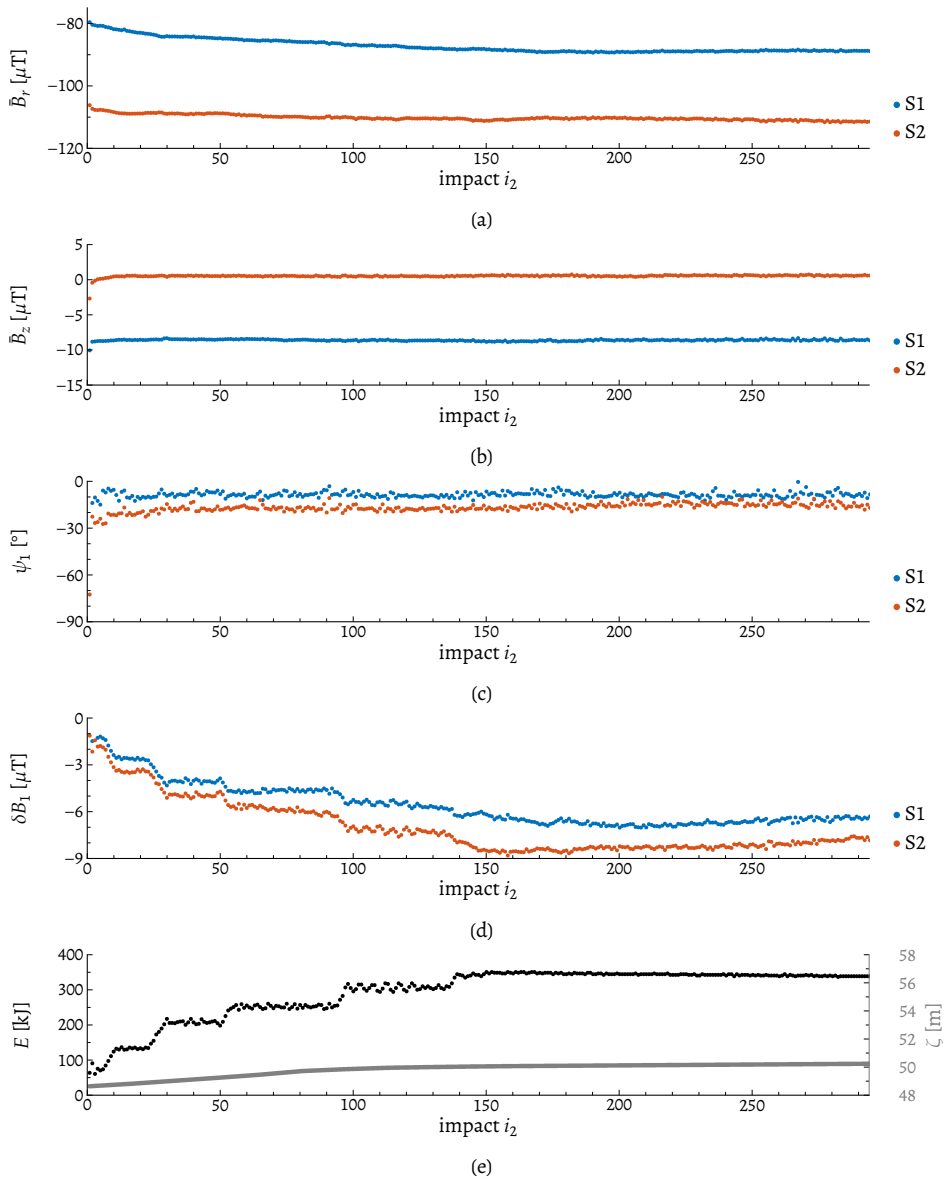


Figure 7.6: Overview of the impact characteristics collected by the sleeve-based sensors of the reduced measurement set-up during the initial phase of the second installation day. (a) Radial component of remanent stray field. (b) Axial component of remanent stray field. (c) Angle of the major principle component with respect to the $r\theta$ -plane. (d) Maximum deviation from the remanent stray field. (e) Hammer energy (black) and pile penetration (grey).

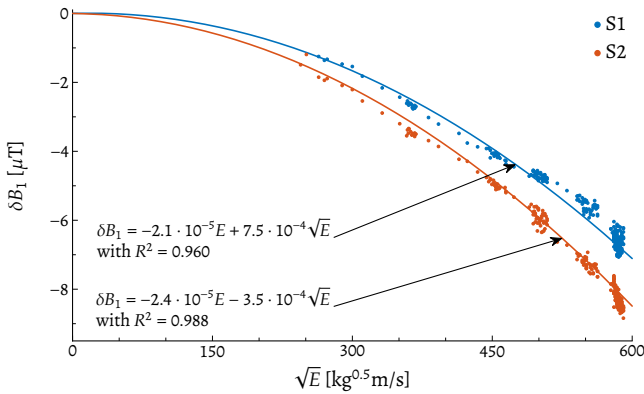


Figure 7.7: Maximum deviation from the remanent field δB_1 plotted against the square root of the impact energy E for S1 and S2 as registered during $i_2 = [1, 294]$. Using linear regression, the constants of the quadratic relation have been determined.

in Figure 7.8. The components of the remanent stray field \vec{B} show a distinct pattern that repeats every 3 m, which is caused by the circumferential welds in the pile. Compared to the fairly homogeneous material in between them, the welds have significantly different magnetic properties, resulting in a local reduction of the magnetic susceptibility, creating the markings in the stray field. Furthermore, the radial component of the remanent stray field increases for increasing ζ , which results from the sensor approaching the top of the pile.

A less regular image emerges for the impact characteristics related to the dynamic response (Figures 7.8c and 7.8d). Although an oscillation in δB_1 and ψ_1 is observed around the weld location, these features are less pronounced than those for the remanent stray field \vec{B} at the same location. The large variability of δB_1 and ψ_1 with penetration depth confirms the conclusion drawn above that the dynamic magnetomechanical response is predominantly determined by the local magnetisation in the vicinity of the sensor.

7.3. Analysis of data collected by the full measurement system

On the final installation day, the full measurement system was employed around the pile. Table 7.4 summarises the used sensors including their circumferential position θ , axial position a , and (for the magnetometers) the distance d from the surface of the pile. A total of eight biaxial magnetometers were used: four were attached to the sleeve (S1–S4) and four were placed on tripods (G1–G4). Each of these configurations completely enclosed the pile as the sensors were placed 90° apart. As the magnetomechanical data collected by a ground-based sensor is less consistent due to the relative motion between the sensor and the pile, this section will focus on the sleeve-based data only. Figure 7.9 shows the circumferential positions of the sleeve-based sensors with respect to the geomagnetic field direction. In

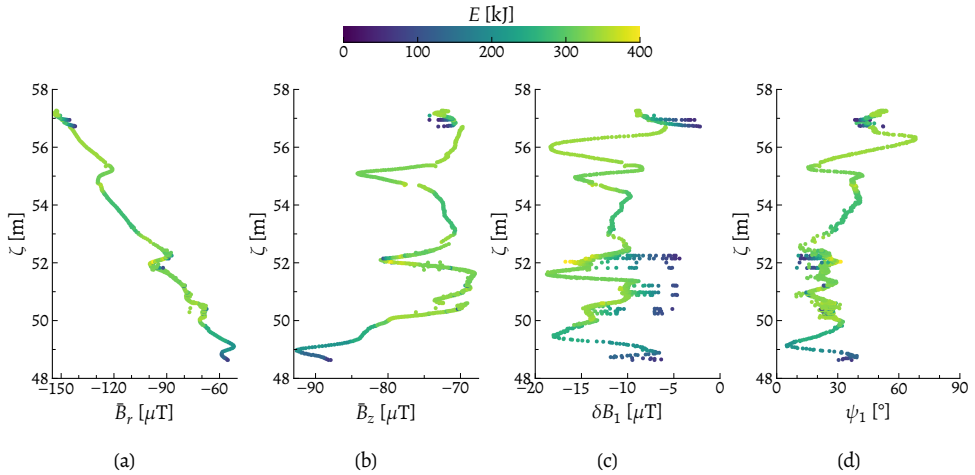


Figure 7.8: Magnetic characteristics measured by ground-based sensor G1 in the reduced system plotted against the penetration depth. The colour of the points indicates the hammer energy. (a) Radial component of the remanent stray field. (b) Axial component of the remanent stray field. (c) Maximum deviation from the remanent field. (d) Angle of the major principle component.

Table 7.4, the index i_3 indicates the number of the hammer blows in which the sensor was active (a total of 141 blows were registered).

Figure 7.10a shows the measurement system during the tests. Compared to the reduced set-up ($a = 3.5$ m), the sleeve-based sensors were closer to the edge of the sleeve ($a = 2.75$ m) to prevent damage to the sensors if the pile would unexpectedly progress into the soil by a considerable amount during the installation. Contrary to the first part of the campaign, the hammer-sleeve assembly did not rotate significantly. Consequently, the circumferential location of all sensors is assumed to be fixed throughout this part of the experimental campaign. During the impacts, penetration data was not collected due to malfunctioning of the optical sensor.

Most importantly, axial strains in the structure were recorded by two diametrically-positioned Pile Driving Analysers (PDAs), which were directly attached to the pile surface using an adhesive. Figure 7.10b shows a close-up of one of the PDA sensors (PDA1). A total of 141 hammer blows were registered with the full measurement system; but only during the first 83 impacts, the strain was recorded. In the subsequent section, the strain is analysed first, whereafter the correlation between the magnetic response and the strain is examined.

7.3.1. Hammer-induced axial strain

As indicated in Table 7.4, two conventional strain measurement devices (PDAs) were diametrically attached to the surface of the pile. Unfortunately, after only seven hammer blows, PDA2 detached from the pile, leaving only PDA1 functioning. The premature failure of PDA2 accentuates the potential benefit of non-contact sensors over classical contact-based devices

Table 7.4: Overview of the full measurement system. For each sensor, the measured quantities are listed; the index i specifies the registered number of impacts in which the listed sensor was active; θ and a are the circumferential and axial positions, respectively; for the biaxial magnetometers, the distance from the surface of the pile is denoted by d .

Sensor	Measurement	i_3	θ [°]	a [m]	d [m]
S1	B_z, B_r	1–141	20	2.75	0.20
S2	B_z, B_r	1–141	110	2.75	0.20
S3	B_z, B_r	1–141	200	2.75	0.20
S4	B_z, B_r	1–141	290	2.75	0.20
PDA1	ϵ_z	1–83	0	3.50	-
PDA2	ϵ_z	1–7	180	3.50	-

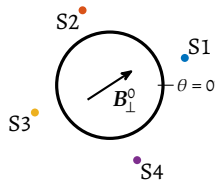


Figure 7.9: Sensor positions for the sleeve-based sensors in the full measurement system. The arrow indicates the direction of the horizontal component of the geomagnetic field B_{\perp}^0 .

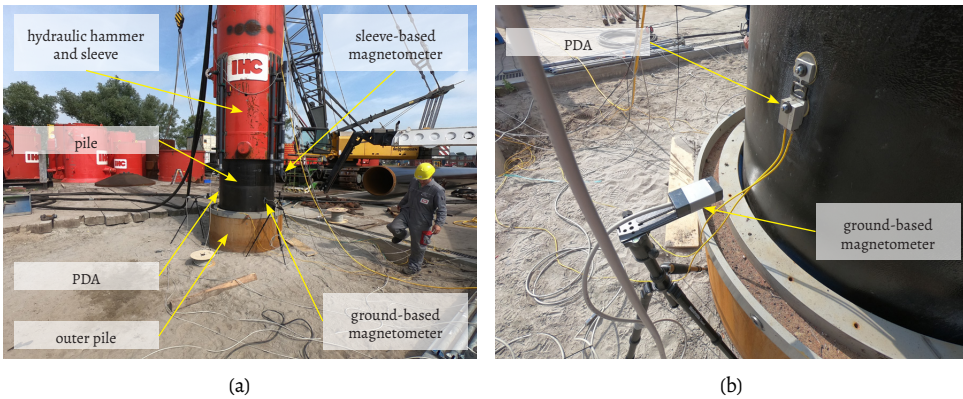


Figure 7.10: Two photographs of the set-up of the full measurement system. (a) Overview of the full measurement system during installation of the inner pile. (b) Close-up of sensor PDA1 attached to the pile; sensor G1 is placed on the tripod.

to monitor the strain in the structure. Due to the malfunctioning of PDA2, the discussion is predominantly based on the data obtained from PDA1.

Figure 7.11 presents the time-frequency analysis of typical signals measured during impact $i_3 = 7$. Directly following the initial compressive strain pulse, the axial strain signals of PDA1 (Figure 7.11a) and PDA2 (Figure 7.11d) display high-frequency oscillations that dominate the measurements. The pronounced peaks in the amplitude spectra confirm their presence; around 800 Hz for PDA1 (Figure 7.11b), and approximately 550 Hz and 1400 Hz for PDA2 (Figure 7.11e). These rapid fluctuations persist much longer ($\Delta t \approx 200$ ms) than the expected duration of an impact-induced strain pulse ($\Delta t \approx 10$ ms). Moreover, these peaks are absent in the time-frequency analysis of the axial component of the magnetic stray field (Figures 7.11g and 7.11h). Consequently, it is reasonable to assume that the oscillations have a different cause than the actual structural vibrations; most probably, they stem from the vibrations of the wire connected to the device. To eliminate these undesired artefacts from the signals, which do not represent physical strains in the structure, a low-pass filter with a cut-off frequency of 450 Hz is applied to the recordings. Figures 7.11c and 7.11f compare the original and filtered strain signals for PDA1 and PDA2, respectively, revealing that, after an initial compressive strain pulse, only relatively small strains are present in the structure. Since these high-frequency oscillations were originally absent in the stray field, the magnetic signal is largely unaffected by the applied filter (Figure 7.11i).

From the filtered strain signals, the peak strains $\delta\varepsilon_z$ are extracted for PDA1 using the procedure described in Section 7.1.3. Figure 7.12a presents the results for impacts $i_3 = [1, 83]$ together with the impact energy registered by the hammer. Apart from their sign, the quantities appear to follow a similar trend. According to the elastic theory of impacting bars (Timoshenko and Goodier, 1951, pp. 438–452), it is expected that the peak strain is proportional to the square root of the impact energy E . The use of this one-dimensional theory is justified here by the fact that a hammer blow excites frequencies well below the ring frequency f_r of the structure, i.e.:

$$f_r = \frac{1}{2\pi R} \sqrt{\frac{E_p}{\rho_p (1 - \nu_p^2)}} = 1416 \text{ Hz.} \quad (7.8)$$

The amplitude spectra presented in Figure 7.11 indicate that the hammer mainly excites frequencies below 450 Hz. Hence, a one-dimensional theory suffices to describe the axial wave propagation in a monopile in this case (Chapter 2).

To determine the relation between the peak strain and the square root of the impact energy from the experimental data, Figure 7.12b shows a plot of these two quantities. A linear fit to the data confirms that the assumed proportionality applies, namely:

$$\delta\varepsilon_z \approx -1.33\sqrt{E}, \quad (7.9)$$

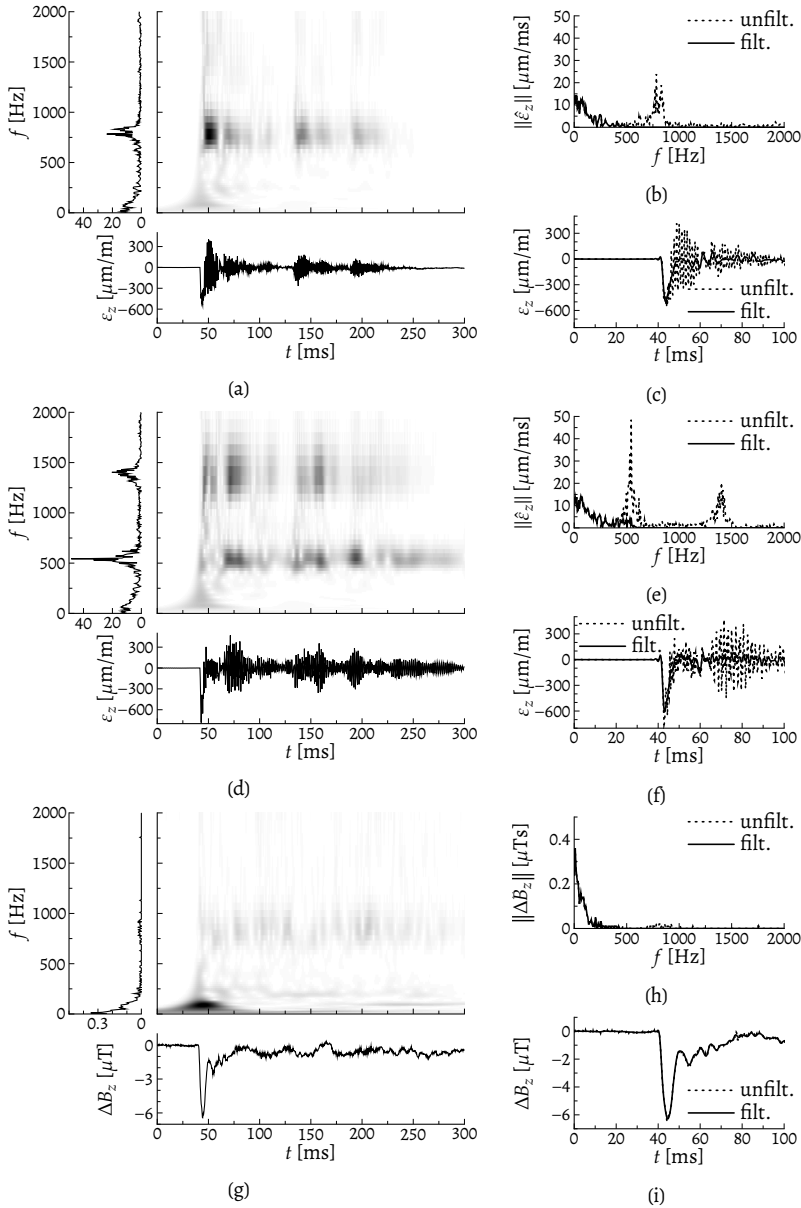


Figure 7.11: Time-frequency analysis of the signals measured during a single hammer blow (impact $i_3 = 7$). The filtered signals are obtained with a low-pass filter with a cut-off frequency of 450 Hz. (a) Time-frequency plot of PDA1. (b) Amplitude spectrum of PDA1. (c) Time series of PDA1. (d) Time-frequency plot of PDA2. (e) Amplitude spectrum of PDA2. (f) Time series of PDA2. (g) Time-frequency plot of the axial component of S4. (h) Amplitude spectrum of the axial component of S4. (i) Time series of the axial component of S4.

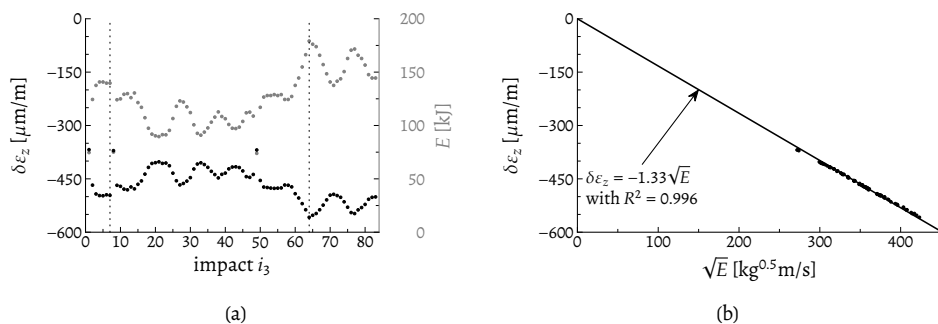


Figure 7.12: Analysis of the measured peak strain and the impact energy registered by the hammer. (a) Peak strain (black) and impact energy (grey) for each hammer blow. (b) Peak strain against the square root of the impact energy including a linear fit to the data.

Table 7.5: Normalised correlation coefficients for the strains and the major principle component of the magnetic signals for impact $i_3 = 7$. The table is symmetric; therefore, only the upper half is shown for clarity.

	PDA1	PDA2	S1	S2	S3	S4
PDA1	1	0.96	0.64	0.86	0.65	0.89
PDA2		1	0.56	0.78	0.57	0.81
S1			1	0.87	0.94	0.85
S2				1	0.86	0.99
S3					1	0.84
S4						1

7

verifying that the elastic one-dimensional theory is adequate in this case. With this relation, the hammer energy can be used to estimate $\delta\epsilon_z$ in absence of an actual strain measurement, which is the case from impact $i_3 = 84$ onwards. The proportionally constant in the above relation only depends on the properties of the hammer, the contact area between the hammer and the pile, and the material properties of the pile. Thus, in principle, the value of this constant may be computed a priori under the assumption of one-dimensional wave propagation.

To assess whether the hammer-induced strains are axially symmetric, the correlation coefficient (Section 6.2.2) for the strain signals collected by PDA1 and PDA2 during impact $i_3 = 7$ is determined (Table 7.5). The two signals correlate extremely well ($c = 0.96$), suggesting that the induced strains at the considered diametric positions are nearly identical in terms of the excited frequency range. This, in turn, indicates that the hammer force is introduced evenly along the circumference of the pile top. Consequently, it seems reasonable to assume that each hammer blow generates an axially symmetric compressive strain field.

7.3.2. Correlation between strain and magnetic stray field measurements

Table 7.5 presents the normalised correlation coefficients (Section 6.2.2) for the axial strains and the magnetic measurements along the major principle component ΔB_1 for impact $i_3 = 7$.

Note that the correlation table is symmetric; only the upper half is presented. From the data, the following is concluded:

- (i) the two strain signals are similar ($c = 0.96$);
- (ii) magnetometer pairs that are placed diametrically (e.g. S1 and S3) exhibit a higher mutual correlation compared to the sensors located 90° apart, e.g. compare S1 and S3 ($c = 0.94$), S1 and S2 ($c = 0.87$), S2 and S4 ($c = 0.99$), and S3 and S4 ($c = 0.84$);
- (iii) the magnetic field signals of S2 and S4 strongly correlate with the strain ($c > 0.78$);
- (iv) for S1 and S3, the correlation between the stray field and the strain is less pronounced ($c > 0.56$).

Given the direction of the geomagnetic field, which is $\beta \approx 33^\circ$ (Figure 7.2b), the radial component of S1 and S3, at $\theta = 20^\circ$ and $\theta = 200^\circ$, is almost aligned with the external field, while the radial component of S2 and S4, at $\theta = 110^\circ$ and $\theta = 290^\circ$, is perpendicular to it. Acknowledging this fact, the above observations show that the orientation of the magnetometer with respect to the external field partly determines the similarity with the impact-induced strains. Since the latter are axially symmetric, the observed magnetomechanical response is caused by the spatial variation of the structure's magnetisation, which is not axi-symmetric due to the presence of the external field.

Naturally, the data presented in Table 7.5 only assesses a single hammer blow. To obtain a more general picture, Figure 7.13 shows the normalised correlation coefficients between the axial strain measured by PDA1 and the major principle component of the magnetic stray field for the first 83 impacts. Again, for the signals measured by S2 and S4 (with a radial component perpendicular to the external field), the correlation is high ($c > 0.8$); while for S1 and S3 (with a radial component aligned to the external field), the correlation is less pronounced, albeit still reasonable ($c > 0.6$). This confirms the aforementioned dependency of the measured magnetomechanical response on the circumferential position relative to the geomagnetic field direction.

7.3.3. Analysis of the impact characteristics

Up to now, the discussion focused on the comparison between the stray field and the strains. However, this does not provide any information regarding the actual amplitude of the changes or the remanent stray field values. In this section, the physical characteristics of these measurements are further analysed.

In Figure 7.14a, the remanent magnetic field \bar{B}_r displays little variation over the course of the reported impacts. However, \bar{B}_z (Figure 7.14b) does exhibit a slight decrease at all four positions, which, at first instance, is not to be expected since the sleeve-based sensors retain their relative position with respect to the pile. A careful examination of the set-up (Figure 7.10a) shows that this is caused by the penetration of the pile, which moves the

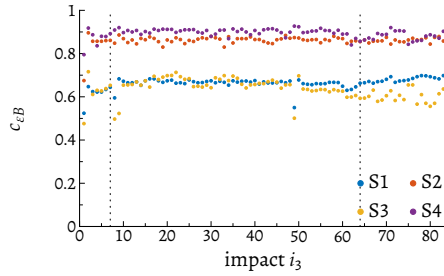


Figure 7.13: Normalised correlation coefficients between the axial strain and the major principle component of stray field.

7

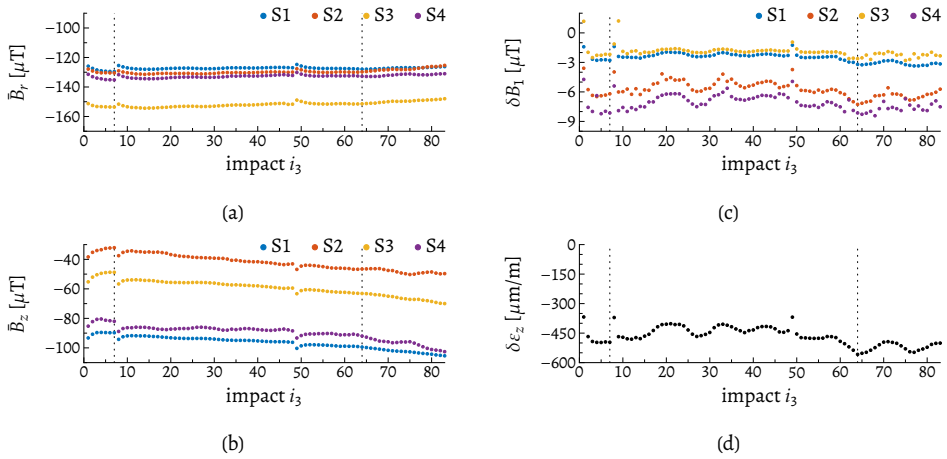


Figure 7.14: Characteristics extracted for impacts 1–83 recorded by the sleeve-based sensors. (a) Radial component of the remanent stray field. (b) Axial component of the remanent stray field. (c) Maximum deviation of the major principle component of the dynamic stray field. (d) Peak strains.

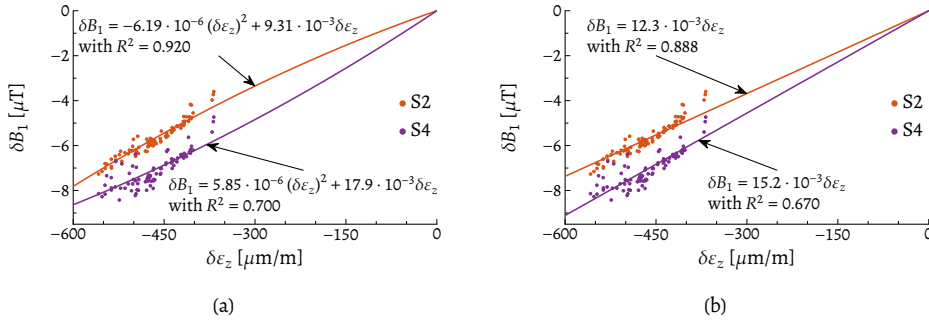


Figure 7.15: The maximum variation of the major principle component versus the peak strain during impacts $i_3 = [1, 83]$ for S2 (orange) and S4 (purple) in conjunction with (a) a quadratic and (b) a linear fit to the data.

sensors closer to the edge of the outer pile (Figure 7.2c); the latter has a significant magnetic stray field of its own, which resembles the stray field of a cylinder caused by a vertical external field (Figure 4.10). This additional stray field simply adds to the external field, and makes the latter spatially varying. For the outer pile, the radial component varies less than the axial component when the pile is approached from above, explaining the observed behaviour for the remanent field.

To assess the amplitude of the dynamic stray field, Figure 7.14c presents the maximum variation of the major principle component δB_1 . For each magnetometer, the strain-induced amplitude is different, which is to be expected given the spatially-varying magnetisation of the structure. Nevertheless, δB_1 displays a trend resembling that of the peak strain (Figure 7.14d). To examine this correspondence in more detail, Figure 7.15 plots the two quantities versus each other for the two sensors with the highest correlation with the strain, i.e. S2 and S4. Similar to the data collected using the reduced set-up (Figure 7.7), a polynomial relation is found:

$$\delta B_1 \approx \alpha_2 (\delta \varepsilon_z)^2 + \alpha_1 \delta \varepsilon_z, \quad (7.10)$$

in which α_2 and α_1 are calibration constants, which are determined by means of polynomial regression. For this particular case, however, the data points suggest that this relation can be approximated by the following linear expression:

$$\delta B_1 \approx \alpha_1 \delta \varepsilon_z, \quad (7.11)$$

in which $\alpha_1 = 12.3 \cdot 10^{-3} \text{ T}$ and $\alpha_1 = 15.2 \cdot 10^{-3} \text{ T}$ for S2 and S4, respectively. In addition to the excellent correlation of the full time series of these two quantities as discussed earlier, the above linear relation implies that the dynamic stray field corresponds one-to-one with the hammer-induced strains as obtained by the full measurement set-up. Consequently, this expression serves as a basis for a method to infer the strains during a monopile installation using non-contact stray field measurements.

7.4. Sources of interference

Before addressing two practical applications of employing magnetometers during a monopile installation, sources of interference for the successful application of such measurements are shortly discussed, which can be divided into two categories. First, in the vicinity of the pile, the total magnetic field is not only determined by the stray field of the pile. Other magnetic sources may contribute to the total magnetic field as well, several of which can be identified during the installation of a pile. Second, movement or rotation of the magnetometer itself will alter the measured signal, since a reorientation of the sensor's sensitive axes relative to the magnetic field is also recorded. In this section, the main sources of interference are identified and possible mitigation strategies are briefly considered.

7.4.1. Evolution towards a magnetic equilibrium

The largest disturbance for the consistency of the magnetic response of a steel structure are irreversible changes of the remanent stray field. As shown in Chapters 5 and 6, the first impacts with a new peak strain can drastically alter the remanent field, as the magnetisation irreversibly progresses towards a new magnetic equilibrium due to the supplied elastic strain energy. Only when a magnetic equilibrium has been reached, the strain-induced transient stray field becomes completely reversible, meaning that subsequent identical impact are consistent and repeatable. So far, the presented data have not shown large irreversible changes in the remanent stray field, since only data from the two final installation days have been analysed. However, since the pile has not been demagnetised prior to the start of the installation, one might anticipate that this progression towards an equilibrium does occur. Naturally, this expectation is correct, and it becomes apparent when the data of the first day is examined.

Figure 7.16 shows the impact characteristics of sleeve-based sensor S2 measured during the first days of the measurement campaign. At the start of the installation (indicated in the Figure by the grey-shaded area), the remanent field (\bar{B}_r and \bar{B}_z) shows large irreversible changes, monotonically moving towards an equilibrium value. Only when the maximum hammer energy ($E = 350 \text{ kJ}$) has been introduced for a sufficient number of times, the remanent values becomes constant. Note that when energy below the previous maximum is introduced (e.g. for $i_1 = [150, 200]$), the remanent field remains constant.

As long as the structure's magnetisation is not at this equilibrium, the magnetomechanical response to a hammer blow with identical energy is not repeatable, which is clear from irregular behaviour of δB_1 during the initial blows. Hence, the data from this in-situ measurement campaign support the conclusion drawn in Chapter 6 that the structure must be at a magnetic equilibrium to create a state in which the impact-induced strain can successfully be inferred from non-contact magnetic field measurements. Fortunately, an ordinary monopile installation requires several thousands of hammer blows, effectively limiting this disturbance to the initial phase of an installation.

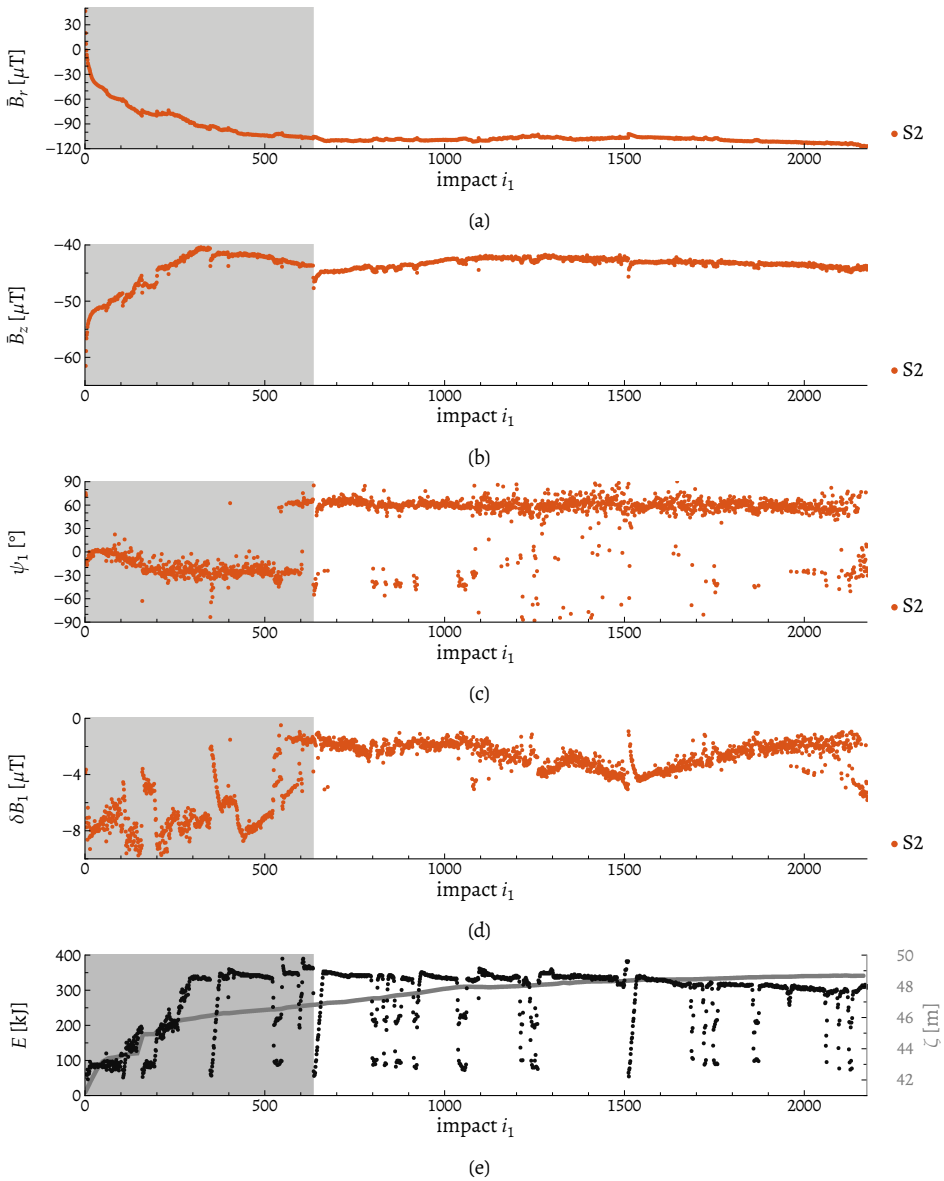


Figure 7.16: Overview of the impact characteristics measured with the reduced measurement set-up on the initial installation day. The grey shaded area indicates the phase in which the remanent stray field approached the magnetic equilibrium. (a) Radial component of remanent stray field. (b) Axial component of remanent stray field. (c) Angle of the major principle component with respect to the $r\theta$ -plane. (d) Maximum deviation from the remanent stray field. (e) Hammer energy (black) and pile penetration (grey).

7.4.2. Magnetic stray fields of other ferromagnetic objects

During the entire installation sequence, two ferromagnetic objects exert their influence on the measured quantities through their own substantial magnetic stray field: the outer pile, which was installed prior to the inner pile; and the hammer-sleeve assembly. Figure 7.10a shows both these disturbing structures.

For a ground-based sensor, the stray field of the outer pile is a time-invariant external field, since the distance between the sensor and the outer pile remains constant throughout the installation. However, for the sleeve-based sensors, it is an additional field which becomes more dominant when the sensors approach the outer pile due to the pile penetrating further into the soil. This effect is most clearly demonstrated in the graph of the impact characteristics of the reduced measurement system (Figures 7.5a and 7.5b), in which, from impact $i_2 = 2400$ onwards, the magnetic stray field of the outer pile starts to influence the remanent field. Due to the change of the local background field, the magnetisation of the top part of the pile alters accordingly. This explains the sudden change of the angle of the major principle component ψ_1 for S1 and S2 (Figure 7.16c), while the provided hammer energy remains unchanged.

For a sleeve-based sensor, the influence of the sleeve's stray field is unclear at present, although it might be expected that strain induced by a hammer blow in the sleeve also alters its stray field via the magnetomechanical effect. Future research should quantify the influence of this structure on the measurements.

7.4.3. Cap pressure

Before each hammer blow, cap pressure is built up inside the hammer, which is released during the impact. This pressure introduces strains in the hammer's casing, which, through the magnetomechanical effect, changes the magnetisation of hammer itself. As a result, the changing pressure could influence the magnetic field measurements. Figure 7.17a shows the build-up and release of the pressure for a series of hammer blows. Next to that, the variation around the remanent field ΔB_1 for two sleeve-based (S1 and S2) and one ground-based (G1) sensors is presented in Figure 7.17b. In the figure, the narrow peaks in the magnetic variation correspond to the hammer blows. Due to the large distance between G1 and the hammer, the magnetic signal is essentially unaffected by the varying cap pressure. On the contrary, the proximity of S1 and S2 to the hammer makes them sensitive to the pressure variations, which are visible as the low-frequency oscillation in between the impacts. Moreover, ΔB_1 displays a sharp increase prior to the first hammer blow. Nonetheless, the signal stabilises, apart from the impact-induced variations, after the initial impacts. It is thus expected that cap pressure does not disturb the actual value of δB_1 .

7.4.4. Rotation of the hammer-sleeve assembly

As seen in Section 7.2, the gradual rotation of the hammer-sleeve assembly around the z -axis hinders the comparison of the magnetomechanical response for non-consecutive

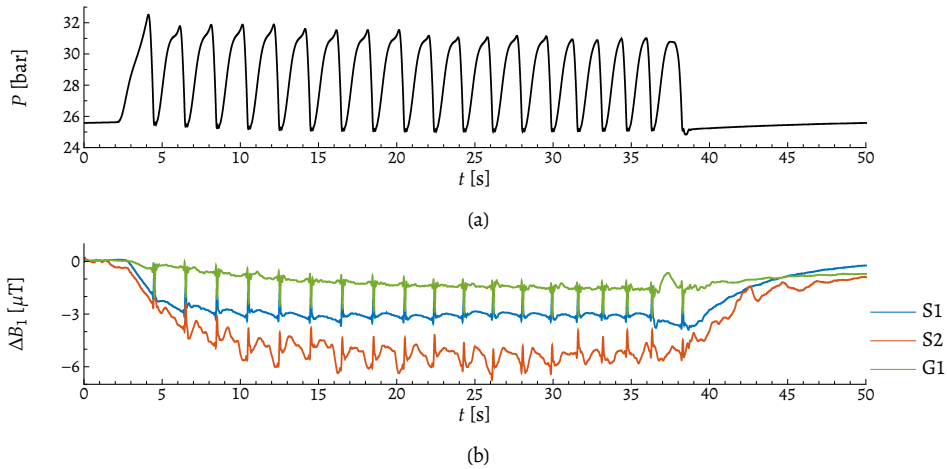


Figure 7.17: Analysis of the effect of cap pressure inside the hydraulic hammer on the magnetomechanical response as measured with the reduced measurement system during a short series of hammer blows. (a) The build-up and release of the cap pressure. (b) The variation of the magnetic field along the major principle axis.

impacts. This is attributed to change of the local magnetisation in the vicinity of the sensor caused by the rotation. A straightforward solution for this complication is to measure the rotation of the hammer-sleeve assembly in real-time. However, knowledge of the current circumferential position of the sensor alone is insufficient to mitigate the problem. For that, a denser array of magnetometers surrounding the circumference of the pile is required. In that case, a full circumferential profile of the stray field is obtained. Although this is possible, it is a complex and cost-ineffective solution. Alternatively, another mechanism may be employed to keep the sensor at the same location relative to the pile. Again, developing such a mechanism is left for future research.

7.5. Non-contact strain measurement

Since the correlation between the measured strain and dynamic stray field is excellent for the sleeve-based sensors (Section 7.3.1), a magnetometer that retains its position relative to the structure can be used to infer the impact-induced strain in the structure. This non-contact method is based on the relation between the peak strain and the maximum deviation from the remanent field. Two of these polynomial expressions have been derived in this chapter, one for the reduced measurement system (Section 7.2.1) and one for the full measurement system (Section 7.3.3). For simplicity, the linear approximation of the latter is used in the following. Nevertheless, this general procedure is identical for the quadratic relation.

After inverting the expression presented in Equation (7.11), the peak axial strain can be inferred from the maximum deviation of the major principle component of the stray field

by applying:*

$$\delta\tilde{\varepsilon}_z = \frac{1}{\alpha_1} \delta B_1, \quad (7.12)$$

in which the tilde denotes an estimated value. For the two magnetometers with the best correlation to the strain (S2 and S4), the estimated peak strains $\delta\tilde{\varepsilon}_z$ are presented in Figure 7.18a in conjunction with the measured peak strains $\delta\varepsilon_z$. For impacts $i_3 = [1, 83]$, the latter are directly obtained from PDA1, while, from impact $i_3 = 84$ onwards, the peak strains are computed from the registered impact energy by applying Equation (7.9). For impacts $i_3 = [1, 95]$, the inferred strain values correspond reasonably well with the peak strain obtained using the conventional methods, since the error in that impact range is generally less than 10% (the grey band in Figure 7.18b). The error becomes large ($\gg 10\%$) for impact $i_3 = 96$ and higher, due the change in the remanent stray field when the sensors approach the outer pile (Section 7.4.2). To illustrate the evolution of the remanent field, Figure 7.18c shows the deviation of the four remanent values from the average remanent value for impacts $i_3 = [1, 83]$ (indicated by $\langle \tilde{B}_j \rangle$). Initially, the remanent values meander around the average; however, from impact $i_3 = 84$ onwards, the values diverge significantly, which coincides with the deterioration of the quality of the estimated peak strains. Clearly, the α_1 -coefficient must be recalibrated when the remanent stray field permanently changes.

Permanent stray field changes reflect irreversible changes of the magnetisation of the structure, for which three situations are relevant here:

- (i) the magnetisation is not yet at a magnetic equilibrium, e.g. at the start of the pile installation, elastic deformation pushes the magnetisation towards this equilibrium (Section 7.4.2);
- (ii) a ferromagnetic object approaches the magnetometer, e.g. the outer pile in the current set-up. Normally, such an auxiliary structure is not present during a monopile installation (Section 7.4.1);
- (iii) a region of plastic deformation develops in the vicinity of the magnetometer (Chapter 5).

Thus, for optimal results, the calibration procedure should be performed as soon as the remanent field stabilises. Naturally, this coefficient should also be recalibrated in case the sensor is repositioned relative to the pile.

Since the time series of the strain and the dynamic stray field correlate well ($c > 0.8$), the calibration coefficient α_1 determined for the peak values is equally valid to express the full

*For the quadratic relation, the peak axial strain may be estimated using:

$$\delta\tilde{\varepsilon}_z = \frac{2}{\alpha_1 \pm \sqrt{\alpha_1^2 + 4\alpha_2\delta B_1}} \delta B_1,$$

which reduces to Equation (7.12) when $\alpha_1^2 \gg 4\alpha_2\delta B_1$. Note that two values for $\delta\tilde{\varepsilon}_z$ are given by this equation. Selecting the physically-admissible solution should be done with care. For simplicity, the linearised expression is used here to demonstrate the proposed method to infer the elastic strain from the dynamic stray field.

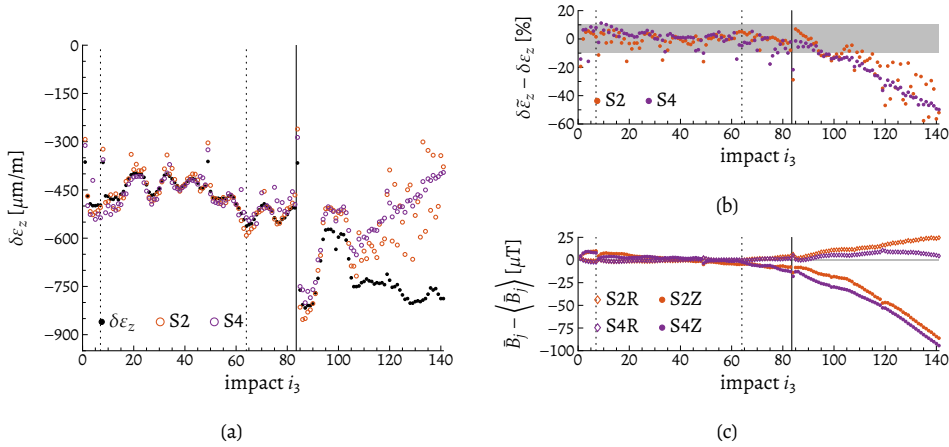


Figure 7.18: Peak strain estimation using the measure stray field variations of S2 and S4. For impacts $i_3 = [1, 83]$, the peak strain is directly measured, while, from impact $i_3 = 84$ onwards, it is computed from the registered impact energy. (a) Peak strain inferred from the magnetic stray field data using the calibrated relation. (b) Error of the estimated peak strain. The grey band indicates the region with $\pm 10\%$ error. (c) Deviation of the remanent stray field from the average remanent stray field during impacts $i_3 = [1, 83]$.

strain history in terms of the major component of the stray field, as follows:

$$\tilde{\epsilon}_z(t) = \frac{1}{\alpha_1} \Delta B_1(t). \quad (7.13)$$

Figure 7.19 shows the resulting time signals for impact $i_3 = 64$. The satisfactory correspondence between the inferred and measured strains demonstrate that data from magnetometer that retains its position relative to the structure can be used to infer the impact-induced strains in the structure using a non-contact sensor.

Using magnetometers to infer the hammer-induced strain has certain benefits over the application of conventional sensors, of which the most important was demonstrated by the premature failure of PDA2 during the reported measurement campaign as a result of the high accelerations experienced by that device. Naturally, a non-contact sensor is not exposed to such high contact forces, providing a more robust alternative. Moreover, the deployment of a magnetometer could be rapid and straightforward, perhaps by incorporating the device into the sleeve of the impact hammer, saving valuable time in the tight installation window. Contrary to optical techniques for non-contact strain measurement, the magnetomechanical approach performs equally well underwater, since the stray field is not disturbed by the presence of water, while optical signals will be distorted or blocked by the fluid. Consequently, the proposed magnetic method can be applied during a complete offshore installation, even for subsea structures.

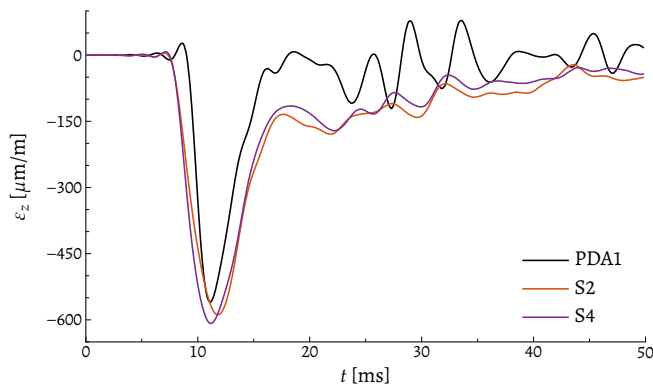


Figure 7.19: Measured axial strain for impact $i_3 = 64$ compared with the strain inferred from the stray field measurements of S2 and S4.

7.6. Pile penetration monitoring

A second application of magnetometers during a monopile installation pertains the non-contact real-time monitoring of the pile penetration. For the reduced measurement system, the results from the ground-based sensor with increasing penetration depth (Section 7.2.2) showed that the circumferential welds in the pile create a distinct pattern in the measured remanent magnetic field, indicating that the pile penetration might be inferred from non-collocated magnetic field measurements. Naturally, the sensor must retain its position relative to a fixed reference while the pile progresses into the soil. In the reported onshore installation, this reference is the ground. Offshore, one may create such a reference by attaching the sensor to the (jack-up) installation vessel.

Real-time knowledge of the pile penetration resulting from each hammer blow is vital to ensure safety during the installation process and to limit the amount of fatigue damage inflicted to the pile, since the energy of the blows can be adjusted accordingly based on the penetration speed. Moreover, after installation, the bearing capacity of the pile is estimated by measuring the pile's response to a single axial impact in a so-called restrike test (Schallert and Klingmüller, 2019).

Several techniques currently exist to monitor pile penetration. By registering the acceleration with a sensor mounted to the pile, the penetration is computed by integrating the signal twice in time (Wisotzki et al., 2019). Disadvantages of this approach include the need to attach the sensor to the surface of the pile, which is a delicate and time-consuming process, and the error in the computed displacement that accumulates due to filtering choices and the integration of the acceleration signal. Alternative techniques rely on optical signals. One such method is to deduce the distance between the top of the pile and a reference level based on the time-of-flight principle (Lee et al., 2002). However, in an offshore environment, a steady reference level is not available, since optical signals, instead of reflecting back to the

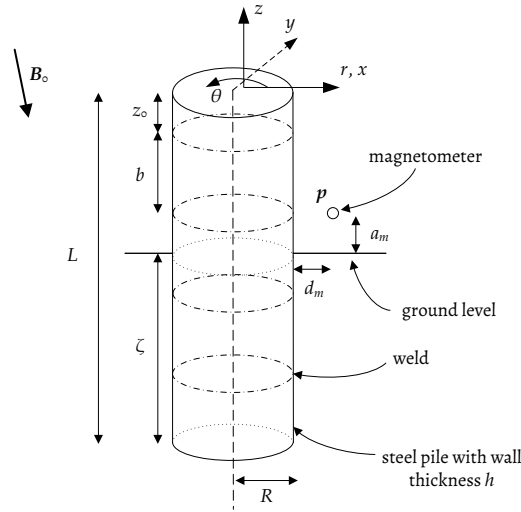


Figure 7.20: Schematic of the monopile installation indicating the parameters of interest.

detector, scatter as result of the surface waves at the water level. A different optical approach is to use a camera to track a predefined pattern that is applied to the surface of the pile, e.g. a black and white banded pattern. Several patterns have successfully been administered over the years, especially in the case of restrike tests (Lim and Lim, 2008; Oliveira et al., 2011; Raza et al., 2019; Yeu et al., 2016). These approaches share the necessity to prepare the surface of the pile with a distinct predefined visual pattern. A method to estimate the penetration from the measured magnetic stray field changes would be non-contact, significantly simplifying the deployment, and it does not require any preparation of the pile's surface to operate, i.e. no pattern has to be introduced. In the following, the pile's stray field is modelled to investigate whether it can be replicated with a simple model, which serves as a basis to infer the penetration from the magnetic signals.

7.6.1. Modelling the pile's stray field

A detailed schematic of the set-up of the pile installation is presented in Figure 7.20, which defines two coordinate systems: a cylindrical $r\theta z$ -coordinate system—in which r , θ , and z denote the radial, the circumferential, and the axial directions, respectively—and a Cartesian xyz -coordinate system. The coordinate systems share their origin, which is located at the top of the pile. Table 7.6 lists the numerical values of the relevant parameters of the pile: the radius R , length L , and wall thickness h . The installed pile is composed of cylindrical steel sections with a height b each, which are stacked on top of each other using circumferential welds. Before installation, the pile has been coated for corrosion protection, obscuring the exact locations of the welds. Despite the lack of visible confirmation, their positions relative to the pile top are known a priori. The distance z_0 reflects the shorter top segment of pile.

Table 7.6: Parameters of interest for the pile installed during the measurement campaign.

Parameter	Value	Parameter	Value
R	0.6096 m	z_0	0.5 m
L	62.0 m	ζ_0	48.62 m
h	0.050 m	a_m	1.5 m
b	3.0 m	θ_m	300°
		d_m	0.2 m

The current penetration depth ζ is defined as the distance from lower end of the pile to the ground level, implying that the pile is fully embedded into the soil when $\zeta = L$. The initial penetration depth ζ_0 is also listed in Table 7.6. The sensor's position p relative to the ground is given by the offset from the pile's surface d_m , the circumferential position θ_m and the height a_m .

In accordance with Chapter 4, the pile's volume is evenly subdividing into N_θ elements in the circumferential and N_z elements in the axial direction, totalling the number of elements to $N = N_\theta N_z$. To express the magnetisation in terms of the magnetic field, an appropriate constitutive equation is required. For a (locally) isotropic material, a scalar magnetic susceptibility χ suffices, and the magnetisation is given by:

$$\mathbf{M} = \chi (\mathbf{I} - \chi \mathbf{G}_r)^{-1} \frac{\mathbf{B}_0}{\mu_0}, \quad (7.14)$$

in which \mathbf{I} is the $2N \times 2N$ identity matrix, \mathbf{G}_r is a $2N \times 2N$ matrix representing the non-local interaction of the structure's magnetisation and $(\cdot)^{-1}$ denotes a matrix inversion. Subsequently, the stray field at p is determined by applying:

$$\mathbf{B}(p) = \mu_0 \mathbf{G}_p \mathbf{M}, \quad (7.15)$$

in which \mathbf{G}_p maps the magnetisation of the elements onto a magnetic field at p .

7.6.2. Model for the magnetic susceptibility

The experimental stray field data suggests that the magnetic properties differ in the vicinity of the circumferential welds. Therefore, the following axial distribution of the magnetic susceptibility is proposed:

$$\chi = \chi_0 - \chi_w \left(\sin \left(\frac{\pi (z - z_0)}{b} \right) \right)^n, \quad (7.16)$$

where χ_0 is the undisturbed susceptibility of the material, χ_w is the reduction of the susceptibility due to the presence of the weld, b is the distance between each weld, z_0 is an offset to correctly position the welds along the pile axis, and n is an even power to localise the reduced susceptibility to a narrow range around the weld's position. In this expression, b

and z_0 are determined by the geometry of the pile alone (Table 7.6). The numerical values of the remaining parameters have to be calibrated.

7.6.3. Simulated magnetic signature

To simulate the relative motion between the sensor and the pile, the stray field is evaluated along a line parallel to the axis of the pile, on which the evaluation points p are given in cylindrical $r\theta z$ -coordinates by:

$$p = \begin{bmatrix} R + d_m \\ \theta_m \\ \zeta + a_m - L \end{bmatrix}, \quad (7.17)$$

where $\zeta = [\zeta_0, \zeta_0 + 8.6]$ m, which coincides with the recorded penetration range on the second installation day (Table 7.2). Table 7.1 presents the corresponding numerical values for these parameters. The volume of pile is discretised in $N_\theta = 25$ and $N_z = 300$ elements. In this case, the penetration is measured independently, and the unknown parameters in the susceptibility formulation are found by comparing the simulated and measured data, resulting in $\chi_0 = 2100$, $\chi_w = 1600$, and $n = 20$. Figure 7.21a shows the susceptibility distribution resulting from these values.

The two components of the simulated magnetic field are presented in Figures 7.21b and 7.21c together with the measured data. Please note that the modelled values are shifted with a constant to match the measured signal; this shift represents the exact background field at the sensor location. From the figure, it is clear that the trend in the measured data is captured correctly by the simulated data. Only \bar{B}_z differs for lower values of ζ , which might be attributed to other material inhomogeneities affecting the susceptibility which are not accounted for in the present model. Nonetheless, the simple relation for the magnetic susceptibility that accounts for the presence of circumferential welds is able to reproduce the measured magnetic signature of the pile.

7.6.4. Discussion

The correspondence between the simulated magnetic signature and the measurements indicates that the simple susceptibility formulation given in Equation (7.16) is sufficient to model the magnetic state of the pile after a proper calibration is applied. In this case, the penetration depth is measured, significantly simplifying the calibration, since a fixed reference is present. Normally, however, this reference measurement of the penetration is obviously not available; only the initial penetration depth is known to some extent. Therefore, the calibration should be founded solely on the measured magnetic field data. Fortunately, the welds create a distinct marking when they pass the sensor, e.g. a peak in the \bar{B}_z value. Accordingly, as the weld positions are known at the start of the installation, the model can be calibrated based on the passage of one of those fixed markings, perhaps even constantly updating the model while new data is collected.

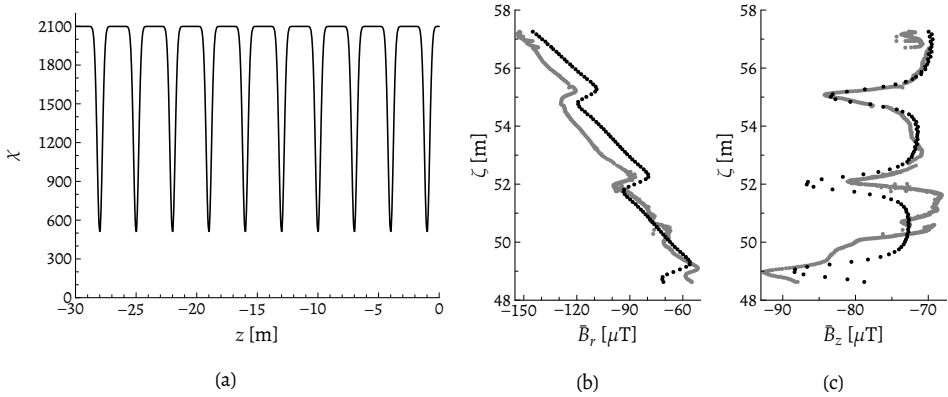


Figure 7.21: Model results for the magnetic stray field. (a) Modelled magnetic susceptibility along a part of the pile's axis. (b) Comparison of the simulated (black) and measured (grey) radial component of the remanent field versus penetration depth. (c) Comparison of the simulated (black) and measured (grey) axial component of the remanent field versus penetration depth.

Once the model is calibrated, the penetration depth can be inferred by comparing the measured stray field to the modelled one. However, the mapping between some values of \bar{B} and ζ is not unique (Figures 7.21b and 7.21c). Fortunately, the pile penetrates gradually into the soil; therefore, the penetration depth closest to the previous value should be selected. This additional step to extract the penetration depth from the magnetic data has not been elaborated on yet, and it is left for future research.

The proposed method to monitor the pile penetration has two benefits compared to currently used monitoring techniques; it relies on non-contact measurements, and it does not require an artificial tracking pattern applied to the pile's surface. The main application of the offered method is to monitor pile penetration during a full installation and not during a single hammer blow, e.g. a restrike test.

7.7. Conclusions

A full-scale in-situ measurement campaign has been conducted during an onshore monopile installation, resulting in a unique data set that contains the magnetomechanical response of a large-scale structure to high impact loads. Stray field data have been collected with two distinct sensor layouts: a set attached to the hammer's sleeve and a set of sensors placed on the ground. The former lay-out ensures that the sensors retain their relative axial position with respect to the pile throughout the installation. For these sleeve-based sensors, the major principle component of the measured dynamic stray field shows a strong correlation with the simultaneously measured axial strain ($c > 0.8$). Moreover, the peak strain and the maximum deviation from the remanent stray field are related through a polynomial relation, of which the degree and the coefficients depend on the position of the sensor relative to the

pile. The dependency of the sensor position on measured magnetomechanical response is confirmed by the data obtained with the ground-based sensors, which vary with increasing penetration depth.

Some sources of interference encountered during the in-situ installation have been discussed. Most importantly, only when the pile's magnetisation is at a magnetic equilibrium, the magnetomechanical response becomes consistent for impacts with identical energy. In a typical monopile installation, it is expected that the magnetic equilibrium is always attained. Other sources of interference, i.e. the stray field of nearby ferromagnetic objects and the rotation of the hammer-sleeve assembly, require further research to quantify their exact influence on the magnetomechanical measurements, which, most likely, will also be case specific.

From the magnetic stray field data, two practical applications of the non-contact magnetic stray field measurements during a monopile installation are identified. First, using the polynomial relation found between the peak strain and the maximum deviation of the dynamic magnetic signal as measured by the sleeve-based sensors, a non-contact method is proposed to infer the hammer-induced strain from the measured stray field data. After calibration, the method yields inferred time signals of the strain that have a satisfactory correspondence with the measured axial strain, provided that the remanent stray field remains constant. It is anticipated that this new method can contribute to improving the possibilities for monitoring the installation of large-scale steel structures, especially in hostile offshore environments.

Second, based on the remanent magnetic field data measured with the ground-based sensors, a new method to monitor the pile penetration during impact pile driving is devised. Contrary to state-of-the-art techniques, the proposed method is non-contact and does not require the application of an artificial pattern onto the surface of the structure. The latter is achieved by taking advantage of the naturally occurring pattern in the magnetic stray field as a result of circumferential welds in the pile. Furthermore, it is shown that this magnetic signature can be simulated by applying simple model for the magnetic susceptibility proposed in this chapter. This modelled magnetic signature provides the basis for the method to monitor the penetration of a monopile during installation in real-time.

8

Conclusions

*Some things should be simple
Even an end has a start*

Editors – An End Has a Start

Given the impracticalities associated with collocated measurements in the offshore environment, the main objective of this thesis has been the development of non-collocated methods to infer deformation of large-diameter monopiles during pile driving. To this end, methods have been investigated in which the information pertaining the deformation from the point of interest is conveyed to the measurement device in two distinct manners: either by means of elasto-plastic stress waves or through the changes in ambient magnetic field induced by magnetomechanical effects. In the analysis of the former, solely mechanical deformation and the accompanying elasto-plastic stress wave propagation have been treated, while in the latter, the interaction between the structure's strain and magnetisation has been analysed. Consequently, this thesis has been divided into two parts.

In the first part, purely mechanical deformations of a monopile due to an axial impact load have been discussed. Starting from the Donnell–Mushtari shell theory, which governs the elastic deformations of a cylindrical shell, Chapter 2 has derived several sets of equations for the axial deformations of large-diameter monopiles by employing justified assumptions of various complexity, restricting their applicability in terms of excitation frequency and wavenumber. In the low-frequency, long-wavelength limit, the classical wave equation is an appropriate approximation of the more complete theory. However, it has been shown that, when energy is introduced around the ring frequency of the pile, the effect of dispersion

on the stress wave propagation is no longer negligible. A comparison of measured strain data from the installation of a large-diameter monopile with simulated data has shown that only an axially symmetric membrane theory as a minimum is capable of predicting the observed strain levels with satisfactory accuracy, when sufficiently high frequencies are excited ($f > 0.5f_r$).

Since the prevailing model for pile driving used in industry employs the non-dispersive one-dimensional wave equation, the effect of stress wave dispersion on the results of a driveability study has been studied in this thesis. An analysis of the simulated data of installations of pile with increasing radii has shown that stress wave dispersion has a profound influence on the driveability results for large-diameter piles. First, due to the dispersion, the predicted stresses display more undulations, which affects the estimated fatigue life of the structure. Second, the computed penetration depth for the dispersive model differs 4% from the currently used non-dispersive model. Consequently, it is recommended that driveability models for large-diameter piles should be improved by describing the structural deformations with an axially symmetric membrane theory, while simultaneously introducing soil resistance in the radial direction.

An analysis of the frequency-dependency of stress state in axially symmetric cylinder has indicated that around the ring frequency, the stress state is biaxial, while for lower frequencies, it is essentially uniaxial. In the low-frequency limit, one of the dispersive approximations for the axial deformations of a pile has been augmented to include physically non-linear material behaviour, allowing for the propagation of elasto-plastic stress waves in the structure. With an elementary energy balance that uses the measured energy fluxes, a non-collocated method to detect and quantify regions of plastic deformation inflicted by a hammer blow has been derived in Chapter 3. The method gives an upper bound for the amount of plastic deformation sustained between the impacted end and the sensor location by comparing the energy contained in the measured strain pulse to that in the expected strain signal, which is computed with a linear elastic model of the structure. Using data from a lab-scale experiment, the proposed non-collocated contact method has successfully been validated.

The second part of this thesis has focused on strain-induced variations of the magnetisation, which is inferred by non-contact measurements of the magnetic stray field permeating the space around the ferromagnetic structure. Chapter 4 has reviewed the main principles of the magnetomechanical effect, which are founded on the (ir)reversible wall motions of the magnetic domains and the pinning site density of the material. Currently, the available strain-induced magnetisation data for large-scale structures, which have a substantial demagnetising field, is limited to static tensile loads. As a hammer blow induces dynamic compressive strain in a monopile, the magnetomechanical response of such a large-scale structure subject to an impact load has to be obtained from a novel experiment. Given the impracticality of generating magnetising fields for a large-scale structure, this experiment has concentrated on the development of a passive magnetic method, relying solely on the

geomagnetic field. In the experimental set-up used in this work, a steel cylinder is subjected to axial impacts from various heights, while the magnetic stray field is measured during and in between impacts, providing unique magnetomechanical data.

To examine the magnetisation and generated magnetic stray field of a thin-walled steel cylinder in the presence of a time- and space-invariant magnetic field, a magneto-static framework has been developed. The magnetisation and stray field are not completely axi-symmetric as a result of the horizontal component of the external magnetic field. Consequently, the circumferential position of a magnetic field sensor is an important parameter when one infers deformations in a non-contact manner. Moreover, such a sensor is ideally employed within one radius distance to the cylinder's surface to obtain a significant signal compared to the external field.

Chapter 5 has presented the evolution of the structure's magnetic stray field in between impacts, reflecting the irreversible magnetisation. The collected magnetic data shows that repeated impact-induced elastic deformations irreversibly pushes the structure's magnetisation towards a global magnetic equilibrium, while plastic deformation tends to reduce the equilibrium value towards zero. For most initial magnetic states, including the demagnetised state, these two processes counteract, manifesting a deviation of the trend towards the global equilibrium with increasing impact energy as soon as plastic deformation forms. This observation provides a basis for a non-located non-contact method to detect and localise regions of plastic deformations, since this behaviour is measured in the vicinity of the affected area. To subsequently quantify the sustained permanent deformation, an accurate magnetomechanical model that includes plastic deformation is required, of which the development has been left for future research.

During an impact, the magnetic stray field displays strain-induced transient behaviour, which has been discussed in Chapter 6. The impact-induced strain field has been analysed with an axi-symmetric mechanical model, which has been developed such that it can be applied to the simulation of large-diameter monopile installations by hydraulic impact hammers. In the laboratory set-up, an impact excites frequencies well below the structure's ring frequency, resulting in a uniaxial stress in the structure, which is confirmed by classical strain gauge measurements.

For repeated impacts, the measured dynamic magnetic stray field indicates that the magnetic response becomes consistent when the structure's magnetisation has attained a magnetic equilibrium. For the primary strain pulse, the axial strain and the major principle component of the stray field show an excellent correlation ($c_{\epsilon_z B_1} > 0.9$), which indicates that magnetic stray field can be used to infer elastic deformation in a non-contact manner provided that a proper calibration procedure is performed. However, the directions of the principle axes depend on the circumferential sensor position and the impact heights, which implies that a separate calibration is required for each sensor position.

Since the strain-induced magnetisation changes become fully reversible after repeated elastic loads, a new reversible vectorial magnetomechanical model has been developed by

assuming isotropic material behaviour and a uniaxial stress state. This model includes the influence of the structure's demagnetising field on the magnetisation, which is normally not incorporated into magnetomechanical models. A comparison between the simulated and measured strain-induced stray fields and an analysis of the stray field's response to distinct magnetisation increments show that an isotropic model is insufficient to predict the measured stray field variations. Inclusion of anisotropy and accounting for the irreversible magnetisation have been identified as promising research directions to improve the magnetomechanical model.

To confirm whether the conclusions drawn from the laboratory experiment are equally valid in a more realistic monopile installation scenario, a full-scale in-situ measurement campaign has been conducted as presented in Chapter 7. Stray field data have been collected with two distinct sensor layouts: a set attached to the hammer's sleeve and a set of sensors placed on the ground. The former layout ensures that the sensors retain their relative axial position with respect to the pile throughout the installation. For these sleeve-based sensors, the major principle component of the measured dynamic stray field shows a strong correlation with the simultaneously measured axial strain ($c > 0.8$). Moreover, the peak strain and the maximum deviation from the remanent stray field are related through a polynomial expression, of which the coefficients depend on the position of the sensor relative to the pile. This dependency has also been found in the laboratory experiments. Sources of interference, i.e. the stray field of nearby ferromagnetic objects and the rotation of the hammer-sleeve assembly, require further research to quantify their influence on the magnetomechanical measurements.

From the magnetic stray field data, two practical applications of the non-contact magnetic stray field measurements during a monopile installation are identified. First, using the polynomial relation found between the peak strain and the maximum deviation of the dynamic magnetic signal as measured by the sleeve-based sensors, a non-contact method is proposed to infer the hammer-induced strain from the measured stray field data. After calibration, the method yields inferred time signals of the strain with satisfactory correspondence to the measured axial strain, provided that the remanent stray field remains constant. Second, based on the remanent magnetic field measured with the ground-based sensors, a new method to monitor the pile penetration during impact pile driving is devised, which takes advantage of the naturally occurring pattern in the magnetic stray field as a result of circumferential welds in the pile. By modelling the magnetic signature, the pile penetration can be monitored in real-time during installation. Although both applications need further development before they can accurately be employed in practice, the presented conclusions provide a solid foundation for the working principles of these novel non-contact methods to monitor the pile driving process.

In conclusion, this thesis has treated the development of several non-collocated methods to infer deformations in large-diameter monopiles. Even though the method to infer plastic deformation based on elasto-plastic stress wave propagation could readily be applied in

practice, it still requires contact measurements. This restraint is removed by the magneto-mechanical methods, which depend on the interpretation of magnetic stray field measured in the vicinity of the steel structure, providing a unified framework to detect, localise and quantify elastic and plastic deformations in monopiles using non-contact sensors. However, the deployment of these non-collocated methods is not limited to the installation of steel foundation piles, as the underlying principles are applicable to a much wider range of steel and other ferromagnetic structures, e.g. bridges, support frames, etc. Thus, the non-collocated methods presented in this thesis can potentially be applied to a broad class of engineering structures that contain ferromagnetic elements.

Bibliography

References for Preface

- Gilbert, W. (1893). *De Magnete* [On the Magnet]. (Original work published 1600)
- Mahon, B. (2004). *The Man Who Changed Everything: The Life of James Clerk Maxwell* (First Edition). Chichester, West Sussex, England, Wiley.
- Newton, I. (1675, February 5). *Isaac Newton letter to Robert Hooke*. Retrieved April 20, 2021, from <https://digitallibrary.hsp.org/index.php/Detail/objects/9792>

References for Chapter 1

- Anderson, M. R. (1987). Nondestructive Testing of Offshore Structures. *NDT International*, 20(1), 17–21.
- Atherton, D. L. & Jiles, D. C. (1983). Effects of Stress on the Magnetization of Steel. *IEEE Transactions on Magnetics*, 19(5), 2021–2023.
- Birss, R. R., Faunce, C. A. & Isaac, E. D. (1971). Magnetomechanical Effects in Iron and Iron-Carbon Alloys. *Journal of Physics D: Applied Physics*, 4(7), 1040.
- Boskalis. (2016). *Veja Mate Project Sheet*. Retrieved January 30, 2020, from <https://boskalis.com/about-us/projects/detail/offshore-wind-farm-monopile-installation-veja-mate.html>
- Bozorth, R. M. & Williams, H. J. (1945). Effect of Small Stresses on Magnetic Properties. *Reviews of Modern Physics*, 17(1), 72–80.
- Chen, T., Wang, X., Gu, X., Zhao, Q., Yuan, G. & Liu, J. (2019). Axial Compression Tests of Grouted Connections in Jacket and Monopile Offshore Wind Turbine Structures. *Engineering Structures*, 196, 109330.
- Chung, J., Wallerand, R. & Hélias-Brault, M. (2013). Pile Fatigue Assessment During Driving. *Procedia Engineering*, 66, 451–463.
- Dallyn, P., El-Hamalawi, A., Palmeri, A. & Knight, R. (2016). Experimental Investigation on the Development of Wear in Grouted Connections for Offshore Wind Turbine Generators. *Engineering Structures*, 113, 89–102.
- Deraemaeker, A. & Worden, K. (Eds.). (2010). *New Trends in Vibration Based Structural Health Monitoring*. Wien New York, Springer.
- Doherty, P. & Gavin, K. (2012). Laterally Loaded Monopile Design for Offshore Wind Farms. *Proceedings of the Institution of Civil Engineers - Energy*, 165(1), 7–17.
- Fan, W. & Qiao, P. (2011). Vibration-Based Damage Identification Methods: A Review and Comparative Study. *Structural Health Monitoring*, 10(1), 83–111.

- Gollub, P., Jensen, J. F., Giese, D. & Güres, S. (2014). Flanged Foundation Connection of the Offshore Wind Farm Amrumbank West - Concept, Approval, Design, Tests and Installation: Flanged Foundation Connection of the Offshore Wind Farm Amrumbank West - Concept, Approval, Design, Tests and Installation. *Stahlbau*, 83(8), 522–528.
- GROW. (2020). *Gentle Driving of Piles (GDP)*. Retrieved January 30, 2020, from <https://grow-offshorewind.nl/project/gentle-driving-of-piles>
- Janele, T. O., Landskröner, S. & Klose, M. (2015). Berechnung Der Rammschädigung an Flanschen von Monopile-Gründungen. *Stahlbau*, 84(7), 494–500.
- Jensen, K. S., Petersen, S. J. & Pedersen, R. R. (2018). European Offshore Wind Engineering – Past, Present and Future. *Proceedings of the Institution of Civil Engineers - Civil Engineering*, 171(4), 159–165.
- Li, Z., Dixon, S., Cawley, P., Jarvis, R., Nagy, P. B. & Cabeza, S. (2017a). Experimental Studies of the Magneto-Mechanical Memory (MMM) Technique Using Permanently Installed Magnetic Sensor Arrays. *NDT & E International*, 92(Supplement C), 136–148.
- Lotsberg, I., Sigurdsson, G., Arnesen, K. & Hall, M. E. (2010a). Recommended Design Fatigue Factors for Reassessment of Piles Subjected to Dynamic Actions From Driving. *Journal of Offshore Mechanics and Arctic Engineering*, 132(4), 041603.
- Massarsch, K. R., Fellenius, B. H. & Bodare, A. (2017). Fundamentals of the Vibratory Driving of Piles and Sheet Piles. *Geotechnik*, 40(2), 126–141.
- Matlack, K. H., Kim, J.-Y., Jacobs, L. J. & Qu, J. (2015). Review of Second Harmonic Generation Measurement Techniques for Material State Determination in Metals. *Journal of Nondestructive Evaluation*, 34(1), 273.
- Munoz, R., Rus, G. & Bochud, N. (2015). Nonlinear Ultrasonics for Early Damage Detection. In *Emerging Design Solutions in Structural Health Monitoring Systems*. Engineering Science Reference.
- Niess, M. J. (2013). *Size Matters*. Retrieved January 27, 2020, from <https://editionmanager.com/edition/a2sea-news-winter-2013>
- Nordenham. (2019, June 11). *Monopiles for wpd's 640 MW Yunlin Offshore Wind Farm in Taiwan* [Press Release]. Retrieved January 29, 2020, from <http://www.steelwind-nordenham.de/steelwind/aktuelles/pressemitteilungen/00088760/index.shtml.en>
- Perveen, R., Kishor, N. & Mohanty, S. R. (2014). Off-Shore Wind Farm Development: Present Status and Challenges. *Renewable and Sustainable Energy Reviews*, 29, 780–792.
- Preumont, A. (2018). *Vibration Control of Active Structures* (Fourth Edition, Vol. 246). New York, NY, Springer Berlin Heidelberg.
- Rausche, F., Nagy, M., Webster, S. & Liang, L. (2009). CAPWAP and Refined Wave Equation Analyses for Driveability Predictions and Capacity Assessment of Offshore Pile Installations, In *ASME 2009 28th International Conference on Ocean, Offshore and Arctic Engineering*, American Society of Mechanical Engineers.
- Rytter, A. (1993). *Vibrational Based Inspection of Civil Engineering Structures* (Doctoral dissertation). Aalborg University. Aalborg, Denmark.

- Schijve, J. (2009). *Fatigue of Structures and Materials* (Second Edition). Dordrecht, Springer.
- Seaway Heavy Lifting Engineering B.V. (2009). *Pile Driveability and Installation* (tech. rep.). Zoetermeer, the Netherlands.
- Smith, E. A. L. (1962). Pile-Driving Analysis by the Wave Equation. *American Society of Civil Engineers Transactions*, 127, 1145–1193.
- Tsouvalas, A. & Metrikine, A. V. (2016). Structure-Borne Wave Radiation by Impact and Vibratory Piling in Offshore Installations: From Sound Prediction to Auditory Damage. *Journal of Marine Science and Engineering*, 4(3), 44.
- Van Vleck, J. H. (1977, December 8). *Quantum mechanics: The key to understanding magnetism* [Nobel Lecture]. Retrieved October 2, 2017, from <https://www.nobelprize.org/prizes/physics/1977/vleck/lecture/>
- Viana, A., Rouve, L.-L., Cauffet, G. & Coulomb, J.-L. (2011b). Analytical Model for External Induction Variations of a Ferromagnetic Cylinder Undergoing High Mechanical Stresses in a Low Magnetic Field of Any Orientation. *IEEE Transactions on Magnetics*, 47(5), 1366–1369.
- Wang, P., Tian, X., Peng, T. & Luo, Y. (2018a). A Review of the State-of-the-Art Developments in the Field Monitoring of Offshore Structures. *Ocean Engineering*, 147, 148–164.
- Webster, S., Givet, R. & Griffith, A. (2008). Offshore Pile Acceptance Using Dynamic Pile Monitoring (J. A. Santos, Ed.). In J. A. Santos (Ed.), *The Application of Stress-Wave Theory to Piles: Science, Technology and Practice: Proceedings of the 8th International Conference on the Application of Stress-Wave Theory to Piles: Lisbon, Portugal, 8-10 September 2008*, IOS Press.
- WindEurope. (2020). *Offshore Wind in Europe. Key Trends and Statistics 2019* (tech. rep.). WindEurope.
- Wisotzki, E., van Foeken, R., van Esch, P. & Novakovic, D. (2019). Strain and Acceleration Measurements at Instrumentation Distances to the Pile Head of 0.5 and 1.0 Times the Diameter—Offshore Pile-Monitoring Experience. In P. Bullock, G. Verbeek, S. Paikowsky & D. Tara (Eds.), *10th International Conference on Stress Wave Theory and Testing Methods for Deep Foundations* (pp. 506–519). ASTM International.
- Yao, K., Wang, Z. D., Deng, B. & Shen, K. (2012). Experimental Research on Metal Magnetic Memory Method. *Experimental Mechanics*, 52(3), 305–314.

References for Chapter 2

- Aldridge, T. R., Carrington, T. M. & Kee, N. R. (2005). Propagation of Pile Tip Damage during Installation. In S. Gourvenec & M. Cassidy (Eds.), *Proceedings of the International Conference on Frontiers in Offshore Geotechnics*. Taylor & Francis.
- Borja, R. I. (1988). Dynamics of Pile Driving by the Finite Element Method. *Computers and Geotechnics*, 5(1), 39–49.
- Bozich, W. F. (1967). *The Vibration and Buckling Characteristics of Cylindrical Shells Under Axial Load and External Pressure* (tech. rep.).
- Chakrabarty, J. (2010). *Applied Plasticity* (Second Edition). Boston, MA, Springer US.

- Chung, J., Wallerand, R. & Hélias-Brault, M. (2013). Pile Fatigue Assessment During Driving. *Procedia Engineering*, 66, 451–463.
- Deeks, A. J. (1992). *Numerical Analysis of Pile Driving Dynamics* (Doctoral dissertation). University of Western Australia. Perth, Australia.
- Deeks, A. J. & Randolph, M. F. (1993). Analytical Modelling of Hammer Impact for Pile Driving. *International Journal for Numerical and Analytical Methods in Geomechanics*, 17(5), 279–302.
- DeVault, G. P. (1965). The Effect of Lateral Inertia on the Propagation of Plastic Strain in a Cylindrical Rod. *Journal of the Mechanics and Physics of Solids*, 13(2), 55–68.
- Gilman, J. J. (1968). Microdynamical Theory of Plasticity. In C. J. McMahon (Ed.), *Advances in Materials Research*. Interscience Publishers.
- Graff, K. F. (1991). *Wave Motion in Elastic Solids*. Mineola, N.Y., Dover Publications. (Original work published 1975)
- Greenspon, J. E. (1961). Vibrations of Thick and Thin Cylindrical Shells Surrounded by Water. *The Journal of the Acoustical Society of America*, 33(10), 1321–1328.
- Hall, M. V. (2015). An Analytical Model for the Underwater Sound Pressure Waveforms Radiated When an Offshore Pile Is Driven. *The Journal of the Acoustical Society of America*, 138(2), 795–806.
- Hodges, C. H., Power, J. & Woodhouse, J. (1985). The Use of the Sonogram in Structural Acoustics and an Application to the Vibrations of Cylindrical Shells. *Journal of Sound and Vibration*, 101(2), 203–218.
- Honeycombe, R. W. K. (1968). *The Plastic Deformation of Metals*. London, UK, Edward Arnold.
- Igwemezie, V., Mehmanparast, A. & Kolios, A. (2019). Current Trend in Offshore Wind Energy Sector and Material Requirements for Fatigue Resistance Improvement in Large Wind Turbine Support Structures – A Review. *Renewable and Sustainable Energy Reviews*, 101, 181–196.
- Isaacs, D. V. (1931). Reinforced Concrete Pile Formulas. *Transactions, Institute of Engineers*, 12, 305–323.
- Lee, S. L., Chow, Y. K., Karunaratne, G. P. & Wong, K. Y. (1988). Rational Wave Equation Model for Pile-Driving Analysis. *Journal of Geotechnical Engineering*, 114(3), 306–325.
- Lee, W.-S. & Lin, C.-F. (2001). Impact Properties and Microstructure Evolution of 304L Stainless Steel. *Materials Science and Engineering: A*, 308(1-2), 124–135.
- Leissa, A. W. (1993). *Vibration of Shells*. Acoustical Society of America New York. (Original work published 1973)
- Liyanapathirana, D. S., Deeks, A. J. & Randolph, M. F. (2001). Numerical Modelling of the Driving Response of Thin-Walled Open-Ended Piles. *International Journal for Numerical and Analytical Methods in Geomechanics*, 25(9), 933–953.
- Logg, A., Mardal, K.-A. & Wells, G. (Eds.). (2012). *Automated Solution of Differential Equations by the Finite Element Method* (Vol. 84). Berlin, Heidelberg, Springer Berlin Heidelberg.

- Lotsberg, I., Sigurdsson, G., Arnesen, K. & Hall, M. E. (2010a). Recommended Design Fatigue Factors for Reassessment of Piles Subjected to Dynamic Actions From Driving. *Journal of Offshore Mechanics and Arctic Engineering*, 132(4), 041603.
- Lotsberg, I., Wästberg, S., Ulle, H., Haagenen, P. & Hall, M. E. (2010b). Fatigue Testing and S-N Data for Fatigue Analysis of Piles. *Journal of Offshore Mechanics and Arctic Engineering*, 132(4), 041602.
- Mabsout, M. E. & Tassoulas, J. L. (1994). A Finite Element Model for the Simulation of Pile Driving. *International Journal for Numerical Methods in Engineering*, 37(2), 257–278.
- Masouleh, S. F. & Fakharian, K. (2008a). Application of a Continuum Numerical Model for Pile Driving Analysis and Comparison with a Real Case. *Computers and Geotechnics*, 35(3), 406–418.
- Masouleh, S. F. & Fakharian, K. (2008b). Verification of Signal Matching Analysis of Pile Driving Using a Finite Difference Based Continuum Numerical Method. *International Journal of Civil Engineering*, 6(3), 174–182.
- Masoumi, H. R. & Degrande, G. (2008). Numerical Modeling of Free Field Vibrations Due to Pile Driving Using a Dynamic Soil-Structure Interaction Formulation. *Journal of Computational and Applied Mathematics*, 215(2), 503–511.
- Meijers, P. C., Tsouvalas, A. & Metrikine, A. V. (2017). The Effect of Stress Wave Dispersion on the Drivability Analysis of Large-Diameter Monopiles. *Procedia Engineering*, 199, 2390–2395.
- Meijers, P. C., Tsouvalas, A. & Metrikine, A. V. (2018a). A Non-Collocated Method to Quantify Plastic Deformation Caused by Impact Pile Driving. *International Journal of Mechanical Sciences*, 148, 1–8.
- Nath, B. (1990). A Continuum Method of Pile Driving Analysis: Comparison with the Wave Equation Method. *Computers and Geotechnics*, 10(4), 265–285.
- Newmark, N. M. (1959). A Method of Computation for Structural Dynamics. *Journal of the Engineering Mechanics Division*, 85(No. EM 3), 67–94.
- Priest, A. H. & Large, M. (1990). Observations on the Effect of Pile Driving on Fatigue Endurance. In *The Proceedings of the First (1990) European Offshore Mechanics Symposium*.
- Ramshaw, C. L. (2002). *Computation of Ground Waves from Pile Driving and Their Effects on Structures* (Doctoral dissertation). Durham University. Durham, UK.
- Randolph, M. F. & Simons, H. A. (1986). An Improved Soil Model for One-Dimensional Pile Driving Analysis. In *Méthodes Numériques de Calcul Des Pieux Pour Les Ouvrages En Mer*. Editions Technip.
- Rasmussen, J. L. & Feld, T. (1999). *Pile Driving Fatigue Damage.: A Case Story* (tech. rep.). Geotechnical Engineering Group.
- Rausche, F. & Goble, G. G. (1979). Determination of Pile Damage by Top Measurements. In *Behavior of Deep Foundations*. ASTM International.

- Rausche, F., Liang, L., Allin, R. & Rancman, D. (2004). Applications and Correlations of the Wave Equation Analysis Program GRLWEAP, In *Proceedings of the Seventh International Conference on the Application of Stresswave Theory to Piles*.
- Reinhal, P. G. & Dahl, P. H. (2011). Underwater Mach Wave Radiation from Impact Pile Driving: Theory and Observation. *The Journal of the Acoustical Society of America*, 130(3), 1209–1216.
- Roters, F., Eisenlohr, P., Hantcherli, L., Tjahjanto, D. D., Bieler, T. R. & Raabe, D. (2010). Overview of Constitutive Laws, Kinematics, Homogenization and Multiscale Methods in Crystal Plasticity Finite-Element Modeling: Theory, Experiments, Applications. *Acta Materialia*, 58(4), 1152–1211.
- Salgado, R., Loukidis, D., Abou-Jaoude, G. & Zhang, Y. (2015). The Role of Soil Stiffness Non-Linearity in 1D Pile Driving Simulations. *Géotechnique*, 65(3), 169–187.
- Simo, J. C. & Hughes, T. J. R. (1998). *Computational Inelasticity* (Vol. 7). Springer Science & Business Media.
- Smith, E. A. L. (1950). Pile Driving Impact, In *Proceedings of the Industrial Computation Seminar, September 1950*.
- Smith, E. A. L. (1962). Pile-Driving Analysis by the Wave Equation. *American Society of Civil Engineers Transactions*, 127, 1145–1193.
- Smith, I. M. & Chow, Y. K. (1982). Three Dimensional Analysis of Pile Drivability, In *Proc. 2nd Int. Conf. on Numerical Methods in Offshore Piling, Austin, Texas*.
- Soedel, W. (2004). *Vibrations of Shells and Plates* (Third Edition). New York, Marcel Dekker.
- Tang, Q., Holloway, G. L. & Wade, B. (2005). Pile Driving Fatigue Damage-Effective Factors and Reduction, In *Proceeding of the 2005 Offshore Technology Conference*, Houston, TX, Offshore Technology Conference.
- Tsouvalas, A. (2015). *Underwater Noise Generated by Offshore Pile Driving* (Doctoral dissertation). Delft University of Technology. Delft, the Netherlands.
- Tsouvalas, A. & Metrikine, A. V. (2013). A Semi-Analytical Model for the Prediction of Underwater Noise from Offshore Pile Driving. *Journal of Sound and Vibration*, 332(13), 3232–3257.
- Tsouvalas, A. & Metrikine, A. V. (2014). A Three-Dimensional Vibroacoustic Model for the Prediction of Underwater Noise from Offshore Pile Driving. *Journal of Sound and Vibration*, 333(8), 2283–2311.
- Tsouvalas, A. (2020). Underwater Noise Emission Due to Offshore Pile Installation: A Review. *Energies*, 13(12), 3037.
- Versteijlen, W. G., de Oliveira Barbosa, J. M., van Dalen, K. N. & Metrikine, A. V. (2018). Dynamic Soil Stiffness for Foundation Piles: Capturing 3D Continuum Effects in an Effective, Non-Local 1D Model. *International Journal of Solids and Structures*, 134, 272–282.
- Versteijlen, W. G., Metrikine, A. V. & van Dalen, K. N. (2016). A Method for Identification of an Effective Winkler Foundation for Large-Diameter Offshore Wind Turbine Support

Structures Based on in-Situ Measured Small-Strain Soil Response and 3D Modelling. *Engineering Structures*, 124, 221–236.

Wu, A., Kuhlemeyer, R. & To, C. (1989). Validity of Smith Model in Pile Driving Analysis. *Journal of Geotechnical Engineering*, 115(9), 1285–1302.

References for Chapter 3

DeVault, G. P. (1965). The Effect of Lateral Inertia on the Propagation of Plastic Strain in a Cylindrical Rod. *Journal of the Mechanics and Physics of Solids*, 13(2), 55–68.

Gómez, S. S., Metrikine, A. V., Carboni, B. & Lacarbonara, W. (2018). Identification of Energy Dissipation in Structural Joints by Means of the Energy Flow Analysis. *Journal of Vibration and Acoustics*, 140(1).

Karagiozova, D., Alves, M. & Jones, N. (2000). Inertia Effects in Axisymmetrically Deformed Cylindrical Shells under Axial Impact. *International Journal of Impact Engineering*, 24(10), 1083–1115.

Karagiozova, D. & Jones, N. (2001). Influence of Stress Waves on the Dynamic Progressive and Dynamic Plastic Buckling of Cylindrical Shells. *International Journal of Solids and Structures*, 38(38), 6723–6749.

Karagiozova, D. & Jones, N. (2000). Dynamic Elastic–plastic Buckling of Circular Cylindrical Shells under Axial Impact. *International Journal of Solids and Structures*, 37(14), 2005–2034.

Khayer Dastjerdi, A., Naghdabadi, R. & Arghavani, J. (2013). An Energy-Based Approach for Analysis of Dynamic Plastic Deformation of Metals. *International Journal of Mechanical Sciences*, 66, 94–100.

Kolsky, H. & Douch, L. S. (1962). Experimental Studies in Plastic Wave Propagation. *Journal of the Mechanics and Physics of Solids*, 10(3), 195–223.

Lepik, Ü. (1999). Bifurcation Analysis of Elastic–plastic Cylindrical Shells. *International Journal of Non-Linear Mechanics*, 34(2), 299–311.

Logg, A., Mardal, K.-A. & Wells, G. (Eds.). (2012). *Automated Solution of Differential Equations by the Finite Element Method* (Vol. 84). Berlin, Heidelberg, Springer Berlin Heidelberg.

Meijers, P. C., Tsouvalas, A. & Metrikine, A. V. (2018a). A Non-Collocated Method to Quantify Plastic Deformation Caused by Impact Pile Driving. *International Journal of Mechanical Sciences*, 148, 1–8.

Meijers, P. C., Tsouvalas, A. & Metrikine, A. V. (2018b). Plasticity Detection and Quantification in Monopile Support Structures Due to Axial Impact Loading. *MATEC Web of Conferences*, 148, 15003.

Murase, K. & Jones, N. (1993). The Variation of Modes in the Dynamic Axial Plastic Buckling of Circular Tubes (N. Gupta, Ed.). In N. Gupta (Ed.), *Plasticity and Impact Mechanics*, New Delhi, Wiley Eastern Limited.

Newmark, N. M. (1959). A Method of Computation for Structural Dynamics. *Journal of the Engineering Mechanics Division*, 85(No. EM 3), 67–94.

- Ren, W., Mingbao, H., Zhuping, H. & Qingchun, Y. (1983). An Experimental Study on the Dynamic Axial Plastic Buckling of Cylindrical Shells. *International Journal of Impact Engineering*, 1(3), 249–256.
- Shea, J. H. (1968). Propagation of Plastic Strain Pulses in Cylindrical Lead Bars. *Journal of Applied Physics*, 39(8), 4004–4011.
- Simo, J. C. & Hughes, T. J. R. (1998). *Computational Inelasticity* (Vol. 7). Springer Science & Business Media.
- Taylor, G. (1948). The Use of Flat-Ended Projectiles for Determining Dynamic Yield Stress I. Theoretical Considerations. *Proc. R. Soc. Lond. A*, 194(1038), 289–299.
- Tsouvalas, A. & Metrikine, A. V. (2014). A Three-Dimensional Vibroacoustic Model for the Prediction of Underwater Noise from Offshore Pile Driving. *Journal of Sound and Vibration*, 333(8), 2283–2311.
- Von Karman, T. & Duwez, P. (1950). The Propagation of Plastic Deformation in Solids. *Journal of Applied Physics*, 21(10), 987–994.

References for Chapter 4

- Atherton, D. L. & Jiles, D. C. (1986). Effects of Stress on Magnetization. *NDT International*, 19(1), 15–19.
- Atherton, D. L., Rao, T. S. & Schobachler, M. (1988). Magnetization Changes Induced by Stress under Constant Applied Field in 2% Mn Pipeline Steel. *IEEE Transactions on Magnetism*, 24(3), 2029–2032.
- Atherton, D. L. & Szpunar, J. A. (1986). Effect of Stress on Magnetization and Magnetostriction in Pipeline Steel. *IEEE Transactions on Magnetism*, 22(5), 514–516.
- Atherton, D. L. & Teitsma, A. (1982). Detection of Anomalous Stresses in Gas Pipelines by Magnetometer Survey (Invited). *Journal of Applied Physics*, 53(11), 8130–8135.
- Augustyniak, M. & Usarek, Z. (2015). Discussion of Derivability of Local Residual Stress Level from Magnetic Stray Field Measurement. *Journal of Nondestructive Evaluation*, 34(3), 21.
- Aydin, U., Rasilo, P., Martin, F., Singh, D., Daniel, L., Belahcen, A., Rezik, M., Hubert, O., Kouhia, R. & Arkkio, A. (2017). Magneto-Mechanical Modeling of Electrical Steel Sheets. *Journal of Magnetism and Magnetic Materials*, 439, 82–90.
- Babbar, V., Bryne, J. & Clapham, L. (2005). Mechanical Damage Detection Using Magnetic Flux Leakage Tools: Modeling the Effect of Dent Geometry and Stresses. *NDT & E International*, 38(6), 471–477.
- Banchet, J., Jouglar, J., Vuillermoz, P. L., Waltz, P. & Weinstock, H. (1995). Magnetomechanical Behavior of Steel via SQUID Magnetometry. *IEEE Transactions on Applied Superconductivity*, 5(2), 2486–2489.
- Bao, S., Fu, M., Gu, Y. & Hu, S. (2016). Evolution of the Piezomagnetic Field of Ferromagnetic Steels Subjected to Cyclic Tensile Stress with Variable Amplitudes. *Experimental Mechanics*, 56(6), 1017–1028.

- Bao, S., Gu, Y., Fu, M., Zhang, D. & Hu, S. (2017b). Effect of Loading Speed on the Stress-Induced Magnetic Behavior of Ferromagnetic Steel. *Journal of Magnetism and Magnetic Materials*, 423(Supplement C), 191–196.
- Bao, S., Jin, P., Zhao, Z. & Fu, M. (2020). A Review of the Metal Magnetic Memory Method. *Journal of Nondestructive Evaluation*, 39(1), 11.
- Beleggia, M., Vokoun, D. & De Graef, M. (2009). Demagnetization Factors for Cylindrical Shells and Related Shapes. *Journal of Magnetism and Magnetic Materials*, 321(9), 1306–1315.
- Benabou, A., Clénet, S. & Piriou, F. (2003). Comparison of Preisach and Jiles–Atherton Models to Take into Account Hysteresis Phenomenon for Finite Element Analysis. *Journal of Magnetism and Magnetic Materials*, 261(1), 139–160.
- Bergqvist, A. J. (1997). Magnetic Vector Hysteresis Model with Dry Friction-like Pinning. *Physica B: Condensed Matter*, 233(4), 342–347.
- Bergqvist, A. J. & Engdahl, G. (1991). A Stress-Dependent Magnetic Preisach Hysteresis Model. *IEEE Transactions on Magnetics*, 27(6), 4796–4798.
- Bernard, L., Mininger, X., Daniel, L., Krebs, G., Bouillault, F. & Gabsi, M. (2011). Effect of Stress on Switched Reluctance Motors: A Magneto-Elastic Finite-Element Approach Based on Multiscale Constitutive Laws. *IEEE Transactions on Magnetics*, 47(9), 2171–2178.
- Birss, R. R., Faunce, C. A. & Isaac, E. D. (1971). Magnetomechanical Effects in Iron and Iron-Carbon Alloys. *Journal of Physics D: Applied Physics*, 4(7), 1040.
- Bobbio, S., Milano, G., Serpico, C. & Visone, C. (1997). Models of Magnetic Hysteresis Based on Play and Stop Hysteresis. *IEEE Transactions on Magnetics*, 33(6), 4417–4426.
- Bonavolontà, C., Peluso, G., Valentino, M., De Iorio, A. & Penta, F. (2009). Detection of Magnetomechanical Effect in Structural Steel Using SQUIDs and Flux-Gate Sensors. *Journal of Superconductivity and Novel Magnetism*, 22(8), 833.
- Bonavolontà, C., Valentino, M., Adamo, M. & Sarnelli, E. (2007). Detection of Plastic Deformation in Structural Steel Using Scanning SQUID Microscopy. *Measurement Science and Technology*, 18(7), 2116–2120.
- Bozorth, R. M. (1993). *Ferromagnetism*. Piscataway, N.J., IEEE Press. (Original work published 1951)
- Bozorth, R. M. & Williams, H. J. (1945). Effect of Small Stresses on Magnetic Properties. *Reviews of Modern Physics*, 17(1), 72–80.
- Buchner, M., Höfler, K., Henne, B., Ney, V. & Ney, A. (2018). Tutorial: Basic Principles, Limits of Detection, and Pitfalls of Highly Sensitive SQUID Magnetometry for Nanomagnetism and Spintronics. *Journal of Applied Physics*, 124(16), 161101.
- Bulte, D. P. & Langman, R. A. (2002). Origins of the Magnetomechanical Effect. *Journal of Magnetism and Magnetic Materials*, 251(2), 229–243.
- Chadebec, O., Coulomb, J.-L. & Janet, F. (2006). A Review of Magnetostatic Moment Method. *IEEE Transactions on Magnetics*, 42(4), 515–520.

- Chadebec, O., Coulomb, J.-L., Leconte, V., Bongiraud, J.-P. & Cauffet, G. (2000). Modeling of Static Magnetic Anomaly Created by Iron Plates. *IEEE Transactions on Magnetics*, 36(4), 667–671.
- Chen, D. X., Brug, J. A. & Goldfarb, R. B. (1991). Demagnetizing Factors for Cylinders. *IEEE Transactions on Magnetics*, 27(4), 3601–3619.
- Chen, H., Wang, C. & Zuo, X. (2017). Research on Methods of Defect Classification Based on Metal Magnetic Memory. *NDT & E International*, 92, 82–87.
- Chikazumi, S. & Graham, C. D. (1997). *Physics of Ferromagnetism* (Second Edition). Oxford, Clarendon Press.
- Christen, R., Bergamini, A. & Motavalli, M. (2009). Influence of Steel Wrapping on Magneto-Inductive Testing of the Main Cables of Suspension Bridges. *NDT & E International*, 42(1), 22–27.
- Craik, D. J. & Tebble, R. S. (1961). Magnetic Domains. *Reports on Progress in Physics*, 24(1), 116.
- Craik, D. J. & Wood, M. J. (1970). Magnetization Changes Induced by Stress in a Constant Applied Field. *Journal of Physics D: Applied Physics*, 3(7), 1009.
- Crum, R. S., Domann, J. P., Carman, G. P. & Gupta, V. (2017). Propagation and Dispersion of Shock Waves in Magnetoelastic Materials. *Smart Materials and Structures*, 26(12), 125027.
- Cullity, B. D. (1971). Fundamentals of Magnetostriction. *Journal of Metals*, 23(1), 35–41.
- Cullity, B. D. & Graham, C. D. (2009). *Introduction to Magnetic Materials* (Second Edition). IEEE Press.
- Daniel, L. (2013). An Analytical Model for the Effect of Multiaxial Stress on the Magnetic Susceptibility of Ferromagnetic Materials. *IEEE Transactions on Magnetics*, 49(5), 2037–2040.
- Daniel, L. (2018). An Analytical Model for the Magnetostriction Strain of Ferromagnetic Materials Subjected to Multiaxial Stress. *The European Physical Journal Applied Physics*, 83(3), 30904.
- Daniel, L., Hubert, O., Buiron, N. & Billardon, R. (2008). Reversible Magneto-Elastic Behavior: A Multiscale Approach. *Journal of the Mechanics and Physics of Solids*, 56(3), 1018–1042.
- Daniel, L., Hubert, O. & Rekik, M. (2015). A Simplified 3-D Constitutive Law for Magneto-mechanical Behavior. *IEEE Transactions on Magnetics*, 51(3), 1–4.
- d'Aquino, M., Serpico, C., Visone, C. & Adly, A. A. (2003). A New Vector Model of Magnetic Hysteresis Based on a Novel Class of Play Hysterons. *IEEE Transactions on Magnetics*, 39(5), 2537–2539.
- Dobranski, L. G., Jiles, D. C. & Atherton, D. L. (1985). Dependence of the An hysteretic Magnetization on Uniaxial Stress in Steel. *Journal of Applied Physics*, 57(8), 4229–4231.
- Domann, J. P., Loeffler, C. M., Martin, B. E. & Carman, G. P. (2015). High Strain-Rate Magnetoelasticity in Galfenol. *Journal of Applied Physics*, 118(12), 123904.

- Dong, L., Xu, B., Dong, S., Song, L., Chen, Q. & Wang, D. (2009). Stress Dependence of the Spontaneous Stray Field Signals of Ferromagnetic Steel. *NDT & E International*, 42(4), 323–327.
- Dubov, A. A. (1997). A Study of Metal Properties Using the Method of Magnetic Memory. *Metal Science and Heat Treatment*, 39(9), 401–405.
- Ege, Y. & Coramik, M. (2018). A New Measurement System Using Magnetic Flux Leakage Method in Pipeline Inspection. *Measurement*, 123, 163–174.
- En, Y., Luming, L. & Xing, C. (2007). Magnetic Field Aberration Induced by Cycle Stress. *Journal of Magnetism and Magnetic Materials*, 312(1), 72–77.
- Everett, D. H. (1955). A General Approach to Hysteresis. Part 4. An Alternative Formulation of the Domain Model. *Transactions of the Faraday Society*, 51(0), 1551–1557.
- Garikepati, P., Chang, T. & Jiles, D. (1988). Theory of Ferromagnetic Hysteresis: Evaluation of Stress from Hysteresis Curves. *IEEE Transactions on Magnetics*, 24(6), 2922–2924.
- Gilman, J. J. (1968). Microdynamical Theory of Plasticity. In C. J. McMahon (Ed.), *Advances in Materials Research*. Interscience Publishers.
- Gorkunov, E. S. (2014). Different Remanence States and Their Resistance to External Effects. Discussing the “Method of Magnetic Memory”. *Russian Journal of Nondestructive Testing*, 50(11), 617–633.
- Griffiths, D. J. (1999). *Introduction to Electromagnetics* (Third Edition). Upper Saddle River, N.J, Prentice Hall.
- Guo, P., Chen, X., Guan, W., Cheng, H. & Jiang, H. (2011). Effect of Tensile Stress on the Variation of Magnetic Field of Low-Alloy Steel. *Journal of Magnetism and Magnetic Materials*, 323(20), 2474–2477.
- Guo, X. & Atherton, D. L. (1995). Magnetization Changes in 2% Mn Pipeline Steel Induced by Uniaxial Tensile Stress Cycles of Increasing Amplitude. *IEEE Transactions on Magnetics*, 31(5), 2510–2521.
- Honeycombe, R. W. K. (1968). *The Plastic Deformation of Metals*. London, UK, Edward Arnold.
- Hubert, A. & Schäfer, R. (1998). *Magnetic Domains: The Analysis of Magnetic Microstructures*. Berlin, Springer.
- Hubert, O. (2019). Multiscale Magneto-Elastic Modeling of Magnetic Materials Including Isotropic Second Order Stress Effect. *Journal of Magnetism and Magnetic Materials*, 491, 165564.
- Hubert, O. & Lazreg, S. (2017). Two Phase Modeling of the Influence of Plastic Strain on the Magnetic and Magnetostrictive Behaviors of Ferromagnetic Materials. *Journal of Magnetism and Magnetic Materials*, 424, 421–442.
- Jiles, D. C. (1988a). The Effect of Compressive Plastic Deformation on the Magnetic Properties of AISI 4130 Steels with Various Microstructures. *Journal of Physics D: Applied Physics*, 21(7), 1196.
- Jiles, D. C. (1988b). Review of Magnetic Methods for Nondestructive Evaluation. *NDT International*, 21(5), 311–319.

- Jiles, D. C. (1990). Review of Magnetic Methods for Nondestructive Evaluation (Part 2). *NDT International*, 23(2), 83–92.
- Jiles, D. C. (1994b). Modelling the Effects of Eddy Current Losses on Frequency Dependent Hysteresis in Electrically Conducting Media. *IEEE Transactions on Magnetics*, 30(6), 4326–4328.
- Jiles, D. C. (1995). Theory of the Magnetomechanical Effect. *Journal of Physics D: Applied Physics*, 28(8), 1537.
- Jiles, D. C. (2015). *Introduction to Magnetism and Magnetic Materials* (Third Edition). CRC Press.
- Jiles, D. C. & Atherton, D. L. (1984). Theory of the Magnetisation Process in Ferromagnets and Its Application to the Magnetomechanical Effect. *Journal of Physics D: Applied Physics*, 17(6), 1265.
- Jiles, D. C. & Atherton, D. L. (1986). Theory of Ferromagnetic Hysteresis. *Journal of Magnetism and Magnetic Materials*, 61(1), 48–60.
- Jiles, D. C., Atherton, D. L., Lassen, H. E., Noble, D., deVette, J. & Astle, T. (1984). Microcomputer-based System for Control of Applied Uniaxial Stress and Magnetic Field. *Review of Scientific Instruments*, 55(11), 1843–1848.
- Jiles, D. C., Thoelke, J. B. & Devine, M. K. (1992). Numerical Determination of Hysteresis Parameters for the Modeling of Magnetic Properties Using the Theory of Ferromagnetic Hysteresis. *IEEE Transactions on Magnetics*, 28(1), 27–35.
- Joule, J. (1847). On the Effects of Magnetism upon the Dimensions of Iron and Steel Bars. *The London, Edinburgh, and Dublin Philosophical Magazine and Journal of Science*, 30(199), 76–87.
- Kittel, C. (1949). Physical Theory of Ferromagnetic Domains. *Reviews of Modern Physics*, 21(4), 541–583.
- Kleber, X. & Vincent, A. (2004). On the Role of Residual Internal Stresses and Dislocations on Barkhausen Noise in Plastically Deformed Steel. *NDT & E International*, 37(6), 439–445.
- Langman, R. A. (1981). Measurement of the Mechanical Stress in Mild Steel by Means of Rotation of Magnetic Field Strength. *NDT International*, 14(5), 255–262.
- Lazreg, S. & Hubert, O. (2012). Influence of Plasticity on Magnetic and Magnetostrictive Behaviors of Dual-Phase Steel. *IEEE Transactions on Magnetics*, 48(4), 1273–1276.
- Lee, E. W. (1955). Magnetostriction and Magnetomechanical Effects. *Reports on Progress in Physics*, 18(1), 184.
- Leite, J. V., Sadowski, N., Kuo-Peng, P., Batistela, N. J., Bastos, J. P. A. & de Espindola, A. A. (2004). Inverse Jiles-Atherton Vector Hysteresis Model. *IEEE Transactions on Magnetics*, 40(4), 1769–1775.
- Leng, J., Xu, M., Zhou, G. & Wu, Z. (2012). Effect of Initial Remanent States on the Variation of Magnetic Memory Signals. *NDT & E International*, 52(Supplement C), 23–27.
- Li, J. & Xu, M. (2012). Influence of Uniaxial Plastic Deformation on Surface Magnetic Field in Steel. *Meccanica*, 47(1), 135–139.

- Li, Z., Dixon, S., Cawley, P., Jarvis, R., Nagy, P. B. & Cabeza, S. (2017a). Experimental Studies of the Magneto-Mechanical Memory (MMM) Technique Using Permanently Installed Magnetic Sensor Arrays. *NDT & E International*, 92(Supplement C), 136–148.
- Li, Z., Jarvis, R., Nagy, P. B., Dixon, S. & Cawley, P. (2017b). Experimental and Simulation Methods to Study the Magnetic Tomography Method (MTM) for Pipe Defect Detection. *NDT & E International*, 92, 59–66.
- Lin, D., Zhou, P. & Bergqvist, A. (2014). Improved Vector Play Model and Parameter Identification for Magnetic Hysteresis Materials. *IEEE Transactions on Magnetics*, 50(2), 357–360.
- Liorzou, F., Phelps, B. & Atherton, D. L. (2000). Macroscopic Models of Magnetization. *IEEE Transactions on Magnetics*, 36(2), 418–428.
- Makar, J. M. & Atherton, D. L. (1994). Effect of Uniaxial Stress on the Reversible and Irreversible Permeabilities of 2% Mn Pipeline Steel. *IEEE Transactions on Magnetics*, 30(4), 1380–1387.
- Makar, J. M. & Atherton, D. L. (1995). Effects of Isofield Uniaxial Cyclic Stress on the Magnetization of 2% Mn Pipeline Steel - Behavior on Minor Hysteresis Loops and Small Major Hysteresis Loops. *IEEE Transactions on Magnetics*, 31(3), 2220–2227.
- Maylin, M. G. (1994). *Magneto-Elastic Processes in Polycrystalline Ferromagnets* (Doctoral dissertation). University of Bath. Bath, UK.
- Maylin, M. G. & Squire, P. T. (1993a). Departures from the Law of Approach to the Principal Anhyseteric in a Ferromagnet. *Journal of Applied Physics*, 73(6), 2948–2955.
- Maylin, M. G. & Squire, P. T. (1993b). The Effects of Stress on Induction, Differential Permeability and Barkhausen Count in a Ferromagnet. *IEEE Transactions on Magnetics*, 29(6), 3499–3501.
- Mignogna, R. B., Browning, V., Gubser, D. U., Schechter, R. S., Simmonds, K. E. & Weinstock, H. (1993). Passive Nondestructive Evaluation of Ferromagnetic Materials during Deformation Using SQUID Gradiometers. *IEEE Transactions on Applied Superconductivity*, 3(1), 1922–1925.
- Parq, J.-H. (2017). Magnetometric Demagnetization Factors for Hollow Cylinders. *Journal of Magnetics*, 22(4), 550–556.
- Pitman, K. C. (1990). The Influence of Stress on Ferromagnetic Hysteresis. *IEEE Transactions on Magnetics*, 26(5), 1978–1980.
- Purcell, E. M. & Morin, D. J. (2013). *Electricity and Magnetism* (Third Edition). Cambridge University Press.
- Raghunathan, A., Melikhov, Y., Snyder, J. E. & Jiles, D. C. (2009). Generalized Form of Anhyseteric Magnetization Function for Jiles–Atherton Theory of Hysteresis. *Applied Physics Letters*, 95(17), 172510.
- Ren, S., Ren, X., Duan, Z. & Fu, Y. (2019). Studies on Influences of Initial Magnetization State on Metal Magnetic Memory Signal. *NDT & E International*, 103, 77–83.
- Ripka, P. (1992). Review of Fluxgate Sensors. *Sensors and Actuators A: Physical*, 33(3), 129–141.

- Robertson, I. M. (1993). Direction of Change of Magnetization of a Ferromagnet Subjected to Stress. *IEEE Transactions on Magnetics*, 29(3), 2077–2080.
- Ruderman, M. (2015). Computationally Efficient Formulation of Relay Operator for Preisach Hysteresis Modeling. *IEEE Transactions on Magnetics*, 51(12), 1–4.
- Sablík, M. J., Burkhardt, G. L., Kwun, H. & Jiles, D. C. (1988). A Model for the Effect of Stress on the Low-frequency Harmonic Content of the Magnetic Induction in Ferromagnetic Materials. *Journal of Applied Physics*, 63(8), 3930–3932.
- Sablík, M. J., Chen, Y. & Jiles, D. C. (2000). Modified Law of Approach for the Magneto-mechanical Model. *AIP Conference Proceedings*, 509(1), 1565–1571.
- Sablík, M. J. & Jiles, D. C. (1993). Coupled Magnetoelastic Theory of Magnetic and Magnetostrictive Hysteresis. *IEEE Transactions on Magnetics*, 29(4), 2113–2123.
- Sablík, M. J., Rubin, S. W., Riley, L. A., Jiles, D. C., Kaminski, D. A. & Biner, S. B. (1993). A Model for Hysteretic Magnetic Properties under the Application of Noncoaxial Stress and Field. *Journal of Applied Physics*, 74(1), 480–488.
- Sablík, M. J., Yonamine, T. & Landgraf, F. J. G. (2004). Modeling Plastic Deformation Effects in Steel on Hysteresis Loops with the Same Maximum Flux Density. *IEEE Transactions on Magnetics*, 40(5), 3219–3226.
- Scheidler, J. J. & Dapino, M. J. (2016). Mechanically Induced Magnetic Diffusion in Cylindrical Magnetoelastic Materials. *Journal of Magnetism and Magnetic Materials*, 397, 233–239.
- Schneider, C. S., Cannell, P. Y. & Watts, K. T. (1992). Magnetoelasticity for Large Stresses. *IEEE Transactions on Magnetics*, 28(5), 2626–2631.
- Sixdenier, F., Messal, O., Hilal, A., Martin, C., Raulet, M. & Scorretti, R. (2016). Temperature-Dependent Extension of a Static Hysteresis Model. *IEEE Transactions on Magnetics*, 52(3), 1–4.
- Staples, S. G. H., Vo, C., Cowell, D. M. J., Freear, S., Ives, C. & Varcoe, B. T. H. (2013). Solving the Inverse Problem of Magnetisation–Stress Resolution. *Journal of Applied Physics*, 113(13), 133905.
- Stoner, E. C. (1950). Ferromagnetism: Magnetization Curves. *Reports on Progress in Physics*, 13(1), 83.
- Takahashi, S., Kobayashi, S., Tomáš, I., Dupre, L. & Vértesy, G. (2017). Comparison of Magnetic Nondestructive Methods Applied for Inspection of Steel Degradation. *NDT & E International*, 91, 54–60.
- Tebble, R. S. & Craik, D. J. (1969). *Magnetic Materials*. Wiley-Interscience.
- Thébault, E., Finlay, C. C., Beggan, C. D., Alken, P., Aubert, J., Barrois, O., Bertrand, F., Bondar, T., Boness, A., Brocco, L., Canet, E., Chambodut, A., Chulliat, A., Coisson, P., Civet, F., Du, A., Fournier, A., Fratter, I., Gillet, N., ... Zvereva, T. (2015). International Geomagnetic Reference Field: The 12th Generation. *Earth, Planets and Space*, 67(1), 79.
- Vanoost, D., Steentjes, S., Peuteman, J., Gielen, G., De Gerssem, H., Pissoort, D. & Hameyer, K. (2016). Magnetic Hysteresis at the Domain Scale of a Multi-Scale Material Model for Magneto-Elastic Behaviour. *Journal of Magnetism and Magnetic Materials*, 414, 168–179.

- Viana, A., Rouve, L.-L., Chadebec, O., Cauffet, G. & Coulomb, J.-L. (2011a). Inverse Problem Approach to Characterize and Model Magnetization Changes in a Thin Shell Structure Undergoing Magneto-Mechanical Effects. *IEEE Transactions on Magnetics*, 47(5), 1450–1453.
- Viana, A., Rouve, L.-L., Cauffet, G. & Coulomb, J.-L. (2010). Magneto-Mechanical Effects Under Low Fields and High Stresses - Application to a Ferromagnetic Cylinder Under Pressure in a Vertical Field. *IEEE Transactions on Magnetics*, 46(8), 2872–2875.
- Viana, A., Rouve, L.-L., Cauffet, G. & Coulomb, J.-L. (2011b). Analytical Model for External Induction Variations of a Ferromagnetic Cylinder Undergoing High Mechanical Stresses in a Low Magnetic Field of Any Orientation. *IEEE Transactions on Magnetics*, 47(5), 1366–1369.
- Villari, E. (1865). Ueber Die Aenderungen Des Magnetischen Moments, Welche Der Zug Und Das Hindurchleiten Eines Galvanischen Stroms in Einem Stabe von Stahl Oder Eisen Hervorbringen. *Annalen der Physik*, 202(9), 87–122.
- Wang, Y., Liu, X., Wu, B., Xiao, J., Wu, D. & He, C. (2018b). Dipole Modeling of Stress-Dependent Magnetic Flux Leakage. *NDT & E International*, 95, 1–8.
- Wang, Z. D., Deng, B. & Yao, K. (2011). Physical Model of Plastic Deformation on Magnetization in Ferromagnetic Materials. *Journal of Applied Physics*, 109(8), 083928.
- Wilson, J. W., Tian, G. Y. & Barrans, S. (2007). Residual Magnetic Field Sensing for Stress Measurement. *Sensors and Actuators A: Physical*, 135(2), 381–387.
- Xu, M., Xu, M., Li, J., Ma, S. & Xing, H. (2012a). Discuss on Using Jiles-Atherton Theory for Charactering Magnetic Memory Effect. *Journal of Applied Physics*, 112(9), 093902.
- Xu, W. J., Duan, N. N., Wang, S. H., Guo, Y. G. & Zhu, J. G. (2015). Modeling the Stress Dependence of Magnetic Hysteresis Based on Stoner-Wohlfarth Theory. In *2015 IEEE International Conference on Applied Superconductivity and Electromagnetic Devices (ASEMD)* (pp. 378–379).

References for Chapter 5

- Atherton, D. L. & Szpunar, J. A. (1986). Effect of Stress on Magnetization and Magnetostriction in Pipeline Steel. *IEEE Transactions on Magnetics*, 22(5), 514–516.
- Atherton, D. L., Welbourn, C., Jiles, D. C., Reynolds, L. & Scott-Thomas, J. (1984). Stress-Induced Magnetization Changes of Steel Pipes—Laboratory Tests, Part II. *IEEE Transactions on Magnetics*, 20(6), 2129–2136.
- Bao, S., Fu, M., Gu, Y. & Hu, S. (2016). Evolution of the Piezomagnetic Field of Ferromagnetic Steels Subjected to Cyclic Tensile Stress with Variable Amplitudes. *Experimental Mechanics*, 56(6), 1017–1028.
- Bao, S. & Gong, S. F. (2012). Magnetomechanical Behavior for Assessment of Fatigue Process in Ferromagnetic Steel. *Journal of Applied Physics*, 112(11), 113902.

- Bao, S., Jin, W. L., Huang, M. F. & Bai, Y. (2010). Piezomagnetic Hysteresis as a Non-Destructive Measure of the Metal Fatigue Process. *NDT & E International*, 43(8), 706–712.
- Bao, S., Fu, M., Lou, H. & Bai, S. (2017a). Defect Identification in Ferromagnetic Steel Based on Residual Magnetic Field Measurements. *Journal of Magnetism and Magnetic Materials*, 441, 590–597.
- Bevington, P. R. & Robinson, D. K. (2003). *Data Reduction and Error Analysis for the Physical Sciences* (Third). New York, NY, McGraw-Hill.
- Bozorth, R. M. (1993). *Ferromagnetism*. Piscataway, N.J., IEEE Press. (Original work published 1951)
- Brown, W. F. (1949). Irreversible Magnetic Effects of Stress. *Physical Review*, 75(1), 147–154.
- Craik, D. J. & Wood, M. J. (1970). Magnetization Changes Induced by Stress in a Constant Applied Field. *Journal of Physics D: Applied Physics*, 3(7), 1009.
- Erber, T., Guralnick, S. A., Desai, R. D. & Kwok, W. (1997). Piezomagnetism and Fatigue. *Journal of Physics D: Applied Physics*, 30(20), 2818–2836.
- Gilman, J. J. (1968). Microdynamical Theory of Plasticity. In C. J. McMahon (Ed.), *Advances in Materials Research*. Interscience Publishers.
- Jiles, D. C. (1988a). The Effect of Compressive Plastic Deformation on the Magnetic Properties of AISI 4130 Steels with Various Microstructures. *Journal of Physics D: Applied Physics*, 21(7), 1196.
- Jiles, D. C. (1994a). Frequency Dependence of Hysteresis Curves in Conducting Magnetic Materials. *Journal of Applied Physics*, 76(10), 5849–5855.
- Jiles, D. C. (1994b). Modelling the Effects of Eddy Current Losses on Frequency Dependent Hysteresis in Electrically Conducting Media. *IEEE Transactions on Magnetics*, 30(6), 4326–4328.
- Jiles, D. C. (1995). Theory of the Magnetomechanical Effect. *Journal of Physics D: Applied Physics*, 28(8), 1537.
- Jiles, D. C. (2015). *Introduction to Magnetism and Magnetic Materials* (Third Edition). CRC Press.
- Jiles, D. C. & Atherton, D. L. (1984). Theory of the Magnetisation Process in Ferromagnets and Its Application to the Magnetomechanical Effect. *Journal of Physics D: Applied Physics*, 17(6), 1265.
- Jolink, C. T. (2018). *Magnetic Stray Field Analysis to Detect Plastic Deformation in Steel Cylinders: Experimental Research into Magnetomechanical Effect Under Impact Loading* (MSc Thesis). Delft University of Technology. Delft, the Netherlands.
- Karagiozova, D. & Jones, N. (2000). Dynamic Elastic–plastic Buckling of Circular Cylindrical Shells under Axial Impact. *International Journal of Solids and Structures*, 37(14), 2005–2034.
- Li, Z., Dixon, S., Cawley, P., Jarvis, R., Nagy, P. B. & Cabeza, S. (2017a). Experimental Studies of the Magneto-Mechanical Memory (MMM) Technique Using Permanently Installed Magnetic Sensor Arrays. *NDT & E International*, 92(Supplement C), 136–148.

- Makar, J. M. & Atherton, D. L. (1995). Effects of Isofield Uniaxial Cyclic Stress on the Magnetization of 2% Mn Pipeline Steel - Behavior on Minor Hysteresis Loops and Small Major Hysteresis Loops. *IEEE Transactions on Magnetics*, 31(3), 2220–2227.
- Maylin, M. G. & Squire, P. T. (1993a). Departures from the Law of Approach to the Principal Anhyseteric in a Ferromagnet. *Journal of Applied Physics*, 73(6), 2948–2955.
- Meijers, P. C., Jolink, C. T., Tsouvalas, A. & Metrikine, A. V. (2021a). Magnetic stray field measurements to identify and localise impact-induced plastic deformation in a steel structure [manuscript prepared]. *International Journal of Mechanical Sciences*.
- Ripka, P. (1992). Review of Fluxgate Sensors. *Sensors and Actuators A: Physical*, 33(3), 129–141.
- Ripka, P. (Ed.). (2000). *Magnetic Sensors and Magnetometers*. Norwood, MA, Artech House Publishers.
- Ruuskanen, P. & Kettunen, P. (1991). Reversible Component ΔB_r of the Stress-Induced Change in Magnetization as a Function of Magnetic Field Strength and Stress Amplitude. *Journal of Magnetism and Magnetic Materials*, 98(3), 349–358.
- Sablik, M. J., Yonamine, T. & Landgraf, F. J. G. (2004). Modeling Plastic Deformation Effects in Steel on Hysteresis Loops with the Same Maximum Flux Density. *IEEE Transactions on Magnetics*, 40(5), 3219–3226.
- Szulim, P., Gontarz, S. & Mączak, J. (2015). Calibration of Magnetic Field Sensors Used for Diagnosis of Steel Construction. *J. Electr. Eng.*, 66(6).
- Tebble, R. S. & Craik, D. J. (1969). *Magnetic Materials*. Wiley-Interscience.
- Wang, Z. D., Deng, B. & Yao, K. (2011). Physical Model of Plastic Deformation on Magnetization in Ferromagnetic Materials. *Journal of Applied Physics*, 109(8), 083928.
- Xu, M., Xu, M., Li, J. & Xing, H. (2012b). Using Modified J–A Model in MMM Detection at Elastic Stress Stage. *Nondestructive Testing and Evaluation*, 27(2), 121–138.

References for Chapter 6

- Belahcen, A., Peussa, T., Singh, D. & Rasilo, P. (2014). Computation of the Inverse Magnetostriction and Its Application in Mechanical Stress Sensing. In *9th IET International Conference on Computation in Electromagnetics (CEM 2014)* (pp. 1–2).
- Bulte, D. P. & Langman, R. A. (2002). Origins of the Magnetomechanical Effect. *Journal of Magnetism and Magnetic Materials*, 251(2), 229–243.
- Chikazumi, S. & Graham, C. D. (1997). *Physics of Ferromagnetism* (Second Edition). Oxford, Clarendon Press.
- Cullity, B. D. (1971). Fundamentals of Magnetostriction. *Journal of Metals*, 23(1), 35–41.
- Cullity, B. D. & Graham, C. D. (2009). *Introduction to Magnetic Materials* (Second Edition). IEEE Press.
- Daniel, L. (2013). An Analytical Model for the Effect of Multiaxial Stress on the Magnetic Susceptibility of Ferromagnetic Materials. *IEEE Transactions on Magnetics*, 49(5), 2037–2040.

- Daniel, L. & Hubert, O. (2009). An Equivalent Stress for the Influence of Multiaxial Stress on the Magnetic Behavior. *Journal of Applied Physics*, 105(7), 07A313.
- Deeks, A. J. & Randolph, M. F. (1993). Analytical Modelling of Hammer Impact for Pile Driving. *International Journal for Numerical and Analytical Methods in Geomechanics*, 17(5), 279–302.
- Edelstein, A. (2007). Advances in Magnetometry. *Journal of Physics: Condensed Matter*, 19(16), 165217.
- Federico, S., Consolo, G. & Valenti, G. (2019). Tensor Representation of Magnetostriction for All Crystal Classes. *Mathematics and Mechanics of Solids*, 24(9), 2814–2843.
- Fehlberg, E. (1969). *Low-Order Classical Runge-Kutta Formulas with Stepsize Control and Their Application to Some Heat Transfer Problems* (tech. rep. TR R-315).
- Hecker, R. & Schulz, R. K. (1997). Messung elastischer Wellen in Stahl- und Gesteinsstäben mit Hilfe des magnetoelastischen Effektes. *Materialwissenschaft und Werkstofftechnik*, 28(12), 571–574.
- Hubert, O. & Rizzo, K.-J. (2008). An hysteretic and dynamic piezomagnetic behavior of a low carbon steel. *Journal of Magnetism and Magnetic Materials*, 320(20), e979–e982.
- Itskov, M. (2019). *Tensor Algebra and Tensor Analysis for Engineers: With Applications to Continuum Mechanics* (Fifth Edition). Cham, Switzerland, Springer.
- Jiles, D. C. (1995). Theory of the magnetomechanical effect. *Journal of Physics D: Applied Physics*, 28(8), 1537.
- Jiles, D. C. & Atherton, D. L. (1984). Theory of the magnetisation process in ferromagnets and its application to the magnetomechanical effect. *Journal of Physics D: Applied Physics*, 17(6), 1265.
- Jogschies, L., Klaas, D., Kruppe, R., Rittinger, J., Taptimthong, P., Wienecke, A., Rissing, L. & Wurz, M. (2015). Recent developments of magnetoresistive sensors for industrial applications. *Sensors*, 15(11), 28665–28689.
- Jolliffe, I. T. & Cadima, J. (2016). Principal component analysis: A review and recent developments. *Philosophical Transactions of the Royal Society A: Mathematical, Physical and Engineering Sciences*, 374(2065), 20150202.
- Kim, Y. Y., Cho, S. H. & Lee, H. C. (2003). Application of magnetomechanical sensors for modal testing. *Journal of Sound and Vibration*, 268(4), 799–808.
- Logg, A., Mardal, K.-A. & Wells, G. (Eds.). (2012). *Automated Solution of Differential Equations by the Finite Element Method* (Vol. 84). Berlin, Heidelberg, Springer Berlin Heidelberg.
- Lollioz, L., Pattofatto, S. & Hubert, O. (2006). Application of piezo-magnetism for the measurement of stress during an impact. *Journal of Electrical Engineering*, 57(8), 6.
- Makar, J. M. & Atherton, D. L. (1995). Effects of isofield uniaxial cyclic stress on the magnetization of 2% Mn pipeline steel - behavior on minor hysteresis loops and small major hysteresis loops. *IEEE Transactions on Magnetics*, 31(3), 2220–2227.

- Meijers, P. C., Tsouvalas, A. & Metrikine, A. V. (2021c). Spatial variation of the dynamic magnetic stray field of a thin-walled steel structure [manuscript in preparation]. *Journal of Sound and Vibration*.
- Peussa, T. & Belahcen, A. (2015). Coupled Wave-Equation and Eddy-Current Model for Modelling and Measuring Propagating Stress-Waves. *Archives of Electrical Engineering*, 64(2), 215–226.
- Ripka, P. (Ed.). (2000). *Magnetic Sensors and Magnetometers*. Norwood, MA, Artech House Publishers.
- Sablik, M. J., Riley, L. A., Burkhardt, G. L., Kwun, H., Cannell, P. Y., Watts, K. T. & Langman, R. A. (1994). Micromagnetic Model for Biaxial Stress Effects on Magnetic Properties. *Journal of Magnetism and Magnetic Materials*, 132(1), 131–148.
- Schneider, C. S., Cannell, P. Y. & Watts, K. T. (1992). Magnetoelasticity for Large Stresses. *IEEE Transactions on Magnetics*, 28(5), 2626–2631.
- Shin, K. & Hammond, J. (2008). *Fundamentals of Signal Processing for Sound and Vibration Engineers* (First Edition). Chichester, England; Hoboken, NJ, Wiley.
- Viana, A., Rouve, L.-L., Cauffet, G. & Coulomb, J.-L. (2010). Magneto-Mechanical Effects Under Low Fields and High Stresses - Application to a Ferromagnetic Cylinder Under Pressure in a Vertical Field. *IEEE Transactions on Magnetics*, 46(8), 2872–2875.

References for Chapter 7

- Atherton, D. L., Coathup, L. W., Jiles, D. C., Longo, L., Welbourn, C. & Teitsma, A. (1983). Stress Induced Magnetization Changes of Steel Pipes–Laboratory Tests. *IEEE Transactions on Magnetics*, 19(4), 1564–1568.
- Atherton, D. L., Welbourn, C., Jiles, D. C., Reynolds, L. & Scott-Thomas, J. (1984). Stress-Induced Magnetization Changes of Steel Pipes–Laboratory Tests, Part II. *IEEE Transactions on Magnetics*, 20(6), 2129–2136.
- Google Maps. (n.d.). *Satellite image of Sliedrecht, the Netherlands*. Retrieved January 31, 2020, from <https://www.google.com/maps/@51.8214026,4.7570626,208m/data=!3m1!1e3>
- Igwemezie, V., Mehmanparast, A. & Kolios, A. (2019). Current Trend in Offshore Wind Energy Sector and Material Requirements for Fatigue Resistance Improvement in Large Wind Turbine Support Structures – A Review. *Renewable and Sustainable Energy Reviews*, 101, 181–196.
- Lee, S.-N., You, B.-J., Limb, M.-S., Oh, S.-R., Han, S.-S. & Lee, S. H. (2002). Visual Measurement of Pile Penetration and Rebound Movement Using a High-Speed Line-Scan Camera. In *Proceedings 2002 IEEE International Conference on Robotics and Automation (Cat. No.02CH37292)* (4307–4312 vol.4).
- Lim, M.-S. & Lim, J. (2008). Visual Measurement of Pile Movements for the Foundation Work Using a High-Speed Line-Scan Camera. *Pattern Recognition*, 41(6), 2025–2033.
- Meijers, P. C., Tsouvalas, A. & Metrikine, A. V. (2020). Monitoring Monopile Penetration through Magnetic Stray Field Measurements. In M. Papadrakakis, M. Fragiadakis & C.

- Papadimitriou (Eds.), *Proceedings of the XI International Conference on Structural Dynamics* (pp. 1272–1280). EASD Procedia.
- Meijers, P. C., Tsouvalas, A. & Metrikine, A. V. (2021b). Magnetomechanical response of a steel monopile during impact pile driving. *Engineering Structures*, 240, 112340.
- Oliveira, J. R. M. S., Nunes, P. R. R. L., Silva, M. R. L., Cabral, D. A., Ferreira, A. C. G., Carneiro, L. A. V. & Giraldo, M. T. M. R. (2011). Field Apparatus for Measurement of Elastic Rebound and Final Set for Driven Pile Capacity Estimation. *Geotechnical Testing Journal*, 34(2), 103103.
- Qiu, J., Zhou, J., Zhao, S., Zhang, H. & Liao, L. (2020). Statistical Quantitative Evaluation of Bending Strength of Corroded RC Beams via SMFL Technique. *Engineering Structures*, 209, 110168.
- Raza, A., Aqil, U., Baneen, U. & Saleem, M. Q. (2019). Deep Foundation Testing Using Immunity-Based Displacement Measurement in Successive-Sparse Images. *KSCE Journal of Civil Engineering*, 23(10), 4212–4222.
- Schallert, M. & Klingmüller, O. (2019). Assessment of Soil Setup from Pile Installation Monitoring and Restrike Tests of Offshore Wind Turbine Foundation Piles. In P. Bullock, G. Verbeek, S. Paikowsky & D. Tara (Eds.), *10th International Conference on Stress Wave Theory and Testing Methods for Deep Foundations* (pp. 681–696). ASTM International.
- Timoshenko, S. & Goodier, J. N. (1951). *Theory of Elasticity* (Second Edition). New York, NY, McGraw-Hill.
- Wisotzki, E., van Foeken, R., van Esch, P. & Novakovic, D. (2019). Strain and Acceleration Measurements at Instrumentation Distances to the Pile Head of 0.5 and 1.0 Times the Diameter—Offshore Pile-Monitoring Experience. In P. Bullock, G. Verbeek, S. Paikowsky & D. Tara (Eds.), *10th International Conference on Stress Wave Theory and Testing Methods for Deep Foundations* (pp. 506–519). ASTM International.
- Yeu, Y., Kim, Y. S. & Kim, D. (2016). Development of Safe and Reliable Real-Time Remote Pile Penetration and Rebound Measurement System Using Close-Range Photogrammetry. *International Journal of Civil Engineering*, 14(7), 439–450.

References for Appendix A

- Bertotti, G. (1998). *Hysteresis in Magnetism: For Physicists, Materials Scientists, and Engineers*. San Diego, Academic Press.
- Leite, J. V., Sadowski, N., Kuo-Peng, P., Batistela, N. J., Bastos, J. P. A. & de Espindola, A. A. (2004). Inverse Jiles-Atherton Vector Hysteresis Model. *IEEE Transactions on Magnetics*, 40(4), 1769–1775.
- Raghunathan, A., Melikhov, Y., Snyder, J. E. & Jiles, D. C. (2009). Generalized Form of An hysteretic Magnetization Function for Jiles–Atherton Theory of Hysteresis. *Applied Physics Letters*, 95(17), 172510.
- Sablík, M. J. & Jiles, D. C. (1993). Coupled Magnetoelastic Theory of Magnetic and Magnetostrictive Hysteresis. *IEEE Transactions on Magnetics*, 29(4), 2113–2123.

References for Appendix C

Sablik, M. J., Rubin, S. W., Riley, L. A., Jiles, D. C., Kaminski, D. A. & Biner, S. B. (1993). A Model for Hysteretic Magnetic Properties under the Application of Noncoaxial Stress and Field. *Journal of Applied Physics*, 74(1), 480–488.

A

Isotropic anhysteretic magnetisation

III

Here, a vectorial expression for the anhysteretic magnetisation in an isotropic material is derived. For a typical magnetic domain with moment \mathbf{m} , the magnetostatic (or potential) energy in an external field \mathbf{H} is (Sablik and Jiles, 1993)

$$E = -\mu_0 \mathbf{m} \cdot \mathbf{H} = -\mu_0 m H \cos \theta, \quad (\text{A.1})$$

in which μ_0 denotes the magnetic constant, $m = \|\mathbf{m}\|$, $H = \|\mathbf{H}\|$, and θ is the angle between the magnetic moment and the field. In a spherical coordinate system in which \mathbf{H} is directed along the positive z -axis (Figure A.1), the single-moment partition function reads (Raghunathan et al., 2009)

$$Z_m = \int_0^{2\pi} \int_0^\pi e^{H/a \cos \theta} \sin \theta \, d\theta \, d\varphi,$$

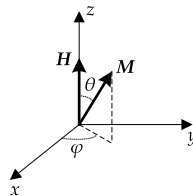


Figure A.1: Spherical coordinate system used in the derivation of the isotropic anhysteretic magnetisation.

in which $a = \frac{k_B T}{\mu_0 m}$, and θ is the polar angle, φ denotes the azimuthal angle, k_B represents Boltzmann's constant and T is the absolute temperature. The above expression sums the contributions for all possible orientations of the moment with respect to the external field. For a collection of N identical moments, the free energy A of the composite system is computed from the total partition function as (Bertotti, 1998, pp. 130–132):

$$A = -k_B T \ln Z_m^N.$$

With this expression, the anhysteretic magnetisation for the N moments occupying a volume ΔV is the derivative of the free energy (Raghunathan et al., 2009):

$$\mathbf{M}_{\text{an}} = -\frac{1}{\mu_0 \Delta V} \left[\frac{\partial A}{\partial \mathbf{H}} \right]_T = \frac{N k_B T}{\mu_0 \Delta V} \left[\frac{\partial}{\partial \mathbf{H}} \ln Z_m \right]_T.$$

Substituting the single-moment partition function and taking the derivative yields:

$$\mathbf{M}_{\text{an}} = \frac{Nm \mathbf{H}}{\Delta V H} \frac{\int_0^{2\pi} \int_0^\pi \cos \theta e^{H/a \cos \theta} \sin \theta \, d\theta \, d\varphi}{\int_0^{2\pi} \int_0^\pi e^{H/a \cos \theta} \sin \theta \, d\theta \, d\varphi},$$

which is rewritten into a simpler form by evaluation of the integrals:

$$\mathbf{M}_{\text{an}} = M_s \mathcal{L} \left(\frac{H}{a} \right) \frac{\mathbf{H}}{H}, \quad (\text{A.2})$$

in which $M_s = \frac{Nm}{\Delta V}$ is the saturation magnetisation and

$$\mathcal{L}(x) = \coth(x) - \frac{1}{x}$$

is the modified Langevin function. Equation (A.2) is identical to the vectorial form presented by Leite et al. (2004). The above expression implies that the anhysteretic magnetisation is always coaxial with the external field for an isotropic solid. In case the external field direction is known a priori, e.g. when the effect of the demagnetising field is negligible, the expression further reduces to:

$$M_{\text{an}} = M_s \mathcal{L} \left(\frac{H}{a} \right), \quad (\text{A.3})$$

which is the formulation for the anhysteretic magnetisation normally encountered in literature (Sablik and Jiles, 1993).

B

Full relations to compute the magnetic field of a thin-walled cylinder

For a cylinder discretised into N elements, the auxiliary field \mathbf{H} at the evaluation point \mathbf{p} is given by

$$\mathbf{H}(\mathbf{p}) = \frac{1}{4\pi} \sum_{i=1}^N \oint_{\Gamma_i} \mathbf{M}(\mathbf{r}) \cdot \mathbf{n}_i \frac{\mathbf{s}}{s^3} d\Gamma_i, \quad (\text{B.1})$$

in which $\mathbf{s} = \mathbf{p} - \mathbf{r}$ is the separation vector, $s = \|\mathbf{s}\|$ represents the corresponding magnitude, and \mathbf{r} denotes the internal points of the structure. By assuming that the magnetisation is constant over an element and that it resides at the barycentre of each element \mathbf{r}_i , the integral is replaced by a matrix-vector multiplication:

$$\mathbf{H}(\mathbf{p}) = \sum_{i=1}^N \mathbf{G}_i \mathbf{M}(\mathbf{r}_i), \quad (\text{B.2})$$

in which \mathbf{G}_i contains the results of the evaluation of the boundary integral, which consists of four line integrals. Figure B.1 shows a systematisation of element i , wherein these line integrals are along boundaries A , B , C and D , which have the following outward normals:

$$\mathbf{n}_A = -1\boldsymbol{\theta},$$

$$\mathbf{n}_B = +1\boldsymbol{\theta},$$

$$\mathbf{n}_C = -1\mathbf{z},$$

$$\mathbf{n}_D = +1\mathbf{z}.$$

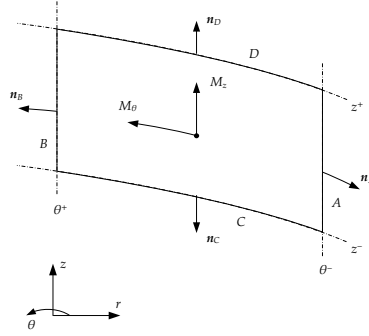


Figure B.1: Schematic representation of element i .

For a cylinder, it is natural to treat the geometry in cylindrical coordinates. However, the resulting contributions to the auxiliary field $\mathbf{H}(\mathbf{p})$ are expressed in Cartesian coordinates. Consequently, the coordinates of the element's barycentre are transformed to the Cartesian system by:

$$x_i = R_i \cos(\theta_i), \quad (\text{B.3a})$$

$$y_i = R_i \sin(\theta_i), \quad (\text{B.3b})$$

in which R_i and θ_i represents the radius at and the circumferential position of the element's barycentre, respectively. Given this, the function for the magnitude of the separation vector is

$$s(\mathbf{p}, R, \theta, z) = \sqrt{(x_p - R \cos(\theta))^2 + (y_p - R \sin(\theta))^2 + (z_p - z)^2}, \quad (\text{B.4})$$

which is simply the Cartesian distance between points \mathbf{p} and \mathbf{r} .

B.1. Cartesian coordinates

In Cartesian coordinates, the evaluation point is expressed as $\mathbf{p} = [x_p \ y_p \ z_p]^T$. For each edge of the element, the contributions to the x -component of \mathbf{H} read:

$$A_x = \frac{h_i}{4\pi} \int_{z_i^-}^{z_i^+} -1 \cdot \frac{x_p - R_i \cos(\theta_i^-)}{s(\mathbf{p}, R_i, \theta_i^-, z)^3} dz,$$

$$B_x = \frac{h_i}{4\pi} \int_{z_i^-}^{z_i^+} +1 \cdot \frac{x_p - R_i \cos(\theta_i^+)}{s(\mathbf{p}, R_i, \theta_i^+, z)^3} dz,$$

$$C_x = \frac{h_i R_i}{4\pi} \int_{\theta_i^-}^{\theta_i^+} -1 \cdot \frac{x_p - R_i \cos(\theta)}{s(\mathbf{p}, R_i, \theta, z_i^-)^3} d\theta,$$

$$D_x = \frac{h_i R_i}{4\pi} \int_{\theta_i^-}^{\theta_i^+} +1 \cdot \frac{x_p - R_i \cos(\theta)}{s(\mathbf{p}, R_i, \theta, z_i^+)^3} d\theta.$$

For the contributions to the y -component of \mathbf{H} , the expressions are:

$$A_y = \frac{h_i}{4\pi} \int_{z_i^-}^{z_i^+} -1 \cdot \frac{y_p - R_i \sin(\theta_i^-)}{s(\mathbf{p}, R_i, \theta_i^-, z)^3} dz,$$

$$B_y = \frac{h_i}{4\pi} \int_{z_i^-}^{z_i^+} +1 \cdot \frac{y_p - R_i \sin(\theta_i^+)}{s(\mathbf{p}, R_i, \theta_i^+, z)^3} dz,$$

$$C_y = \frac{h_i R_i}{4\pi} \int_{\theta_i^-}^{\theta_i^+} -1 \cdot \frac{y_p - R_i \sin(\theta)}{s(\mathbf{p}, R_i, \theta, z_i^-)^3} d\theta,$$

$$D_y = \frac{h_i R_i}{4\pi} \int_{\theta_i^-}^{\theta_i^+} +1 \cdot \frac{y_p - R_i \sin(\theta)}{s(\mathbf{p}, R_i, \theta, z_i^+)^3} d\theta.$$

For the contributions to the z -component of \mathbf{H} , the expressions become:

$$A_z = \frac{h_i}{4\pi} \int_{z_i^-}^{z_i^+} -1 \cdot \frac{z_p - z}{s(\mathbf{p}, R_i, \theta_i^-, z)^3} dz,$$

$$B_z = \frac{h_i}{4\pi} \int_{z_i^-}^{z_i^+} +1 \cdot \frac{z_p - z}{s(\mathbf{p}, R_i, \theta_i^+, z)^3} dz,$$

$$C_z = \frac{h_i R_i}{4\pi} \int_{\theta_i^-}^{\theta_i^+} -1 \cdot \frac{z_p - z_i^-}{s(\mathbf{p}, R_i, \theta, z_i^-)^3} d\theta,$$

$$D_z = \frac{h_i R_i}{4\pi} \int_{\theta_i^-}^{\theta_i^+} +1 \cdot \frac{z_p - z_i^+}{s(\mathbf{p}, R_i, \theta, z_i^+)^3} d\theta.$$

Since the tangential magnetisation M_θ can only contribute through sides A and B , and the axial component M_z solely adds via sides C and D , the total contribution of each component yields

$$G_{x\theta} = A_x + B_x, \quad (\text{B.5a})$$

$$G_{xz} = C_x + D_x, \quad (\text{B.5b})$$

$$G_{y\theta} = A_y + B_y, \quad (\text{B.5c})$$

$$G_{zz} = C_y + D_y, \quad (\text{B.5d})$$

$$G_{z\theta} = A_z + B_z, \quad (\text{B.5e})$$

$$G_{zz} = C_z + D_z. \quad (\text{B.5f})$$

More compactly, these relations are assembled into a matrix as:

$$\mathbf{H}(\mathbf{p}) = \begin{bmatrix} H_x \\ H_y \\ H_z \end{bmatrix} = \sum_{i=1}^N \begin{bmatrix} G_{x\theta} & G_{xz} \\ G_{y\theta} & G_{yz} \\ G_{z\theta} & G_{zz} \end{bmatrix}_i \begin{bmatrix} M_\theta \\ M_z \end{bmatrix}_i. \quad (\text{B.6})$$

In the above, $(G_{x\theta})_i$ represents the influence of the circumferential magnetisation component of element i to the auxiliary field in the x -direction, etc.

B.2. Cylindrical coordinates

When the evaluation point $(\mathbf{p} = [r_p \ \theta_p \ z_p]^T)$ and the auxiliary field are expressed in cylindrical coordinates, the contributions to the radial and circumferential auxiliary field are determined from the Cartesian counterparts presented in Equations (B.5), yielding:

$$G_{r\theta} = \cos(\theta_p) G_{x\theta} + \sin(\theta_p) G_{y\theta}, \quad (\text{B.7a})$$

$$G_{rz} = \cos(\theta_p) G_{xz} + \sin(\theta_p) G_{yz}, \quad (\text{B.7b})$$

$$G_{\theta\theta} = -\sin(\theta_p) G_{x\theta} + \cos(\theta_p) G_{y\theta}, \quad (\text{B.7c})$$

$$G_{\theta z} = -\sin(\theta_p) G_{xz} + \cos(\theta_p) G_{yz}. \quad (\text{B.7d})$$

Naturally, the contributions to the axial auxiliary field are identical to the Cartesian expressions under this transformation. Collecting all cylindrical terms gives rise to the following summation over the structure's elements:

$$\mathbf{H}(\mathbf{p}) = \begin{bmatrix} H_r \\ H_\theta \\ H_z \end{bmatrix} = \sum_{i=1}^N \begin{bmatrix} G_{r\theta} & G_{rz} \\ G_{\theta\theta} & G_{\theta z} \\ G_{z\theta} & G_{zz} \end{bmatrix}_i \begin{bmatrix} M_\theta \\ M_z \end{bmatrix}_i, \quad (\text{B.8})$$

in which $(G_{r\theta})_i$ represents the influence of the circumferential magnetisation component of element i to the auxiliary field in the radial direction, etc.

B.3. Restrictions on the element size

To ensure the accuracy of the computed stray field, the elements should be sufficiently small, especially for evaluation points close to the cylinder's surface. For this, the following heuristic measure should be employed: for a given distance d from the surface, the number of elements in circumferential (N_θ) and axial direction (N_z) must be such that

$$d > \min(d_\theta, d_z), \quad (\text{B.9})$$

in which

$$d_{\theta} = \frac{1}{2} \frac{2\pi R}{N_{\theta}},$$
$$d_z = \frac{1}{2} \frac{L}{N_z},$$

in which R and L denote the radius and the length of the cylinder, respectively. These quantities are half the width of an element in each direction.

C

Effective stress for coaxial fields

When the magnetisation and the external magnetic field are approximately coaxial, e.g. in rod-shaped specimens, the stress-induced effective field due to a uniaxial stress is often assumed to be parallel to the other field, which, in that case, is expressed as

$$H_{\sigma} = \frac{3\sigma_0}{2\mu_0} \frac{\partial \lambda}{\partial M}, \quad (\text{C.1})$$

in which σ_0 is the signed magnitude of the uniaxial stress. In case this stress is applied along a line that differs from the magnetic field direction, this expression can still be applied by introducing an effective stress σ . Projecting the stress-induced effective field vector (Equation (6.24)) onto the magnetisation direction m yields

$$H_{\sigma} = \frac{3\sigma_0}{2\mu_0} \frac{\partial \lambda}{\partial M} \left(\cos^2 \varphi - \frac{1}{3} \right), \quad (\text{C.2})$$

in which φ is the angle between the magnetisation and the stress direction. By comparing the two above expressions, the effective stress is

$$\sigma = \sigma_0 \left(\cos^2 \varphi - \frac{1}{3} \right). \quad (\text{C.3})$$

This expression results directly from the assumption that the magnetostrictive strain tensor is isotropic and isochoric.

Sablik et al. (1993) derive an alternative expression for the effective stress in this situation by treating the magnetostrictive strain as a principal strain and rotating it towards the

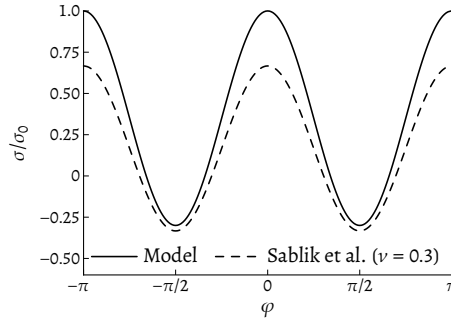


Figure C.1: Comparison of the two expressions for the effective stress σ in the magnetisation direction for different angles.

magnetisation direction, resulting in

$$\sigma = \sigma_0 (\cos^2 \varphi - \nu \sin^2 \varphi) = \sigma_0 ((1 + \nu) \cos^2 \varphi - \nu), \quad (\text{C.4})$$

in which ν is Poisson's ratio. Figure C.1 shows the effective stress for varying angles computed by Equations (C.3) and (C.4). Although they display identical behaviour when the angle φ is varied, their amplitudes differ, which results from the different approach pursued here and by Sablik et al. (1993). Since the amplitude of the final expression is highly dependent on other model parameters, this discrepancy does not have a large influence on the final results. Coincidentally, a common value of Poisson's ratio for metals is $\nu = 0.3$, which is close to the $1/3$ that emerges from the isochoric assumption.

Curriculum Vitæ

Peter Christiaan Meijers

14-12-1990 Born in Woudrichem, the Netherlands

Education

2003–2009 VWO
Lyceum de Hoven, Gorinchem, the Netherlands

2009–2013 Bachelor in Civil Engineering
Delft University of Technology

2013–2016 Master in Civil Engineering
Delft University of Technology
Thesis: Development of the Generalised Hybrid Turbulence Model
for RANS simulations
Supervisors: Prof.dr.ir. W. S. J. Uijttewaal, Dr.ir. A. H. van Zuijlen, Ir. L.
Florentie

2016–2020 PhD research
Delft University of Technology
Thesis: Non-located methods to infer deformation in steel
structures—The magnetomechanical effect in cylindrical
structures subjected to impact loads
Promotor: Prof.dr. A. V. Metrikine
Copromotor: Dr.ir. A. Tsouvalas

2020– Post-doctoral research
Delft University of Technology

List of Publications

Journal publications

4. **Meijers, P. C.**, Tsouvalas, A. & Metrikine, A. V. (2021). Spatial variation of the dynamic magnetic stray field of a thin-walled steel structure [manuscript in preparation]. *Journal of Sound and Vibration*
3. **Meijers, P. C.**, Jolink, C. T., Tsouvalas, A. & Metrikine, A. V. (2021). Magnetic stray field measurements to identify and localise impact-induced plastic deformation in a steel structure [manuscript prepared]. *International Journal of Mechanical Sciences*
2. **Meijers, P. C.**, Tsouvalas, A. & Metrikine, A. V. (2021). Magnetomechanical response of a steel monopile during impact pile driving. *Engineering Structures*, 240, 112340
1. **Meijers, P. C.**, Tsouvalas, A. & Metrikine, A. V. (2018). A Non-Collocated Method to Quantify Plastic Deformation Caused by Impact Pile Driving. *International Journal of Mechanical Sciences*, 148, 1–8

Conference publications

4. **Meijers, P. C.**, Tsouvalas, A. & Metrikine, A. V. (2020). Monitoring Monopile Penetration through Magnetic Stray Field Measurements. In M. Papadrakakis, M. Fragiadakis & C. Papadimitriou (Eds.), *Proceedings of the XI International Conference on Structural Dynamics* (pp. 1272–1280). EASD Procedia
3. Ivanov, H. I., Ermolaeva, N. S., Breukels, J., de Jong, B. C., de Vries, P. A. & **Meijers, P. C.** (2019). Steel wire rope sling breaking load reduction due to bending, 'Exploring Opportunities – Synthetic/Steel', *Proceedings of the OIPEEC Conference 2019, The Hague, The Netherlands*, The Hague, the Netherlands, OIPEEC
2. **Meijers, P. C.**, Tsouvalas, A. & Metrikine, A. V. (2018). Plasticity Detection and Quantification in Monopile Support Structures Due to Axial Impact Loading. *MATEC Web of Conferences*, 148, 15003
1. **Meijers, P. C.**, Tsouvalas, A. & Metrikine, A. V. (2017). The Effect of Stress Wave Dispersion on the Drivability Analysis of Large-Diameter Monopiles. *Procedia Engineering*, 199, 2390–2395

Patents

1. **Meijers, P. C.**, Tsouvalas, A. & Metrikine, A. V. (2019, June 25). *Non-contact system for monitoring a metallic magnetic structure under dynamic load* (N2023374)

